The effect of pressure, temperature and oxygen fugacity on the stability of subducted carbonates and implications for the deep carbon cycle

Der Bayreuther Graduiertenschule für Mathematik und Naturwissenschaften

zur Erlangung der Würde eines

Doktors der Naturwissenschaften

- Dr. rer. nat. -

Dissertation

vorgelegt von

Valerio Cerantola

aus Bassano del Grappa (Italien)

Bayreuth, 2016

Die vorliegende Arbeit wurde in der Zeit von November 2012 bis Februar 2016 am Bayerisches Geoinstitut, Universität Bayreuth und ESRF (European Synchrotron Radiation Facility) Grenoble unter Leitung von Prof. Dr. L.S. Dubrovinsky und Dr. A. Chumakov angefertigt.

Vollständiger Abdruck der von der Bayreuther Graduiertenschule für Mathematik und Naturwissenschaften (BayNAT) der Universität Bayreuth genehmigten Dissertation zur Erlangung des akademischen Grades eines Doktors der Naturwissenschaften (Dr. rer. nat.).

Datum der Einreichung der Dissertation: 12.10.2016

Zulassung durch das Leitungsgremium: 19.10.2016

Wissenschaftlichen Kolloquiums: 10.02.2017

Amtierender Direktor: Prof. Dr. Stephan Kümmel

Prüfungsausschuss:
Prof. Dr. Leonid Dubrovinsky (Erstgutachter)
Prof. Dr. Daniel Frost (Zweitgutachter)
Dr. Hauke Marquardt (Vorsitz)
Prof. Dr. David Rubie

Beginnings are usually scary,
and endings are usually sad,
but its everything in between
that makes it all worth living.

R.N.M.

Abstract

This cumulative thesis reports an experimental investigation of the stability of Fe-carbonates at mantle pressures and temperatures as well as analysis of an inclusion in diamond from the shallow lower mantle. The goal of the work is first to determine the stability regions of iron (or iron-bearing) carbonates inside the Earth, their phase transformation(s) and decomposition product(s) at specific conditions of the Earth's interior, and second to elucidate the physical and chemical mechanisms behind these processes. The major tools used in these studies are laser heated diamond anvil cells (to generate pressures and temperatures of the Earth's interior), powder and single crystal X-ray diffraction (for phase identification and structure determination), and ^{57}Fe Mössbauer spectroscopy (to detect structural and spin changes in Fe-bearing materials). Additionally, Raman spectroscopy and X-ray Absorption Near Edge Spectroscopy (XANES) are utilized to investigate changes in lattice vibrations and the local environment around specific atoms.

Compression of siderite ($FeCO_3$) at quasi-hydrostatic conditions and ambient temperature reveal that spin crossover in ferrous iron takes place over a broad pressure range, between 40 and 47 GPa. This observation is in contrast to previous X-ray diffraction data that described the transition as a sharp volume collapse at approximately 43 GPa. Based on these results, electron spin pairing in $FeCO_3$ is considered to be a dynamic process, where Fe atoms can be either in the high spin or low spin states in the crossover region. Experimentally observed and simulated XANES spectra in the spin crossover pressure region are in good agreement. Mössbauer spectroscopy data provide information on the effects of differential stress on the local structure around iron atoms in $FeCO_3$. Experiments performed on single crystals (under quasi-hydrostatic conditions) and powder (under non-hydrostatic conditions) demonstrate that local distortions of the FeO_6 octahedra in powder samples cause spin crossover to start at higher pressure than for single crystals and broaden its transition pressure range. Heating of $FeCO_3$ at pressures of ~ 50 GPa to temperatures corresponding to the geotherm causes partial dissociation with formation of iron oxides such as α-Fe_2O_3, orthorhombic hp-Fe_3O_4, and Fe_5O_7. Heating of $FeCO_3$ at pressures above ~70 GPa to temperatures above ~1400 K produces two new compounds, tetrairon (III) orthocarbonate, $Fe_4^{3+}C_3O_{12}$, and diiron (II) diiron (III) tetracarbonate, $Fe_2^{2+}Fe_2^{3+}C_4O_{13}$, where both contain CO_4 tetrahedra in their crystal

structures. $Fe_4^{3+}C_3O_{12}$ is stable only at limited temperatures in between ~1400 K and ~2000 K; however it can be used as a precursor to synthesize $Fe_2^{2+}Fe_2^{3+}C_3O_{13}$ through self-oxidation-reduction reactions. Diiron (II) diiron (III) tetracarbonate is stable at conditions along the entire geotherm to depths of at least 2500 km, thus demonstrating that high-pressure carbonates are stable in the Earth's lower mantle.

The origin of lower mantle diamonds might be linked to the charge balance of iron oxidation in ferropericlase ((Mg,Fe)O) and carbon reduction in subducted carbonates. Here, a ferropericlase inclusion still contained within its diamond host from Juina (Brazil) was studied using the Synchrotron Mössbauer Source. This non-destructive technique with high spatial resolution (~15 μm^2) enabled measurements in multiple regions of the 150×150 μm^2 inclusion to be sampled. Beside the dominant signal of ferropericlase, a minor magnetic component was also observed, whose abundance varies systematically across the inclusion. Hyperfine parameters of the magnetic component are consistent with magnesioferrite, and the absence of superparamagnetism allows the minimum particle size of the magnetic phase to be estimated as ~ 30 nm. Fe^{3+}/Fe_{tot} values in ferropericlase are below the detection limit (0.02) and are consistent with those reported for other ferropericlase inclusions from Juina. The study of Fe^{3+}/Fe_{tot} in ferropericlase can provide constraints on its history, and ultimately on the process of diamond formation and exhumation from the transition zone and shallow lower mantle regions.

Zusammenfassung

Diese kumultative Dissertation behandelt experimentelle Untersuchungen sowohl zur Stabilität von Eisenkarbonaten unter Drücken und Temperaturen, wie sie im Erdmantel vorliegen, als auch eines Diamanteinschlusses aus den oberen Regionen des unteren Mantels. Das Ziel der Arbeit ist es, zum einen die Stabilitätsbereiche von Eisen- bzw. eisenhaltigen Karbonaten innerhalb des Erdinneren, ihre Phasenumwandlungen und ihre Entmischungsprodukte unter Berücksichtigung der speziellen Bedingungen des Erdinneren zu bestimmen und zum anderen die zugrundeliegenden physikalischen und chemischen Mechanismen aufzuklären. Die wichtigsten experimentellen Verfahren, die für für diese Studien benutzt wurden, sind lasergeheizte Diamantstempelzellen (DAC) zur Erzeugung der Drücke und Temperaturen vorliegend im Erdinneren, Pulver- und Einkristallbeugung zur Phasen- und Strukturbestimmung, und (Eisen) Mössbauerspektroskopie zur Bestimmung struktureller und Spin-Änderungen eisenhaltiger Verbindungen. Zusätzlich wurden RAMAN und XANES (X-ray Absorption Near Edge Spectroscopy) Techniken benutzt, um Änderungen der Gitterschwingungen bzw. die lokale Umgebung ausgesuchter Atome zu untersuchen.

Die Kompression von Siderit ($FeCO_3$) unter quasi-hydrostatischen Bedingungen und bei Raumtemperatur zeigt, dass Spinübergänge in zweiwertigem Eisen über einen weiten Druckbereich von 40 bis 47 GPa stattfinden. Dieses Ergebnis steht im Widerspruch zu früheren Röntgenbeugungsdaten, die den Übergang als einen scharfen Volumenkollaps bei etwa 43 GPa beschreiben. Auf Grund dieser Ergebnisse wird die Elektronenpaarung in $FeCO_3$ als dynamischer Prozeß im Spinübergangsbereich beschrieben, bei dem die Eisenatome entweder einen Hochspin- oder Niedrigspinzustand einnehmen können. In diesem Spinübergangsbereich stimmen experimentelle und simulierte XANES Spektren gut überein. Mössbauerdaten machen Angaben über Effekte, hervorgerufen von Spannungsgradienten, auf die lokale Struktur der Eisenatome in $FeCO_3$. Experimente mit Einkristallen unter quasi-hydrostatischen Bedingungen und mit Pulverproben unter nicht-hydrostatischen Bedingungen zeigen, dass die lokalen Verzerrungen der FeO_6 Oktaeder in Pulverproben sowohl den Spinübergang erst bei höheren Drücken als bei Einkristallen hervorrufen als auch deren Druckbereich verbreitern. Heizen von $FeCO_3$ auf Temperaturen der Geotherme führt bei Drücken um 50 GPa zur teilweisen

Dissoziation unter Bildung von Eisenoxiden wie α-Fe_2O_3, orthorombischen hp-Fe_3O_4 und Fe_5O_7. Bei Drücken über 70 GPa und bei Temperaturen jenseits von 1400 K entstehen aus $FeCO_3$ zwei neue Verbindungen, Tetraeisen (III) Orthokarbonat, $Fe_4^{3+}C_3O_{12}$, and Dieisen (II) Dieisen (III) Tetrakarbonat, $Fe_2^{2+}Fe_2^{3+}C_4O_{13}$. Beide enthalten CO_4 Tetraeder in ihrer Kristallstruktur. $Fe_4^{3+}C_3O_{12}$ ist nur in einem begrenzten Temperaturbereich zwischen etwa 1400 K und etwa 2000 K stabil. Es kann jedoch als Vorstufe zur Herstellung von $Fe_2^{2+}Fe_2^{3+}C_4O_{13}$ durch Disproportionierung benutzt werden. Dieisen (II) Dieisen (III) Tetrakarbonat ist unter Konditionen der gesamten Geotherme bis zu Tiefen von wenigstens 2500 km stabil. Das zeigt, dass hp-Karbonate im unteren Erdmantel stabil sind.

Der Ursprung von Diamanten aus dem unteren Mantel kann vielleicht mit dem Ladungsgleichgewicht bei der Eisenoxidation in Ferroperiklas ((Mg,Fe)O) und der Kohlenstoffreduktion von subduzierten Karbonaten in Verbindung gebracht werden. Ein Ferroperiklas-Einschluss, noch unversehrt innerhalb eines Diamanten aus Juina (Brasilien), wurde mit Hilfe der Synchrotron Mössbauer Source (SMS) untersucht. Diese zerstörungsfreie Methode mit ihrer hohen Ortsauflösung (~ 15 μm^2) erlaubte detaillierte Messungen in unterschiedlichen Bereichen des 150 ×150 μm^2 großen Einschlusses. Neben des dominanten Signals von Ferropericlas wurde auch eine schwache magnetische Komponente, deren Anteil sich systematisch über den Einschluss veränderte, beobachtet. Die Hyperfeinwechselwirkungparameter dieser magnetischen Komponente stimmen mit denen von Magnesioferrit überein. Da kein Superparamagnetismus beobachtet wurde, läßt sich die minimale Partikelgröße der magnetischen Komponente zu etwa 30 nm annehmen. Die Fe^{3+}/Fe_{tot} Werte in Ferroperiklas liegen unterhalb der Nachweisgrenze (0.02) und damit im Einklang mit anderen veröffentlichten Werten von Ferroperiklas-Einschlüssen aus Juina. Untersuchungen des Fe^{3+}/Fe_{tot} Verhältnisses in Ferroperiklas kann Randbedingungen bezüglich ihrer Historie und letztendlich ihrer Entstehung und ihres Erscheinens aus der Übergangszone und den oberen Regionen des unteren Mantels setzen.

Acknowledgements

I want to thank my supervisors Prof. Dr. Leonid Dubrovinsky and Dr. Catherine McCammon for giving me the chance to work on this project and being always ready to help and support me during this period. Their guidance during the all PhD was for me of great inspiration and motivation to persevere on my project as well as to develop my own scientific ideas and interests. Further, I also want to thank Dr. Alexandr I. Chumakov and Dr. Rudolf Rüffer, my scientific advisors at ESRF, for their support, experience and assistance during my permanence at the synchrotron. A grateful thank to Dr. Leyla Ismailova, Dr. Ilya Kupenko, Stella Chariton, Dr. Elena Bykova, Dr. Maxim Bykov, Dr. Sylvain Petitgirard, Dr. Alexander Kurnosov, George Aprilis and Denis Vaiuskov for their precious support during the preparation of many synchrotron experiments, as well as during the experimental runs themselves. A special thank goes to Petra Buchert, Lydia Kison-Herzing, Detlef Krausse, Dr. Stefan Keyssner, Getrude Gollner, Hubert Schulze and Nicole Fischer for their help and patience after all questions and requests I had during my staying in BGI (54 months!). The time spent in Bayreuth at Bayerisches Geoinstitut was an amazing and important experience in my life, I want to specially thank all present and former BGI members for the nice time and stimulating discussions (not only scientific of course) we had together. The research of my PhD was funded by the Bayerischen Eliteförderungsgesetz "BayEFG" program of the Bavarian State Ministry of Science, Research and Arts.

I would also like to thank my office mates and fellow colleagues for their support and friendship. Special thanks go to Dr. Vincent Soustelle, Stephan Blaha, Dr. Matteo Masotta, Dr. Davide Frapporti, Dr. Davide Novella, Dr. Martha Pamato, Esther Posner, Dr. Mattia Giannini, Lin Wang, Dr. Natalia Solopova, Dr. Ana Cernok and Takahiro Yoshioka.

Explicitly, I want to thank my family, my parents Giovanni Cerantola and Diana Dall'Agnol, my sister Silvia Cerantola, and my grandparents Angelo Dall'Agnol, Lelia Passalenti and Agnese Cavalli for the patience the support during all my life. An immense thanks goes unavoidably to Martina Bonato, for her love, patience and support during the all period of my PhD, which has an incredible effect on personal life and relations.

Table of contents

14

6. Experimental investigations on FeCO3 (siderite) stability in the Earth's lower mantle by XANES spectroscopy **141**

1. Introduction

1.1 Origin of carbon in the Solar System

The Big Bang created only significant amount of hydrogen, helium and lithium, all other elements formed by nucleosynthesis in stars (e.g. Burbidge et al. 1957). The origin of carbon present in the Earth goes back to the formation of the solar system, the chondrites being considered the main contributing cosmochemical reservoirs to provide the building blocks of the terrestrial planets. In terms of chemical composition, the so-called chondritic Earth model well approximate for refractory elements, but for volatiles other reservoirs such as the solar nebula and cometary matter could have contributed in the primordial Earth's elemental and isotopic growth (Owen et al. 1992; Dauphas 2003; Pepin 2006). In particular the composition of one group of primitive meoteorites, the CI chondrites, closely resemble the non-volatile Sun's photosphere composition. In these primitive meteorites carbon results depleted relative to refractory elements, indication of its volatile element behavior, like hydrogen, nitrogen and noble gases (e.g. Anders and Grevesse 1989). Indeed, the physical and chemical processes acting in the solar nebula during the formation of the solar system, produced several carriers of volatile elements (e.g. H_2, H_2O, CO, CH_4, NH_3, N_2 etc.) with different volatilities that were physically and isotopically fractionated relative to one another, so that was impossible for the CI chondrites to accrete all of these carrier when they formed.

In the primordial cloud of gases and dusts, carbon was mainly in the form of gaseous CO, organic-rich carbonaceous dust. Small proportions of CH_4 and nanodiamonds were also probably present. During the planetary accretion, carbon and other volatile species were mainly transported and delivered in condensing proto-planets by comets, interplanetary dust particles and meteorites, below a short description of their chemistry and constituent materials.

Comets – Based on the data obtained by VEGA-1 spacecraft flying by the comet Halley, most of the carbon in the comet is in C-, H-, O-, and N-rich (CHON) dust particles (Kissel and Krueger 1987; Jessberger et al. 1988). The C/Mg ratio in Halley dust is 6-12 times higher than in CI chondrites. The estimated bulk composition for comet Halley is 43 wt% water, 26 wt% organics and 31 wt% silicates. If we consider most of the organics to be CHON-like material, this would mean that Halley-like

comets have ~18 wt% carbon. A similar composition for comets in general was obtained by Greenberg (1998).

Meteorites – are broadly divided into primitive chondrites, and achondrites that have undergone melting and differentiation on their parent bodies. Achondrites generally have low abundance of volatiles, most likely due to melting of the carriers. Chondrites instead can keep some amount of carbon trapped in their fine-grained matrices, formed predominantly by presolar circumstellar grains. Chondrules and refractory materials, the other two components forming the chondrites, are high-temperature objects containing no carbon or just little amounts. In all chondrites the carbon content decreases with increasing thermal metamorphism, hence the range of carbon contents in chondritic meteorites can vary from 0.12 to 4.1 wt% (Marty et al. 2013).

Interplanetary dust particles (IDPs) – are small particles (diameter < 50-100 μm) that are collected for instance in the upper Earth's atmosphere (Bradley 2003). Due to their small size, IDPs slow down relatively gently during atmospheric entry and are less severely heated, which prevent melting and often vaporization, preserving a highly enrichment in volatile elements, with an average abundance of carbon ~12 wt% (Thomas et al. 1993). However, for a dynamical point of view, IDPs cannot be considered a plausible source for the bulk of Earth's carbon. Indeed during planetary growth, dust is accreted by the forming protoplanets and it is only after the late stages of planetary formation that the interplanetary dust is able to drift over large radial distances delivering volatiles (e.g. C and H_2O) to Earth. Hence the contribution of IDPs to the present volatile content on Earth is post-planetary formation.

Despite carbonaceous chondrites have carbon concentration on the order of weight percent, due to the low condensation temperatures for carbon bearing gases, ices, and other solid phases (e.g. CO, CH_4 and graphite; 41-626 K) carbon is thought to be largely lost during Earth's accretion (e.g Abe 1997). Figure 1.1 shows six snapshots in time of the orbital configuration of a simulation of late-stage terrestrial accretion (Raymond et al. 2006). A direct observation of such decrease is the carbon abundance of the solar photosphere respect to CI-type chondrites, the latter incorporating only 10 % of the photospheric carbon (Lodders 2003). Estimates of bulk Earth carbon varies from below 0.1 wt% (McDonough 2003; Marty 2012) to as high as 0.37 wt% (Trull et al. 1993). Despite the big uncertainties regarding the

amount and the timing when this amount was acquired, it is probable that Earth inherited its present carbon budget from chondritic materials, comets and parents body of IDPs during (and after) accretion (Alexander 2005; Morbidelli et al. 2012; Marty et al. 2013, Dasgupta 2013).
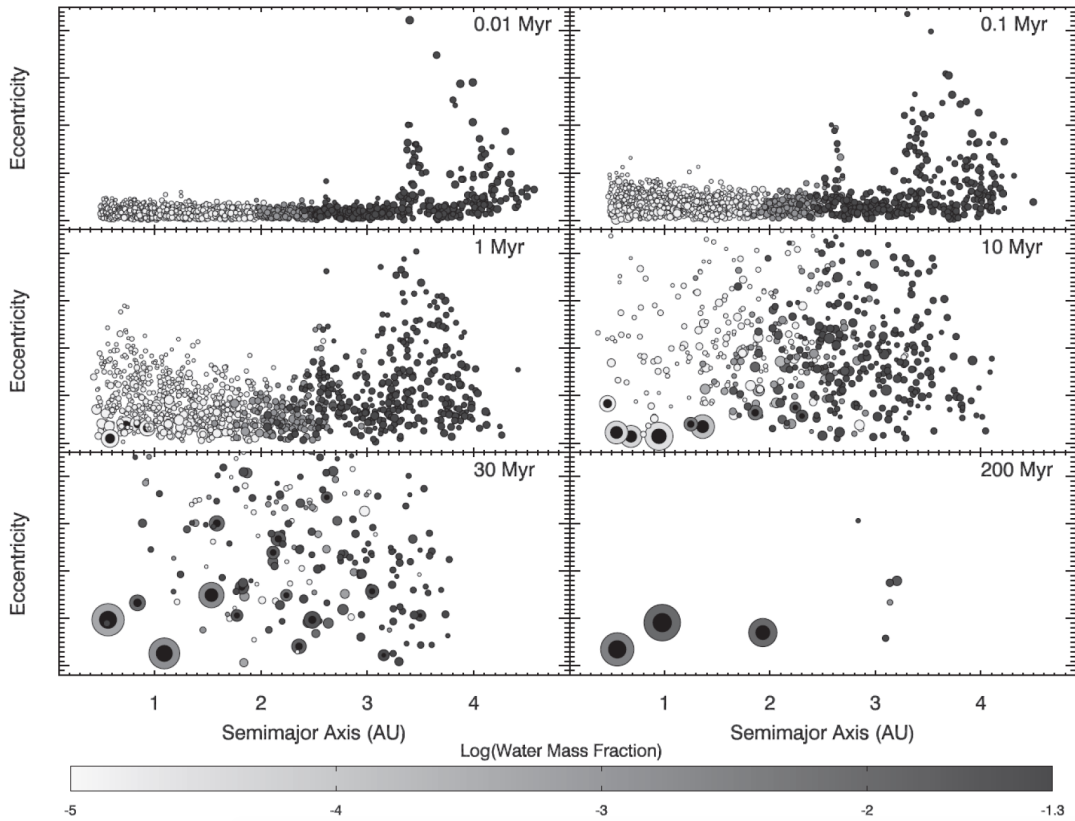
Figure 1.1. *From Raymond et al. (2006).* Six snapshots in time of the orbital configuration of a simulation of late-stage terrestrial accretion. The size of each body is proportional to its relative physical size and scales as its mass. The color of each particle corresponds to its water content: particles inside 2AU started the simulation dry, particles that started from 2 to 2.5 AU have 0.1 % water by mass, and particles that started beyond 2.5 AU have 5 % water by mass; during collision the water mass fraction is calculated using a simple mass balance. The Earth analogues in this simulation accreted a large volume of water of roughly ten times Earth's current water budget, although water loss during impact was not taken into account.

According to present estimates the delivery of volatile elements to Earth required the contribution of 1 to 3 wt% of wet material (e.g. from CI chondrites). By comparison

however, platinum groups elements, which follow chondritic proportion in the mantle, require a lower contribution of chondritic material of about 0.3 wt% (Marty et al. 2013) after core formation. This difference suggests that the delivery of volatile elements was not a late veneer event but was already ongoing during the planetary differentiation. An early delivery of volatile-rich material is also supported by recent planetary accretion models, e.g. the Gran Tack model (Walsh et al. 2005), which set the accretion of volatiles mostly in the first 50 Ma of Earth's history.

Despite the big uncertainties on the total Earth's carbon budget and the time of its delivery, if we assume that most of the carbon was inherited during planetary accretion it is conceivable to speculate on carbon's fate inside our planet.

1.2 Carbon in the Earth

1.2.1 Origin of carbon in the Earth

A number of studies discussed the importance of carbon *fractionation in a magma ocean* (Fig. 1.2) (e.g. Kuramoto 1997; Dasgupta and Walker 2008; Dasgupta and Hirchmann 2010; Hirschmann 2012).
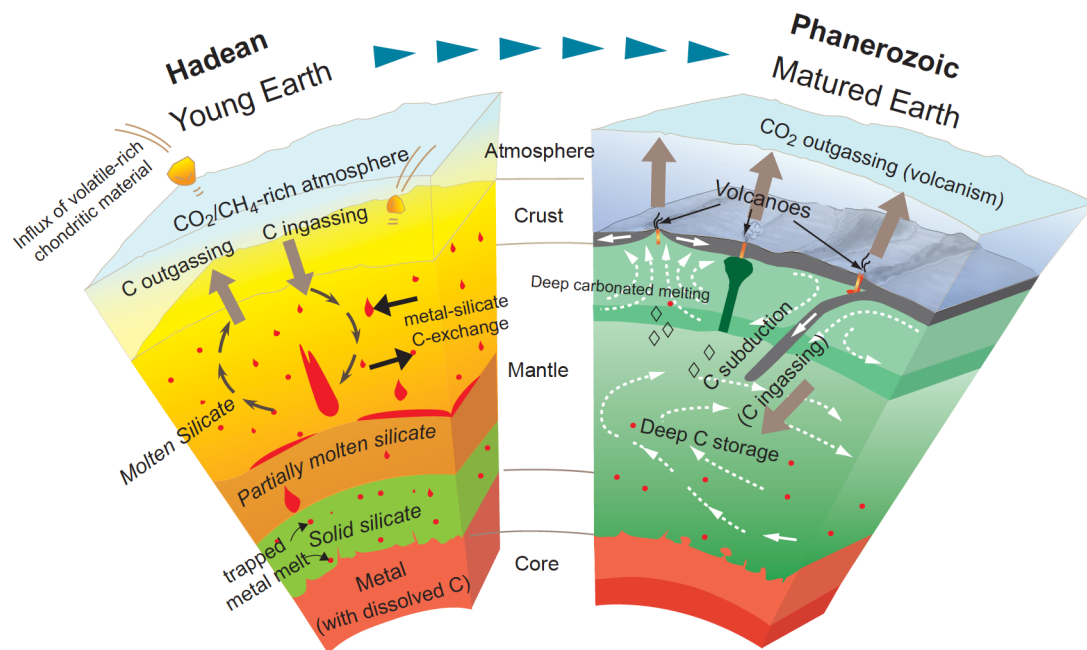
Figure 1.2. *From Dasgupta (2013b)*. Cartoon illustrating the range of deep-Earth processes from magma ocean stage of Hadean Eon to plate tectonic framework of the modern world.

The initial fractionation is extremely important since it surely had an effect on Earth's early thermal and dynamical evolution, its geochemical differentiation, its path to an equable climate and development of life. In order to understand the present distribution of carbon in the Earth, one has to look back at the element's partitioning between various reservoirs during early Earth differentiation, core, mantle and proto-atmosphere.

Fractionation of elements, e.g. siderophile elements, between the metallic core and the silicate mantle at the magma ocean stage during Earth's evolution (e.g. Rubie et al. 2007) was responsible for initial elemental distribution in Earth's reservoirs and setting the conditions for the evolution of crust and mantle chemistry. Similarly, the same process influenced the partition of volatile elements, carbon in particular (Kuramoto 1997; Dasgupta and Walker 2008; Dasgupta et al. 2013a). The partition coefficient of carbon between metal and silicate $D_c^{metal/silicate}$ (mass fraction of carbon in metal melt divided by the mass fraction of carbon in the silicate melt) is a good way to estimate carbon distribution at specific conditions. If $D_c^{metal/silicate} < 1$ carbon would be mainly in the silicate mantle. If $D_c^{metal/silicate} >> 1$ then carbon would be mostly concentrated in the Earth's core and would have much less influence on the long-term carbon cycle (Dasgupta 2013b). In this scenario, a late volatile-rich veneer or after differentiation processes would be responsible for moving carbon inside the planet. A third possibility sees carbon preferentially partitioned into the core forming liquid, but with much less iron affinity, $D_c^{metal/silicate} > 1$. In this case Earth's molten silicates might have retained enough carbon to justify Earth's present-day carbon budget of the mantle, which varies from 30 to 1100 ppm C depending on the sources, e.g. depleted mantle in middle ocean ridge basalt (MORB) and hot spot volcanism (e.g. Hawaii, Yellowston etc.). However the lack of experimental data aiming to quantify the $D_c^{metal/silicate}$ at different depths, oxygen fugacity (fO_2) and with different bulk compositions forbids introducing solid constraints on carbon behavior at Earth's magma ocean conditions.

A simple estimation based on the available bulk Earth's carbon during the Earth's differentiation (730 ppm C, yielding to molten mantle residual of 0.1-4.5 ppm C) and present day mantle carbon concentration (14-136 ppm C), indicates that whatever the exact carbon content of the present-day bulk silicate Earth (BSE) is, this concentration is in excess with respect to predicted by magma ocean chemical equilibration. This means that possibly up to more than 99% of silicate carbon needs to be derived from

post core-segregation processes. Or in other words, most of the primordial carbon dating back to before the core formation and is not lost in the space and/or degassed in the atmosphere, is trapped in the core. Present estimations suggest carbon core content varying from 0.23 wt% (Dasgupta et al. 2013a) to 1.2 wt% (Yi et al. 2000). Owing to the siderophile nature of carbon in core-forming magma ocean conditions, and hence the metallic core taking possession of Earth's carbon during the early planetary differentiation, some later carbon replenishment event/processes must have happened in order to explain the modern mantle carbon budget. Following a short description of the possible processes.

Heterogeneous accretion and imperfect metal-silicate equilibration – In order to have perfect equilibration during core-mantle separation, emulsified sinking metal droplets should have diameters in the range of 1 cm (Rubie et al. 2007). From geochemistry of Hf-W isotopes (Halliday 2004) and Ni, Co and W (Rubie et al. 2011) systems, the composition of the present mantle requires imperfect equilibration. This scenario occurs when for instance giant impactors merge directly with the Earth's forming proto-core, without going through major chemical interaction with the separating mantle. In this situation, only a very small fraction of metallic liquid would equilibrate with molten silicate (1 to 20% of the cumulative core mass could have equilibrated, Dahl and Stevenson 2010), causing the over-saturation of graphite/diamond, which would float from the segregating core liquid and contribute to the overlying molten silicate carbon budget (Hirschmann 2012).

Magma ocean-atmosphere interaction – The BSE could have gained quiet a substantial amount of carbon through interactions between the magma ocean with the primordial (Hadean) atmosphere (Hirschmann 2012; Dsgupta et al. 2013a). Carbon/CO_2 solubility is positively correlated to the temperature and hence the depolymerization of a silicate melt, and oxygen fugacity. On the contrary and extremely important for this particular process of carbon ingassing, the C/CO_2 solubility diminishes with pressure (e.g. Dasgupta et al. 2013b). The carbon storage capacity of magma ocean at shallow depths is greater and diminishes at the expense of graphite/diamond or carbide-rich metallic melt at greater depths. In this scenario, the magma ocean could have dissolved carbon from a C-rich early atmosphere in its shallower part, and precipitate graphite/diamond at greater depths as convection

brought the melts downwards. After graphite/diamond precipitation, the magmas would become C-depleted and thus upon upwelling more C/CO_2 could be dissolved from the atmosphere. This efficient cycling alone could justify the mantle inventory of carbon up to the nowadays value.

Carbon addition by late veneer – A late veneer carbon injection in the BSE is possible and well received, however not entirely satisfactory. For instance, the identical values for tungsten (W) isotopic composition between the BSE and the Moon, limit the amount of material that can be added as late veneer after the giant impact to less than 0.3 wt% and 0.5-0.6 wt% of Earth's mass ordinary and carbonaceous chondrites respectively (Halliday 2008). Indeed, assuming an addition of carbonaceous chondrites in these range of values containing 3.5 wt% of carbon, it would add only 105-245 ppm of C, to Earth after core formation, which however even if substantial is not enough to compensate for the present BSE carbon abundance (Marty 2012). Addition of chondritic material in a late veneer to bring carbon levels needed to match BSE without increasing the highly siderophile elements is not possible. Therefore, any late delivery mechanisms may need to resort more than one source geochemically different than the known chondrites (e.g. comets).

Inefficient core formation – In this model, part of the core-forming metallic liquid would stay trapped in the solid silicate matrix, providing a source of carbon and highly siderophile element in the mantle. This is possible due to the dihedral angles of liquid metals and mantle minerals that generally are > 60° (mostly around 90-100°)(e.g. Shannon and Agee 1996; Cerantola et al. 2015a), with the threshold for liquid interconnectivity and settle at 60°. Dihedral angles < 60° creates interconnected liquid networks, with the liquid ideally propagating around the matrix crystals and promoting full segregation, hence liquid metal percolation through the Earth's proto-core. In this scenario, the Earth's lower mantle would start off being more C-rich, and solid state convection after the crystallization of the magma ocean would homogenize the mantle with accessory Fe-rich alloys, Fe-rich carbides (e.g. Fe_7C_3 or Fe_3C solid solutions) and C-bearing metallic liquid (Dasgupta et al. 2013b). The present estimation of the carbon content in the BSE stays in between 30-1100 ppm C, and it is assumed that the mantle attained that carbon content similar to the inventory of the Earth's early life. And if the mantle is characterized by a carbon

budget similar to that of the primordial Earth, how was this budget preserved and processed in the light of the ongoing differentiation and varying geodynamic processes of the planet for more than 4 billion years?

1.2.2 Carbon retention: from the past to the present

The carbon cycle post magma ocean crystallization was controlled by the temperature induced solid-state convection and plate tectonics. Carbon inventory went through finite changes during time, the key processes being the efficiency of crustal carbon recycling and CO_2 escaping along oceanic spreading ridges and arc volcanism, both processes governed by the evolving Earth's thermal state.

The Earth's mantle was hotter in the Archean (from 4 to 2.5 billions year ago) respect to the present day of ~200 ° (Herzberg et al. 2010; Lee et al. 2010). Decompression melting, which is the main controller of carbon release and lies at the solidus of carbonated peridotite, was surely at much greater depths than the present one, located at a minimum depth of ~300 km. Taking any hot mantle adiabat for the Archean and part of the Proterozoic (from 2.5 to 0.54 billion years ago) (Herzberg et al. 2010), one would expect that in that period the entire mantle may have experienced temperatures above the carbonated peridotite solidus, hence the mantle could have been very efficiently processed. However, the onset of partial melting was not only governed by the thermal state of the mantle, but also as a function of oxygen fugacity, or in other words the mode of carbon storage in the mantle, e.g. carbonates, graphite/diamond, carbides, etc. Nowadays we tend to address the control of the oxygen fugacity in the mantle by the equilibria involving the exchange of Fe^{3+} and Fe^{2+} in silicates, the most abundant minerals in the mantle (Rohrbach et al. 2007; Frost and McCammon 2008). However mantle fO_2 may have been buffered also by carbon-carbonate equilibria (e.g. Luth 1999), especially considering the possible higher efficiency of carbon recycling do to the higher thermal vigor of the mantle at those times, e.g. convection in a magma ocean instead of solid state convection, and owing to the inefficient core formation, magma ocean-atmosphere interactions etc. In this scenario, if we assume a carbon content of the BSE during the Hadean and Archean Eons to be between 765-3700 ppm as estimated by Marty (2012) and Trull et al. (1993) for the present day Earth, then carbon-carbonate redox reactions would control the fO_2 of the deep mantle, at the expenses of the buffering capacity of Fe^{3+}-Fe^{2+} exchanges in silicates.

Of primary importance for the early recycling of carbon inside the Earth is the onset of active (ancient) subduction zones. From extremely old diamonds inclusions (as old as 3.5 billion years) subduction may have initiated ~3 billion years ago (Shirey and Richardson 2011). Based on thermobarometric estimates of ancient zircons' inclusions, subduction could have started as early as ~4-4.2 billion years ago (Hopkins et al. 2008). The thermal state of the Earth's mantle at that time is crucial, because it affects the stability of potential carbon carriers, and hence carbon subduction and early-recycling. The compositions and proportions of carbon-bearing rocks during the ancient times are not well constrained, however one can easily predict what could happen if the three major carbonated lithologies that subduct in the modern Earth (carbonated oceanic sediments, carbonated altered basalt, carbonated peridotite) took part in ancient subduction processes. On average, carbonated oceanic sediments have the lower decarbonation and melting temperatures. This rock-type, considering a subducting slab temperature 100 ° higher than the hottest subducting plate in the modern Earth (due to higher thermal state of the ancient mantle), will be completely carbon-free by depths of 100-150 km (Dasgupta 2013b). At similar conditions altered ocean floor basalts would undego complete decarbonation by 80-120 km (e.g. Yaxley and Green 1994; Kiseeva et al. 2012). Basaltic eclogites instead, characterized by more magnesian crystalline carbonate, would decarbonate completely and/or melt by 125-170 km depth (Gerbode and Dasgupta 2010). Even if phase relations of altered lithospheric mantle (e.g. serpentinized carbonate peridotite and their dehydrated products) are poorly constrained experimentally, thermodynamic calculations relevant for "low-pressure" devolatilization, melting and decarbonation of carbonated peridotite (Kerrick and Connolly 1998) and fertile peridotite (e.g. Wallace and Green 1988; Dasgupta and Hirschmann 2010) indicate that carbonated lithosphere had the best prospect of carrying carbon at depths. This follow because peridotitic rocks provide the best thermal stability for crystalline carbonates and they go down along the coolest paths during subduction. Only as recent as 1.2-1.5 billion years subduction is considered to be cold enough to favor significant subduction of crustal carbonate beyond sub-arc depths of 170 km (Dasgupta 2013).

In conclusion, owing to the more efficient decarbonation mechanisms at relatively shallow depths, in the Archean the CO_2 outgassing through volcanic arcs was higher than at present day, and deep subduction of carbon may have been hindered, due to the higher thermal state of the ancient Earth, which causes

decarbonation and melting of carbon-bearing lithologies at shallow depths in the mantle.

1.2.3 Deep carbon cycle in modern Earth

Carbon fluxes in the modern Earth have been extensively investigated in the last years but are still poorly constrained due to difficulties in precisely determine the amount of carbon input inside the planet, its fate once subducted, and the amount of carbon output from arc volcanism. Recent investigations (e.g. Dasgupta and Hirschmann 2010; Dasgupta 2013b; Alt et al. 2013; Jerrard 2004; Gorman et al. 2006) in average estimate that half of the subducted carbon is removed from the downgoing plate beneath arcs and returned to the surface, the rest being transported deeper replenishing the deep carbon reservoirs. For instance, according to Dasgupta (2013b) the revised estimate of the present-day subduction input of carbon, combining all lithologies (oceanic mantle lithosphere) is between 5.4-8.8 $\times$ 10^{13} g C/yr. However, a more recent review from Kelemen and Manning (2015) that takes into account new estimates of carbon concentration in subducting mantle peridotites, consideration of carbon solubility in aqueous fluid along subduction geotherms, and diapirism, states that relatively little carbon may be recycled and substantial quantities of carbon are stored in the mantle lithosphere and crust, having as a bottom barrier during subduction the sub-arc depths of 70-170 km, characteristic threshold causing the majority of decarbonation and melting processes (Dasgupta 2013b). In a recent study, Thomson et al. 2016 investigated the melting curve of carbonated oceanic crust, showing that the majority of slab geotherms (Syracuse et al. 2010) intersect a deep depression along the melting curve at depths of approximately 300 to 700 km, creating a barrier for further carbonate subduction and thus hindering the participation of carbon recycling in a much longer time scale involving the deep mantle. In this scenario, almost all of the carbon in subducting sediments and oceanic plates may be extracted in fluids and melts that rise into the mantle wedge or generally at shallow upper mantle depths.

Despite the barrier present in the mid-upper mantle hindering carbon recycling at greater depths, there are special conditions that might be considered in order to preserve the high carbon content of the mantle (especially for those values measured in ocean island basalt "OIB" regions > 700 ppm C), such as the sinking of cold and

fast subducting slabs, redox freezing, interaction of subducted water and metallic core.

The surface temperature of subducting plates can consistently vary based for instance on the age of the slab and on their fluids content. The older a slab is, the colder it is and the faster it sinks. Hence, cold subducting plates, characterized by surface temperatures of ~ 1100 °C at ~ 600 km depth (~20 GPa) (Syracuse et al. 2010), are the only way to bring crustal material deep down the lower mantle, avoiding breakdown reactions such as decarbonation and/or melting of carbonate- and more generally carbon-rich lithologies.

Redox freezing is a dynamic process caused by carbonate-induced melting of subducted oceanic lithosphere that become unstable when infiltrating the ambient mantle, and get reduced to immobile diamonds when recycled at depths greater than ~250 km, where mantle redox conditions are determined by the presence of (Fe,Ni) metal phases (Rohrbach and Schmidt 2011). Thus redox freezing may be considered an active and fundamental mechanism for carbon recycling (as diamonds/graphite) into the convecting mantle, however displacing only a small fraction of the global carbon inventory (Kelemen and Manning 2015).

More complex is the case of mantle carbon acquisition via interaction of subducted 'water' (as hydrous phases) and metallic core. The initiation of plate-tectonics is responsible for the recycle not just of carbon but also other volatiles inside the Earth, most of all water in the form of hydrous and nominally anhydrous minerals. Dasgupta et al. 2013a proposed that if subduction of oceanic plate brings water to the core-mantle boundary regions, the interaction between the released water from the breakdown of hydrous phases and the metallic alloy melt from the outer core would trigger a series of reactions to form Fe-hydrates. However oxygen, being less soluble in the metallic core and released in the process, may also react with the released carbon in the core to form CO_2, CO and possibly $FeCO_3$, following the reactions (Dasgupta 2013b):

$$Fe + H_2O = FeO + 2H \tag{1.1},$$

$$Fe + xH = FeHx \tag{1.2},$$

$$FeO + C = Fe + CO \tag{1.3},$$

$$2FeO + C = 2Fe + CO_2 \tag{1.4},$$

$$FeO + CO_2 = FeCO_3 \tag{1.5},$$

Excess of hydrogen could also react forming hydrogenated phases like methane:

$$C + 2H_2 = CH_4 \tag{1.6},$$

These products, CO, CO_2, carbonates and/or hydrocarbons, are most likely present phases in the lowermost past of the lower mantle, either as solid either as melt. Similarly to the model of inefficient core formation, this mechanism could make the lower mantle more carbon-rich.

Deep ingassing has been considered to be more (e.g. Dasgupta and Hirschmann 2010; Dasgupta R. 2013b; Alt et al. 2012, etc.) or less (Kelemen and Manning 2015, Thomson et al. 2016) efficient in the modern Earth. Different conclusions arise due to highly uncertain estimates. We still lack quantitative data on carbon key reservoirs, hence on stable carbon carriers ideally down to the core mantle boundary. For instance, what happens to subducted carbonates that survive sub-arc decarbonation and enter the transition zone or the Earth's lower mantle? What happens at the interaction boundaries between subducting plates and surrounding mantle at different pressures, temperatures and oxygen fugacities?

1.3 Example of carbon-iron driven redox reactions in the modern Earth's mantle: redox freezing and redox melting

Deep carbon is predominantly stored in accessory phases as a consequence of its low solubility in dominant mantle minerals (e.g., Keppler et al., 2003; Shcheka et al. 2006), where these accessory phases include carbonates, diamonds/graphite, methane and carbides, depending on pressure, temperature, and oxygen fugacity. In highly reducing environments (i.e., low oxygen fugacity), the crystalline form of carbon is graphite or diamond. At more oxidizing conditions, carbonates are favored due to the reaction between elemental carbon and oxygen to form $(CO_3)^{2-}$ groups that bond to other cations such as Ca^{2+}, Mg^{2+}, Fe^{2+}, Ni^{2+} and Na^+ depending on the composition of the original bulk assemblage. In shallow oceanic mantle, carbonates and carbonatitic melts (carbonatites and/or carbonates silicate melt) could dominate the carbon budget to ~300 km depth (e.g. Dalton and Presnall 1998; Dasgupta and Hirschmann 2006). However, due to redox freezing processes, it is possible that carbonated melts freeze at the expense of diamond/graphite. Starting from a

subducting, locally carbonated, relatively oxidized mafic to ultramafic lithospheres, carbonatite melts will be generated in such lithosphere on thermal relaxation (Rohrbach and Schmidt 2011). This may occur when the lithosphere deflects into the transition zone above the 660-km discontinuity or when stagnating in the lower mantle. On a local scale, oxidized carbonatite melt migrating into the mantle will consume metal (Fe^0) to first form iron carbide in an intermittent stage, and then further oxidize the Fe and Ni contained in the carbide to leave a mantle domain that contains all iron as Fe^{2+} and Fe^{3+} in silicates (e.g. bridgmanite) and ferropericlase and all carbon as diamond (Rohrbach and Schmidt 2011). Owing to its low viscosity and high wetting properties, any excess carbonatite not consumed by redox reactions would percolate upwards along grain boundaries and exhaust further (Fe,Ni)-metal and carbide until complete redox freezing—that is, immobilization due to reduction of CO_2 to C^0—is achieved. This presumably very efficient process will eventually exhaust all buffering metal and carbide through precipitation of diamond, and result in a metal-free mantle domain where diamonds coexists with Fe^{3+}-bearing garnets, perovskite and possibly Fe^{3+}-enriched ferropericlase (Fig. 1.3).
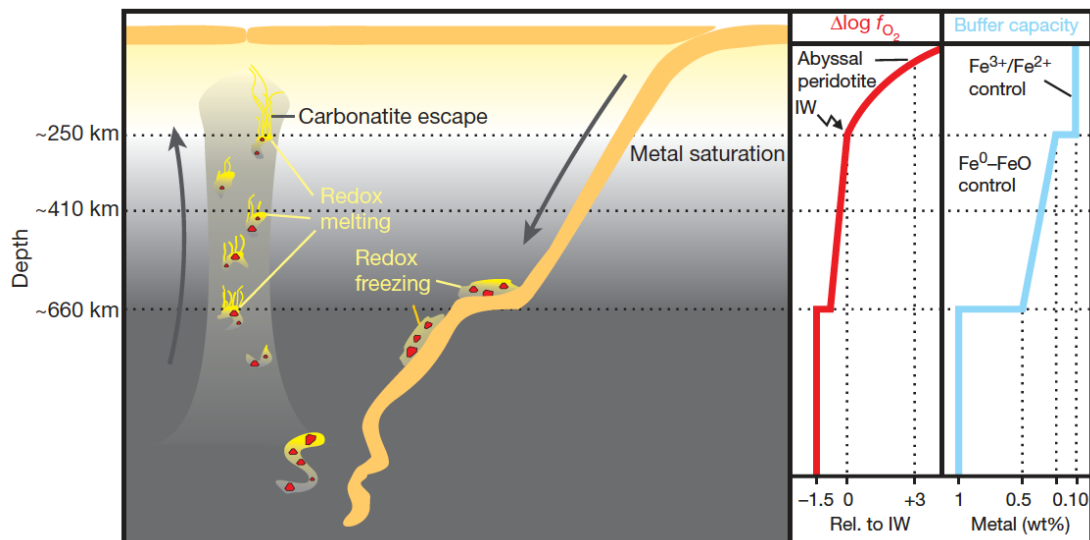
Figure 1.3. *From Rohrbach and Schmidt (2011)*. Carbonatitic redox freezing and redox melting caused by redox capacity changes in Earth's mantle. Main panel, cartoon illustrating a possible sequence of redox freezing and redox melting events driven by oxidation state contrasts between subducted lithosphere and ambient asthenospheric mantle. Right, potential mantle fO2 (red line) and redox buffer capacity (blue line) as function of depth.

On the other hand, redox melting transforms diamond to carbonatite melts, which potentially control the onset of ultra-deep melting.
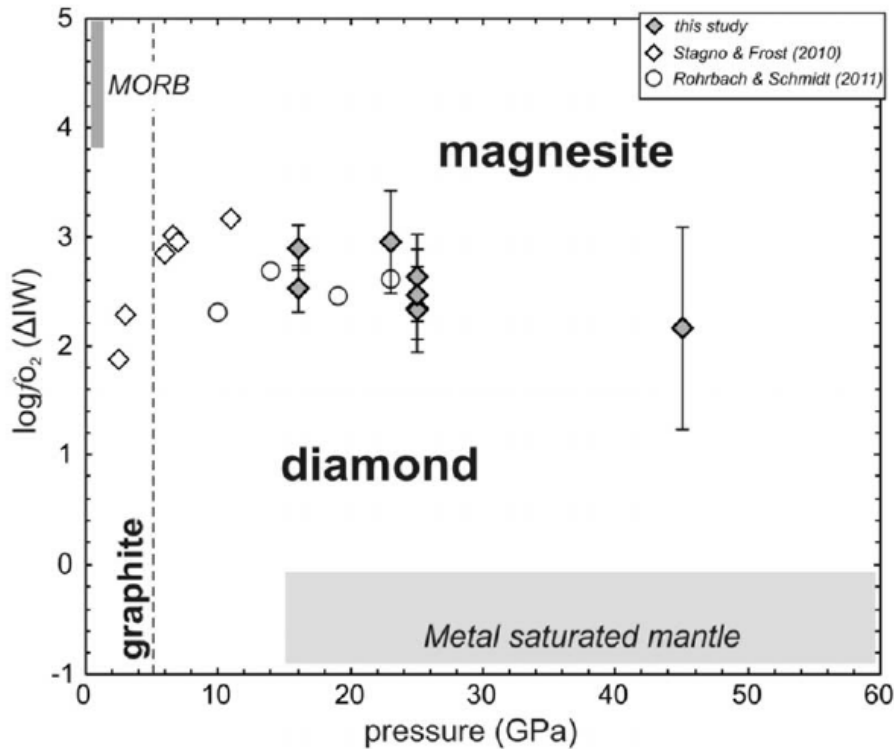
Figure 1.4. *From Stagno et al. (2011)*. The log fO_2 (normalized to IW) buffered by a diamond and magnesite bearing mantle assemblage is shown as a function of pressure for experiments performed between 1500–1700°C (gray diamonds). The data points the higher fO_2 region where magnesite is stable from the lower region where diamond forms. Previous measurements of the carbonmagnesite/carbonate melt buffer determined along a mantle adiabat between 3 and 11 GPa (Stagno and Frost, 2010) are also shown (open diamonds). White circles are fO_2 measurements from Rohrbach and Schmidt (2011) using IrFe alloy as a redox sensor. The gray shaded regions indicate the fO_2 of MORB mantle and the likely fO_2 of the transition zone and lower mantle after Frost and McCammon (2008).

However, the depth of reduction is under debate: Stagno and Frost (2010) propose the bottom boundary for redox freezing at 100-150 km, whereas Rohrbach and Schmidt (2011) argued it should be slightly deeper at ~250 km. This difference has surely profound consequences in terms of carbon releasing and outgassing, for instance affecting the composition of the produced melt, which shows kimberlitic affinities

when it forms at ~250 km rather than being a pure carbonatitic melt (Dasgupta et al. 2013a). However, despite the carbonate melt/mineral stability condition due to iron disproportionation-induced redox freezing, local carbonate-rich environments could proceed on their journey through the Earth' interior entering the Earth's lower mantle (e.g. Biellmann et al. 1993; Stagno et al. 2011). Interestingly, an experimental determination of the solidus of carbonated peridotite at transition zone and lower mantle depths, shows that following the mantle adiabat for temperature of ~1650 K there could be two crossing of the carbonated peridotite solidus, at ~ 10 GPa and at ~ 30 GPa. This means two things: 1) carbonatite generation happens not only at ~ 300 km depth, but also at around 900 km; 2) the transition zone and the shallow lower mantle may be below the carbonatite solidus, hence they could be considered carbon reservoirs, with carbon stored as iron-magnesite minerals, this proven that the $fO_2 >$ IW+2, Figure 1.4 (Stagno et al. 2011).
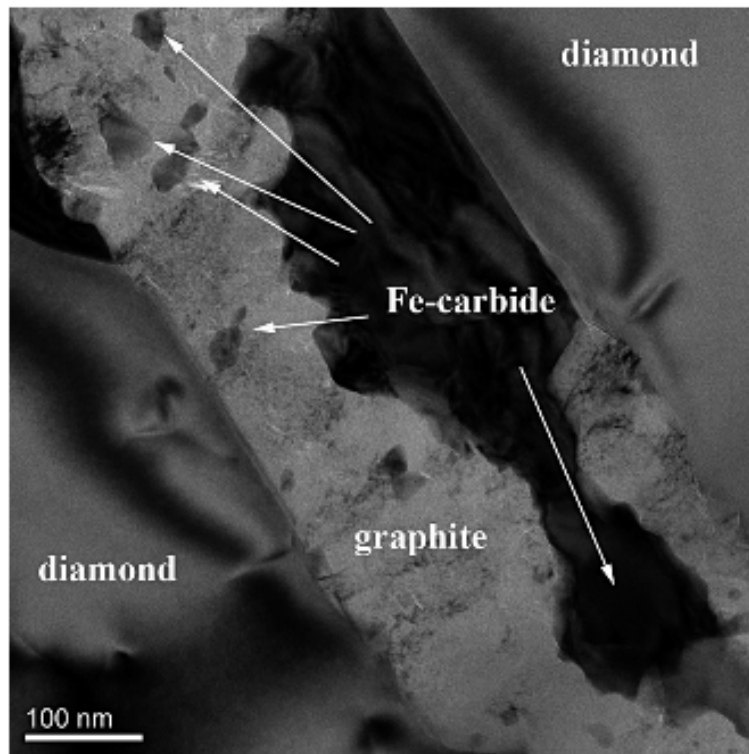
Figure 1.5. *From Kaminski and Wirth (2011)*. TEM bright-field image showing a section of the plate-like inclusion in diamond (foil #2053). Note the even interface between iron carbide and diamond, whereas the interface between iron carbide and graphite is invariably irregular. Small fragments of iron carbide of an originally larger grain are present in the graphite matrix.

One should remember however that the diminishing oxygen fugacity with depth (e.g. Woodland and Koch 2003; McCammon and Kopylova 2004; McCammon 2005; Stagno and Frost 2010), suggest that diamonds, iron carbides, and more in general iron-nickel carbon-rich alloys may become the stable phase at the expense of carbonates and carbonate melts in the Earth's lower mantle (e.g. Jacob et al. 2004; Dasgupta et al. 2009a; Kaminsky and Wirth 2011, Fig. 1.5).

1.4 Carbonates and ferropericlase associations in the Earth's lower mantle

Owing to the scarce knowledge on the stability of carbon-bearing compounds inside the Earth, in this thesis we address a further piece of the puzzle, experimentally investigating the stability of iron-bearing carbonates at Earth's mantle conditions and the role of ferropericlase from the transition zone/shallow lower mantle on the processes behind for instance the formation of ultra deep diamonds.

Experimental investigations and studies of mantle rocks show that the oxygen fugacity of the upper mantle is relatively high despite the low abundance of ferric iron (Fe^{3+}) in olivine, which is the most abundant mineral in the upper mantle (McCammon 2005). On the contrary, bridgmanite stabilizes in its structure almost half of the iron atoms as ferric ions, which however does not have any influence on the reducing conditions characteristic of the lower mantle due to the self-reduction reaction $3Fe^{2+} \rightarrow Fe^0 + 2Fe^{3+}$, which results in the production of ~1 weight % metallic iron in the lower mantle (Frost et al. 2004). The change in oxygen fugacities in different regions of our planet are primarily controlled by the charge balance between iron cations but could also be driven by the buffering activity of carbon (see above section), which profoundly affects the stability of subducted materials.

Slabs penetration into the lower mantle requires a redox reaction in order to balance the Fe^{3+}-oxidation in bridgmanite, involving primarily ferropericlase, the second most abundant phase in the Earth's lower mantle, and oxidized species present in subducting plates. In this way, the charge balance of iron oxidation could be compensated by reduction of carbon in C-rich subducting phases as for instance carbonates through the reaction,

$$4FeO + MgCO_3 \rightarrow MgO + C + 2Fe_2O_3 \qquad\qquad 1.7,$$
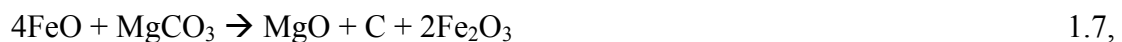
a likely mechanism behind the formation of diamonds in the Earth's lower mantle and one of the possible reasons for the high presence of ferropericlase's inclusions in diamonds from those regions (McCammon 2006).

The intriguing relations between carbonates and ferropericlase genesis and influence on the local oxygen fugacity environment made us perform for the first time a systematic study of Fe^{3+} distribution in a ferropericlase still trapped in its lower mantle diamond's host (Chapter 7). In particular the ferropericlase we investigated could have formed through equation 1.7 and/or redox freezing processes, hence involving the presence of carbonates minerals and/or oxidized melts of carbonatitic compositions in the Earth's lower mantle.

1.5 Carbonates at extreme conditions

Carbonates are important constituents of marine sediments and play a fundamental role in the recycling of carbon into the Earth's deep interior via subduction of oceanic crust and sediments (e.g. Becker and Altherr 1992; Rea and Ruff 1996, Biellmann et al. 1993).

The three major carbonate components in the crust and upper mantle are $CaCO_3$ (calcite), $MgCO_3$ (magnesite), and $FeCO_3$ (siderite). Their atomic arrangement can be envisioned as a distorted rocksalt structure with Fe as the cation and CO_3 groups as the anions. They exhibits space-group symmetry R-3c (calcite-group rhombohedral carbonates), where, in the hexagonal setting, iron is located at the cell origin (6b), oxygen is at x, 0, 1/4 (18e), and carbon is at 0, 0, 1/4 (6a) (Bragg, W. 1913).

Calcite is one of the most abundant mineral species on the surface of the planet. It has bot biogenic and inorganic origin, occurring as precipitated sediments in sedimentary rocks. It occurs also in igneous carbonatites and kimberlites thought to be derived from deep mantle sources. It can definitely be considered the major source and sink for atmospheric CO_2 inside the Earth. Magnesite instead occurs at the surface as veins in alteration product of ultramafic rocks, serpentinite and other magnesium-rich lithologies in metamorphic regions. However, due to the abundant content of magnesium in the mantle, it is considered the potential host for oxidized carbon in the Earth's mantle, owing to its stability up to pressures and temperatures of the core mantle boundary (e.g. Fiquet and Reynard 1999, Isshiki et al. 2004). Siderite is commonly found in hydrothermal veins and as a diagenetic mineral in shales and

sandstones. In sedimentary rocks it forms at shallow depths and its composition is often related to the depositional environment of the enclosing sediments (Mozley, 1989). Because of reactions between solid carbonates and silicates such as pyroxenes and silicate perovskite (e.g. Biellmann et al., 1993; Wood et al., 1996), Mg-Fe carbonates should represent the dominant oxidized carbon species in the Earth's mantle. Hence siderite, the iron end-member, have to be considered together with magnesite a potential carbon-carrier deep inside our planet, and its behavior and stability at extreme conditions must be investigated in order to put solid constraints and progress in modeling the carbon budget in the entire Earth's system.

The $CaCO_3$-$MgCO_3$-$FeCO_3$ system has been experimentally investigated at relatively low pressures and moderate temperatures (P < 3.5 GPa, T < 1100° C) since many decades (e.g., Goldsmith et al., 1962; Rosenberg, 1967; Merrill and Bassett, 1975; Franzolin et al., 2011). These conditions are representative for the shallower part of the upper mantle, and the experimentally obtained low-pressure ternary phase diagrams indicate the formation of extensive solid solutions between the three end-members, with compositions depending on pressure and temperature. However, observations from geophysics (e.g., Fukao et al., 2009) and natural samples (e.g., Brenker et al., 2007; Walter et al., 2011) suggest that some subducted slabs could go much deeper and penetrate the lower mantle. Proven "cold" temperatures are preserved at the surface of these particular slabs and owing to the higher oxygen fugacity in such regions, subducted carbonates could be stable phases locally in the lower mantle. For this reasons, carbonate's properties at much higher pressures and temperatures should be explored, as well as their stability regions at the varying of pressures, temperatures, composition and fO_2.

There are two major mechanisms which could affect carbonates phase stability and carbon oxidation state in Earth interiors – chemical reaction(s) with surrounding minerals or transformations (including self-oxidation-reduction) of carbonates themselves at certain pressures and temperatures.

Previous high-pressure studies on the carbonate endmembers $CaCO_3$, $MgCO_3$, and $FeCO_3$ revealed high-pressure phase transitions in all phases in the pressure range up to 140 GPa and limited temperatures (e.g., Ono et al., 2005; Merlini et al., 2012; Biellmann et al., 1993; Isshki et al., 2004). Investigations on the stability of $MgCO_3$ in the transition zone and upper part of lower mantle as a function of oxygen fugacity,

determined that carbon in the bulk mantle (when homogenously distributed) is expected to occur as diamond, carbides and other reduced phases rather than carbonates (Stagno and Frost 2011). Magnesite shows a structural change at 115 GPa and 2100-2200 K (Isshki et al., 2004), whereas magnesiosiderite experiences a volume collapse of almost 10 % between 40 and 50 GPa at ambient temperature, caused by a high-spin to low-spin (HS-LS) transition of iron (Lavina et al., 2009). Indeed, iron can radically change the thermodynamic stability of carbonate phases preserving them from breaking apart down to pressures and temperatures of the lower mantle. The iron atoms in Fe-carbonates occupy an octahedral site, which leads to a splitting of the six 3d electron energy levels into two lower eg and three higher t2g energy levels (Fig. 1.5) (Burns, 1993). This energy splitting leads to two possible spin configurations: (1) HS state with four unpaired and two paired electrons; and (2) LS state with 6 paired electrons. The electrons pairing causes a volume collapse of the iron atomic volume, followed by a shrink of the octahedral site (the oxygens getting closer to the iron atom) and finally of the unit cell.
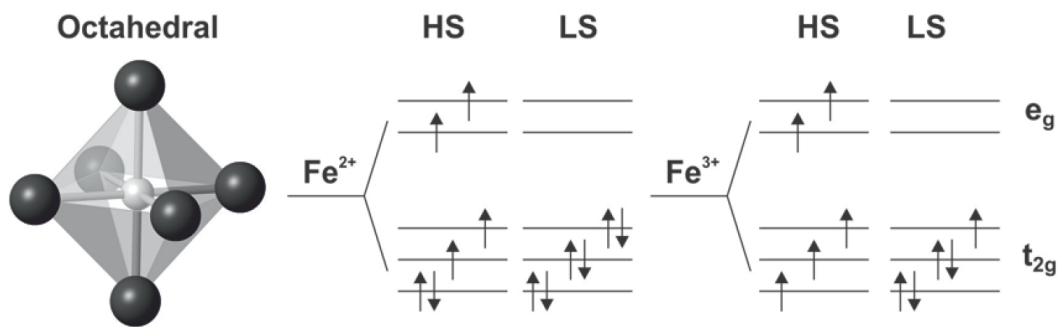
Figure 1.5. *Modified after Lin and Wheat (2011)*. Diagrams for the crystal field splitting of iron in octahedral site. Electronic configurations for iron as 2+ and 3+ are shown for high-spin (HS) and low-spin (LS) states.

Shi et al. (2008) predicted the spin transition of Fe in pure siderite by *ab initio* simulations to be between 15 to 28 GPa, while the first experimental observation was reported by Mattila et al. (2007) to occur at roughly 50 GPa from natural siderite powder using X-ray emission spectroscopy. Lavina et al. (2009) described a sharp volume collapse at 43 GPa from X-ray single crystal diffraction, whereas Farfan et al. (2012) observed spin crossover in a (Mn,Mg)-siderite at 46 GPa using Raman

spectroscopy and X-ray single crystal diffraction. Lin et al. (2012) studied $Mg_{0.35}Fe_{0.65}CO_3$ up to 80 GPa at ambient temperature and observed the spin transition at 45 GPa, where their data suggested that the low-spin state has different vibrational and elastic properties compared to the high-spin state. Temperature extends the spin crossover region of magnesiosiderite (Liu et al., 2014) to over 50 GPa at ~1200 K for the endmember $FeCO_3$. Merlini et al. (2012) postulated that the low-spin state could contribute to the stabilization of Fe-bearing Ca,Mg-carbonate (so-called dolomite-III) above 35 GPa and 2000 K, and Liu et al. (2015) reported an orthorhombic phase of magnesiosiderite above 50 GPa and 1400 K that also appeared to be stabilized by spin crossover. It is therefore clear that iron can play a fundamental role in the behavior of carbonates at high pressure and high temperature.

Interest in high-pressure behaviour of carbonates was busted recently by reports on synthesis of novel compounds containing tetrahedral CO_4^{4-} groups (instead of common at ambient conditions flat triangle CO_3^{2-} ions) (e.g. Isshiki et al. 2004; Boulard et al. 2011; Boulard et al. 2012; Boulard et al. 2015; Merlini et al. 2015; Cerantola et al. 2017). Theoretical predictions indicate potential analogies between CO_4-bearing carbonates and silicates (Lasaga and Gibbs 1987; Oganov et al. 2013). For instance, as a speculative example, one could assume that the higher degree of polymerization in the in high pressure carbonate due to the presence of chains and rings of CO_4-tetrahedra, is at least in a first sight comparable to the chains and rings formed by SiO_4-metalisicates. However, due to the extremely different behaviors of the intertetrahedral Si-O-Si and C-O-C bonding angles, these similarities seem to be limited (Oganov et al. 2008). Moreover, silicates have extremely flexible bonding angles (Lasaga and Gibbs 1987) whereas polycarbonate ions are much less flexible, which might be the cause of the more limited structural variability for tetrahedral carbonates, lower compressibility (e.g. Lin et al. 2012; Cerantola et al. 2015b) and lower propensity to amorphisation. However, due to the limited (and rather controversial) amount of solid experimental information about structures, any conclusions regarding their crystal chemistry are groundless.

1.6 Aims of the thesis

In a general perspective our work is focused on the deep carbon cycle, or in other words on the discovery and understanding of the plausible mantle minerals, fluids and melts that are potentially involved in deep carbon recycling. The primary goal of this thesis is the experimental investigation of the high-pressure high temperature behaviour of iron carbonate using as starting material synthetic siderite ($FeCO_3$). Experimental conditions of our work cover the entire mantle giving new insights into the physics of spin transition in $FeCO_3$ at extreme conditions, and revealing two novel compounds containing tetrahedral CO_4 groups, as well as the complex role of ferrous and ferric iron in the stabilization of carbonates at high pressures and temperatures. Our discoveries are discussed envisioning the present day Earth's thermal state and geodynamic, and address some open questions about the stability of Fe-bearing carbonates in the Earth's mantle and their role in the deep carbon cycle.

The unique role of iron as oxygen fugacity buffer inside the Earth led us to conduct a parallel study aiming to investigate the abundance of ferric iron in a ferropericlase inclusion still trapped in its hosting diamond from the shallow lower mantle. The presence of varying Fe^{3+} contents in different regions of the same inclusion are indicators of a dynamic and evolving environment during the growth of the crystal before its encapsulation in the host.

To conclude, we investigated the stability of iron carbonates in the Earth's mantle and the ferric iron abundance in ferropericlase inclusions from the shallow lower mantle with the final aim to define the potential C-carriers inside the deep Earth, and tackle the role of iron oxidation state in the stabilization of reduced and oxidized carbon-bearing phases inside the Earth's mantle.

2. Methods

2.1 High-pressure experiments

2.1.1 Diamond anvil cells

A diamond anvil cell (DAC) is a high-pressure device introduced in the late 50th (Weir et al., 1959). A DAC consists of two opposing gem quality diamonds with a sample compressed between the culets (tips) (Fig. 2.1.1).
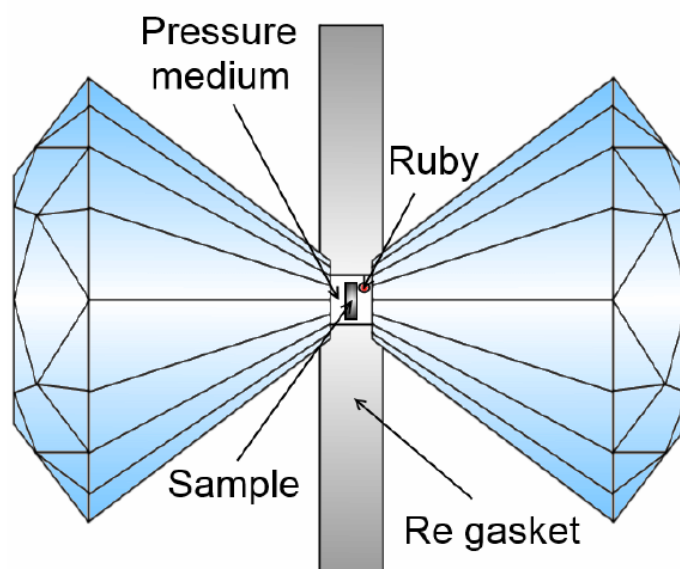
Figure. 2.1.1. *From Kupenko PhD thesis 2014*. Schematic diagram of diamond anvil cell loading.

Based on the principle that Pressure = Force/Area, different pressure ranges can be achieved by varying the diamond culet size. For instance, it is possible to attain relatively "low pressure" of few kbar or GPa using diamonds with culets large than 500 μm in diameter and/or reach extremely high pressures above 100-200 GPa with diamonds culets smaller than 120 μm. The highest static pressure reported so far is the compression of metal osmium up to 770 GPa (Dubrovinsky et al. 2015), by using a double stage DAC.

The preparation of a diamond anvil cell starts by gluing a pair of gem quality diamonds to hard-metal seats, usually made of tungsten-carbide alloys, which transmit the load from the cell body to the diamonds. The seats are directly fixed to the two mobile parts of the DAC body. For the correct application two diamonds

should be perfectly aligned with respect to each other. Moreover the diamonds have to lie in a perfectly flat position on the seats in order to avoid possible tilting between them. Tilt between the diamonds leads to an achievable pressure reduction and may result in diamonds destruction at high pressures.

The sample is constrained inside a gasket, typically made of rhenium, which is beforehand pre-indented to 30 μm from an initial thickness of ~200 μm. The so-called "indentation" in the gasket has the shape and the size of the diamonds culets, and a hole of different dimension (depending on the culets size) is drilled in the its centre as a pressure chamber where the sample is placed with or without pressure medium. Re gaskets have good mechanical properties and contain no iron that is critical for instance for Mössbauer spectroscopy experiments.

The force is usually applied in two ways: 1) mechanical screw driven, or in other words by screwing the two parts of the DACs together, and 2) by using membrane cells, where an expandable membrane can contract or expand depending on the amount of gas applied, which in turn compress or release the two parts of the DACs in contact with the membrane. In the current work we used both piston-cylinder type BX90 mechanical DACs (Kantor et al. 2012) and membrane cells provided by the European Synchrotron (ESRF).

This experimental work was aimed for studying materials at lower mantle pressures, therefore diamonds with 120 μm, 250 μm and 300 μm culets were used, allowing us to reach pressures up to ~110 GPa.

2.1.2 Loading of pressure media

The intrinsic design of a DAC causes non-uniform stress upon compression. The stress is uniaxial perpendicular to the diamonds culets surfaces, thus producing non-uniform strain. For this reason aiming to overcome the "non-hydrostaticity" problem in DACs different pressure-media (solid, liquid or gas) have been used. In order to achieve quasi-hydrostatic conditions during the experiments, the best pressure-media are noble gases: He, Ne, Ar. They all crystallize at relatively high pressures and remain quasi-hydrostatic even after crystallization due to relatively low yield strength. In this work He and Ne have been used, however during high temperature experiments only Ne, or other solid phases, such as NaCl, KCl and LiF were utilized. Indeed laser heating to several thousand degrees using He provokes its

intense diffusion in nano- and micro-cracks in the anvils causing their breakage at extreme conditions.

There are several ways to load pressure media inside the gasket. For solid and liquid media, mechanical loading performed under microscope by using very thin needles is the fastest and simplest way. Gases such as Argon, nitrogen and some other can be loaded cryogenically, but for neon and helium special high-pressure loading devices are used. A cell at ambient pressure and slightly open (100-200 μm between the diamonds is enough) is placed inside a "bomb", which once closed is pumped with gas. After this, the DAC is closed while still under pressure inside the "bomb", and only after the gas is released. For this work, the gas loading system (Kurnosov et al. 2008) designed in Bayerisches Geoinstitut (BGI) and the one present at ESRF (sample environment of ESRF) were used for the loadings of BX90- and membrane-type cells, respectively.

2.1.3 Pressure measurements

Pressure determination in diamond anvil cell is crucial in order to precisely to set the experimental conditions. Diffraction is by far the best technique, since it directly exploit the equation of states of the materials (sample and/or pressure medium) under analysis. Equations of states (EoS) of a many materials are known, hence pressure can be directly derived by their diffraction patterns during diffraction experiments, i.e. Ne (Fei et al. 2007).

If diffraction is unavailable two other techniques are widely used: ruby fluorescence spectroscopy and Raman spectroscopy of the diamonds culets. The ruby fluorence method is based on the pressure dependence of the wavelength λ of the $Al_2O_3:C^{3+}$ R_1 peak (Fig. 2.1.2) obtained from the shock wave equations of states of metals (Dewaele et al. 2008). The pressure can be derived from the equation:

$$P(GPa) = \frac{A}{B}\left[\left(\frac{\lambda}{\lambda_0}\right)^B - 1\right]$$ (2.1),

where λ is the measure wavelength of the peak and λ_0 is the wavelength of the peak at ambient pressure, A = 1905, B = 5 for non-hydrostatic conditions and B = 7.665 for quasi-hydrostatic conditions. In the current work we utilized commercially available

ruby spheres from few to tens of microns in diameter size. The ruby should not touch the two diamonds' culets during the experiment in order to minimize the deviatoric stresses acting on it to prevent wrong pressure measurements and distortion of the ruby spectra.
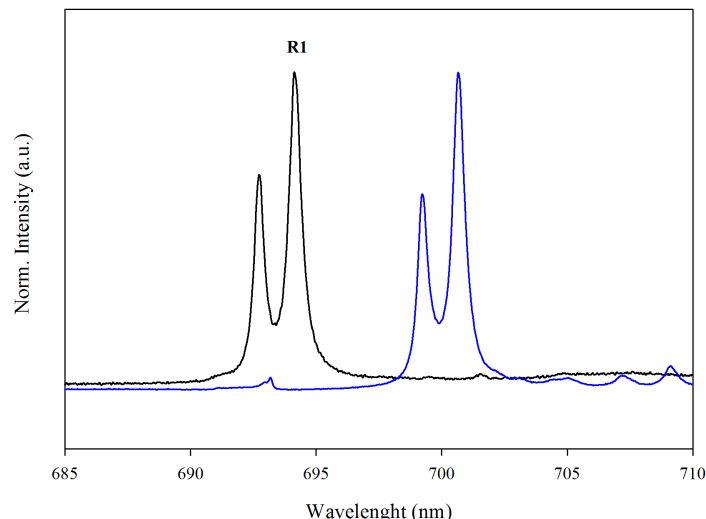
Figure 2.1.2. Typical spectrum of the ruby fluorescence in the DAC at different pressures. A ruby sphere is loaded in the cell along with a single-crystal sample, and the laser-induced fluorescence is visible in the corresponding images. The wavelength shift of the R1 ruby fluorescence peak is used to measure the pressure in the DAC. The black and blue spectra show the ruby fluorescence at 1 bar and 19 GPa respectively. Helium was used as quasi-hydrostatic pressure medium.

The ruby fluorescence method cannot measure pressures higher than ~ 100 GPa due to weakening of the R_1 peak signal. Hence a second technique can be used, the pressure dependence of the first order Raman mode of the diamond' culets (Fig. 2.1.3). The wave number of the Raman band of the diamond is positively correlated with the normal stress experienced by the culet's face, so that the higher the stress the higher the pressure (Akahama and Kawamura, 2006).
Quasi-hydrostatic pressure can be derived from the equation

$$P(GPa) = K_0 \left(\frac{\Delta v}{v_0} \right) \left[1 + \frac{1}{2} \left(K_0^{'} - 1 \right) \left(\frac{\Delta v}{v_0} \right) \right] \tag{2.2},$$

where Δv is the measured wavenumber of the high-frequency edge and Δv_0 is the edge frequency at ambient pressure, $K_0 = 547$ GPa and $K_0{}' = 3.75$. The position of the high-wavenumber edge is defined as the minimum of the first derivative of the spectrum (Fig. 2.1.3).
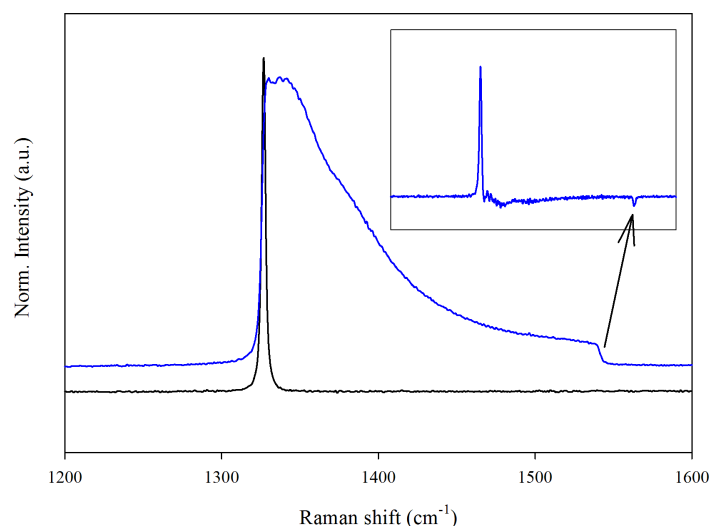
Figure 2.1.3. Typical Raman spectra from the center of the diamond anvil culet at ambient pressure (black) and at 105 GPa (blue). The inset shows a first derivative of the spectrum used for the correct determination of the high-wavenumber edge.

Note that other calibrants have been utilized together with these standard techniques, in order to have other references for specific scopes. For instance, the Sm:YAG crystal calibration (Trots et al. 2013) is used during externally heated DAC experiments, where to precisely measure the temperature in the pressure chamber is applied a correlation between ruby fluorescence (affected by both pressure and temperature) and Sm:YAG fluorescence (pressure dependent but independent from temperature).

2.1.4 Laser heating in DAC

Previously we defined the scope of this work to be the investigation of the stability of Fe-carbonates inside the Earth's interior. The extreme conditions present deep inside our planet can only be achieved experimentally by using laser heated diamond anvil cell (LHDAC). The LHDAC allow studying materials under almost all conditions relevant for the Earth's interior. Indeed by means of LHDAC it is possible

to reach pressures as high as 300 GPa and 6000 K simultaneously (Chandra Shekar et al. 2003). However, laser heating in DAC usually results in high temperature gradients in the sample chamber, which can lead to non-homogeneous heating, thermally induced diffusion and/or movement of the sample. In order to reduce the temperature gradients in DAC, double-sided laser heating systems coupled with P-shapers positioned along the beams path, have been developed.

In this work, we extensively utilized the double-sided laser heating system described by Kupenko et al. 2012. The system consists of two main components: 1) the sources of laser light and 2) the universal laser-heating heads (UniHeads). Two SPI modulated fiber lasers are used as laser sources, with a maxim output power of 50 W and 100 W (excitation wavelength of 1071 nm). At present, the 100 W laser has been replaced by a 200 W one. Both lasers can be operated in continuous or pulsed modes with pulse frequencies up to 100 kHz. The output of the lasers is collected by p-shapers in order to convert the original laser beam with a Gaussian shape intensity distribution to flatten the top distribution down to roughly 50 μm of full width at half maximum (FWHM). The UniHeads are necessary in order to focus the incoming laser radiation on the sample inside the DAC, providing high magnification images of the sample and its illumination and finally to collect thermal radiation from the sample for temperature measurements. Mirrors positioned at different angles depending on the experimental set-up (e.g. Synchrotron Mössbauer Source or Nuclear Inelastic Scattering experiments), are utilized to make laser beam and X-Rays coaxial. The sample is illuminated using light emitting diodes built inside the UniHeads. Both UniHeads are equipped with modules for in situ temperature measurements and visual observation. The temperature measurements are performed with a multi-wavelenght spectroradiometry method by fitting the thermal radiation in a given wavelength range (normally 600 to 850 nm) to the Plank function. For our experiments an Ocean Optics QE65000 spectrometer or an Acton SP2300 spectrometer (Princeton Instruments) with a PIXIS400 CCD detector were used. In Figure 2.1.4, the schematic diagram of the optical components of the laser-heating system.
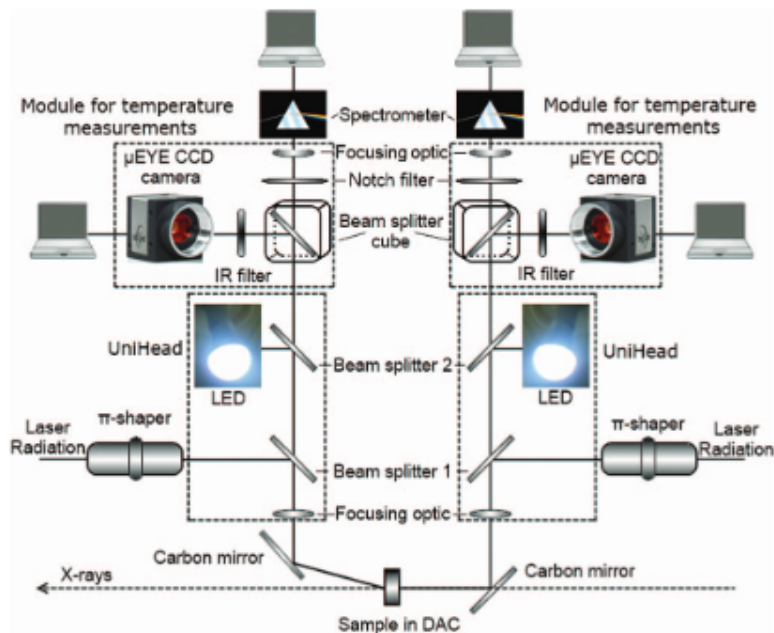
Figure 2.1.4. *From Kupenko et al. (2012)*. Schematic diagram of the optical components of the laser heating system.

Note that to perform our experiments we also employed the YAG double-sided laser heating systems present at the beamlines ID27 at ESRF and at 13 IDD at the Argonne Photon Source (APS).

2.2 Mössbauer Spectroscopy
2.2.1 Basic Principles

Mössbauer spectroscopy is a versatile technique that can be used to provide information in many areas of science such as Physics, Chemistry, Biology and Metallurgy. It can give very precise information about the chemical, structural, magnetic and time-dependent properties of a material. Key to the success of the technique is the discovery of recoilless gamma ray emission and absorption, now referred to as the 'Mössbauer Effect', after its discoverer Rudolph Mössbauer, who first observed the effect in 1957 and received the Nobel Prize in Physics in 1961 for his work.

Nuclei in atoms undergo a variety of energy level transitions, often associated with the emission or absorption of a gamma ray. These energy levels are influenced by their surrounding environment, both electronic and magnetic, which can change or

split these energy levels. These changes in the energy levels can provide information about the atom's local environment within a system and ought to be observed using resonance-fluorescence. There are, however, two major obstacles in obtaining this information: the 'hyperfine' interactions between the nucleus and its environment are extremely small in energy, and the recoil of the nucleus as the gamma-ray is emitted or absorbed prevents resonance.

In a free nucleus during emission or absorption of a gamma ray it recoils due to conservation of momentum, just like a gun recoils when firing a bullet, with a recoil energy E_R. The recoil energy E_R is given by

$$E_R = \frac{E_\gamma^2}{2Mc^2} \qquad (2.3),$$

where E_γ is the energy of the gamma ray, M is the mass of the emitting nucleus and *c* is the velocity of light.

The emitted gamma ray has ER less energy than the nuclear transition but to be resonantly absorbed it must be ER greater than the transition energy due to the recoil of the absorbing nucleus. To achieve resonance the loss of the recoil energy must be overcome in some way. As the atoms will be moving due to random thermal motion the gamma-ray energy has a spread of values E_D caused by the Doppler effect.

What Mössbauer discovered is that when the atoms are within a solid matrix the effective mass of the nucleus is very much greater. The recoiling mass is now effectively the mass of the whole system, making E_R and E_D very small. If the gamma-ray energy is small enough the recoil of the nucleus is too low to be transmitted as a phonon (vibration in the crystal lattice) and so the whole system recoils, making the recoil energy practically zero: a recoil-free event. In this situation, if the emitting and absorbing nuclei are in a solid matrix the emitted and absorbed gamma-ray is the same energy: resonance.

Resonant emission and absorption can be used to probe the hyperfine interactions between an atom's nucleus and its environment. The limiting resolution is the natural linewidth of the excited nuclear state. This is defined by the Heisenberg uncertainty principle which sets a limit on how accurately one can simultaneously measure two complementary variables. In hit case the two quantities are the uncertainties in energy and time, ΔE and Δt respectively, such that $\Delta E\, \Delta t \geq \hbar$, where $\hbar$ is the Planck constant

divided by 2π. The time uncertainty, Δt is interpreted as the mean life, τ, of the level emitting the gamma ray and is related to the more familiar half life, $T_{1/2}$, by $\tau = T_{1/2}/\ln 2$. For ^{57}Fe the half life of the 14.4 keV level is 97.7 ns which gives the uncertainty in the energy as 4.67×10^{-9} eV. This uncertainty becomes the natural linewidth, Γ, of the transition, where $\Gamma = \hbar/\tau$, and this sets the best resolution which can be obtained when utilizing the entire time spectrum of the gammas. Electromagnetic considerations tell us that the intensity, I(E), of the emission line as a function of energy, E, will have the Lorentzian shape given by

$$I(E) = \frac{(\Gamma/2)^2}{(E - E_0)^2 + (\Gamma/2)^2} \tag{2.4},$$

where E_0 is the centre of the emission line. Γ is the full width of the line at half maximum (FWHM).

The narrow linewidth of ^{57}Fe, $\sim 5 \times 10^{-9}$ eV, is of the order necessary to detect the hyperfine interactions in the nucleus.

As resonance only occurs when the transition energy of the emitting and absorbing nucleus match exactly the effect is isotope specific. The relative number of recoil-free events (and hence the strength of the signal) is strongly dependent upon the gamma-ray energy and so the Mössbauer effect is only detected in isotopes with very low lying excited states. Similarly the resolution is dependent upon the lifetime of the excited state limiting the number of isotopes that can be used successfully for Mössbauer spectroscopy.

The electron-nucleus interactions were first observed in optical spectra as smaller splittings than the previously observed "fine structures" (which are due to electon-electron interactions), and hence were defined as hyperfine splittings.

The most important electron-nucleus interaction is the Coulomb interaction that bind the electrons to the nucleus, even if it is not strictly considered to be a hyperfine interaction as it is approximately 10^{10} times as strong as the "true" hyperfine interactions. The three hyperfine interactions of importance here are the *isomer shift*, the *electric quadrupole interaction* and the *magnetic dipole interaction*. Moreover the

thermal or second order Doppler shift should be treated because similar to the isomer shift it produces the same effect on the spectrum.

Isomer shift – The Coulomb interaction assumes that the electrons move around the nucleus at sufficiently large distance to consider the source as a point charge. Even if most the electron charge density is outside the nucleus, s-electrons and partially p-electrons as well have a small but finite probability of being inside the nucleus. This effect is dominated by 1s-electrons and has the effect of shifting the energies of all the nuclear levels. The nucleus undergoes a transition from an excited state to a lower state upon emitting a gamma ray, the radius of the nucleus being different in these two levels $R_g \neq R_e$. The interaction in each level is the integration of the product of the nuclear charge density and the electron charge density over the region of overlap. Since the volume of the overlap region is different for the two nuclear states, the shift of each nuclear level is different (Fig. 2.1).
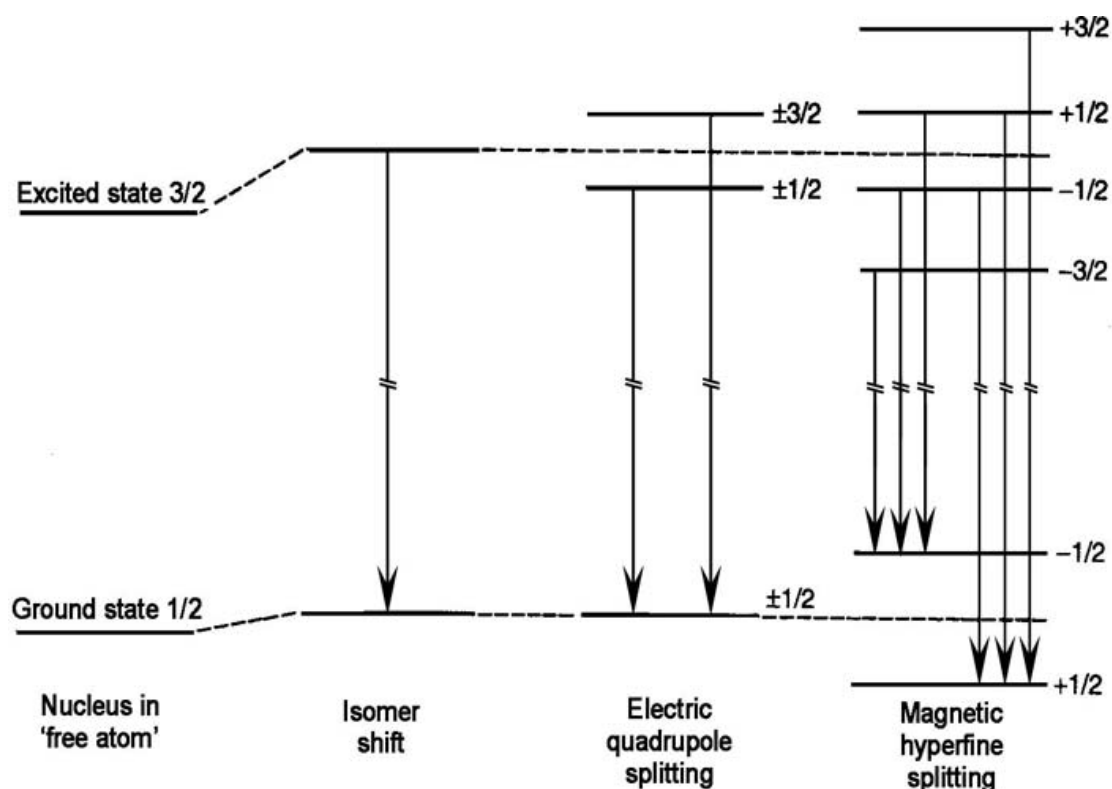
Figure 2.2.1. *From Kaye & Laby, Tables of Physical & Chemical Constants*. The energy level diagram for ^{57}Fe showing the change in transition energy due to isomer shift, quadruple and magnetic splitting.

The difference between the shifts is effectively a measure of the electron density in the very thin annular shell, which makes up the difference in volumes of the two nuclear states. This, principally s-electron density will change in accord with the bonding of the atom and hence will be different for every compound which the atom can be part of.

The mathematical expression for the isomer shift δ

$$\delta = \Delta E_A - \Delta E_S = \frac{2}{3}\pi Z e^2 (\rho_A - \rho_S)(R_e^2 - R_g^2) \qquad (2.5),$$

where ΔE_S and ΔE_A are energy differences between the excited and ground states of a source material and an absorber material consequently. The monopole interaction does not change degeneracy of the energy levels and, therefore, does not cause splitting of the absorption lines.

The second component that contributed to the shift between the emission and the absorption lines is the second-order Doppler shift that is related to the vibration of the atoms on its lattice site

$$\frac{\Delta_{SOD}^E}{E} = -\frac{\langle v^2 \rangle}{2c^2} \qquad (2.6),$$

where *v* is the velocity of the atom. It depends on Debye temperature and absolute temperature of the solid. In a single Mössbauer spectrum it is impossible to separate contributions of the isomer shift and second-order Doppler shift, so one always operates with a sum of both called a centre shift (CS). The CS varies for different valence and spin states and for different coordination numbers of i.e. [57]Fe-atoms.

Electric quadrupole splitting – Any nucleus with an angular momentum, I, greater than ½ is allowed to be non-spherical, e.g. ellipsoid. The measure of the deviation of the nuclear shape from being spherical is called the nuclear quadrupole moment and it causes non-spherical charge distribution. The core quadrupole moment interacts with the electrical field gradient, which are caused by deviation from the spherical symmetry in the electronic environments of the nucleus, and split the degenerate I=3/2 level into two sub levels, with magnetic spin quantum numbers m1=±3/2 and ±1/2 (Fig. 2.2.1).

There are two sources that can contribute to the total electrical field gradients: 1) lattice contribution that is produced by electrons of ligands around the Mössbauer central atom and 2) valence contribution that is the product of the electrons in the valence orbitals of the Mössbauer atom. The electric quadrupole splitting gives information on the oxidation state, the spin state, and the local symmetry of the Mössbauer atoms and in a general case depends on the pressure and temperature.

Magnetic Splitting – Since both protons and neutrons have a magnetic moment, all nuclei have magnetic dipole moments, except of course for those with an even number of protons and neutrons, for which the ground state will have a total angular momentum, I, of zero. The nuclear magnetic moment interacts with the magnetic moment of the electrons to produce the magnetic hyperfine interaction.

In the presence of a magnetic field the nuclear spin moment experiences a dipolar interaction with the magnetic field i.e. Zeeman splitting. There are many sources of magnetic fields that can be experienced by the nucleus. The total effective magnetic field at the nucleus, B_{eff} is given by

$$B_{eff} = (B_{contact} + B_{orbital} + B_{dipolar}) + B_{applied}$$

the first three terms being due to the atom's own partially filled electron shells. $B_{contact}$ is due to the spin on those electrons polarising the spin density at the nucleus, $B_{orbital}$ is due to the orbital moment on those electrons, and $B_{dipolar}$ is the dipolar field due to the spin of those electrons.

This magnetic field splits nuclear levels with a spin of I into (2I+1) substates (Fig. XY_5). Transitions between the excited state and ground state can only occur where m_I changes by 0 or 1. This gives six possible transitions for a 3/2 to 1/2 transition, giving a sextet as illustrated in Figure XY_5, with the line spacing being proportional to B_{eff}.

2.2.2 Radioactive Mössbauer Source

In standard laboratory experiments radioactive sources are utilized in order to get emission of γ-quanta after the decay of the parent excited nuclei to several excited "daughter levels", which in turn decay to the ground state emitting γ-rays. For instance, in order to study the Mössbauer effect in iron bearing compounds, ^{57}Co radioactive sources are employed, which decay to ^{57}Fe emitting γ-quanta, $^{57}Co + e^{1-} \rightarrow$ ^{57}Fe. All laboratory Mössbauer experiments discussed in this doctorate thesis have

been performed at Bayerisches Geoinstitut (BGI) using ^{57}Co radioactive sources. The ^{57}Co isotope has sufficient activity and approximately 9 month half-life, which makes experiments and source replacement operations relatively convenient and not very frequent. For experiments performed in DAC or in general on very little sample (< 100 μm in size) a highly collimated source, "point source", has to be used.

In order to get resonant emission and absorption lines, the Doppler modulation is used. The source is mounted to a velocity drive and is accelerated though a range of velocities producing a Doppler effect and hence scan the gamma ray energy through a specific range. The energy indeed is expressed in "mm/s" units. A typical velocity range for ^{57}Fe bearing compounds is between ±5-15 mm/s (1mm/s = 48.075 neV), where the higher velocities are utilized for "magnetic" samples, or more in general samples having structural sites characterized by magnetism. The absorption spectrum is then collected in gas-proportional detector.

In the present work, we always utilized synthetic samples enriched in ^{57}Fe to optimize the collection time, which in DAC is anyway of roughly 3-4 days, depending on the iron amount of the sample. Not enriched samples in DAC could probably be collected for weeks or months giving probably worse results. All spectra have been fitted using a normalized Lorentzian source lineshape present in the MossA software package (Prescher et al. 2012).

2.2.3 Synchrotron Mössbauer Source

Conventional Mössbauer radioactive sources are an excellent way to study the Mössbauer effect on big samples (millimeter size), possibly "on air" and containing several weight percent of iron. However, in this study we are interested in the study of single crystals of ^{57}FeCO$_3$ not bigger than 15 μm in diameter and inside DACs. Recently, at the ID18 beamline at ESRF has been developed the Synchrotron Mössbauer Source (SMS) technique (Potapkin et al. 2012), which has been used to perform energy domain Mössbauer spectroscopy at conditions relevant for the whole Earth's mantle. The optical scheme for the high-pressure experiments with DACs using the SMS is shown in Figure 2.2.2.

The key element of the SMS is the iron borate ^{57}FeCO$_3$ single crystal that provides ^{57}Fe resonant radiation at 14.4 keV within a bandwidth of ~ 6 neV, which is tunable in energy over a range of about ± 0.6 μeV. In this crystal all (NNN) reflections with odd N (i.e. (111), (333), etc.) are forbidden for electronic diffraction, but they are

allowed for nuclear diffraction because of a specific polarization factor of nuclear resonant scattering in the presence of hyperfine interactions (Smirnov et al. 1997). These reflections are employed to extract nuclear scattering radiation. In the presence of hyperfine splitting of the nuclear levels the crystal functions as a multi-line nuclear radiator. However, close to the Neel temperature of the iron borate crystal and while applying a weak external magnetic field a special condition of combined magnetic dipole and quadrupole interactions can be obtained, where a single-line spectrum of emitted radiation is observed (Smirnov et al. 1997). The energy width of the emitted line is close to the natural linewidth of the Mössbauer resonance. SMS spectra were collected during operation in multibunch mode (7/8 + 1 filling) with the beam focused to a spot size of roughly 10×15 μm^2 using Kirkpatrick-Baez multilayer optics, thus allowing collection during laser heating in within the heating spot. The velocity scale was calibrated using 25 μm thick natural α-iron foil. For the current work, the typical collection time ranged around 30 minutes to few hours, depending mainly on the sample size and composition, the pressure during collection and the temperature (while heating or at ambient temperature). Also in this case the spectra were fitted using MossA software package (Prescher et al. 2012), however in this specific case using a full transmission integral with a normalized Lorentzian-squared source lineshape.
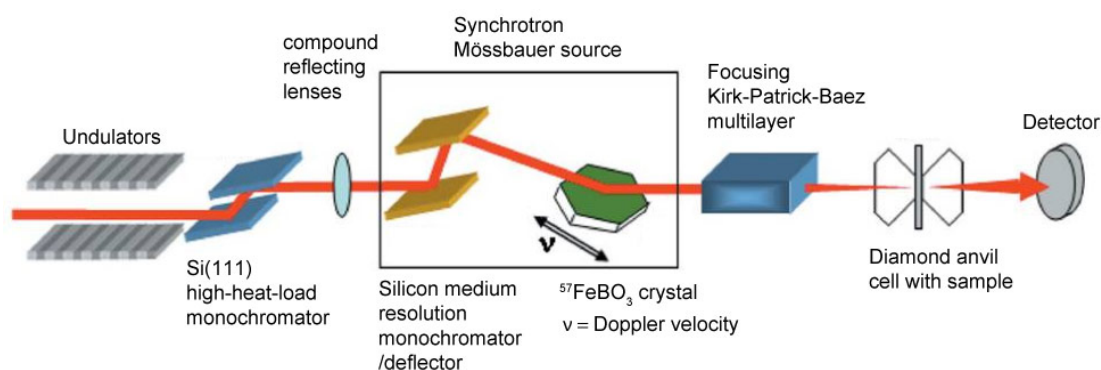
Figure 2.2.2. *From Potapkin et al. (2012).* Optical scheme for high-pressure experiments with DACs using the Synchrotron Mössbauer Source (SMS) at ID18 (ESRF).

2.3 X-Ray Diffraction

2.3.1 Basic principles

X-ray diffraction is the most powerful tool used for identifying the atomic and molecular structure of a crystal. A crystal is a solid material whose constituents, such as atoms, molecules and/or ions, are arranged in a highly ordered microscopic structure, forming a crystal lattice that extends in all directions. The atoms in crystalline solid cause a beam of incident X-rays to diffract into many specific directions. The wavelength of X-ray radiation is indeed well suited for resolving atoms separated by the distance of a covalent bond. The energy of a quantum of this radiation is approximately 8 keV, which is approximately the energy of electrons in their orbitals. This equivalence of energy leads to interactions so that the electrons of an atoms will primarily be responsible for the scattering of X-rays. The number of electrons in a given volume of space, also called *electron density*, determines how strongly an atom scatter X-rays. Scattering simply refers to the ability of objects to change the direction of a wave. The interference of the scattered X-rays leads to the phenomenon of diffraction.

The origin of scattering can be developed starting with Huygen's principle, which states that every point along a wavefront can be considered to be the origin of a new wavefront (Fig. 2.3.1).

(a)   (b)
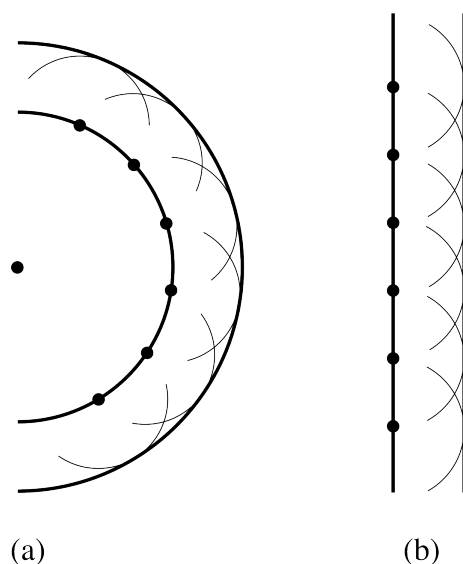
Figure 2.3.1. *Adapted from met.reading.ac.uk*. The Huygens' construction for an unrestricted wavefront in the case of a spherical wavefront (a) and a plane wavefront (b).

The velocity of the new wavefront is equal to that of the original. Objects placed in the path of a wavefront act as points of propagation for new wavefronts, and the entirely new wavefront is called a scattered wave.

If we place two point objects *A* and *B* in the path of the wavefront, each of the two points will propagate a new wavefront having identical wavelengths and velocities. The offset in the maximum amplitude of the two waved depends on the position of *A* and *B* relative to the origin of the initial wavefront. At some position in space, the wave propagating from *A* will reinforce the scattered wave from *B* through constructive interference if the two scattered waves are in phase, or alternatively the wave from *A* will reduce the amplitude of the wave from *B* thgough destructive interference if the amplitudes are out of phase. This is called *diffraction*, the sum of the two waved propagated from *A* and *B* results in an amplitude that's is dependent on the relative positions of *A* and *B* and is also dependent on where the new wavefronts are being observed.

In 1912 W.L. Bragg developed a relationship to understand how diffraction related to the relative position of point objects in space. Stacking a set of reflecting planes at regularly spaced intervals *d* creates a simple model of a one-dimensional crystal (Fig. 2.3.2).

In this model, a wave of X-rays (with wavelength λ) is incident on the reflecting planes at an angle *θ*. The wave is scattered by reflection from the planes at an identical angle *θ*. We assume that the distance to our point of observation is very large compared to *d*, so the individual paths of scattered light are essentially parallel. Because we have a large number of planes, we observe constructive interference only when the reflected waves are perfectly in phase. This only occurs when the difference in the length of the path of the incident and reflected waves of each plane (DE + EF in Fig. 2.3.2), is equal to some integer *n* of the wavelength of the incident X-rays. So that DEF = *n* λ, with the path difference that is related to the distance separating the reflecting planes by the trigonometric relationship 1/2DEF = *d*sin *θ*. Substituting *n* λ with DEF we derive Bragg's law of diffraction

$$2d\sin\theta = n\lambda \tag{2.7}$$

This simple relationship means that larger spacing of repeating units in a crystal results in smaller diffraction angles. As an example of the powder of diffraction, if we consider a simple one-dimensional crystal containing a single atom per unit cell along the c-axis, Bragg's law tells us that we can determine the length of the unit cell along the c-axis just by measuring the Bragg angle.
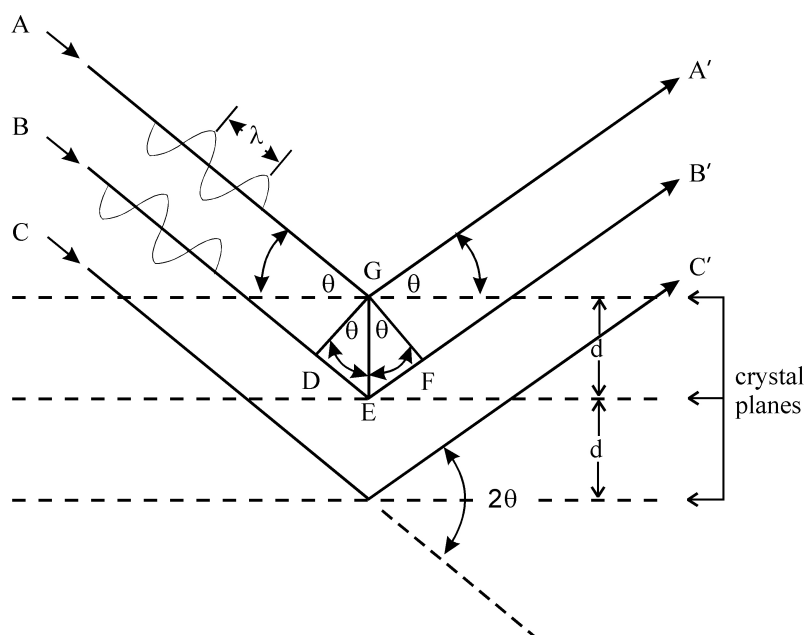
Figure 2.3.2. *Adapted from soils.ifas.ufl.edu*. Bragg's law of diffraction. Incident beams A, B and C of X-rays of wavelength λ hits a regular array of reflecting planes at an angle *θ* b and is reflected at the sample angle. Constructive interference of the reflected or scattered X-rays occurs when the path difference between adjacent planes (spaced by a distance *d*) is equal to some integer number of wavelengths.

2.3.2 X-Ray Powder Diffraction

X-ray powder diffraction (XRPD) is a rapid analytical technique primarily used for phase identification of a crystalline material and can provide information on unit cell dimensions. The analyzed material is finely ground, homogenized, and average bulk composition is determined.

The interaction of the incident rays with the sample produces constructive interference (and a diffracted ray) when conditions satisfy Bragg's law (eq. 7). This law relates the wavelength of electromagnetic radiation to the diffraction angle and the lattice spacing in a crystalline sample. These diffracted X-rays are then detected,

processed and counted. By scanning the sample through a range of 2θangles, all possible diffraction directions of the lattice should be attained due to the random orientation of the powdered material. Conversion of the diffraction peaks to *d*-spacings allows identification of the mineral because each mineral has a set of unique *d*-spacings, which serve as fingerprint of the material.

X-ray powder diffraction is most widely used for the identification of unknown crystalline materials (e.g. minerals, inorganic compounds). Determination of unknown solids is critical to studies in geology, environmental science, material science, engineering and biology.

Other applications include for instance characterization of crystalline materials, identification of fine-grained minerals such as clays and mixed layer clays that are difficult to determine optically, determination of unit cell dimensions, measurement of sample purity. With more sophisticated techniques, XRPD can be used to determine crystal structures using Rietveld refinement, determine of modal amounts of minerals (quantitative analysis), characterize thin films samples and make textural measurements, such as the orientation of grains, in a polycrystalline sample. In the present study, we performed XRPD experiments at ID27 beamline at ESRF, and we analyzed the data first by integrating the diffractograms using Fit2d (Hammersley, 1997) software package and subsequently GSAS/EXPUI software package to fit the data (Larson and Von Dreele, 2000; Toby 2001).

2.3.3 X-Ray Single Crystal Diffraction

Single-crystal X-ray Diffraction is a non-destructive analytical technique which provides detailed information about the internal lattice of crystalline substances, including unit cell dimensions, bond-lengths, bond-angles, and details of site-ordering. Directly related is single-crystal refinement, where the data generated from the X-ray analysis is interpreted and refined to obtain the crystal structure.

As already discussed above, X-ray diffraction is based on constructive interference of monochromatic X-rays and a crystalline sample. When the sample is a single crystal, by changing the geometry of the incident rays, the orientation of the centered crystal and the detector, all possible diffraction directions of the lattice can be attained.

Typical mineral structures contain several thousand unique reflections, whose spatial arrangement is referred to as a diffraction pattern. Indices (*hkl*) may be assigned to each reflection, indicating its position within the diffraction pattern. This pattern has a

reciprocal Fourier transform relationship to the crystalline lattice and the unit cell in real space. This step is referred to as the solution of the crystal structure. After the structure is solved, it is further refined using least-squares techniques.

Single-crystal X-ray diffraction is most commonly used for precise determination of a unit cell, including cell dimensions and positions of atoms within the lattice. Bond-lengths and angles are directly related to the atomic positions. The crystal structure of a mineral is a characteristic property that is the basis for understanding many of the properties of each mineral. Specific applications of single-crystal diffraction include new mineral identification, crystal solution and refinement, determination of unit cell, bond-lengths, bond-angles and site-ordering, characterization of cation-anion coordination, variations in crystal lattice with chemistry and also discovery and determination of new compounds at extreme conditions (high pressure and/or temperature).

In the current study, single-crystal X-ray diffraction experiments have been performed on the ID09a and ID27 beamlines at ESRF, on the 13-IDD beamline at the Advanced Photon Source (APS). The small beam size provided at synchrotron facilities allows to perform XRSD at extreme conditions, making it possible to solve the structure of unique and never seen before phases that are possibly present in the deep interior of our planet. Integration of the reflection and intensities and absorption corrections were performed using CrysAlisPro software (CrysAlisPro Software system, Agilent Technologies). The structures were solved by the direct method and refined in the isotropic approximation by full matrix least-squares refinements using SHELXS and SHELXL softwares (Sheldrick 2008).

2.4 Raman Spectroscopy

Raman spectroscopy has become an important analytical and research tool. It can be used for applications as wide ranging as pharmaceuticals, forensic science, polymers, thin films, semiconductors, geoscience, high-pressure high-temperature physics (i.e. mineral physics).

Raman spectroscopy is a light scattering technique, and it is based on the inelastic scattering of incident monochromatic radiation, usually from a laser. If one analyze the frequency of the scattered radiation will observe two different radiations: 1) the incident radiation wavelength (Rayleigh scattering), which is the scattering process without a change in the frequency hence the radiation scattered from a lattice with no

interaction with phonons and is e.g. the same process that accounts for the blue color of the sky; 2) a small change in the scatter radiation wavelength, which is due to excitation (Stokes) or absorption (Anti-Stokes) of phonons and hence results in scattered radiation at lower and higher energy respectively, depending upon the vibrational state of the molecule. Intensity ratios of Stokes and Anti-Stokes Raman lines are determined by Boltzmann's law. Therefore, the stronger of the two processes is the Stokes scattering, whereby the photon is scattered at lower energy (shifted wavelength towards the red end of the spectrum), since at room temperature the population state of a molecule is principally in its ground vibrational state this is the larger Raman scattering effect. A small number of molecules will be in a higher vibrational level, and hence the scattered photon can actually be scattered at a higher energy, (a gain in energy and a shift to higher energy and a blue shifted wavelength). This is the much weaker Anti-Stokes Raman scattering (Fig. 2.4).
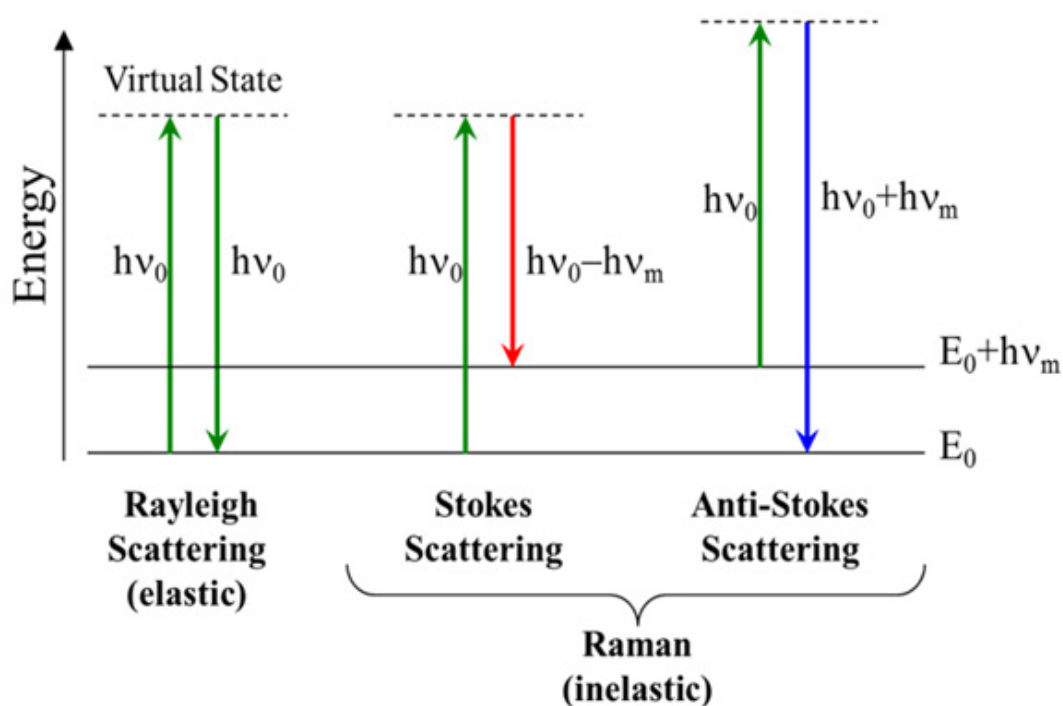
Figure 2.4. Jablonski Diagram (*adapted from Polytec Inc)*. Scattering process scheme, v_0 is the incident laser frequency, h is the Planck constant and v_m is the frequency of the molecular vibration.

The incident photons will thus interact with the present molecule, and the amount of energy change (either lost or gained) by a photon is characteristic of the nature of each bond (vibration) present. Not all vibrations will be observable with Raman spectroscopy (depending upon the symmetry of the molecule.) but sufficient information is usually present to enable a very precise characterization of the molecular structure. As an example, the amount of energy shift for a C-H bond is different to that seen with a C-O bond, and different again to that seen with a Metal-O bond. By looking at all these various wavelengths of scattered light, one can detect a range of wavelengths associated with the different bonds and vibrations.

For the present study Raman spectroscopy was performed by exciting Raman modes using the 514.5 nm Ar^{3+} ion (green) laser in order to avoid overlapping of ruby fluorescence and Raman lines. He scattered radiation was collected in backscattering geometry and analysed by a T64000 system (Dilor XY) with a liquid nitrogen cooled CCD detector. A 1800 grove/mm grating was used with a final resolution of 0.6 cm^{-1}.

2.5 X-Ray Absorption Near Edge Structure (XANES) Spectroscopy

X-ray Absorption Near Edge Structure (XANES) spectroscopy is one of the most powerful tools available for mapping local structure around specific atoms. A sample is probed with x-rays that are tuned to the energy of a core electron shell of the element under investigation (e.g. Fe, Ni, Mn, etc.). In X-ray absorption spectroscopy (XAS), the absorption of X-rays is monitored as a function of their energy. If taken with sufficient accuracy, the spectrum exhibits small oscillations that are the result of the local environment's influence on the target element's basic absorption probability. From the spectrum it is possible to extract the distances between the absorber and its near-neighbor atoms, the number and type of those atoms, and the oxidation state of the absorbing element-all parameters that determine local structure.

The XANES principle is based on the determination of the X-ray absorption coefficient *m* depending on the photon energy *hn* at a fixed angle of illumination *q*. As the optical excitation of a core level electron requires the binding energy E_B as a minimum photon energy, the transgression of this energy will coincide with an increased absorption coefficient. This leads to the formation of absorption edges, which may be indexed by their atomic subshells (K,L,M, and so on). Beyond the

absorption edge the intensity of a monochromatic X-ray passing through a medium of thickness *d* will follow the absorption law

$$I \propto e^{(-\mu d)} \tag{2.8},$$

$$\mu \propto \frac{Z^x}{(hv)^3} \tag{2.9},$$

whereby $3 < x < 4$ and *m* depends the atomic number *Z* of the medium and decreases with increasing photon energy *hn* (Koningsberger 1996). However, the fine structure of this element-specific edge of the absorption coefficient is influenced by the energy of unoccupied electronic levels (Fig. 2.5). Only a sufficient photon energy enables the photoexcitation of a core level electron beyond the vacuum level E_{vac}. After 10×10^{-14} sec (Wagner et al. 1979) the ionized atom may relax by occupation of the core hole with an electron from the valence band (VB), while the generated energy will normally not be used for the emission of a flourescence photon (probability 1 %), but will be absorbed for the vacuum emission of an *Auger electron* (probability 99%) from the valence band. In case of a non-sufficient energy for the emission of the primary electron, it may be excited into a conduction band (CB) level, so that a similar relaxation process becomes possible. This process (spectator process) then results in the emission of only one Auger electron. Alternatively the core hole may be reoccupied by the core level electron itself, so that the excitation energy is finally used for the emission of a valence electron (participator process). The number of generated secondary electrons is thereby directly proportional to the X-ray absorption cross section (Wöll and Wühn 1999). On their way to the crystal surface these electrons undergo multiple scattering processes with other electrons (Fig. 2.5), so that their number is multiplied while their averaged energy is reduced.

The typical XANES experiment measures the photoelectron intensity for photon energies beginning from the absorption edge till 50 eV beyond the edge energy (e.g. Bunker 2010). Although photon energies below the ionization threshold allow electronic transitions into unoccupied electronic bands or molecular orbitals, the spectral features are not directly related to the unoccupied density of states, which instead can be probed with inverse photoemission spectroscopy. In any case, the well-

structured molecular absorption spectra are a powerful tool for the identification of chemical components and redox-induced changes.

In the current work we performed Fe K-edge XANES measurements at ESRF at the energy dispersive X-ray absorption spectroscopy (XAS) beamline ID24 (Pascarelli et al. 2006). The XANES spectra were normalized using the Athena software package (Ravel et al. 2005), and the second-order polynomial for the pixel to energy conversion parameters was calibrated using a reference α-Fe foil.
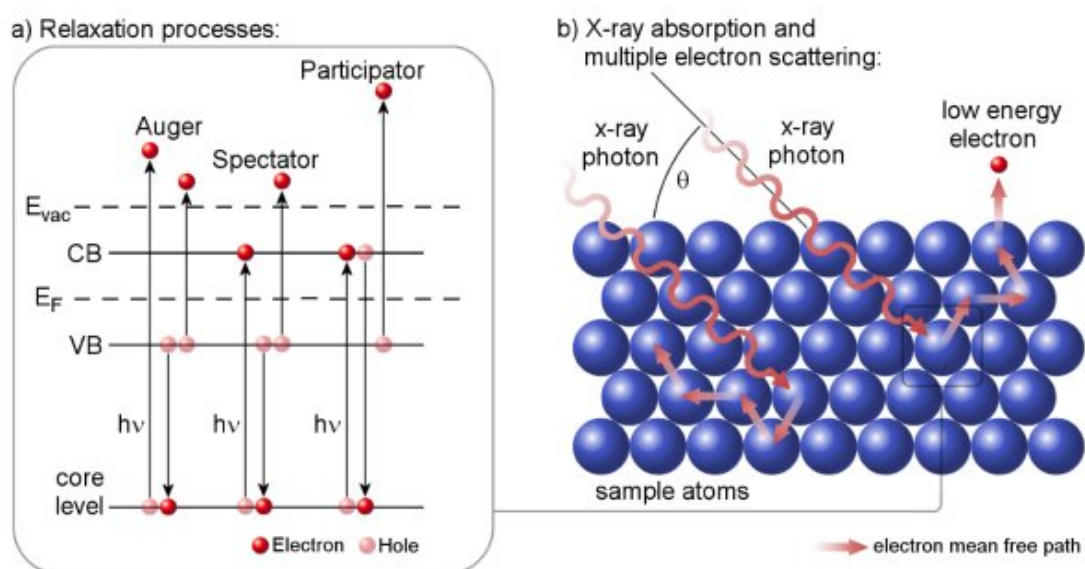
Figure 2.5. *From S. Woedtke, Ph.D. thesis*. Following the excitation of a core level electron several ways of relaxation are possible (a). Thereby secondary electrons are generated which undergo multiple scattering processes before they leave the crystal structure as low-energy photoelelecrons (b).

3. Summary and linkage of research studies

The overall aim of this dissertation is the investigation of the physical and chemical properties of $FeCO_3$ in the Earth's mantle, its stability regions and the characterization of the new structures adopted after the phase transformation and/or decomposition products at specific pressures and temperatures. In a more global perspective we are interested in the fate of subducted carbon, or in other words which are the plausible carbon-carriers inside our planet.

In this cumulative thesis I present the results of four research articles. The first article investigates the spin crossover in $FeCO_3$ at high pressures and ambient temperature using three different analytical techniques Raman, Mössbauer and XANES (Chapter 4), and it is of fundamental importance in order to set solid constraints on $FeCO_3$ behavior at extreme pressures. In the second article (Chapter 5) we investigate the stability regions of $FeCO_3$ at high pressures and temperatures by means of X-ray diffraction and Mössbauer spectroscopy. We describe two new structures characterized by CO_4^{4-} groups and trivalent iron after the transformation of $FeCO_3$ at extreme conditions. Article three (Chapter 6) strengthens and complements the phase diagram proposed in article two by including XANES results. Moreover, the spin transition in XANES spectra (already qualitatively explained in article one) is analyzed by means of *ab initio* simulations. Bulk Fe^{3+}/Fe_{tot} values for a ferropericlase inclusion still contained in a diamond from Juina (Brazil) were measured in different regions of the same inclusion by SMS and reported in Article four (Chapter 7). Changes in the hyperfine parameters and/or of Fe^{3+}/Fe_{tot} values across the inclusion can provide constraints on the diamond's history and on the local deep carbon geodynamic.

3.1 Summary of the articles

Chapter 4 (published in *American Mineralogist*) investigates the spin crossover and its effects on $FeCO_3$ at high pressures and ambient temperature by means of Raman, Mössbauer and XANES spectroscopies. Changes observed in all spectra take place between ~40 and 45 GPa (or 47 GPa according to Raman data) and are the result from electronic spin crossover of *3d* electrons of Fe^{2+} atoms (Fig. 3.1). In Mössbauer spectroscopy Fe^{2+} in octahedral environment and in high-spin (HS)

state is represented by a doublet. Mössbauer spectra of single crystal $FeCO_3$ show decreasing values of the doublet's CS with increasing pressure up to 40 GPa, which can be explained by increasing *s* electron density at the Fe-nucleus due to progressive reduction of interatomic distances. At 40 GPa a new component (singlet) appears (Fig. 3.1a) in the spectra characterized by much lower CS and zero QS. It corresponds to low-spin (LS) Fe^{2+} in octahedral coordination that has no unpaired electrons with nearly spherical charge distribution and hence essentially zero electrical field gradient, because all *3d* energy level are nearly equally occupied. Moreover, the Mössbauer spectra of $FeCO_3$ powder were measured at pressures and, differently from the single-crystal ones, set the beginning of the electrons pairing at ~ 50 GPa and a broader crossover pressure range (> 12 GPa).

In Raman spectra we observe an abrupt shifts to lower frequency of the A_{1g} Raman mode (Fig. 3.1b), which is attributed to internal stretching vibration of the carbonate groups and is therefore strongly dependent on the C-O distance. The shift to lower frequency is a clear sign of increase distance between C-O atoms, which is consistent with what reported by Lavina et al. (2010a), who observed an increase in the C-O bond length due to the structural re-organization caused by the spin pairing of Fe^{2+} atoms. In contrasts, we detect a frequency increase of the external and internal E_g bands at the spin transition. The external modes are translational modes between the anion CO_3^{2-} and cation (Fe^{2+} coordinated by oxygen) sites, and are also influenced by the volume collapse of Fe-O octahedra at the transition. The distances between carbonates groups and cations become shorter, hence the frequency increases.

In XANES spectra the spin crossover is observed in the pre-edge region by the abrupt appearance of an additional peak at 7117 eV at 44 GPa, which is related to excitation of *1s* to *4p* electron states of the valence band and shifts to lower energy with decreasing Fe-O distance. In the actual pre-edge regions at ~ 7112 eV, related to *1s* $\rightarrow$ *3d* transitions, a change from a doublet feature for HS to a singlet for LS states was expected (Westre et al. 1997) and observed experimentally (this study) by a sharpening of the pre-edge peak between 40 and 48 GPa. In the energy region of the main edge (7120-7140 eV) the peaks (peak 1 and peak 2) correspond to a combination of *1s* $\rightarrow$ *4p* electronic transitions and/or multiple scattering of the photoelectron by neighboring atoms. The peaks position shift to higher energy from 1 bar to ~40 GPa due to unit cell compression and the resulting Fe-O bond length decrease, which is also responsible for the increase in the intensity of peak 2 with

pressure. Between 40 and 44 GPa, the spectra show an abrupt change in the relative amplitudes of peak 1 and 2, the appearance of peak 3 and the sudden shift to higher energies of the first EXAFS oscillation (Fig. 3.1c). All these changes are related to the collapse of the Fe coordination polyhedron.

Our results support the idea of a dynamic nature of spin crossover, which involves a non-static distribution of HS and LS states until the transition is complete. Indeed, a static distribution of the two spin states, which could be considered as a long range ordered feature should be easily resolved by XRD, but so far it has not been reported, and has instead been described by XRD as a sharp discontinuity at ~43 GPa. We propose that if a static distribution of the two spin states can be excluded because not observed by XRD, the only way to explain the broad and transient pressure range over which the spin crossover takes place is a dynamic distribution of HS and LS state in the transition region.
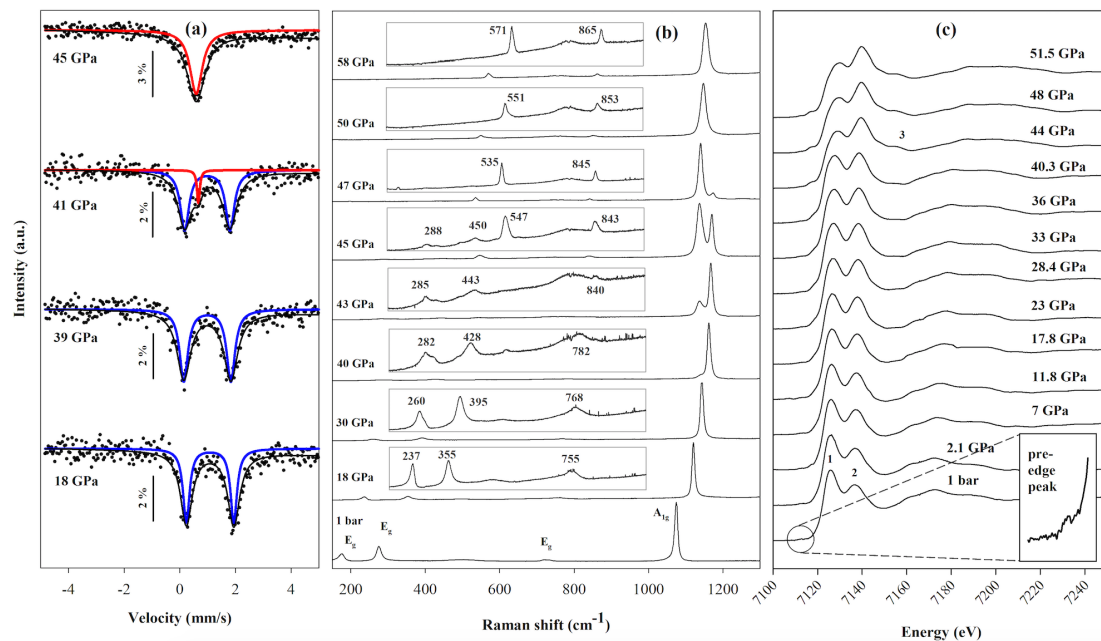
Figure 3.1. Selected (a) Mössbauer (b) Raman and (c) XANES spectra of $FeCO_3$ single crystals collected at ambient temperature and the indicated pressures. (a) Solid circles: experimental data; black lines: full transmission integral fit; blue and red lines: individual subspectra. Percentage bars indicate the relative absorption. (b) the insets indicate the lower frequency Raman bands for the spectra on a different scale. (c) The inset at the bottom right highlights the pre-edge region of the 1 bar spectrum. The spectra are shifted vertically for clarity.

Chapter 5 (published in *Nature Communications*) presents a study on the stability of $FeCO_3$ at pressures over 100 GPa and temperatures over 2500 K using single crystal X-ray diffraction and Mössbauer spectroscopy in laser heated diamond anvil cells. $FeCO_3$ is stable in HS state up to ~ 43 GPa and ambient temperature (Chapter 4), whereas high temperatures preserve Fe^{2+} in HS state so that higher pressures have to be reached in order to observe the electrons pairing (Fig. 3.2). In the pressure region between ~7 GPa to ~70 GPa and temperatures higher than ~1750 K $FeCO_3$ undergoes to incongruent melting, which results in the partial decomposition of the melted material with formation of iron oxides (α-Fe_2O_3 below ~25 GPa and high-pressure orthorhombic h-Fe_3O_4 at higher pressure) (Fig. 3.2). However, while the degree of carbonate decomposition appears to increase at increasing temperature (at a given pressure) and increasing pressure (at a given temperature), we cannot quantify the process based on our existing data. Nevertheless it is clear that all experiments performed below ~51 GPa produced only partial decomposition of the carbonate. Heating $FeCO_3$ above 74(1) GPa and over 1750(100) K results in the formation of both *tetrairon orthocarbonate $Fe_4C_3O_{12}$* and *diiron(II) diiron(III) tetracarbonate, $Fe_4C_4O_{13}$* (Fig. 3.2). In $Fe_4C_3O_{12}$ (hexagonal, space group *R3c*) Each carbon atom is surrounded by four oxygen atoms, forming isolated (i.e., not linked to each other) tetrahedral (Fig. 3.3a). The structure is characterized by two distinct iron position: one Fe atom is situated on a 3-fold axis, while the other is in a general position. Both iron atoms are located in either bicapped or tricapped trigonal prisms formed by oxygen. Both iron sites are considered to be in HS state. A 3-fold symmetry ring is formed by corner- and edge-shared CO_4-tetrahedra and three FeO_8-bicapped prisms. The rings form layers that are stacked along the *c*-axis. In $Fe_4C_4O_{13}$ (monoclinic, space group *C2/c*) each carbon atom is tetrahedrally coordinated by oxygen atoms and four CO_4 groups are linked in truncated chains (Fig. 3.3b). The atomic arrangement of the structure is based on corner-linked infinite chains of FeO_8 bicapped prisms connected in a 3-D framework by dimers of edge-shared FeO_7 monocapped prisms and zigzag-shaped C_4O_{13} chains. Similarity in the sizes of iron polyhedra may indicate that Fe cations are in a mixed valence state (intermediate between +2 and +3). Crystallographic considerations on these two new structures based on interatomic distances and angles allow us to conclude that high-pressure

carbonates can display a great varieties of different structures, contrary to what have been previously predicted (e.g. Oganov et al. 2008).
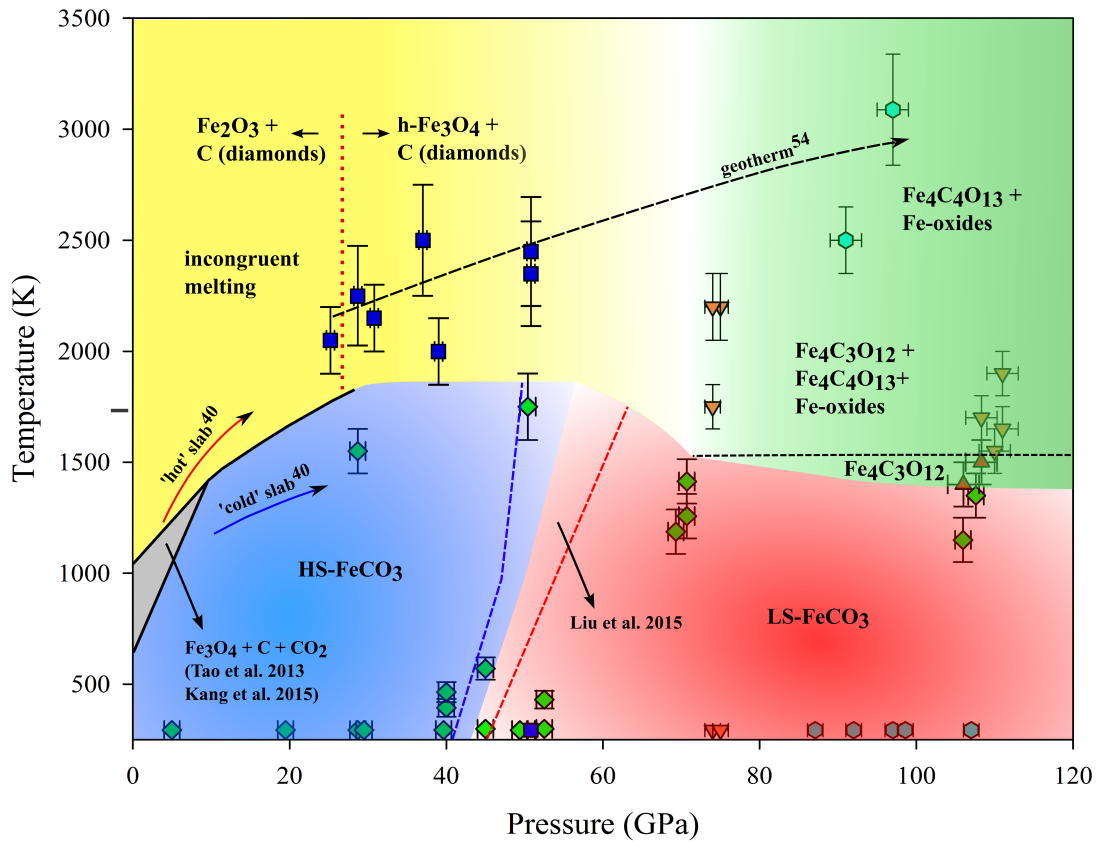
Figure 3.2. Stability diagram of $FeCO_3$ at high *P-T*. Symbols and phase regions identified in experiments: magnesite-structured $FeCO_3$ (green diamonds), oxide(s) and recrystallized $FeCO_3$ (blue squares), tetrairon (III) orthocarbonate $Fe_4C_3O_{12}$ (red triangles), diiron (II) diiron (III) tetracarbonate $Fe_4C_4O_{13}$ + $Fe_4C_3O_{12}$ + oxide(s) (orange inverse triangles), $Fe_4C_4O_{13}$ + oxides (cyan hexagons), $FeCO_3$ decomposition to Fe_3O_4 + C + CO_2 (Tao et al. 2013; Kang et al. 2015) (grey area), high spin $FeCO_3$ (liu et al. 2015) (blue area), low spin $FeCO_3$ (Liu et al. 2015) (red area), incongruent melting of $FeCO_3$ (yellow area), and formation of HP-carbonates $Fe_4C_3O_{12}$ and $Fe_4C_4O_{13}$ (green area). The black dashed curve is an expected mantle geotherm (Katsura et al. 2010). Blue and red solid lines are, respectively, cold and hot slab surface temperature profiles (Syracuse et al. 2010). The black solid lines are from Tao et al. 2013 and Kang et al. 2015. The blue and red dashed lines indicate the region delimiting the spin transition in magnesiosiderite at HPHT from Liu et al. 2015. The vertical dotted red line separates the regions in which the formation of α-Fe_2O_3 and h-Fe_3O_4 was observed upon incongruent melting of $FeCO_3$.

The simultaneous formation of $Fe_4C_3O_{12}$ and $Fe_4C_4O_{13}$ after heating $FeCO_3$ at 74(1) GPa and 1750(100) K may be the result of successive transformations between carbonate phases that are so closely located in P-T space that they cannot be distinguished (Fig. 3.2). Indeed this result is further confirmed by experiments performed at higher pressures: heating a $FeCO_3$ single crystal to 1400(100) K at 107(2) GPa resulted in the formation of $Fe_4C_3O_{12}$. $Fe_4C_4O_{13}$ appeared only after prolonged (about one hour) laser heating above 1650(100) K. In all cases, the appearance of $Fe_4C_4O_{13}$ upon heating at pressures above ~74 GPa was associated with the formation of orthorhombic η-Fe_2O_3, monoclinic Fe_5O_7 and orthorhombic h-Fe_3O_4 phases. The highest temperature at which $Fe_4C_4O_{13}$ was observed is ~3090(250) K at 97(2) GPa, hence stating its plausible existence at Earth's lower mantle conditions. Moreover, the presence of diamonds as subproducts of the HP-carbonates synthesis redox reactions has been also unambiguously documented in previous studies.
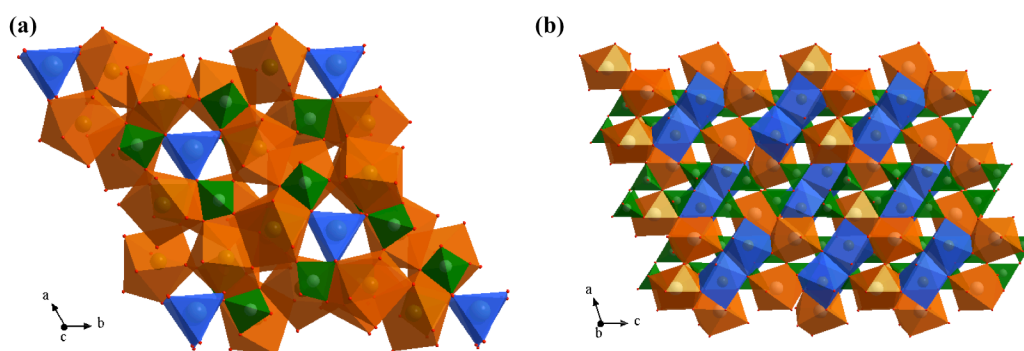
Figure 3.3. Crystal structures of high-pressure carbonates. (a) Tetrairon (III) orthocarbonate $Fe_4C_3O_{12}$ and (b) diiron (II) diiron (III) tetracarbonate $Fe_4C_4O_{13}$, at ambient temperature and 106(2) and 97(2) GPa, respectively.

Chapter 6 (for submission to *American Mineralogist*) explores the stability of $FeCO_3$ at pressures up to ~50 GPa and temperatures above 2000 K by means of XANES spectroscopy, aiming to strengthen the results reported in chapter 5. Moreover theoretical simulations of the absorption spectra, which include both core-hole and spin-polarization effects, were performed in order to quantitatively analyze the spin crossover at high pressures and 0 K in $FeCO_3$.

XANES spectra collected at 36(1) GPa and 51(1) GPa showed that at temperatures higher than 1700-1800 K the characteristic $FeCO_3$ XANES fingerprint is lost and new features emerge. The combination of *ab initio* simulation performed on the Fe K-edge

for h-Fe_3O_4 and $FeCO_3$ at similar pressures strikingly match the experimental spectra (Fig. 3.4), hence confirming the incongruent melting and partial decomposition of $FeCO_3$ during (partial) melting and the formation of Fe-oxide(s).
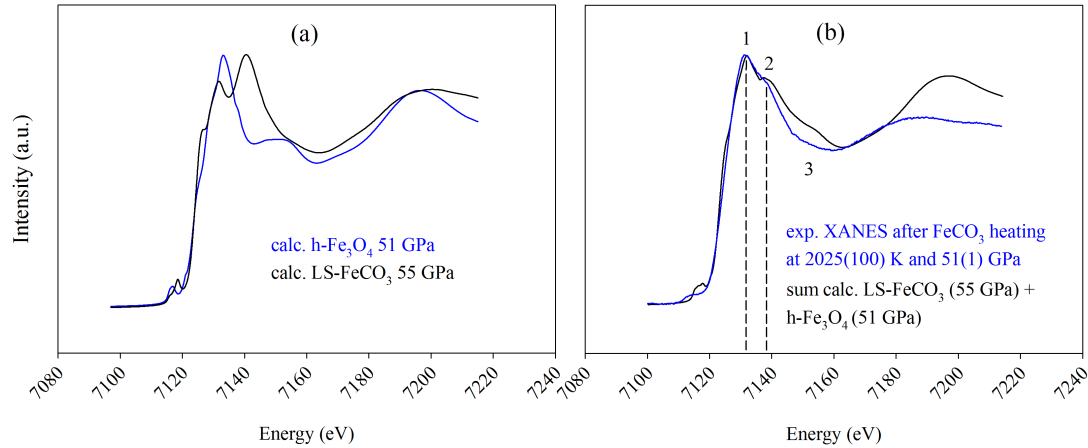
Figure 3.4. (a) Comparison between LS-$FeCO_3$ calculated XANES spectrum at 55 GPa (black) and h-Fe_3O_4 calculated XANES spectrum at 51 GPa (blue). (b) Comparison between the sum of h-Fe_3O_4 and LS-$FeCO_3$ calculated spectra (see Fig. 6.8a) (black) and the experimental spectrum of the system LS-$FeCO_3$ + run product(s) at 51(1) GPa after heating at 2025(100) K (blue). Note that the presence of recrystallized h-Fe_3O_4 after $FeCO_3$ (partial) melting at 51(1) has been observed by XRSD by Cerantola et al. 2017. The presence of other Fe-oxide phases cannot be excluded. Small differences between theoretical and experimental spectra most likely derive by the different extent of decomposition in the experimental runs, which instead in the simulation has been set to 50 % h-Fe_3O_4 and 50 % $FeCO_3$ for practical reasons. The temperature effect on the spin crossover in $FeCO_3$ is also nicely observed in the XANES spectra collected at 51(1) GPa and 53(1) GPa, where is clear for instance that at ~1700 K $FeCO_3$ is completely in HS state by looking at the main peaks relative intensities switch at high temperatures, and still not de composition has taken place. Moreover, one experiment performed at 51(1) GPa allowed us to precisely locate the thermodynamic phase boundary between incongruent melting and LS-$FeCO_3$ at ~1800 K (Fig. 3.5). In the same experimental run the sample has been heated above 2000 K, hence loosing its $FeCO_3$ signatures, and afterwards annealed at lower temperatures, below 1700 K. After annealing, the XANES spectrum went back to almost its original shape, hence showing $FeCO_3$ recrystallization at lower temperatures.
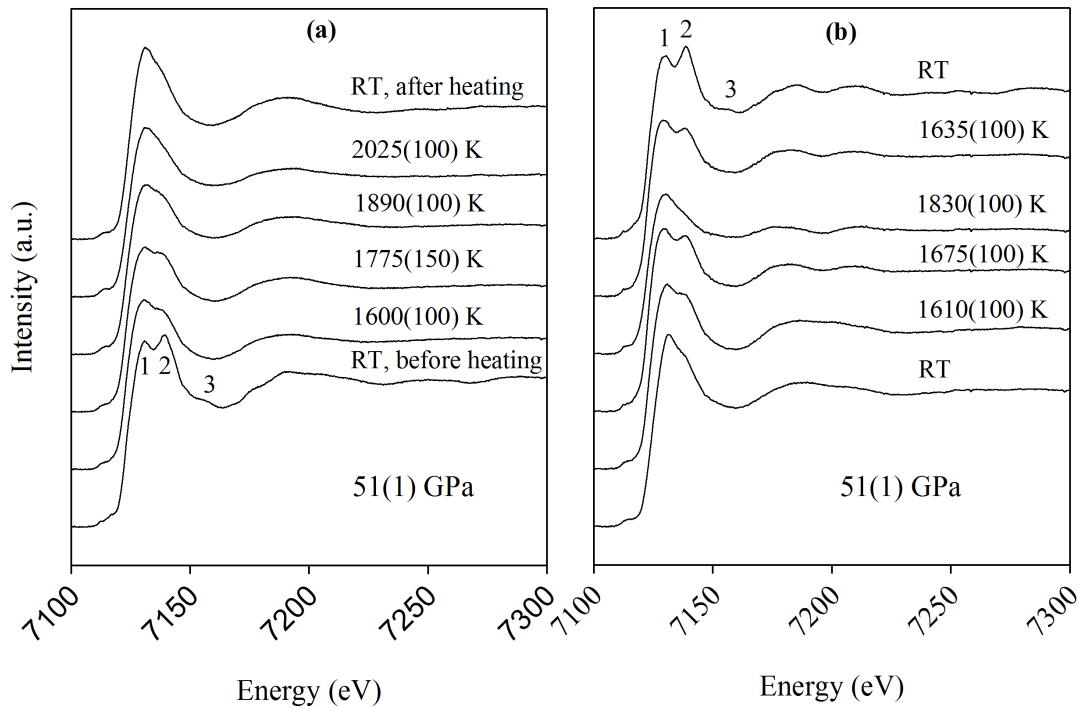
Figure 6.2. Experimental normalized $FeCO_3$ XANES spectra taken at 51(1) GPa and different temperatures. (a) From room temperature till ~1775 K, the $FeCO_3$ fingerprint is still visible in the spectra. Due to the high temperatures, all iron atoms are in high spin state. Above 1775 K the spectra radically change. (b) "Moderate" temperature annealing of the run product(s) obtained after heating at higher temperature (T > 2000 K).

In conclusion, this XANES study confirmed and further constrained the phase boundary of $FeCO_3$ between high and low spin state, as well as the incongruent melting with subsequent non-stoichiometric recrystallization of $FeCO_3$ + h-Fe_3O_4 and perhaps other Fe-oxide phases, which however have not been observed by XRD.

The similarity between simulated and experimental spectra is quite remarkable. In particular, the double peak feature at the main edge (peaks 1 and 2) has been simulated. This feature is the one that is most indicative for the change in Fe spin state in spectra. In the pre-edge region instead, simulated spectra show slight differences between HS and LS state, but a comparison to experiment is difficult due to low resolution and low statistical quality of the experimental data.

Overall, the theoretical spectra and analysis of the *l*-projected density of states show that the changes in the main-edge XANES region of the spectra are mainly related to

the shift of p-states to higher energies, which is induced by the reduction of the Fe-O distance.

Chapter 7 (published in *Lithos*) describes a new methodology to collect energy domain Mössbauer spectra of inclusions in natural diamonds using a Synchrotron Mössbauer Source (SMS). In particular the diamond used in this study comes from a suite of alluvial diamonds from São Luiz (Juina, Brazil) (Fig. 3.6). This locality is considered the main world locality of super-deep diamonds. For the first time it was possible to measure the Fe^{3+}/Fe_{tot} values across a black tabular inclusion (dimensions of roughly 192 x 85 x 105 μm^3) identified as ferropericlase by XRD, without removing it from its diamond host. Any variation of Fe^{3+}/Fe_{tot} values across the inclusion provide information about the growth of the crystal and its growing environment, which can vary due to changes in external conditions such as pressure, temperature and fO_2 from the moment of the inclusion's nucleation to the encapsulation inside the hosting diamond.

Figure 7.1. Diamond containing ferropericlase inclusion AZ2 (indicated with a red circle).

Mössbauer spectra collected in five different spots are dominated by a broad quadrupole. Qualitatively they look similar to spectra collected from ferropericlase inclusions in diamond using a radioactive source with the difference that SMS spectra probe individual regions of ~15 μm diameter while radioactive source spectra provide

only an average measurement of the entire ferropericlase inclusion (> 100 μm diameter). From the fitting the detection limit for Fe^{3+}/Fe_{tot} in ferropericlase was estimated to be 0.02, however, all spots show the presence of a magnetic component at varying levels above experimental uncertainty (e.g. Fig. 3.7), and correlation of amounts with their estimated positions on the inclusion based on the absorption profiles reveal that the magnetic component abundance is highest in the centre and left region of the inclusion. The centre shift and magnetic hyperfine field of the magnetic component are indicative of Fe^{3+} and fall close to values for synthetic $MgFe_2O_4$ and Fe_3O_4 as well as solid solutions in between. The absence of superparamgnetism allows the minimum particle size for this phase to be estimated as ~ 30 nm. The amount of the magnetic phase present in the different regions of the ferropericlase inclusion can be determined from the relative areas of the Mössbauer spectra based on the estimated iron concentration in each phase. Assuming endmember magnesioferrite and an iron-poor ferropericlase composition (Fe# = 0.15), the volume fractions range between 0.5 and 2% for the different regions, while for an iron-rich composition (Fe# = 0.6) the range is 2 to 7%.
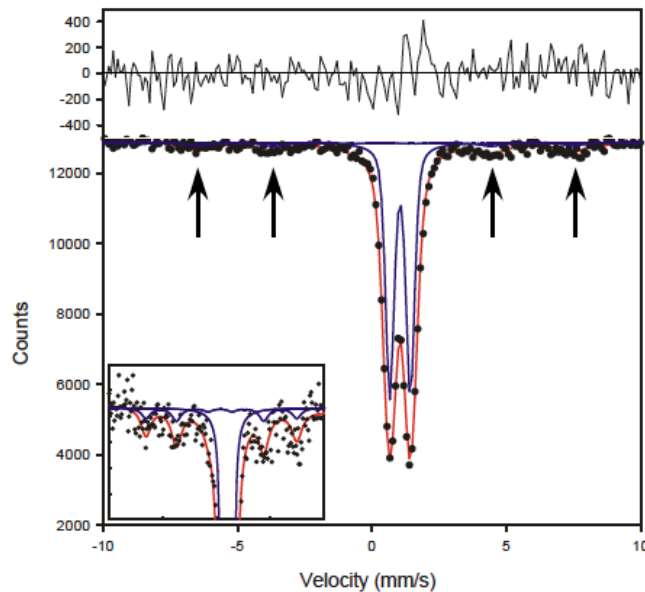
Figure 3.7. Room temperature SMS spectrum of spot #6 (see chapter 7) on ferropericlase inclusion AZ2 collected over a large velocity range. The spectrum was fitted to one quadrupole doublet and one magnetic sextet. The arrows indicate the positions of four peaks of the magnetic sextet, which can be seen more clearly in the inset that shows a magnified view near the baseline.

3.2 List of manuscripts and statement of author's contribution

[1] <u>Cerantola, V.</u>, McCammon, C., Kupenko, I., Kantor, I.Y., Marini, C., Wilke, M., Ismailova, L., Solopova, N., Chumakov, A.I., Pascarelli, S., and Dubrovinsky, L. (2015) High-pressure spectroscopic study of siderite ($FeCO_3$) with focus on spin crossover. American Mineralogist, 100, 2670-2681, doi: 10.2138/am-2015-5319.

L.D., C.M. and V.C. proposed the research and did the project planning. V.C. synthesized the samples. V.C., L.I. and N.S. prepared the high-pressure cells. V.C., C.M., K.I., K.I.Y., C.Ma., A.I.C., L.D. performed the experiments. V.C., C.M. and L.D. analyzed Raman and Mössbauer spectroscopy data. V.C., M.W., P.S. and L.D. analyzed the XANES data. V.C., L.D. and C.M interpreted the results and wrote the manuscript with contributions of all authors.

[2] <u>Cerantola, V.</u>, Bykova, E., Kupenko, I., Merlini, M., Ismailova, L., McCammon, C., Bykov, M., Chumakov, A.I., Petitgirard, S., Kantor, I., Svitlyk, V., Jacobs, J., Hanfland, M., Mezouar, M., Prescher, C., Rüffer, R., and Dubrovinsky, L. (2016) Stability of iron-bearing carbonates in the deep Earth's interior. Under Review in Nature Communications.

L.D., C.M. and V.C. proposed the research, did the project planning and provided the sample. E.B. and L.I. selected the single-crystals. V.C., L.D., L.I., I. Yu. K. and J.J. prepared the high-pressure experimental setups. V.C., L.D., E.B., M.M., L.I., M.B., V .S., S.P., M.H., C.P., and M.M. conducted the HPHT single-crystal X-Ray diffraction experiments. V.C., L.D., C.M., I.K., A.I.C, and R.R. conducted the SMS experiments. E.B., L.D. and M.M. analyzed the X-Ray Single Crystal Diffraction data. V.C. and L.D analyzed the X-Ray Powder Diffraction data. V.C., C.M. and L.D. analyzed the Mössbauer data. V.C., L.D. and C.M interpreted the results and wrote the manuscript with contributions of all authors.

[3] <u>Cerantola, V.</u>, Wilke, M., Kantor, I.Y., Ismailova, L., Kupenko, I., McCammon, C. and Dubrovinsky, L.S. (2016) Experimental investigations on $FeCO_3$ (siderite) stability in the Earth's lower mantle by XANES spectroscopy. For submission to American Mineralogist.

L.D., C.M. and V.C. proposed the research and did the project planning. V.C. synthesized the samples. V.C., and L.I., prepared the high-pressure cells. C.V., K.I.Y., I.L., K.I., C.M. and L.D. performed the experiments. V.C. and M.W. analyzed the data. M.W. performed the theoretical simulations. V.C., and M.W. interpreted the results and wrote the manuscript with contributions of all authors.

[4] Nestola, F., <u>Cerantola, V.</u>, Milani, S., Anzolini, C., McCammon, C., Novella, D., Kupenko, I., Chumakov, A.I., Rüffer, R., and Harris J.W. (2016) Synchrotron Mössbauer Source technique for *in situ* measurement of iron-bearing inclusions in natural diamonds. Lithos, doi:10.1016/j.lithos.2016.06.016.

V.C. and F.N. proposed the research and did the project planning. J.W.H. provided the sample. V.C., S.M., C.A., C.M., I.K. A.C.I., R.R. and D.N. performed the experiments. C.M. and V.C. (minor contribution) analyzed the data. F.N., C.M., and V.C. interpreted the results and wrote the manuscript with contribution of all authors.

4. High-pressure spectroscopic study of siderite (FeCO₃) with focus on spin crossover

Cerantola Valerio,[1,*] McCammon Catherine,[1] Kupenko Ilya,[1,2] Kantor Innokentiy,[2] Marini Carlo,[2] Wilke Max,[3] Ismailova Leyla,[1] Solopova Natalia,[1] Chumakov Aleksandr I.,[2] Pascarelli Sakura,[2] and Dubrovinsky Leonid[1]

[1] Bayerisches Geoinstitut, Universitat Bayreuth, D-95440 Bayreuth, Germany

[2] European Synchrotron Radiation Facility, 38043 Grenoble, France

[3] Deutsch GeoForschungsZentrum GFZ, D-14473 Potsdam, Germany

* Valerio Cerantola, M.Sc. valerio.cerantola@gmail.com

4.1 Abstract

Fe-bearing carbonates have been proposed as possible candidate host minerals for carbon inside the Earth's interior and hence their spectroscopic properties can provide constraints on the deep carbon cycle. Here we investigate high-pressure spin crossover in synthetic $FeCO_3$ (siderite) using a combination of Mössbauer, Raman and X-Ray Absorption Near Edge Structure spectroscopy in diamond anvil cells. These techniques sensitive to the short-range atomic environment show that at room temperature and under quasi-hydrostatic conditions, spin crossover in siderite takes place over a broad pressure range, between 40 and 47 GPa, in contrast to previous X-Ray diffraction data that described the transition as a sharp volume collapse at approximately 43 GPa. Based on these observations we consider electron spin pairing in siderite to be a dynamic process, where Fe atoms can be either high spin or low spin in the crossover region. Mode Grüneisen parameters extracted from Raman spectra collected at pressures below and above spin crossover show a drastic change in stiffness of the Fe-O octahedra after the transition, where they become more compact and hence less compressible. Mössbauer experiments performed on siderite single crystals as well as powder samples demonstrate the effect of differential stress on the local structure of siderite Fe atoms in a diamond anvil cell. Differences in quadrupole splitting values between powder and single crystals show that local

distortions of the Fe site in powder samples cause spin crossover to start at higher pressure and broaden the spin crossover pressure range.

4.2 Introduction

Chemical and physical interactions between atmosphere, biosphere and geosphere are well known and established processes on our planet. However, the mechanisms governing the dynamics and the stability of materials in the deep Earth's interior are still the subject of ongoing debate. The possibility of carbon cycling through the deep Earth (e.g., Dasgupta and Hirschmann, 2010) is demonstrated by observations such as the occurrence of diamonds from the lower mantle, carbonate inclusions in mantle xenoliths and diamonds, and the presence of CO_2 in gases from volcanic eruptions (e.g., Brenker et al., 2007; Harte, 2011; Walter et al., 2011). However, the size of the carbon reservoir inside the Earth is still not well constrained, and is closely linked to the nature of the dominant carrier(s) of carbon down to the core-mantle boundary (e.g., Biellmann et al., 1993; Lavina et al., 2009; Stagno et al., 2011; Boulard et al., 2011).

Deep carbon is predominantly stored in accessory phases as a consequence of its low solubility in dominant mantle minerals (e.g., Keppler et al., 2003), where these accessory phases include carbonates, diamonds/graphite, methane and carbides, depending on pressure, temperature, and oxygen fugacity. In highly reducing environments (i.e., low oxygen fugacity), the crystalline form of carbon is graphite or diamond. At more oxidizing conditions, carbonates are favored due to the reaction between elemental carbon and oxygen to form $(CO_3)^{2-}$ groups that bond to other cations such as Ca^{2+}, Mg^{2+}, Fe^{2+}, Ni^{2+} and Na^+ depending on the composition of the original bulk assemblage.

The three major carbonate components in the crust and upper mantle are $CaCO_3$ (calcite), $MgCO_3$ (magnesite), and $FeCO_3$ (siderite). The presence of carbonates in the Earth's interior is related to the subduction process, one of the first steps in cycling carbon through the Earth. The $CaCO_3$-$MgCO_3$-$FeCO_3$ system has been experimentally investigated at relatively low pressures and moderate temperatures (P < 3.5 GPa, T < 1100° C) since many decades (e.g., Goldsmith et al., 1962; Rosenberg, 1967; Merrill and Bassett, 1975; Franzolin et al., 2011). Low-pressure ternary phase diagrams indicate the formation of extensive solid solutions,

with compositions depending on pressure and temperature. Observations from geophysics (e.g., Fukao et al., 2009) and natural samples (e.g., Brenker et al., 2007; Walter et al., 2011) suggest that some subducted slabs penetrate the lower mantle. In this case, carbonates could be stable phases due to the proposed higher oxygen fugacity in the region of the slab. The properties of carbonates are, however, not well understood, and many questions remain open regarding their stability, composition and geophysical properties.

Previous high-pressure studies on the carbonate endmembers $CaCO_3$, $MgCO_3$, and $FeCO_3$ revealed high-pressure phase transitions in all phases (e.g., Ono et al., 2005; Merlini et al., 2012; Biellmann et al., 1993; Isshki et al., 2004). Magnesite shows a structural change at 115 GPa and 2100-2200 K (Isshki et al., 2004), whereas magnesiosiderite experiences a volume collapse of almost 10 % between 40 and 50 GPa at ambient temperature, caused by a high-spin to low-spin (HS-LS) transition of iron (Lavina et al., 2009). Shi et al. (2008) predicted the spin transition of Fe in pure siderite by *ab initio* simulations to be between 15 to 28 GPa, while the first experimental observation was reported by Mattila et al. (2007) to occur at roughly 50 GPa from natural siderite powder using X-ray emission spectroscopy. Lavina et al. (2009) described a sharp volume collapse at 43 GPa from X-ray single crystal diffraction, whereas Farfan et al. (2012) observed spin crossover in a (Mn,Mg)-siderite at 46 GPa using Raman spectroscopy and X-ray single crystal diffraction. Lin et al. (2012) studied $Mg_{0.35}Fe_{0.65}CO_3$ up to 80 GPa at ambient temperature and observed the spin transition at 45 GPa, where their data suggested that the low-spin state has different vibrational and elastic properties compared to the high-spin state. Temperature extends the spin crossover region of magnesiosiderite (Liu et al., 2014). Merlini et al. (2012) postulated that the low-spin state could contribute to the stabilization of Fe-bearing Ca,Mg-carbonate (so-called dolomite-III) above 35 GPa and 2000 K, and Liu et al. (2015) reported an orthorhombic phase of magnesiosiderite above 50 GPa and 1400 K that also appeared to be stabilized by spin crossover. It is therefore clear that iron can play a fundamental role in the behavior of carbonates at high pressure and high temperature.

To elucidate the effect of iron on the behavior of carbonates at high pressure, in particular the nature of spin crossover, we undertook a combined spectroscopic study of the siderite endmember. Nuclear resonance techniques (including Mössbauer spectroscopy) provide a sensitive method to detect the response of Fe atoms to

physical changes like spin crossover, and X-ray Absorption Near Edge Structure (XANES) and Raman spectroscopies provide complementary information.

4.3 Methods

4.3.1 Synthesis

Iron oxalate (FeC_2O_4) was used as a starting material to synthesize $FeCO_3$. Commercial FeC_2O_4 from Alfa Aesar was used for ^{57}Fe-unenriched samples, while for ^{57}Fe-enriched samples, iron oxalate was synthesized by chemical reaction of ^{57}Fe metal with acetic acid, forming ^{57}Fe-diacetate precipitate, $^{57}Fe(C_2H_3O_2)_2$. The precipitate was then reacted in the presence of oxalic acid to produce ^{57}Fe-enriched iron oxalate. All chemical reactions were run under argon to prevent oxidation of iron to Fe^{3+} at ambient conditions. FeC_2O_4 powder was then sealed in gold capsules of 2.3 mm outer diameter and loaded into an externally heated cold seal vessel and run at 2 kbars and 360 °C for seven days, following French (1971). The obtained powder was used to grow $FeCO_3$ single crystals using a multi-anvil press at Bayerisches Geoinstitut. The powder was pressed inside Re capsules to avoid loss of Fe and placed inside assemblies with $LaCrO_3$ heaters where temperature was measured using $W_{75}Re_{25}/W_{97}Re_3$ thermocouples. The samples were annealed for 10 minutes at 18 GPa and 1600 °C, which yielded single crystals of approximately 5 to 50 µm diameter. The same procedure was used to synthesize both ^{57}Fe-enriched (96% ^{57}Fe) and unenriched (2% ^{57}Fe) $FeCO_3$ single crystals.

4.3.2 High pressure experiments

Diamond anvil cells (DACs), type BX-90 (Kantor et al., 2012), were mounted with diamonds with culet sizes of 250 µm and rhenium gaskets with 120 µm starting diameter hole were employed in all experiments. We used neon gas loaded under pressure (1.4 kbar) (Kurnosov et al., 2008) as a pressure-transmitting medium to obtain hydrostatic conditions, and we measured the wavelength of the ruby fluorescence before and after each experimental run to calculate pressure (Mao et al., 1986). The difference in values contributed to the pressure uncertainty, which was estimated to be 1 and 3 GPa for single crystal and powder experiments, respectively. All DACs were prepared by loading a ~ 15 - 20 µm diameter isomeric $FeCO_3$ single-crystal chip and a smaller ruby crystal (Fig. 4.1a), with the exception of Mössbauer

measurements using a radioactive source where more than ten [57]Fe-enriched crystals were used in the pressure chamber to optimize signal acquisition time and signal to noise ratio (Fig. 4.1b). A similar series of Mössbauer measurements was also performed using $FeCO_3$ powder, which was compressed to a pellet before loading in the DAC in order to reduce porosity between the grains. All single crystals survived intact throughout each experimental run without breaking or cracking. To test the degree of hydrostaticity, in some experiments we placed two or three ruby crystals in different positions inside the pressure chamber. In all cases we measured the pressure from each ruby within the same experiment to be within ± 1 GPa of each other.
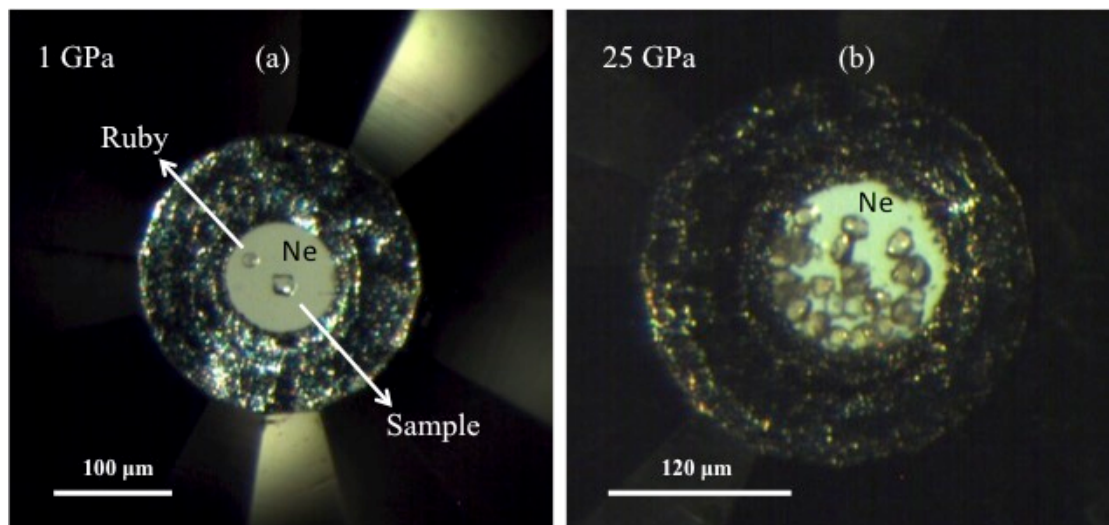
Figure 4.1. Photographs of $FeCO_3$ samples in DACs at the indicated pressures with (a) one single crystal and (b) multiple single crystals, each surrounded by Ne. Both loadings contain a small ruby crystal as a pressure calibrant.

4.3.3 *In situ* analytical techniques

4.3.3.1 Mössbauer spectroscopy

[57]Fe Mössbauer spectra were recorded at room temperature in transmission mode on a constant acceleration Mössbauer spectrometer with a nominal 370 MBq [57]Co high specific activity source in a 12 μm-thick Rh matrix (referred to below as "in house" spectra). Spectra collection took 2 to 4 days for each pressure point. A set of Mössbauer spectra was also collected during compression using the Synchrotron Mössbauer Source (SMS) at the European Synchrotron Radiation Facility (ESRF), Grenoble, France on the Nuclear Resonance beamline (Rüffer et al., 1996) ID18. The

narrow (~6 neV) energy component of X-rays at the Mössbauer energy of 14.4 keV was extracted from a wide spectrum of synchrotron radiation using a $^{57}FeBO_3$ single crystal monochromator and focused to a beam width of size of 10x15 μm^2 using Kirkpatrick-Baez mirrors (Potapkin et al., 2012). Each SMS spectrum took approximately thirty minutes to collect. The velocity scales of all Mössbauer spectra were calibrated relative to 25 μm thick α-Fe foil, and all spectra were fitted using the software package MossA (Prescher et al., 2012a). All Mössbauer measurements were performed on ^{57}Fe-enriched $FeCO_3$.

4.3.3.2 Raman spectroscopy

Raman measurements were performed on a DILOR XY triple spectrometer using the 514 nm line of Ar^+ laser with 2 cm^{-1} spectral resolution and 2 μm spatial resolution at 300 mW of power. Data acquisition was performed with a frequency range extending from 150 to 1300 cm^{-1}. In order to maximize the signal to noise ratio, each spectrum was collected in three steps over three smaller regions of frequency, where each region was measured five times using an exposure time of 60 seconds, and then merged together at the end of the acquisition. Orientation effects of the single crystals and hence any polarization effects on the spectra are considered to be negligible since we used an unpolarized green Raman source and all crystals were maintained in the same orientation during the experiment. All Raman data presented in the paper were collected on the same single crystal up to the target pressure. Raman measurements were performed at Bayerisches Geoinstitut, Bayreuth, Germany, and spectral fitting was carried out using the software package PeakFit (Systat Software).

4.3.3.3 XANES spectroscopy

Fe K-edge XANES measurements were performed at ESRF at the energy dispersive X-ray absorption spectroscopy (XAS) beamline ID24 (e.g., Pascarelli et al., 2006). The beam was focused horizontally using a curved polychromator Si 111 crystal in Bragg geometry and vertically with a bent Si mirror. The obtained cross-section is about 3x5 (HxV) μm^2. The measured XANES spectra were normalized using the Athena software package (Ravel et al., 2005), and the second-order polynomial for the pixel to energy conversion parameters was calibrated using a reference α-Fe foil spectrum.

4.4 Results

4.4.1 Mössbauer spectroscopy

Mössbauer spectroscopy provides information about the electronic, magnetic and structural properties of specific elements within a material. The extremely narrow line width of gamma rays (4.5×10^{-9} eV in the case of ^{57}Fe) provides Mössbauer spectroscopy with the sensitivity to detect spin transitions in compounds with Mössbauer-active nuclei.

The evolution of $FeCO_3$ Mössbauer spectra at 298 K and increasing pressure is similar to spectra already reported for other non-magnetic compounds containing Fe^{2+} in an octahedral environment, for example ferropericlase (Fe,MgO) (Kantor et al., 2006b).
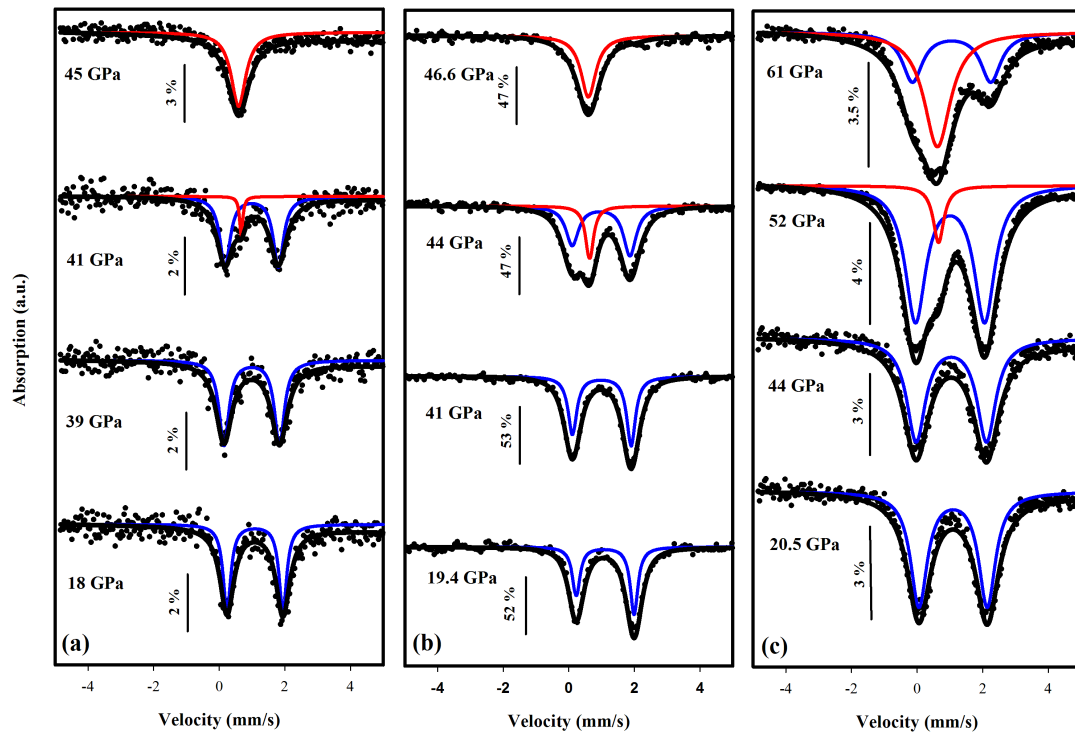
Figure 4.2. Room temperature Mössbauer spectra of $FeCO_3$ (a) single crystals and (c) powder collected in house at the indicated pressures. (b) SMS spectra of one $FeCO_3$ single crystal collected at ESRF, Grenoble (France). Solid circles: experimental data; black lines: full transmission integral fit; blue and red lines: individual subspectra. Note that the subspectra do not add up to the total spectrum due to the properties of the full transmission integral fit. Percentage bars indicate the relative absorption.

At pressures below 40 GPa, Fe^{2+} in octahedral coordination is represented by a doublet, while at higher pressures the doublet is progressively replaced by a singlet, which at pressures higher than 45 GPa is the only component present in the spectra of single-crystal $FeCO_3$ (Fig. 4.2a, 4.2b). Mössbauer spectra of powder $FeCO_3$ show a similar evolution with increasing pressure, but over a larger pressure interval (Fig. 4.2c).

The centre shift (CS) is sensitive to the s-electron density at the nucleus, while the quadrupole splitting (QS) measures the electric field gradient (EFG) caused by a non-symmetrical charge distribution around the nucleus. The evolution of hyperfine parameters with increasing pressure for both single crystals and powder samples is shown for CS and QS in Figs. 4.3a and 4.3b, respectively.
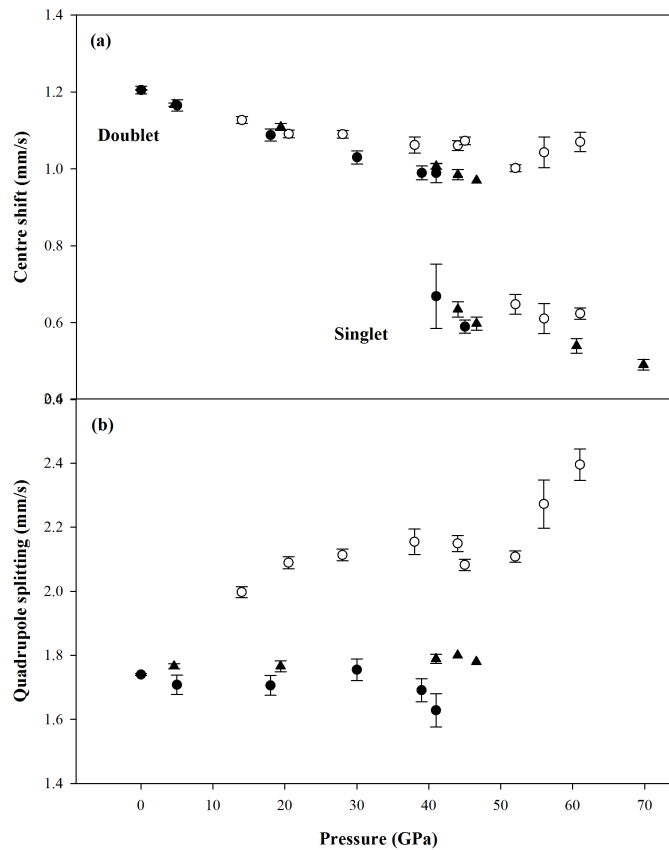
Figure 4.3. Room temperature centre shift (a) and quadrupole splitting (b) (relative to α-Fe) of $FeCO_3$ as a function of pressure. Solid circles: in house single crystals experiments; open circles: in house powder experiment; solid triangles: SMS single crystal experiment.

The general trend of the CS of is to decrease with increasing pressure, where the CS of the singlet is approximately 0.3 mm/s lower than the CS for the doublet (Fig. 4.3a). The behavior of the CS is similar for single crystals and powder; however for the QS the behavior differs, which will be discussed in more detail below. Here we just mention that the QS of the doublet for single crystals remains essentially constant with increasing pressure with a slight decrease just before the singlet appears at 45 GPa.

Mössbauer spectra of $FeCO_3$ single crystals collected in house and using the SMS are slightly different. Each SMS spectrum shows significantly higher resonant absorption and unequal areas of doublet components compared to spectra collected using a radioactive source (Fig. 4.4).
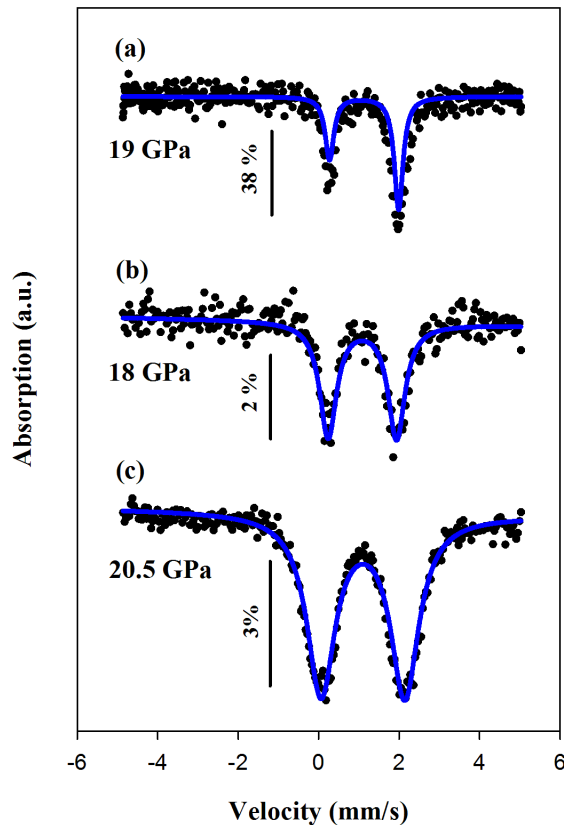
Figure 4.4. Comparison of room temperature $FeCO_3$ Mössbauer spectra: (a) SMS collected on one single crystal at 19 GPa; (b) in house collected on multiple single crystals at 18 GPa; and (c) in house collected on powder at 20.5 GPa. The area asymmetry of the doublet in (a) is due to polarization of the synchrotron Mössbauer source. Percentage bars indicate the relative absorption.

Both of these features are due to properties of the synchrotron X-ray source, namely the low amount of non-resonant radiation and the polarization of the source, which leads to selective excitations of nuclear levels. However all hyperfine parameters of single crystal spectra are the same within experimental uncertainty (Figs. 4.2, 4.3, 4.5), hence SMS and in house spectra can be used interchangeably for interpreting hyperfine parameter variations. In contrast there are significant differences between in house spectra of single crystal and powder $FeCO_3$, including the linewidths (Fig. 4.5), which will be discussed below in the context of the effect of stress in DACs.
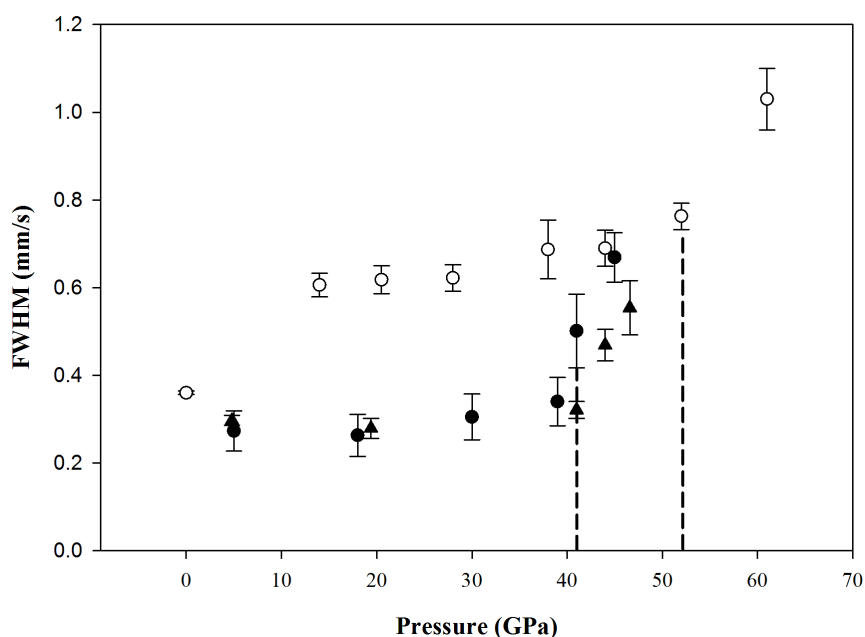
Figure 4.5. Effect of pressure on the full-width at half-maximum (FWHM) of $FeCO_3$ spectra. Open circles: in house powder; solid circles: in house single crystals; solid triangles: SMS single crystal. Dashed lines indicate the pressure at which spin crossover starts for single crystal (41 GPa) and powder (52 GPa) measurements.

4.4.2 Raman Spectroscopy

Raman spectroscopy provides direct insight into the vibrational behavior of ions or groups of ions bonded together, such as $(CO_3)^{2-}$, and their variation as a response to changes of external parameters such as pressure and temperature. In $FeCO_3$, $(CO_3)^{2-}$ groups form planes perpendicular to the c axis with Fe occupying the interstitial space between them to form octahedral sites coordinated by oxygen atoms. This structural arrangement is typical for carbonates and is known as the calcite or

magnesite-type structure. For symmetry reasons (e.g., Rutt and Nicola 1974) the cations give rise to modes that are Raman inactive. Hence, typical Raman spectra of calcite-type carbonates show mainly external and internal vibrations due to the motion of $(CO_3)^{2-}$ ions.

At ambient conditions carbonate spectra show six Raman bands in the region from 200 to 1800 cm^{-1}. However, above 1300 cm^{-1} only two bands are detected and correspond to weak asymmetric stretching vibrations of $(CO_3)^{2-}$. We neglect these bands to avoid the signal from the diamonds and focus on frequencies below 1300 cm^{-1}. In this region the FeCO₃ Raman spectrum has four vibrational modes (176, 274, 728 and 1077 cm^{-1}) (Fig. 4.6).
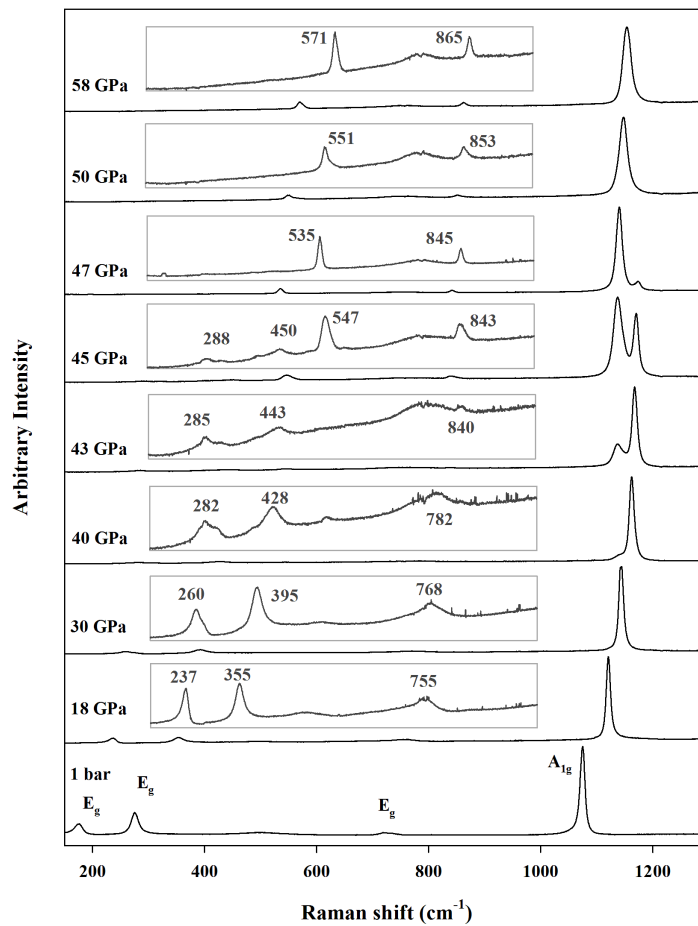
Figure 4.6. Raman spectra of FeCO₃ collected at ambient temperature and the indicated pressures. The two modes below 500 cm^{-1} are external or lattice vibrations of CO_3^{2-} relative to Fe atoms, while modes above 700 cm^{-1} are internal vibrations of CO_3^{2-}. The insets indicate the lower frequency Raman bands for the spectra on a different scale.

Based on previous studies (Popkov et al., 1973, Rutt and Nicola, 1974) we assign the two lower frequency lines to external E_g modes that are translations between cation and anion groups and the two higher frequency lines to internal modes, E_g and A_{1g}, that are caused by symmetric bending and stretching of $(CO_3)^{2-}$, respectively. A broad low intensity peak was also observed in the region around 500 cm^{-1}, which is attributed to electronic Raman scattering from the Fe^{2+} ion (Rutt and Nicola, 1974). However, the peak is only visible at ambient conditions and is too weak to be observed at higher pressures.

All bands shift to higher frequencies with increasing pressure up to 40 GPa, but at slightly higher pressure there is a clear change in the behavior of Raman modes (Fig. 4.6 and 4.7).
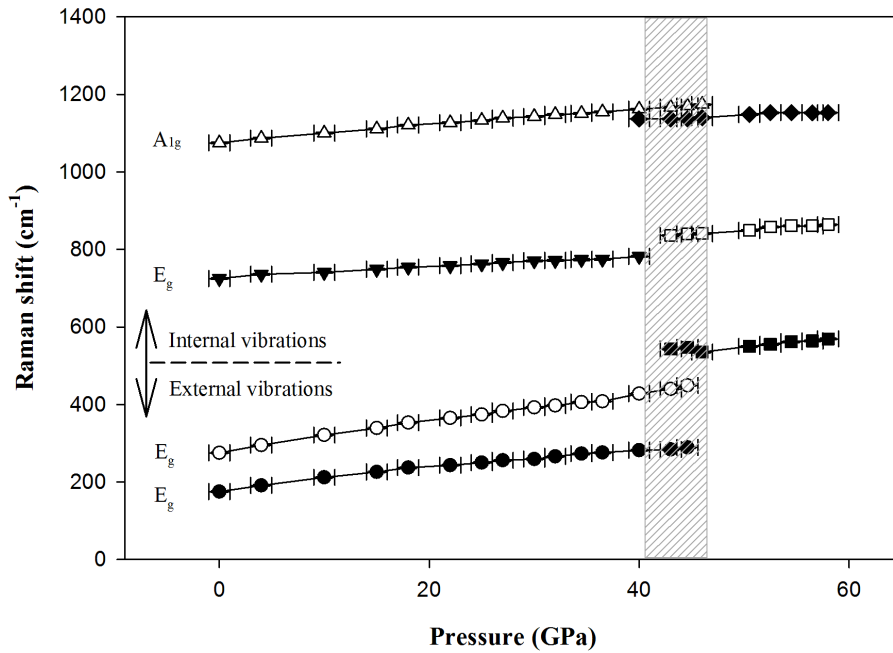
Figure 4.7. Pressure variation of the peak shift of observed Raman modes of FeCO₃. Dashed grey area indicates the spin crossover pressure range. The frequency uncertainty is smaller than the size of the symbols.

The A_{1g} mode splits with the growth of a second peak at slightly lower frequencies. With increasing pressure the new Raman band becomes progressively more intense, growing at the expense of the higher frequency peak until the latter completely disappears between 47 and 50 GPa. The internal E_g line jumps discontinuously to higher wavenumbers (from 782 to 840 cm^{-1}) at roughly 43 GPa, and a broad hump

emerges at 755 cm^{-1}, which might also be attributed to the electronic Raman scattering of the Fe^{2+} ions at high pressures. The external E$_g$ vibrations are also affected by the transition. The E$_g$ vibrational mode at 289 cm^{-1} completely disappears after 45 GPa, while the higher frequency external E$_g$ vibration shifts from 449 cm^{-1} to 543 cm^{-1} between 43 and 45 GPa (Figs. 4.6 and 4.7). Above 47 GPa and up to 58 GPa, the highest pressure reached by Raman spectroscopy, the new HP Raman modes continue to shift to higher frequencies, although with lower slopes than observed at pressures below the transition.

Normalized spectral intensities highlight the progressive decrease of intensity of lower frequency bands between 0 and 40 GPa (Fig. 4.8). At higher pressures (> 45 GPa) the high frequency external and internal E$_g$ modes, which are weak and difficult to distinguish in spectra near the transition pressure, gradually become more intense.
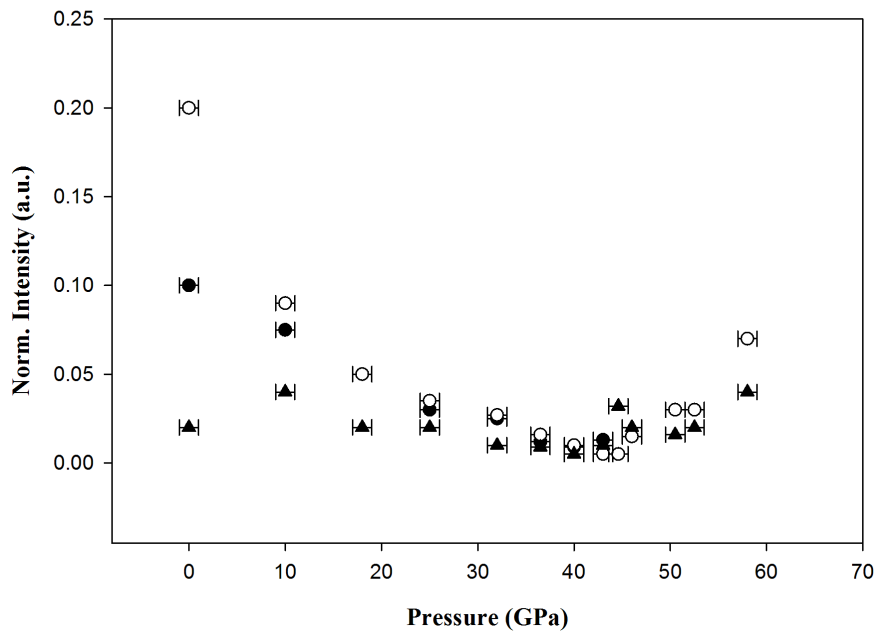
Figure 4.8. Pressure variation of Raman mode intensity normalized to the most intense mode, A$_{1g}$, in FeCO$_3$. Solid circles: lower frequency external E$_g$ vibration; open circles: higher frequency external E$_g$ vibration; solid triangles: internal E$_g$ vibration (see also Figs. 4.7 and 4.8). Note that the lowest frequency external E$_g$ mode disappears completely above 45 GPa.

4.4.3 XANES spectroscopy

X-ray Absorption Fine Structure (XAFS) spectroscopy is an element-specific method to study the local atomic structure within a material. XAFS spectra can be divided into different regions based on the energy range from the absorption edge in the spectrum. Our study focuses on the XANES region, which is generally taken to extend 50 eV beyond the edge itself.

Figure 4.9 shows normalized XANES spectra of $FeCO_3$ collected during compression.
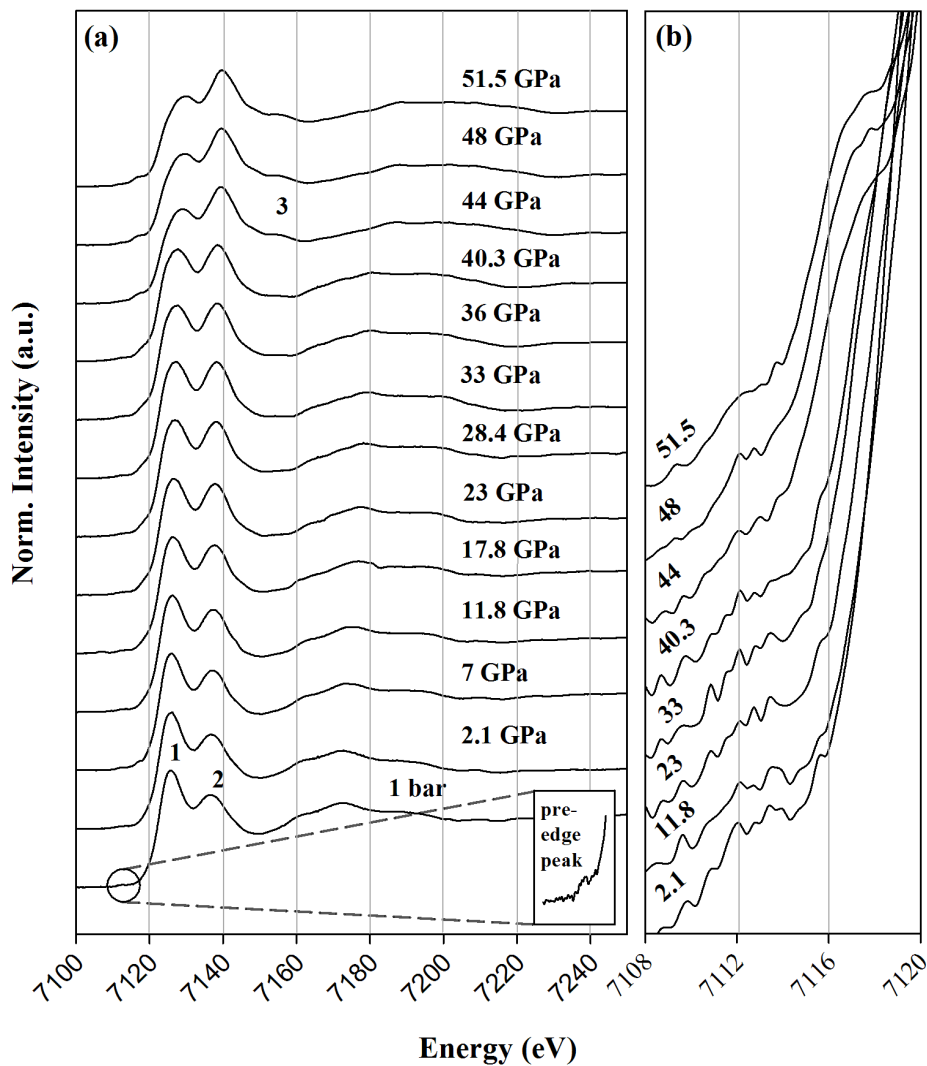
Figure 4.9. (a) Normalized XAS spectra of $FeCO_3$ at room temperature collected on compression at the indicated pressures. The inset at the bottom right highlights the pre-edge region of the 1 bar spectrum. (b) Close up on the evolution of the pre-edge region with pressure. The spectra are shifted vertically for clarity.

The 1 bar spectrum is consistent with the data of Wilke et al. (2001), although the pre-edge peak is less pronounced in our study due to differences in energy resolution. Each spectrum is characterized by two peaks (identified in Fig. 4.9 as "1" and "2") below 7150 eV. Their relative intensities change at increasing pressure and their positions shift to higher energies (Fig. 4.10). Peak shifts of the main-edge energy on compression was already observed in previous studies on ferropericlase (Kantor et al., 2006a; Narygina et al., 2009) and bridgmanite (Narygina et al., 2009) and is related to changes in the electronic structure due to shortening of Fe-O distances. This shortening is directly reflected in the shift of the first EXAFS maximum between 7160 and 7180 eV to higher energy, which may be described by the relation ΔE x R^2 = const. (e.g.,Bianconi et al., 1983, Wilke et al., 2007), where ΔE is the energy difference between the onset of the edge and the first EXAFS maximum and R is the Fe-O distance.
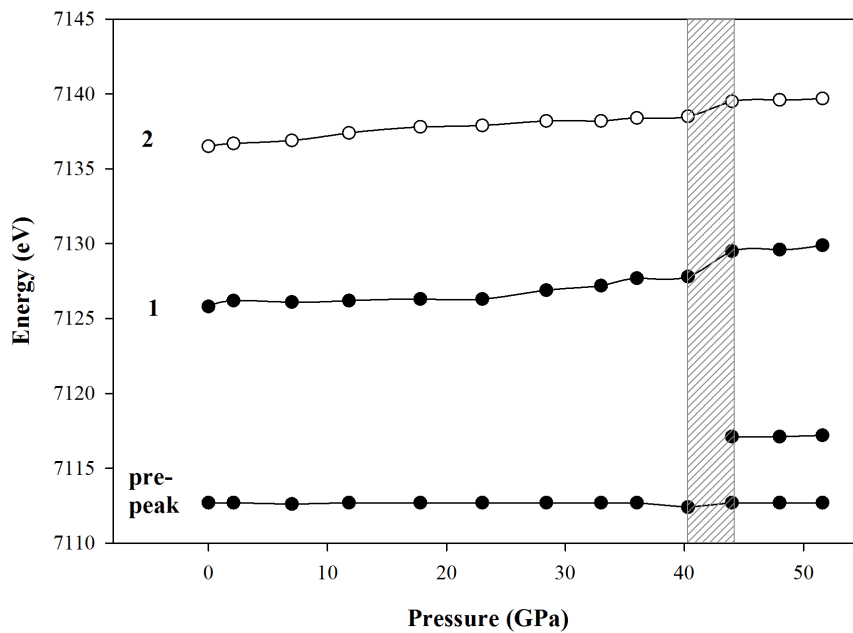
Figure 4.10. Pressure variation of maximum peak positions for FeCO₃ XANES spectra. The peaks are labeled according to Fig. 4.9 and the grey dashed area indicates where the transition is observed in the XANES spectra.

All peaks change strongly between 40 and 44 GPa, where the pre-edge region shows the largest variation (Fig. 4.9a and 4.10). The pre-edge peak at ~ 7112 eV, which is not well resolved in this dataset, becomes more intense and sharper above 44

GPa (Fig. 4.9b). At ~ 7117 eV, ~ 5 eV higher than the pre-edge, a shoulder present at lower pressure evolves into a better-resolved feature, so that it appears like an additional pre-edge. The grey dashed area in Fig. 4.10 marks the energy where the appearance of this feature is observed, matching the discontinuity in the trends of the main and pre-edge peaks. Similarly, the main-edge region (7120-7140 eV) shows considerable changes between 40 and 44 GPa. The intensities of the main peaks are reversed for spectra above 40 GPa, where the second peak becomes more intense than the first (Figs. 4.9 and 4.12). Additionally, all spectra above 44 GPa show the presence of a new pronounced feature, identified as "3" in Fig. 4.9.

The derivative $\delta\mu/\delta E$ provides a more sensitive probe of changes in the spectra (Fig. 4.11).
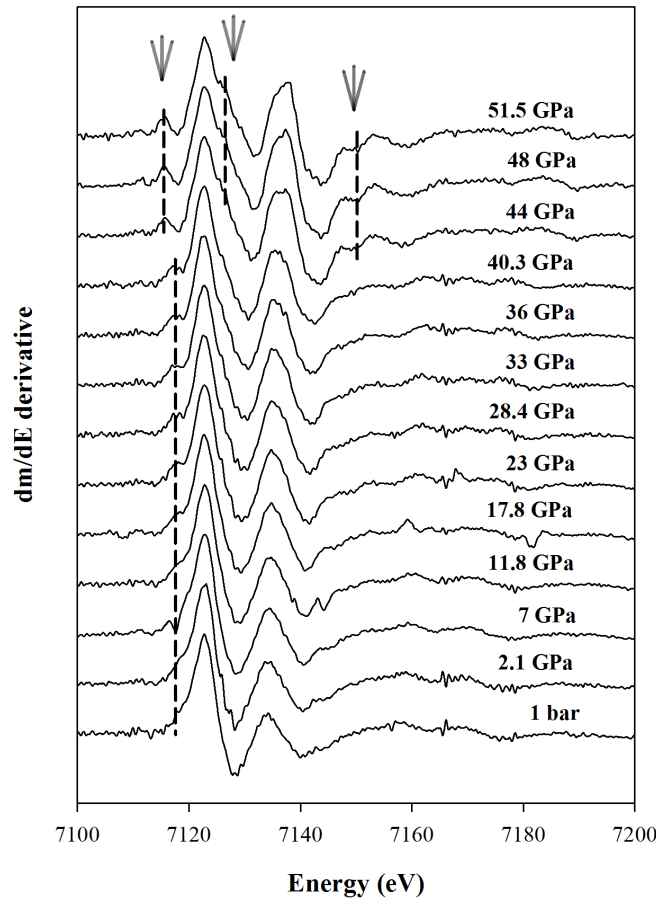
Figure 4.11. $\delta\mu/\delta E$ derivatives of room temperature XANES spectra of FeCO₃ at the indicated pressures. The vertical unit is arbitrary, and the derivatives are taken from the normalized spectra (Fig. 4.10). Grey arrows and dashed lines indicate the energies at which changes are observed at 44 GPa.

The grey arrows together with the dashed lines highlight three features that are related to the changes observed in the spectra: 1) the derivative maximum at ~ 7115 eV that disappears below 44 GPa and is substituted by another maximum at ~ 7117 eV; 2) a shoulder at ~ 7128 eV that appears above 44 GPa and sharpens on further increase of pressure to 51.5 GPa; 3) the derivative minimum at ~ 7150 eV that appears above 44 GPa. These changes in the pre-edge, XANES and low-energy EXAFS regions imply modification of the local structure around Fe atoms and/or chemical bonding between 40 and 44 GPa.

The intensity ratio of the two peaks at the main edge, I_1/I_2, provides another qualitative probe of changes in the local structure. The intensity ratio decreases monotonously until 40 GPa, where it then sharply decreases by 18.5 % in one step to 44 GPa (Fig. 4.12). Above 44 GPa the intensity ratio does not vary significantly with pressure up to 51.5 GPa, the highest pressure reached.
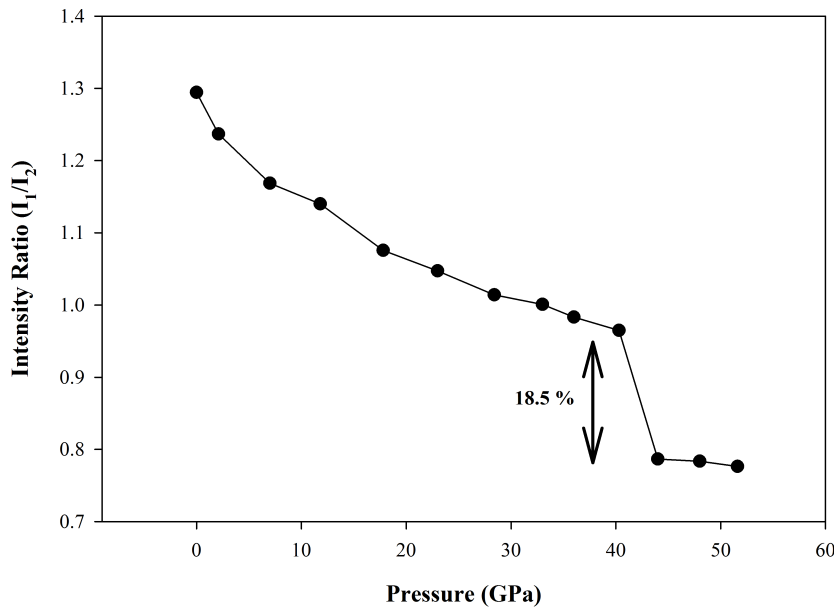
Figure 4.12. Pressure variation of the intensity ratio (I1/I2) of the main peaks (see Fig. 4.9) of FeCO₃ XANES spectra. The percentage change at the transition pressure is indicated.

4.5 Discussion

4.5.1 Spin transition

Changes observed in the Mössbauer, Raman and XANES spectra of $FeCO_3$ that take place between ~ 40 and 45 GPa (or 47 GPa according to Raman data) result from electronic spin crossover of *3d* electrons of Fe^{2+} atoms. Mössbauer spectra of single crystal $FeCO_3$ show decreasing values of CS with increasing pressure up to 40 GPa that can be explained by increasing *s* electron density at the Fe nucleus due to the progressive reduction of interatomic distances. The new component that appears at 40 GPa has zero QS and a CS that is much smaller than the HS component, similar to LS Fe^{2+} in ferropericlase and bridgmanite (e.g., Kantor, 2007, McCammon et al., 2010). LS Fe^{2+} in octahedral coordination has no unpaired electrons with nearly spherical charge distribution; hence the EFG is essentially zero because all *3d* energy levels are nearly equally occupied. Spin pairing changes abruptly the degree to which *s*-electron density at the Fe nuclei is shielded by *3d* electrons; hence the CS drops considerably. The decrease in CS at the transition is roughly 0.3 mm/s, which is higher than the value observed for ferropericlase (~ 0.17 mm/s, Kantor 2007), but lower than for iron-organic complexes (~0.5 mm/s, Gütlich et al., 1978) at ambient or low (< 5 GPa) pressure.

Raman spectroscopy also provides evidence of the spin transition in $FeCO_3$, but through the interatomic vibrations in the sample that are probed by inelastic scattering of light. Unit cell compression between 1 bar and 40 GPa causes a shift of the Raman bands to higher frequencies, to a first approximation following eq. (4.1):

$$v = \frac{1}{2\pi} \sqrt{\frac{F_r}{\mu}} \tag{4.1},$$

where v is the frequency, F_r is the restoring force and μ is the weighted mass of the molecule or group of atoms.

Between 40 and 47 GPa the A_{1g} mode shifts abruptly to lower frequency, comparable to observations by Farfan et al. (2012) and Lin et al. (2012) for natural siderite enriched in manganese and magnesium, respectively. The A_{1g} mode is attributed to the internal stretching vibration of the carbonate groups. It is therefore strongly dependent on the distance between C and O, and its frequency will decrease with increasing distance. The shift to lower frequency is thus a clear sign of an

increase of the C-O distance. This interpretation is consistent with observations by Lavina et al. (2010a), who observed an increase in the C-O bond length in natural siderite at 43 GPa and attributed it to structural re-organization caused by spin pairing of Fe^{2+} atoms, where shared oxygen atoms that are shared by CO_3-groups and Fe^{2+} are displaced due to the volume collapse of the octahedral site. In contrast, we observed a frequency increase of the external and internal E_g bands at the spin transition. The external modes, which in $FeCO_3$ are translational modes between the anion $(CO_3)^{2-}$ and cation (octahedral Fe^{2+} coordinated by oxygen) sites, are clearly influenced by the volume collapse of Fe-O octahedra at the transition. The distances between carbonate groups and cations become shorter; hence the frequency increases. The internal E_g mode, which is caused by in-plane symmetric bending of the carbonate molecule, shifts to higher frequency due to the systematic decrease in the O-O bond length after the transition (Lavina et al., 2010a), which induces higher vibrational frequencies due to the decrease of the atomic distance between neighboring oxygen atoms.

Both Mössbauer and Raman data highlight an important point regarding spin pairing in $FeCO_3$: under quasi-hydrostatic conditions the process occurs over a pressure interval of at least 5 GPa (Figs. 4.2, 4.6, 4.7 and 4.9). The integrated area of the two components in the Mössbauer spectra and the two A_{1g} bands in Raman spectra allow the percentage of iron atoms in the HS and LS states to be estimated. From Mössbauer spectra at 41 GPa, 12% of Fe^{2+} atoms are in the LS state. This observation suggests that the proportion of Fe atoms changing to the LS state does affect the local symmetry and hence the position of the surrounding atoms, inducing short-range (on the Ångstrom scale) local "structural relaxation" that broadens the transition pressure range. Indeed, since there is a mixture of Fe atoms in HS and LS in the transition region that progressively change to LS, a local structural relaxation that results in stretched bonds between Fe and O will enable some Fe atoms to persist in the HS state over a broader pressure range, being less compressed by the surrounding oxygen atoms.

While a detailed quantitative analysis of XANES spectra incorporating *ab initio* simulation is beyond the scope of this study, our XANES data can be used to investigate the degree to which spin crossover in $FeCO_3$ can be detected qualitatively, and how well changes in the local structure can be derived from empirical analysis of the spectra.

The most striking change in the pre-edge region is the abrupt appearance of an additional peak at 7117 eV at 44 GPa. This feature shifted from higher energy, where it was present only as a shoulder in the onset of the main edge. This feature is related to excitations of $1s$ to $4p$ electron states of the valence band (e.g., Caliebe et al., 1997), which shift to lower energy with decreasing Fe-O distance. In the actual pre-edge region at $\sim$ 7112 eV which is related to $1s \rightarrow 3d$ transitions, a change from a doublet feature for HS to a singlet in LS is expected as shown by Westre et al. (1997) by experiment and multiplet analysis on octahedral high and low spin complexes. The quality of the data shown here is insufficient for a detailed analysis of the pre-edge due to limited energy resolution and a high level of noise. Nevertheless, a detectable "sharpening" of the pre-edge peak between 40 and 48 GPa can be observed as seen in Fig. 4.9b. Westre et al. (1997) explains the change in the pre-edge region as a change in the accessible electronic states that contribute to the pre-edge after the change in spin state of $3d$ electrons. In the HS state the octahedral crystal field splits the $3d$ electron levels into e_g and t_{2g} states, giving rise to three possible transitions from the $1s$ level. Two of the levels are close in energy; hence an apparent doublet is observed for octahedral site symmetry (see also Westre et al., 1997, Wilke et al., 2001). In the LS state only the e_g level is unoccupied, so only one transition is possible.

In the energy region of the main edge (7120-7140 eV) the peaks in the spectrum of FeCO₃ correspond to a combination of $1s \rightarrow 4p$ electronic transitions and/or multiple scattering of the photoelectron by neighboring atoms (Fig. 4.9a, peaks 1 and 2) (Caliebe et al., 1997, Mottana, 2004). The positions of these peaks shift to higher energy from 1 bar to 40 GPa (Fig. 4.10) due to unit cell compression and the resulting decrease in Fe-O bond length, that is also responsible for the increase in the intensity of peak 2 with increasing pressure. The decrease in intensity is likely related to a decrease in the density of p-like states in that energy region as a consequence of changes in bond length. Between 40 and 44 GPa where spin crossover occurs, the spectra show an abrupt change in the relative amplitudes of peaks 1 and 2, the appearance of peak 3 and the sudden shift to higher energies of the first EXAFS oscillation (roughly from 7170 to 7180 eV, see Figs. 4.9 and 4.11). Again, these changes are directly related to the collapse of the Fe coordination polyhedron, i.e., the change in Fe-O distance (Wilke et al., 2007, Bianconi et al., 1983). In addition, the appearance of peak 3 above 44 GPa could arise from multiple scattering of the

photoelectron from the neighboring O atoms, which move closer to the Fe atoms after the transition.

While a comprehensive quantitative analysis of the spectra in terms of structural changes would require *ab initio* calculations that are beyond the scope of this paper, we may use the relation $\Delta E \times R^2 = const.$ to estimate the change in the Fe-O distance with pressure from the XANES spectra. To perform this analysis, we use the spectral feature that is located at 7172.5 eV at 0 GPa and define the onset of the edge at the position of the pre-edge (7112 eV) (see also Wilke et al., 2007). This analysis yields $\Delta E_0 = 60.5$ eV at 0 GPa, $\Delta E_{40} = 68.9$ eV at 40 GPa and $\Delta E_{48} = 75$ eV at 48 GPa. Assuming that the constant in the relation given above is independent of pressure, we can write for 0 and 40 GPa:

$$\Delta E_0 \times R_0^2 = \Delta E_{40} \times R_{40}^2, \tag{4.2}$$

which can be rearranged to

$$(\Delta E_0 / \Delta E_{40})^{0.5} = R_{40} / R_0. \tag{4.3}$$

From the two values obtained at 0 GPa and 40 GPa, a shortening of the Fe-O distance by a factor of 0.94 is estimated, while across the spin transition from 40 and 48 GPa, we obtain a value of 0.95. This is comparable to the value of 0.92 obtained by Lavina et al. (2010) based on single crystal diffraction data (their Fig. 4.7). The consistency of results is striking, particularly considering the large simplifications made in our analysis, and highlights the sensitivity of XANES to the local environment.

Our results clearly demonstrate the capability of XANES spectra to detect spin crossover in FeCO$_3$. Indeed, the sensitivity has improved markedly since previous studies of other geophysically relevant phases such as ferropericlase (Kantor et al., 2006a) and bridgmanite (Narygina et al., 2009) due to the newly upgraded experimental setup for high-pressure XAFS studies on beamline ID24 at ESRF, together with the implementation of more hydrostatic conditions in the DAC, for example through the use of neon as a quasi-hydrostatic pressure medium. The higher sensitivity could also be related in part to the specific structural arrangement in carbonates (planes of $(CO_3)^{2-}$ alternated by octahedrally coordinated cations).

Simulations to quantitatively evaluate the effect of spin crossover on the XAFS spectra are ongoing and will be reported elsewhere.

4.5.1.1 Dynamic spin state distribution

Previous X-ray diffraction (XRD) experiments on siderite and ferromagnesite (e.g., Lavina et al., 2009, 2010a, Merlini et al., 2012, Lin et al., 2012) interpreted spin crossover to be a relatively sharp discontinuity taking place at roughly 43 GPa and causing a discontinuous volume reduction of the unit cell. Indeed, XRD is a technique sensitive to long-range structures and cannot probe short-range order such as, for example, HS and LS state distributions. Raman, Mössbauer and XANES spectroscopy probe the local structure of neighboring atoms and groups of atoms and are therefore sensitive to short-range order features that are not always evident from XRD. Our results, i.e., a successive change of all spectra from HS to LS across a relatively wide pressure range, support the idea of a dynamic nature of spin crossover, which involves a non-static distribution of HS and LS states until the transition is complete. Indeed, a static distribution of the two spin states, which could be considered as a long-range order feature, should be easily resolved by XRD, but so far it has not been reported. Hence, we propose that if a static distribution of the two spin states can be excluded because it was not observed by XRD, the only way to explain the broad and transient pressure range over which spin crossover takes place is a dynamic distribution of HS and LS states in the transition region. On the basis of our result, we suggest that previous XRD studies could be re-examined to investigate if certain features (i.e., the peak splitting and diffuse scattering in Lavina et al., 2010a or the small deviation in the low pressure equation of state before the volume collapse in Merlini et al., 2013), could reflect a more complex transition.

A direct consequence of the broad spin crossover pressure range is highlighted by the weakening of all Raman E_g bands as spin crossover is approached, followed by an intensity increase once the final LS state is achieved (Fig. 4.8). All modes become progressively weaker during compression due to the gradual pressure increase that affects the interaction between the probing laser and the sample, hence reducing signal quality. However, the laser-sample coupling does not explain the almost complete disappearance and reappearance of the lower frequency modes at the transition. Lavina et al. (2009) described a change in the color of the crystals, where they become progressively darker during and after spin pairing. We observed a

similar behavior, where crystals changed from a light reddish color to a slightly darker one. Since we used a green laser with 514 nm wavelength one might attribute the decrease in intensity of the Raman bands to a change in phonon scattering in the visible light region. However, we consider this not to be the case since this does not account for the regain in intensity of the other Raman bands after the transition, and also the internal symmetric stretching vibration A_{1g} is not affected. Hence, we attribute these intensity minima (Fig. 4.6) to static disorder caused by spin pairing through the decreased percentage of atoms scattering in the HS state, and consequently the increased amount of scattering by LS atoms. Once the transition is complete, all atoms/molecules in the LS state scatter again equally based on their different vibrational symmetries and new and more intense modes reappear in the spectra. One mode is completely lost after the transition (the external vibration that occurs at 176 cm^{-1} at 1 bar); however it is the lowest frequency E_g translatory oscillation and might be simply too weak to be detected.

4.5.1.2 Grüneisen parameters

We calculated the mode Grüneisen parameters (γ_i) for each vibrational mode with increase of pressure using the following equation:

$$\gamma_i = \frac{K}{\omega}\frac{d\omega}{dP}$$

(4.4),

where the bulk modulus (K) is 117±1 GPa (Zhang and Reeder, 1999) and 148±12 GPa (Lavina et al., 2010) for the HS and LS states, respectively. We also calculated the pressure shift ($d\omega/dP$) in order to verify that the differences in the Grüneisen parameters before and after the spin transition were not caused simply by the use of a different bulk modulus (Table 1).

The Grüneisen parameters of HS FeCO₃ discriminate the two different vibration typologies, internal and external, characterized by smaller and larger values, respectively. In both cases our results match the observations of Santillán and Williams (2004) that were based on infrared measurements. Indeed, the Grüneisen parameters reflect the effect that changing the volume of a crystal lattice has on its vibrational properties, in this case due to the increase of pressure. The higher values of the external translatory oscillations are consistent with values reported by Ross and Reeder (1992), who described by means of single-crystal XRD the higher

compressibility of Fe-O octahedra with respect to the relative incompressibility of the CO_3 group. Hence, the vibrations associated with the relative translation of the cation with respect to the anionic group are expected to have higher Grüneisen parameters, where the cation site is more affected by the pressure increase due to its higher compressibility.

The Grüneisen parameters measured at spin crossover are also characteristic of the vibrational typology: the internal modes show no variation (A_{1g}) or a moderate increase (E_g) in their values; whereas the remaining external mode (E_g) drops drastically from 1.16 to 0.72, similar to observations by Lin et al. (2012) for ferromagnesite. Indeed at spin pairing the Fe-O octahedra shrink, pulling the oxygen atoms towards the iron atoms and consequently stretching the C-O bonds in the carbonate groups. The external vibration (translatory oscillation) is affected by the shape and the size of the cation site, which is less distorted (Lavina et al., 2010a) and has a smaller volume after the transition due to the more compact environment (lower Grüneisen parameter). On the other hand, the stretching of the C-O bond does not influence the carbonate groups; hence the Grüneisen values for the internal vibrations remain constant for symmetric stretching (A_{1g}) or show a slight increase for symmetric bending (E_g), where the difference is probably related to the different vibrational geometry.

Compared to the study of Lin et al. (2012), we obtain lower values of calculated Grüneisen parameters for both HS and LS states. This may be attributed to the difference in composition and its effect on the bulk modulus, since the latter is the only adjustable parameter used to calculate γ_i (Eq. 4). Indeed, the frequency variation with pressure ($d\omega/dP$) of each mode displays similar values in both studies.

Our calculations relate to the mean mode Grüneisen parameter for all observed vibrations in HS and LS states. Since we recognize that not all phonon modes are taken into account, for example all Raman bands above 1300 cm^{-1} are excluded, it is not appropriate to compare it with the thermodynamic Grüneisen parameter (e.g., Santillán and Williams, 2004, Lin et al., 2012, Liu et al., 2014). Instead our aim is to provide an indication of the difference in compressibility of the $FeCO_3$ structure before and after the transition based only on a limited number of vibrations. From our calculations, the average Grüneisen parameters of HS and LS states are, respectively, 0.69 and 0.42. As stated by Lin et al. (2012), the LS state is expected to have a thermodynamic Grüneisen parameter lower than ~1.1, which is the value for the HS

state. Our available data suggests the decrease of the Grüneisen parameter to be ~ 30%, but this should be tested by further experiments.

Table 1

Grüneisen parameter (Υ_i) for Raman vibrational modes

Modes	Assignment	$d\omega/dP$ (cm^{-1}GPa^{-1})		Mean mode Υ_i	
		HS	LS	HS	LS
A_{1g} (internal)	Symmetric (in plane) stretching	2.17	1.6	0.22	0.21
E_g (internal)	Symmetric (in plane) bending	1.37	1.86	0.21	0.32
E_g (external)	Translatory oscillations of the CO₃ groups	3.82	2.68	1.16	0.72
E_g (external)		2.51		1.18	

Mean mode Grüneisen parameter for observed vibrational mode in HS state: 0.69
Mean mode Grüneisen parameter for observed vibrational mode in LS state: 0.42
Bulk moduli from Zhang and Reeder (1998) and Lavina et al. (2010) for HS and LS configuration respectively.
Band assignments from Rutt and Nicola (1974).

4.5.2 Effect of stress on Mössbauer spectra collected in a DAC

Differences between powder and single crystal Mössbauer spectra of FeCO₃ provide information on the effects of deviatoric and local stresses caused by non-hydrostatic conditions. Any DAC, due to its intrinsic geometry, causes cylindrically symmetric non-hydrostatic stress fields during compression that affect all materials with non-zero yield strength (e.g., Meng et al., 1993; Dubrovinsky and Dubrovinskaia, 2004; Kenichi T., 2000; Zhao et al., 2010). For any type of pressure-transmitting medium there is a pressure limit at which hydrostatic behavior of the medium is lost and consequently deviatoric stresses develop within the sample. These stresses are macroscopic when they are caused by the action of the transmitting medium on the sample and microscopic when they develop at the grain boundaries of polycrystalline samples, i.e., powders (Weidner et al., 1994). Observables from Mössbauer experiments provide qualitative insight into the effects of deviatoric stress on the nuclear behavior and spin crossover of Fe atoms in siderite powder in DACs gas-loaded with neon.

The observed differences between powder and single crystal Mössbauer spectra arise from the action of microscopic local stresses present at grain boundaries. Indeed, the powder sample was compressed with the intention of producing a pellet with reduced interstitial porosity (20 μm size in diameter), so that Ne was acting more as a lubricant between powder grains than as an effective pressure-transmitting medium. This effect is apparent from the influence of pressure on the FWHM of Mössbauer absorption peaks for powder and single crystals experiments (Fig. 4.5). With the exception of the

1 bar powder spectrum, all peaks at higher pressures are at least twice as broad for powder compared to single crystals, where the difference increases at higher pressure. The broadening originates from pressure gradients in the gasket hole, which in turn create pressure gradients within the sample. Due to the relatively large cross section of the gamma-ray beam in our laboratory (~ 500 μm) compared to the size of the gasket hole, at each pressure point the resultant Mössbauer spectrum that is measured represents the combination of several spectra collected at slightly higher and lower pressures compared to the pressure measured by ruby fluorescence due to the pressure gradient. In this way spectra characterized by higher and lower CS are merged together and the components in the final spectrum appear broadened. There is little difference in the measured CS of powder and crystals (Fig. 4.3a), but the differences measured for QS are significant (Fig. 4.3b). Indeed, the QS values for powder spectra are systematically (except at 1 bar) at least 15% higher than for the single crystal measurements. The physical explanation is straightforward: powder experiments involve grain-grain interactions that develop under compression and cause the formation of deviatoric stress acting on the local structure around the Fe atoms, causing the Fe-O octahedra to be more distorted than in "regular" quasi-hydrostatic experiments. The distortion induces variations in the shape and size of the charge distribution around the Fe nuclei and ultimately on the electric field gradient, hence on the quadrupole splitting.

The macroscopic and microscopic stresses that develop inside the gasket hole also influence spin crossover. Important differences between powder and single crystal Mössbauer spectra are: 1) spin crossover starts at lower pressure for single crystals (~ 40 GPa) compared to powder (~ 50 GPa); and 2) the pressure range over which spin crossover occurs is smaller for single crystals (~ 5 GPa) than for powder (> 10 GPa). Moreover, the sudden increase (~ 15 %) of QS in powder spectra at the start of spin crossover is caused by enhanced distortion of Fe octahedra in the crystal structure. Indeed at the spin pairing transition, the dynamic distribution of HS and LS states, with respectively larger and smaller octahedra, unbalances the surrounding atomic distribution, stretching or shortening atomic bonds that favor the formation of local stresses.

4.6 Implications

On the basis of this study, we found that spectroscopic techniques provide insight into the short-range atomic order during FeCO$_3$ compression from 1 bar to 58 GPa. In addition to XRD, which measures long-range atomic order in crystals, we observed that the spin transition in synthetic FeCO$_3$ is a transient process that takes place over a finite range of pressure under quasi-hydrostatic conditions. Moreover, our results demonstrate that spin crossover is a dynamic process during which the Fe atoms in HS and LS states coexist until the LS configuration is fully reached. A static distribution of the two spin states can be excluded based on previous XRD studies that reported only a sudden collapse of unit cell volume, but no other ordering features.

The calculated Grüneisen parameters for all observed Raman modes agree with the structural arrangement for FeCO$_3$ in HS and LS states reported previously in single crystal XRD studies. While the CO$_3$ groups are relatively incompressible over the entire pressure range investigated, Fe-O octahedra show a drastic change in their stiffness after spin crossover, becoming more compact and hence harder to compress.

Deviatoric stress, both macroscopic and microscopic, causes remarkable changes in the high-pressure behavior of FeCO$_3$. Local distortions of the Fe site cause spin crossover to start at higher pressure and a broadening of the spin transition pressure range.

Our results contribute to understanding the fate of iron-bearing carbonates during subduction. Our experiments clearly show that deformation, which in the Earth is caused by differential stress in the matrix due to processes such as convection, increases the depth at which spin crossover starts and broadens its pressure range beyond 5 GPa. This conclusion is valid both for our room temperature experiments as well as for mantle conditions. Combined with the results of Liu et al. (2014) who demonstrated that temperature extends the spin crossover region to higher pressure, spin crossover in magnesiosiderite would start at much greater depths (> 150 km) than postulated so far in previous work (e.g., Lavina et al., 2009), and would be prolonged over a depth range of at least 300-350 km instead of being a sharp discontinuity in the shallower part of the lower mantle. However, further experiments are required in order to quantify more precisely the effect of temperature on natural systems under the influence of deviatoric stress.

4.7 Acknowledgments

References

Bianconi, A., Dell'Ariccia, M., Gargano, A., and Natoli, C.R. (1983) Bond length determination using XANES. In A. Bianconi, L. Incoccia, and S. Stilpcich, Eds., EXAFS and Near Edge Structure, 27, p. 57-61. Springer Series in Chemistry and Physics, Berlin.

Biellmann, C., Gillet, P., Guyot, F., Peyronneau, J., and Reynard, B. (1993) Experimental evidence for carbonate stability in the Earth's lower mantle. Earth and Planetary Science Letters, 118, 31-41.

Boulard, E., Menguy, N., Auzende, A.L., Benzerara, K., Bureau, H., Antonangeli, D., Corgne, A., Morard, G., Siebert, J., Perrillat, J.P., Guyot, F., and Fiquet, G. (2012) Experimental investigation of the stability of Fe-rich carbonates in the lower mantle. Journal of Geophysical Research, 117, B02208.

Brenker, F.E., Vollmer, C., Vincze, L., Vekemans, B., Szymansky, A., Janssens, K., Szaloki, I., Nasdala, L., Joswig, W., and Kaminsky, F. (2007) Carbonates from the lower part of the transition zone or even the lower mantle. Earth and Planetary Science Letters, 260, 1-9.

Caliebe, W.A., Kao, C.C., Hastings, J.B., Taguchi, M., Kotani, A., Uozumi, T., and de Groot, F.M.F. (1998) 1s2p resonant inelastic x-ray scattering in γ-Fe₂O₃. Physical Review B, 58, 13452-13458.

Dasgupta, R. and Hirschmann, M.M. (2010) The deep carbon cycle and melting in Earth's interior. Earth and Planetary Science Letters, 298, 1-13.

Dubrovinsky, L., and Dubrovinskaia, N. (2004) Angle-dispersive diffraction under non-hydrostatic stress in diamond anvil cells. Journal of Alloys and Compounds, 375, 86-92.

Farfan, G., Wang, S., Ma, H., Caracas, R., and Mao, W.L. Bonding and structural changes in siderite at high pressure (2012). American Mineralogist, 97, 1421-1427.

Franzolin, E., Schmidt, M.W., and Poli, S. (2011) Ternary Ca-Fe-Mg carbonates: subsolidus phase relations at 3.5 GPa and a thermodynamic solid solution model including order/disorder. Contributions to Mineralogy and Petrology, 161, 213-227.

French, B.M. (1971) Stability relations of siderite ($FeCO_3$) in the system Fe-C-O. American Journal of Science, 27, pp. 37 -78.

Fukao, Y., Obayashi, M., and Nakakuki, T. (2009) Stagnant Slab: A Review. Annual Review of Earth and Planetary Science, 37, 19.

Goldsmith, J.R., Graf, D.L., Witters, J., and Northrop, D.A. (1962) Dolomite-Magnesian calcite relations at elevated temperature and CO_2 pressures. *Geochimica* et *Cosmochimica Acta*, 7(3-4), 109-128.

Gütlich, P. (1978) Mössbauer spectroscopy and transition metal chemistry. Berlin, Heidelberg: Springer-Verlag.

Harte, B. (2011) Diamond Window into the Lower Mantle. Science, 334, 51-52.

Isshiki, M., Irifune, T., Hirose, K., Ono, S., Ohishi, Y., Watanuki, T., Nishibori, E., Takata, M., and Sakata, M. (2004) Stability of magnesite and its high-pressure form in the lowermost mantle. Nature, 427, 60-63.

Kantor, I., Dubrovinsky, L., McCammon, C., Kantor, A., Pascarelli, S., Aquilanti, G., Crichton, W., M., R., Almeida, J., and Urusov, V. (2006a) Pressure-induced phase transition in $Mg_{0.80}Fe_{0.20}O$ ferropericlase. Physics and Chemistry of Minerals, 33, 35-44.

Kantor, I. Yu., Dubrovinsky, L. S., and McCammon, C. (2006b) Spin crossover in (Mg,Fe)O: A Mössbauer effect study with an alternative interpretation of x-ray emission spectroscopy data. Physical Review B, 73, 100101(R).

Kantor, I. (2007) High-pressure and high-temperature structural and electronic properties of (Mg,Fe)O and FeO. 150 p. Ph.D Thesis, University of Bayreuth, Bayreuth.

Kantor, I. Yu., Prakapenka, V., Kantor, A., Dera, P., Kurnosov, A., Sinogeikin, S., Dubrovinskaia, N., and Dubrovinsky, L. (2012) BX90: A new diamond anvil cell design for X-ray diffraction and optical measurements. Review of Scientific Instruments, 83, 125102.

Keppler, H., Wiedenbeck, M., and Shcheka, S.S. (2003) Carbon solubility in olivine and the mode of carbon storage in the Earth's mantle. Nature, 242, 414-416.

Kurnosov, A., Kantor, I., Boffa-Ballaran, T., Lindhardt, S., Dubrovisnky, L., Kuznetsov, A., and Zehnder, B.H. (2008) A novel gas-loading system for mechanically closing of various types of diamond anvil cells. Review of Scientific Instruments, 79, 045110.

Lavina B., Dera P., Downs R.T., Prakapenka V., Rivers M., Sutton S., and Nicol M. (2009) Siderite at lower mantle conditions and the effects of the pressure-induced spin-pairing transition. Geophysical Research Letters, 36, L23306.

Lavina, B., Dera, P., Downs, R. T., Yang, W., Sinogeikin, S., Meng, Y., Shenand, G., and Schiferl, D. (2010a) Structure of siderite FeCO3 to 56 GPa and hysteresis of its spin-pairing transition. Physical Review B, 82, 064110.

Lavina, B., Dera, P., Downs, R. T., Tschauner, O., Yang, W., Shebanova, O., and Shen, G. (2010b) Effect of dilution on the spin pairing transition in rhombohedral carbonates. High Pressure Research, 30, 224-229.

Lin, J.F., Liu, J., Jacobs, C., and Prakapenka, V.B. (2012) Vibrational and elastic properties of ferromagnesite across the electronic spin-pairing transition of iron. American Mineralogist, 97, 583-591.

Liu, J., Lin, J.F., Mao, Z., and Prakapenka, V.B. (2014) Thermal equation of state and spin transition of magnesiosiderite at high pressure and temperature. American Mineralogist, 99, 84-93.

Liu, J., Lin, J.-F., and Prakapenka, V.B. (2015) High-pressure orthorhombic ferromagnesite as a potential deep-mantle carbon carrier. Scientific Reports, 5, 7640, doi: 10.1038/srep07640.

Mao, H.K., Xu, J., and Bell, P.M. (1986) Calibration of the ruby pressure gauge to 800 kbar under quasi-hydrostatic conditions. Journal of Geophysical Research, 91, 4673.

Mao, Z., Armentrout, M., Rainey, E., Manning, C.E., and Dera, P. (2011) Dolomite III: A new candidate lower mantle carbonate. Geophysical Research Letters, 38, L22303.

Mattila, A., Pylkkänen, T., Rueff, J.P., Huotari, S., Vankó, G., Hanfland, M., Lehtinen, M., and Hämäläinen K. (2007) Pressure induced magnetic transition in siderite FeCO₃ studied by x-ray emission spectroscopy. Journal of Physics: Condensed Matter, 19, 38, 386206.

McCammon, C., Dubrovinsky, L., Narygina, O., Kantor, I., Wu, X., Glazyrin, K., Sergueev, I., and Chumakov, A.I. (2010) Low-spin Fe^{2+} in silicate perovskite and a possible layer at the base of the lower mantle. Physics of the Earth and Planetary Interiors, 180, 215-221.

Meng, Y., Weidner, D.J., and Fei, Y. (1993) Deviatoric stress in a quasi-hydrostatic diamond anvil cell: Effect on the volume-based pressure calibration. Geophysical Research Letters, 20, 1147-1150.

Merlini, M., Crichton, W.A., Hanfland, M., Gemmi, M., Mueller, H., Kupenko, I., and Dubrovinsky, L. (2012) Structures of dolomite at ultrahigh pressure and their influence on the deep carbon cycle. Proceedings of the National Academy of Sciences, 109, 13509-13514.

Merlini, M., and Hanfland, M. (2013) Single-crystal diffraction at megabar conditions by synchrotron radiation. High Pressure Research: an International Journal, 33, 511-522.

Merrill, L., and Basset, W.A. (1975) The crystal structure of $CaCO_3$-(II), a high-pressure metastable phase of calcium carbonate. Acta Cryst., B31, 343-349.

Mottana, A. (2004) X-ray absorption spectroscopy in mineralogy: Theory and experiment in the XANES region. EMU Notes in Mineralogy, 6, 465-552.

Narygina, O., Mattesini, M., Kantor, I., Pascarelli, S., Wu, X., Aquilanti, G., McCammon, C., and Dubrovinsky, L. (2009) High-pressure experimental and computational XANES studies of $(Mg,Fe)(Si,Al)O_3$ perovskite and $(Mg,Fe)O$ ferropericlase as in the Earth's lower mantle. Physical Review B, 79, 174115.

Ono, S., Kikegawa, T., Ohishi, Y., and Tsuchya, J. (2005) Post-aragonite phase transformation in CaCO3 at 40 GPa. American Mineralogist, 90, 667-671.

Pascarelli, S., Mathon, O., Muñoz, M., Mairs, T., and Susini J. (2006) Energy-dispersive absorption spectroscopy for hard-X-ray micro-XAS applications. Journal of Synchrotron Radiation, 13, 351-358.

Popkov, Yu. A., Eremenko, V.V., Fomin, V.I., and Mokhir, A.P. (1973) Raman scattering of light in antiferromagnetic siderite. Soviet Physics - Solid State, 14, 1985-1989.

Potapkin, V., Chumakov, A.I., Smirnov, G.V., Celse, J.P., Rüffer, R., McCammon, C., and Dubrovinsky, L. (2012) The [57]Fe Synchrotron Mössbauer Source at the ESRF. Journal of Synchrotron Radiation, 19, 559-569.

Prescher, C., McCammon, C., and Dubrovisnky, L. (2012a) MossA: a program for analyzing energy-domain Mössbauer spectra from conventional and synchrotron sources. Journal of Applied Crystallography, 45, 329-331.

Prescher, C., Dubrovinsky, L., McCammon, C., Glazyrin, K., Nakajima, Y., Kantor, A., Merlini, M., and Hanfland, M. (2012b) Structurally hidden magnetic transitions in Fe3C at high pressures. Physical Review B, 85, 140402.

Ravel, B., and Newville, M. (2005) ATHENA, ARTEMIS, HEPHAESTUS: data analysis for X-ray absorption spectroscopy using IFEFFIT. Journal of synchrotron radiation, 12, 537–41.

Rosenberg, P. E. (1967) Subsolidus relations in system $CaCO_3$-$MgCO_3$-$FeCO_3$ between 350° and 500° C. American Mineralogist, 52, 787-796.

Ross, N.L., and Reeder, R.J. (1992) High –pressure structural study of dolomite and ankerite. American Mineralogist, 77, 412-421.

Rüffer, R., and Chumakov, A.I. (1996) Nuclear Resonance Beamline at ESRF. Hyperfine Interactions, 97/98, 589-604.

Rutt, H.N., and Nicola, J.H. (1974) Raman spectra of carbonates of calcite structure. Journal of Physics C: Solid State Physics, 7, 4522.

Santillán, J., and Williams, Q. (2004) A high-pressure infrared and X-ray study of $FeCO_3$ and $MnCO_3$: comparison with $CaMg(CO_3)_2$-dolomite. Physics of the Earth and Planetary Interiors, 143-144, 291-304.

Shi, H., Luo, W. Johansson, B., and Ahuja, R. (2008) First-principles calculations of the electronic structure and pressure-induced magnetic transition in siderite $FeCO_3$. Physical Review B, 78, 155119.

Stagno, V., Tange, Y., Miyajima, N., McCammon, C.A., Irifune, T., and Frost, D.J. (2011) The stability of magnesite in the transition zone and lower mantle as function of oxygen fugacity. Geophysical Research Letters, 38, L19309.

Sturhahn, W., Jackson, J. M., and Lin, J.F. (2005) The spin state of iron in minerals of Earth's lower mantle. Geophysical Research Letters, 32, 1-5.

Takemura, K. (2001) Evaluation of the hydrostaticity of a helium-pressure medium with powder x-ray diffraction techniques. Journal of Applied Physics, 89, 662, DOI: 10.1063/1.1328410.

Walter, M.J., Kohn, S.C., Araujo, D., Bulanova, G.P., Smith, C.B., Gaillou, E., Wang, J., Steele, A., and Shirey, S.B. (2011) Deep Mantle Cycling of Oceanic Crust: Evidence from Diamonds and Their Mineral Inclusions. Science, 334, 54-57.

Weidner, D.J., Wang, Y., and Vaughan, M.T. (1994) Yield strength at high pressure and temperature. Geophysical Research Letters, 21, 753-756.

Westre, T. E., Kennepohl, P., DeWitt, J. G., Hedman, B., Hodgson, K. O., and Solomon, O. E. (1997) A Multiplet Analysis of Fe K-Edge 1s → 3d Pre-Edge Features of Iron Complexes. Journal of the American Chemical Society, 119, 6297-6314.

Wilke, M., Farges, F., Petit, P. E., Brown, Jr. G. E., and Martin, F. (2001) Oxidation state and coordination of Fe in minerals: an Fe K XANES spectroscopic study. American Mineralogist, 86, 714-730.

Wilke, M., Farges, F., Partzsch, G.M., Schmidt, C., and Behrens, H. (2007) Speciation of iron in silicate glasses and melts by in-situ XANES spectroscopy. American Mineralogist, 92, 44-56.

Wood, B. J. (1993) Carbon in the Core. Earth and Planetary Science Letters, 117, 593-607.

Zhao, J., Angel, R.J., and Ross N.L. (2010) Effects of deviatoric stresses in diamonds-anvil cell on single-crystal samples. Journal of Applied Crystallography, 43, 743-751.

Zhang, J., and Reeder, R.J. (1999). Comparative compressibilities of calcite-structure carbonates: deviations from empirical relations. American Mineralogist, 84, 861–870.

5. Stability of iron-bearing carbonates in the deep Earth's interior

Cerantola Valerio[1,2,*], Bykova Elena[2], Kupenko Ilya[1,¥], Merlini Marco[3], Ismailova Leyla[2], McCammon Catherine[2], Bykov Maxim[2], Chumakov Alexandr I.[1], Petitgirard Sylvain[2], Kantor Innokenty[1,†], Svitlyk Volodymyr[1], Jacobs Jeroen[1], Hanfland Michael[1], Mezouar Mohamed[1], Prescher Clemens[4], Rüffer Rudolf[1], and Dubrovinsky Leonid[2*]

[1]European Synchrotron Radiation Facility, BP 40220, Grenoble F-38043, France; [2]Bayerisches Geoinstitut, Universität Bayreuth, D-95440 Bayreuth, Germany; [3]Dipartimento di Scienze della Terra, Università degli Studi di Milano, Via Botticelli 23, I-20133 Milano, Italy; [4]Institute of Geology and Mineralogy, Universität zu Köln, Greinstraße 4-6, D- 50939 Köln, Germany. [¥]Present address: *Institut für Mineralogie, Universität Münster, Corrensstraße 24, D-48149 Münster, Germany.* [†]Present address: *MAX IV Laboratory, Fotongatan 2, 225 94 Lund, Sweden.*

*valerio.cerantola@gmail.com
*Leonid.Dubrovinsky@Uni-Bayreuth.DE

5.1 Abstract

The presence of carbonates in inclusions in diamonds coming from depths exceeding 670 km are obvious evidence that carbonates indeed exist in the Earth's lower mantle. However, their range of stability, crystal structures, and the thermodynamic conditions of the decarbonation process in iron-bearing carbonates remains poorly constrained. We investigated the behaviour of pure iron carbonate at pressures over 100 GPa and temperatures over 2500 K using single crystal X-ray diffraction and Mössbauer spectroscopy in laser-heated diamond anvil cells. Upon heating to temperatures of the Earth's geotherm at pressures to about 50 GPa siderite, $FeCO_3$, partially dissociates to form various iron oxides. We synthesised two new compounds at higher pressures and solved their structures – *tetrairon (III) orthocarbonate*, $Fe_4^{3+}C_3O_{12}$, and *diiron (II) diiron (III) tetracarbonate*, $Fe_2^{2+}Fe_2^{3+}C_4O_{13}$. Both phases contain CO_4 tetrahedra, and the former has a unique

structure, thus high pressure carbonates may not resemble other compounds (including silicates). $Fe_4C_4O_{13}$ was found to be stable at conditions along the entire geotherm to depths of at least 2500 km, thus demonstrating that self-oxidation-reduction reactions can preserve carbonates in the Earth's lower mantle.

5.2 Introduction

Plate tectonics drives subduction of carbonate-bearing oceanic plates, that are responsible for recycling carbon from the surface down to the deepest regions of our planet. Indeed, geophysical, geochemical, and petrological evidence (Christensen, 1996; Fukao et al. 2001; Walter et al. 2011; Thomson et al. 2015) suggest that sufficiently cold and/or fast subducting slabs can penetrate the transition zone and the Earth's lower mantle, possibly even reaching the core mantle boundary (CMB). Subducting plates are the major source of carbon influx inside the Earth, due to the abundant presence of carbonate minerals in oceanic sediments (Kelemen and Manning, 2015). Observation of carbonates inclusions in super-deep diamonds of lower mantle origin is evidence for their existence at depths greater than 700 km (Kaminsky, 2012). Untangling the behaviour of carbonates at extreme conditions, i.e., determining their stability regions and properties, is a key to understanding the deep carbon cycle.

There are two major mechanisms that could affect carbonate phase stability and carbon oxidation state in the Earth's interior – chemical reaction(s) with surrounding minerals or transformations (including self-oxidation-reduction) of carbonates themselves at specific pressures and temperatures. Previous studies on the Ca, Mg, Fe-bearing carbonates have established that they all undergo several high-pressure high temperature (HPHT) phase transitions without decomposing in the pressure range up to 140 GPa and restricted temperatures (Merlini et al. 2012; Ono et al. 2007; Isshiki et al. 2004; Boulard et al. 2012; Liu et al. 2015). Investigations of the stability of $MgCO_3$ in the transition zone and upper part of the lower mantle as a function of oxygen fugacity demonstrated that carbon is expected to occur as diamond and carbides in the bulk mantle (when homogenously distributed) rather than carbonates (Stagno et al. 2013). However, in subducting slabs carbonates are expected to be stable due to the more oxidizing conditions compared to the surrounding mantle (Rohrbach and Schmidt, 2011), which may preserve them to the bottom of the lower mantle. The presence of iron is crucial to the fate of high-temperature carbonates (Liu

et al. 2015; Boulard et al. 2011). Iron can radically change the thermodynamic stability of carbonate phases, thereby preserving them from breaking down. This behavior may be a direct consequence of pressure-induced spin crossover (Lavina et al. 2009; Lobanov et al. 2015; Cerantola et al. 2015b; Lin et al. 2012), which has been observed to occur at ~ 43 GPa at room temperature over 50 GPa at ~1200 K (Liu et al. 2014) for the endmember $FeCO_3$. The presence of Fe-bearing carbonates in the lower mantle is supported by experimental evidence (Liu et al. 2015). Iron plays a fundamental role in the redox state of the mantle (McCammon, 2005) due to its ability to exist in multiple valence states, and its abundance in the mantle is sufficient to govern the redox state of other elements, carbon in particular.

Interest in the high-pressure behaviour of carbonates has been enhanced by recent reports of novel compounds containing tetrahedral CO_4^{4-} groups instead of the triangular planar CO_3^{2-} groups that occur at ambient pressure (Merlini et al. 2012; Boulard et al. 2012; Merlini et al. 2015; Boulard et al. 2015). Theoretical predictions indicate potential analogues between CO_4-bearing carbonates and silicates (Lasaga and Gibbs, 1987), but so far experimental information about structures of high pressure carbonates are too limited (and indeed controversial) to speculate about their crystal chemistry.

In this study, we performed an experimental investigation of the high-pressure high-temperature behaviour of synthetic iron carbonate ($FeCO_3$). Experimental conditions of our work cover the entire mantle and reveal two novel compounds containing tetrahedral CO_4 groups, as well as the complex role of ferrous and ferric iron in stabilizing carbonates at extreme conditions. Our single-crystal X-ray diffraction data unambiguously establish the existence of at least one carbonate with a unique structural type (not known for silicates or other tetrahedral anion-bearing compounds), and demonstrate that the conditions in the Earth's lower mantle do not lead to full decomposition of Fe-based carbonates due to self-oxidation-reduction reaction(s).

5.3 Procedure and results

Synthesis of $FeCO_3$ single crystals and their characterization at ambient conditions was described by Cerantola *et al.* 2015b. HPHT experiments were performed in laser-heated diamond anvil cells (see *Methods* for details). We

employed single crystal X-ray diffraction as the primary method for sample characterization, and powder X-ray diffraction when analysis of single crystal data was not possible. We used energy-domain Mössbauer spectroscopy (Synchrotron Mössbauer Source, SMS) (see *Methods* for details) as a complementary method of phase analysis and to determine the iron oxidation state.

5.3.1 Synthesis and structures of CO$_4$-bearing Fe-carbonates

5.3.1.1 Tetrairon(III) Orthocarbonate, Fe$_4^{3+}$C$_3$O$_{12}$

We observed new phases after laser heating of FeCO$_3$ single crystals at 1750(100) K at 74(1) GPa and at 1400(100) K at 107(2) GPa (Fig. 5.1). A full single crystal dataset was collected on a temperature-quenched sample (Table S1, Table S2 in Supplementary Materials). The pattern of one of the phases (containing more than 300 independent reflections, Table S1) was indexed as hexagonal (space group *R3c*, # 161). The structure was solved and refined, leading to the chemical composition *Fe$_4$C$_3$O$_{12}$*. Charge balance considerations show that all iron is ferric. Each carbon atom is surrounded by four oxygen atoms (C-O distances ~1.31-1.39 Å at 74 GPa), forming isolated (i.e., not linked to each other) tetrahedra (Fig. 5.2a). Thus, the new compound is referred to as *tetrairon(III) orthocarbonate*.

There are two structurally distinct iron positions in the phase: one Fe atom is situated on a 3-fold axis, while the other is in a general position (Table S1). Both iron atoms are located in either bicapped or tricapped trigonal prisms formed by oxygen. However, in tricapped prisms three of the oxygen atoms are much further away than the other six (~2.33 Å vs ~1.98 Å at 74(1) GPa); hence this polyhedron can be considered to be a regular trigonal prism (Fig. 5.2a). The individual (and average) Fe-O distances in both of the iron polyhedra in *Fe$_4$C$_3$O$_{12}$* are longer than in low-spin iron (III)-bearing oxides and compounds (~ 1.8 Å) at corresponding pressures, which suggests that the phase contains high-spin iron. Although a precise characterisation of the pure phase using Mössbauer spectroscopy is difficult due to presence of other iron compounds in the laser-heated samples, the available information supports the presence of iron in the high-spin state (see Fig. S5.2, *Supplementary Materials*).

The 3-fold symmetry ring formed by corner- and edge-shared CO$_4$-tetrahedra and three FeO$_8$-bicapped prisms is a notable characteristic of the *tetrairon orthocarbonate*

structure (Fig. 5.2a). The rings form layers that are stacked along the *c*-axis (where each subsequent layer is rotated by 120° with respect to the original one
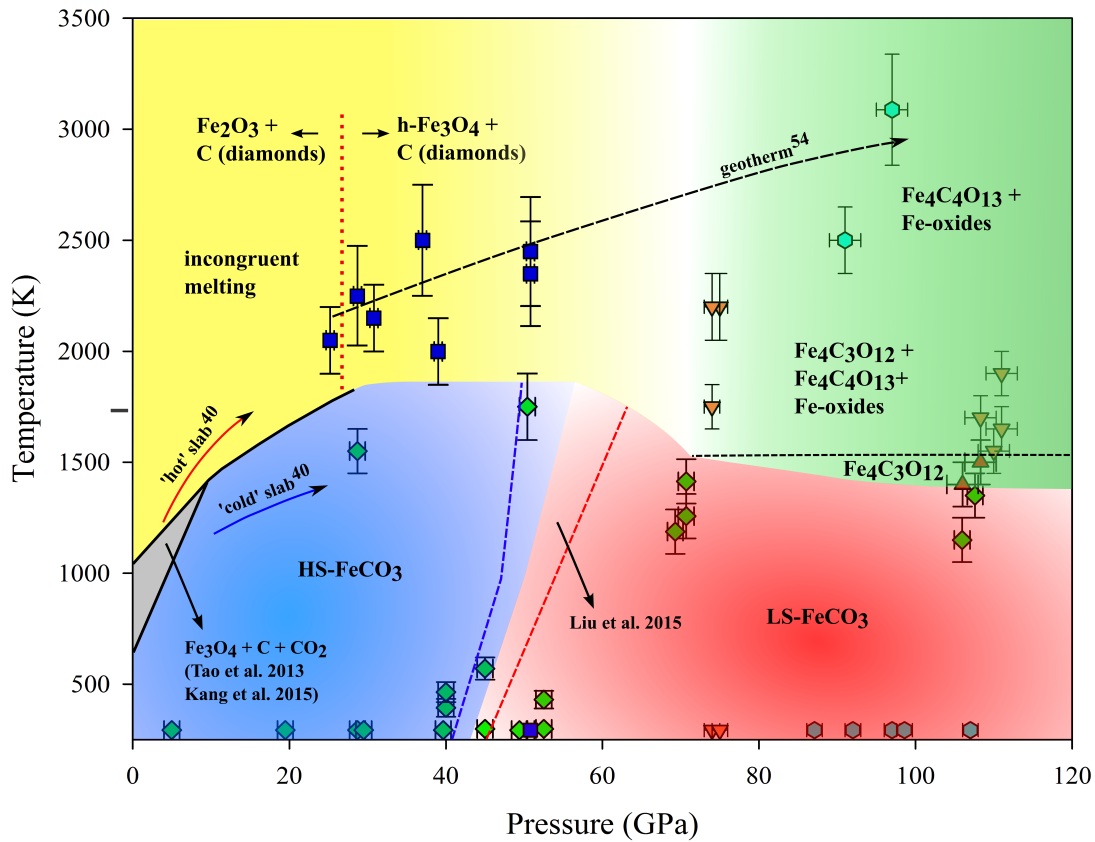
Figure 5.1 | Stability diagram of FeCO$_3$ at high *P-T*. Symbols and phase regions identified in experiments: magnesite-structured FeCO$_3$ (green diamonds), oxide(s) and recrystallized FeCO$_3$ (blue squares), tetrairon (III) orthocarbonate Fe$_4$C$_3$O$_{12}$ (red triangles), diiron (II) diiron (III) tetracarbonate Fe$_4$C$_4$O$_{13}$ + Fe$_4$C$_3$O$_{12}$ + oxide(s) (orange inverse triangles), Fe$_4$C$_4$O$_{13}$ + oxides (cyan hexagons), FeCO$_3$ decomposition to Fe$_3$O$_4$ + C + CO$_2$ (Tao et al. 2013; Kang et al. 2015) (grey area), high spin FeCO$_3$ (liu et al. 2015) (blue area), low spin FeCO$_3$ (Liu et al. 2015) (red area), incongruent melting of FeCO$_3$ (yellow area), and formation of HP-carbonates Fe$_4$C$_3$O$_{12}$ and Fe$_4$C$_4$O$_{13}$ (green area). The black dashed curve is an expected mantle geotherm (Katsura et al. 2010). Blue and red solid lines are, respectively, cold and hot slab surface temperature profiles (Syracuse et al. 2010). The black solid lines are from Tao et al. 2013 and Kang et al. 2015. The blue and red dashed lines indicate the region delimiting the spin transition in magnesiosiderite at HPHT from Liu et al. 2015. The vertical dotted red line separates the regions in which the formation of α-Fe$_2$O$_3$ and h-Fe$_3$O$_4$ was observed upon incongruent melting of FeCO$_3$.

Fig. 5.2a). The trigonal FeO_6-prisms are connected via triangular bases that are located in the channels formed by stacked rings. We are not aware of any other compounds that form the same structure.
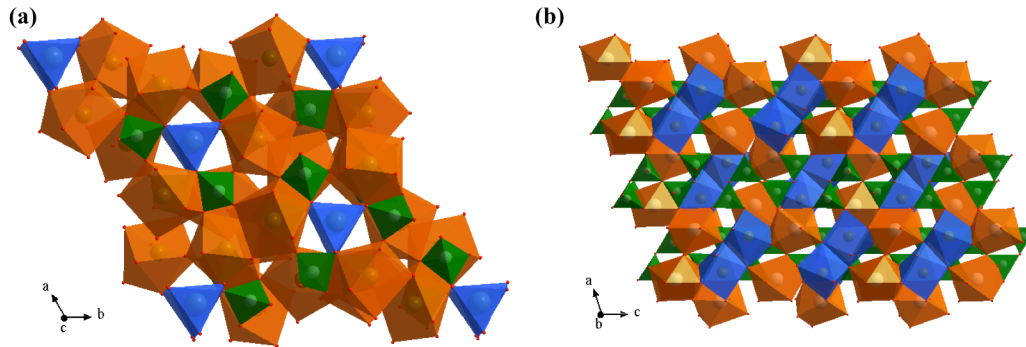
Figure 5.2 | Crystal structures of high-pressure carbonates. (a) Tetrairon (III) orthocarbonate $Fe_4C_3O_{12}$ and (b) diiron (II) diiron (III) tetracarbonate $Fe_4C_4O_{13}$, at ambient temperature and 106(2) and 97(2) GPa, respectively. In (a), three FeO_8 bicapped prisms (brown) and three CO_4-tetrahedra (green) form a ring with 3-fold symmetry by corner and edge sharing. The rings form layers that are stacked along the *c*-axis. FeO_6-prisms (blue) are connected by triangular bases and located in the channels created by the rings. In (b), FeO_8 bi-capped prisms (brown) are connected in a 3-D framework by dimers of edge-shared FeO_7 monocapped prisms (blue) and zigzag-shaped C_4O_{13} chains (green).

5.3.1.2 Diiron(II) Diiron(III) Tetracarbonate, $Fe_2^{2+}Fe_2^{3+}C_4O_{13}$.

Laser heating of $FeCO_3$ at temperatures above 1750(100) K at pressures above ~74 GPa resulted in formation of not only $Fe_4C_3O_{12}$ and iron oxides (see below), but also a monoclinic phase (space group *C2/c*, #15) (Table S1). We collected full single-crystal datasets on temperature-quenched samples at different pressures, where the best results were obtained for the sample at 97(2) GPa (Fig. 5.1, Tables S1 and S2). We solved and refined the structure, leading to the chemical composition $Fe_4C_4O_{13}$, or more specifically $Fe^{2+}_2Fe^{3+}_2C_4O_{13}$. Each carbon atom is tetrahedrally coordinated by oxygen atoms (C-O distances ~1.27-1.39 Å at 97(2) GPa), and four CO_4 groups are linked in truncated chains (Fig. 5.2b). Thus, we refer to the new compound as *diiron(II) diiron(III) tetracarbonate*.

The atomic arrangement of the structure is based on corner-linked infinite chains of FeO_8 bicapped prisms connected in a 3-D framework by dimers of edge-shared FeO_7 monocapped prisms and zigzag-shaped C_4O_{13} chains (Fig. 5.2b). The average Fe-O distances in FeO_7 and FeO_8 polyhedra are similar to one another (~1.97 Å and ~2.03 Å, respectively, at 97(2) GPa) and longer than expected for low-spin ferric or ferrous iron (Bykova et al. 2016). Similarity in the sizes of iron polyhedra may indicate that Fe cations are in a mixed valence state (intermediate between +2 and +3) as proposed for high-pressure iron oxides (Bykova et al. 2016; Ovsyannikov et al. 2016).

$Fe_4C_4O_{13}$ is isostructural with recently reported $Mg_{1.6}Fe_{2.4}C_4O_{13}$ (Merlini et al. 2015) obtained by annealing Mg-bearing natural siderite at 141 GPa and 2650 K. Indeed there is an entire family of tetrasilicates containing four-member Si_4O_{13} groups (Wierzbicka et al. 2010), as well as germanates, vanadates, and arsenates.

5.3.2 FeCO₃ behaviour at high pressures and high temperatures

5.3.2.1 Spin crossover

Fe^{2+} in $FeCO_3$ is known (Lavina et al. 2009; Lobanov et al. 2015; Cerantola et al. 2015b) to undergo spin crossover from high to low spin at about 40 GPa. Although the goal of this work was not to investigate the pressure-temperature dependence of spin crossover, Mössbauer spectroscopy (SMS) was able to show the temperature effect on the spin state at different pressures (examples of spectra are given in Fig. 5.3a). The corresponding data point(s) are shown on Fig. 5.1 and are reasonably consistent with the data reported by Lin *et al.* 2012 and Liu *et al.* 2015 for magnesiosiderite $Mg_{0.35}Fe_{0.65}CO_3$.

5.3.2.2 Incongruent Melting

Recent studies of $FeCO_3$ at pressures up to 20 GPa (Tao et al. 2013; Kang et al. 2015) have shown that while it melts above ~ 6 GPa, below this pressure the phase dissociates to the mixture $Fe_3O_4 + C + CO_2$ before melting. Heating $FeCO_3$ single crystals at 28.7(1) GPa and 1550(100) K does not result in any phase or structural changes or destruction of the single crystal (Fig. 5.4). Heating the same sample at higher temperatures (2250(150) K) causes complete recrystallization of the material (Fig. 5.4), thus indicating melting. Mössbauer spectra of material quenched from the
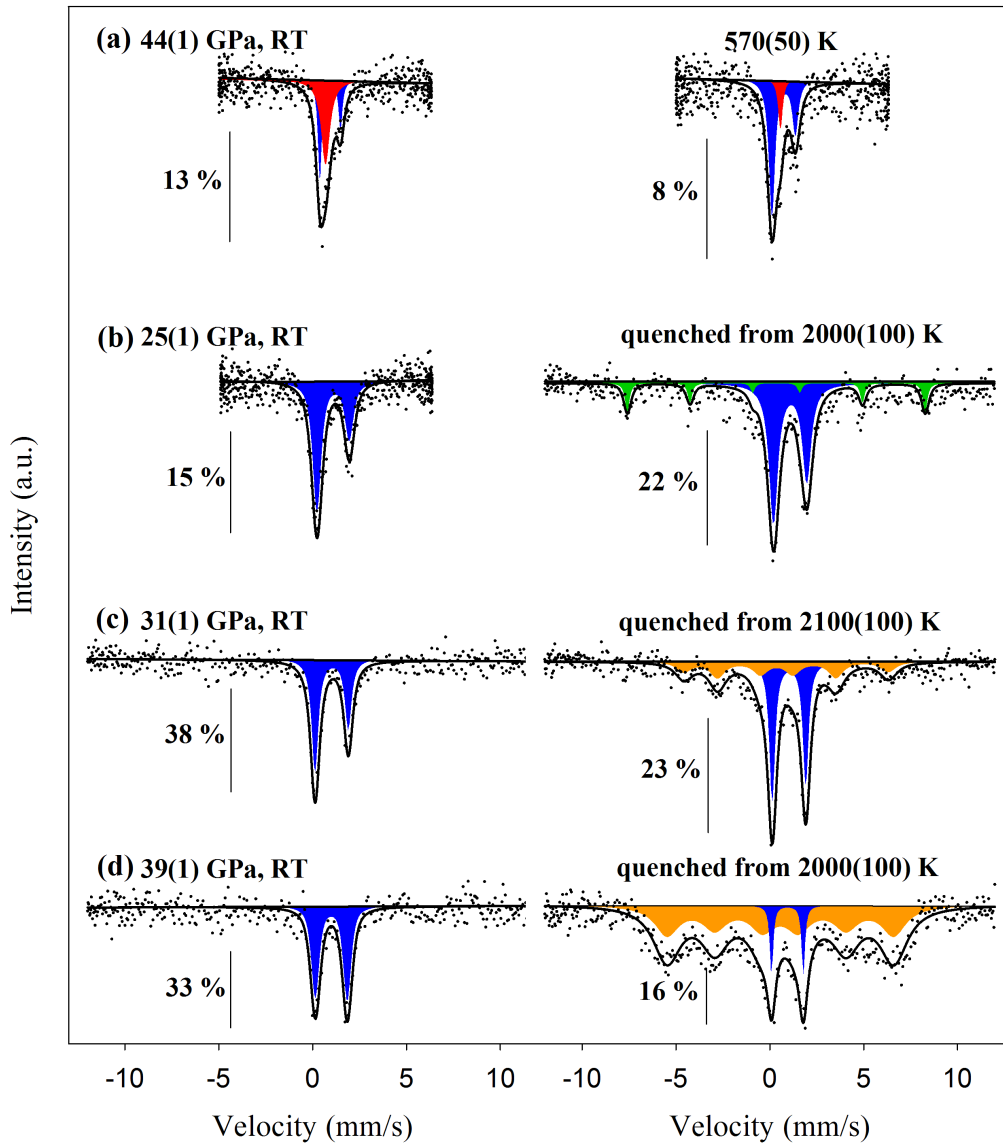
Figure 5.3 | Selected synchrotron Mössbauer spectra from high *P-T* treatment of FeCO₃. (a)-(d) Spectra collected at the indicated pressures at room temperature before heating (left) and either during or after heating at the indicated temperatures (right). Subspectra are shaded as follows: blue doublet – high spin ferrous iron, red singlet – low spin ferrous iron; green sextet – α-Fe₂O₃, orange sextet – h-Fe₃O₄. Note that in (a) the intensity (amount) of high spin ferrous iron increases with increasing temperature. The appearance of h-Fe₃O₄ in (c-d) is the result of progressive decomposition of FeCO₃ upon melting at high pressure. Note that the subspectra do not add up to the total spectrum due to the properties of the full transmission integral fit (see *Methods*). Percentages on the left of each spectrum indicate the relative absorption.

molten state show unambiguously the presence of $FeCO_3$ as well as iron oxides: α-Fe_2O_3 (hematite) at pressures below ~25 GPa and h-Fe_3O_4 (Bykova et al. 2016) above ~28 GPa (Fig. 5.1, Fig. 5.3b and 5.3c, Table S4). We observed a similar behavior for $FeCO_3$ upon heating to ~51 GPa (Fig. 5.1, Table S3). However, while the degree of carbonate decomposition appears to increase at increasing temperature (at a given pressure) and increasing pressure (at a given temperature), we cannot quantify the process based on our existing data.

Nevertheless it is clear that all experiments performed below ~51 GPa produced only partial decomposition of the carbonate. Even heating above ~2500 K for up to one hour always showed diffraction lines of recrystallized $FeCO_3$ and/or its presence in SMS spectra. However, we cannot exclude that heating at sufficiently high temperature (and for a sufficiently long time) could result in complete breakdown of $FeCO_3$.
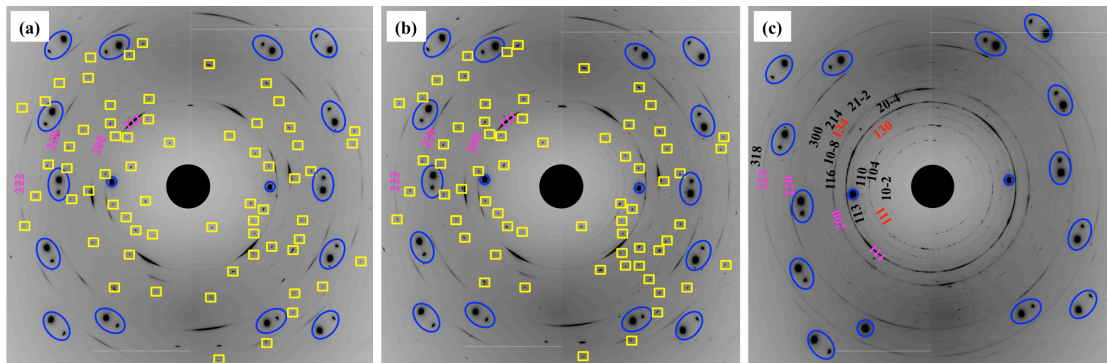
Figure 5.4 | Selected 2-D diffraction images of $FeCO_3$ before and after heating. Single crystal diffraction images were collected at 28(1) GPa at (*a*) ambient temperature before heating, (*b*) after heating at 1550(100) K, and (*c*) 2250(100) K. Melting and re-crystallization of starting material is evidenced by the appearance of $FeCO_3$ powder diffraction rings after heating to the highest temperature. Appearance of diffraction lines of h-Fe_3O_4 indicates incongruent melting of $FeCO_3$. Blue ellipsoids indicate diamond diffraction spots from the diamond anvils and yellow squares mark the single crystal diffraction spots of $FeCO_3$. Numbers designate diffraction lines of $FeCO_3$ (black), neon pressure transmitting medium (magenta) and h-Fe_3O_4 (red).

5.3.2.3 Transformation to new HP-carbonates

Heating $FeCO_3$ at 74(1) GPa and 1750(100) K resulted in the formation of both *tetrairon orthocarbonate $Fe_4C_3O_{12}$* and *diiron(II) diiron(III) tetracarbonate, $Fe_4C_4O_{13}$* (Fig. 5.1). The result is reproducible: the simultaneous appearance of both phases was observed at the same pressure and temperature on heating of different crystals in different loadings. The observations may (*a*) indicate non-equilibrium conditions in laser-heated DACs, (*b*) be a consequence of complex redox chemical reactions that form both phases simultaneously, or (*c*) be a result of successive transformations between carbonate phases that are so closely located in P-T space that they cannot be distinguished. Indeed the results of further experiments at higher pressures (103-110 GPa) suggests that scenario (*c*) is the most plausible. Heating a $FeCO_3$ single crystal to 1400(100) K at 107(2) GPa resulted in the formation of hexagonal *tetrairon orthocarbonate $Fe_4C_3O_{12}$* (Fig. 5.1, Fig. 5.5). Monoclinic *diiron(II) diiron(III) tetracarbonate, $Fe_4C_4O_{13}$* appeared only after prolonged (about one hour) laser heating above 1650(100) K (Fig. 5.1 & Fig. 5.5). The highest temperature at which *$Fe_4C_4O_{13}$* was observed is ~3090(250) K at 97(2) GPa (Fig. 5.5).

Close examination of X-ray diffraction patterns containing *diiron(II) diiron(III) tetracarbonate, $Fe_4C_4O_{13}$* reveal the presence of further reflections which do not belong in any obvious way to the previously identified carbonates. While in some cases it was not possible to identify phase(s) unambiguously due to close overlapping of reflections and/or their low amount, for most data points we were able to determine lattice parameters and even refine structure(s). In all cases, the appearance of *$Fe_4C_4O_{13}$* upon heating at pressures above ~74 GPa was associated with the formation of orthorhombic (space group *Cmcm*) CaIrO_3-structured η-Fe_2O_3 (Bykova et al. 2016) (Fig. 5.1, Table S3). Additionally, in several experiments after heating at different pressures but always at temperatures above ~2300 K, we observed monoclinic (space group *C2/m*) Fe_5O_7 and orthorhombic (space group *Bbmm*) CaTi_2O_4-type structured h-Fe_3O_4 phases (Fig. 5.1, Table S3) (Dubrovinsky et al. 2003; Bykova et al. 2016).

Samples recovered after experiments at pressures above ~30 GPa at temperatures higher than ~1800 K show strong broad features in Raman spectra that are typical for nano-diamond (Solopova et al. 2014) and sometimes a band at 1330 cm^{-1} that is
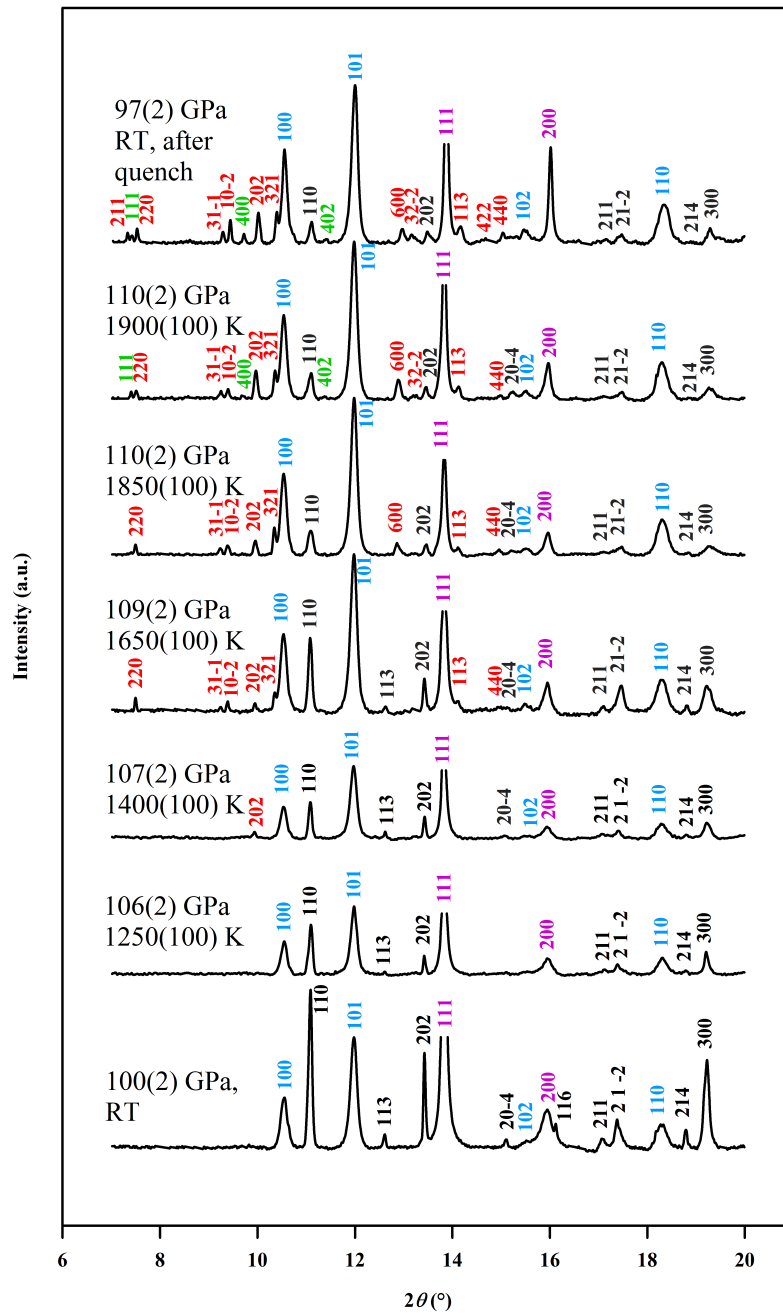
Figure 5.5 | Selected integrated X-ray diffraction patterns collected on heating of FeCO₃ near or above 100 GPa. Patterns are labelled with the pressure and temperature during data collection. Indices of different phases are colored as follows: $FeCO_3$ starting material (black), Ne (magenta), Re (light blue), tetrairon (III) orthocarbonate $Fe_4C_3O_{12}$ (red), and diiron (II) diiron (III) tetracarbonate $Fe_4C_4O_{13}$ (green). Neon was used both as a quasi-hydrostatic pressure medium and a pressure calibrant (see Methods). Data were collected at ID09 at ESRF with an X-ray wavelength of 0.4126 Å.

characteristic for diamond, even though *in situ* X-ray measurements were not able to detect the presence of diamond (or any other carbon phases) after laser heating of $FeCO_3$ crystals. The formation of diamond upon heating of $FeCO_3$ at high pressures and temperatures has been unambiguously documented in previous studies (Boulard et al. 2012; Tao et al. 2013; Kang et al. 2015).

5.4 Discussion

5.4.1 Crystal chemistry of CO_4-bearing Fe-carbonates

The increase of carbon coordination number from three (CO_3^{2-} triangles) to four (CO_4^{4-} tetrahedra) under compression is the obvious consequence of rules known for decades (Müller, 2007). Numerous theoretical studies have predicted the formation of CO_4-bearing carbonates at pressures ranging from over 80 GPa to 150 GPa (Oganov et al. 2006; Skoromudova et al. 2005; Oganov et al. 2008) depending on chemical composition and computational methods. Different configurations, from isolated tetrahedra to pyroxene-like chains, were anticipated for compounds with carbon tetra-coordinated by oxygen. In general, theoretical analysis of possible carbonates with condensed CO_4 groups suggests that there should be analogues with silicates, but expected variations of C-O-C angles are much smaller than for Si-O-Si angles in silicates (Oganov et al. 2008; Buoibes and Zaoui, 2014; Oganov et al. 2013). We are not aware of dedicated theoretical studies of pure iron CO_4-bearing carbonates. However, the predicted (Oganov et al. 2008) structure of Mg-carbonate containing three-membered rings $(C_3O_9)^{6-}$ made of CO_4 tetrahedra was used to index peaks in powder diffraction data of HPHT Fe- and Fe/Mg carbonates (Boulard et al. 2011; Boulard et al. 2012). The same structural model has been used to interpret IR spectra of magnesiosiderite (Boulard et al. 2015) However, important structural details predicted by theory (Oganov et al. 2008) and obtained by powder X-ray diffraction experiments (Boulard et al. 2011; Boulard et al. 2012) are not in agreement (even reported space groups are different). Moreover, it is not obvious how reliable structural information can be extracted based on LeBail fits with large unit cells (Liu et al. 2015) or from powder X-ray diffraction of complex mixtures of different phases: for example, α-Fe_2O_3 (hematite) was one of the phases reported to co-exist

with carbonate at 88 GPa (Boulard et. 2012) while it is well documented by now (Bykova et al. 2016) that above ~50 GPa iron (III) oxide adopts different structures. Heating magnesio-siderite $(Fe_{0.65}Mg_{0.35})CO_3$ at pressures of approximately 50(1) GPa and 1400(100) K resulted (Liu et al. 2015) in formation of a new phase which Liu et al. (2015) called "siderite II" and described as orthorhombic. The same phase was reported (Liu et al. 2015) at pressures up to ~120 GPa and temperatures up to 2200 K. Liu et al. (2015) provided us with the powder X-ray diffraction pattern collected at 90 GPa after heating at 2200 K. We fit this data using the Rietveld method (as implemented in the GSAS package) using the model of hexagonal tetrairon orthocarbonate $Fe_4C_3O_{12}$ (Fig. S5.1, Supplementary Material). The good quality of the fit (Fig. S5.1) unambiguously confirms that "siderite II" has the structure of tetrairon orthocarbonate. The quality of the powder X-ray diffraction data does not allow the occupancy of cation positions to be refined so we do not know how much magnesium is incorporated in the phase. However, the absence of reflections of any other phases (apart from the gold standard and Ne pressure transmitting medium) suggests that at least 35% of magnesium may be incorporated in the structure of orthocarbonate.

Single crystal X-ray diffraction data on iron-bearing carbonates subjected to high pressures and high temperatures are very limited. Studies of ankerite (Merlini et al. 2012) up to about 60 GPa reveal the formation of a phase with non-planar CO_3 groups as a tendency to increase the coordination number of carbon. Magnesium-siderite exposed to pressures and temperatures corresponding to the top of the Earth's D″ layer (135 GPa and 2650 K) was shown (Merlini et al. 2015) to transform to iron(II)-bearing dimagnesium diiron(III) tetracarbonate $Mg_{1.6}Fe_{2.4}C_4O_{13}$. It contains tetrahedrally coordinated carbon units, corner-shared in truncated C_4O_{13} chains, and up until the present work it was the only unambiguously proven case of carbonate with CO_4 groups. In this work we report for the first time two pure iron CO_4-carbonates. While three cases are too few for a comprehensive analysis of carbonate crystal chemistry, they do provide a valuable opportunity to discuss general rules that can be applied to tetrahedral carbonates.

The average interatomic C-O distance in the CO_3^{2-} ion in magnesite-structured $FeCO_3$, $MnCO_3$, and $CoCO_3$ (Lavina et al. 2009; Merlini et al. 2015) extrapolated to 75 GPa is ~1.24 Å, and is ~1.26 Å (Merlini et al. 2012) in dolomite-III. In iron ortho-

and tetracarbonates at the same pressure the average C-O distance is ~1.34 Å, where the larger value is consistent with the increase of coordination number upon transformation and quantitatively similar to borates (the typical difference in ionic radius of B^{3+} in trianglar BO_3 and BO_4 tetrahedra is about 0.1 Å) (Müller 2007). Notably, the average O-O distance (2.175 Å) in the CO_4 group in iron orthocarbonate at ~75 GPa is, for example, almost the same as in magnesite-structured Fe, Mn, and Co carbonates (about 2.15 Å) and in dolomite-III (about 2.17 Å) (Lavina et al. 2009; Merlini et al. 2015). This observation indicates that is not the size of the carbon cation, but rather the oxygen-oxygen contacts that define the size of CO_4 tetrahedra.

The shapes of CO_4 tetrahedra in HP-carbonates are far from ideal. The polyhedron is especially distorted in *tetrairon orthocarbonate Fe4C3O12* with dissimilar individual C-O distances (varying from 1.254 to 1.385 Å at 74(1) GPa) and O-C-O angles (varying from 98 to 115° with bond angle variance of 61.4 deg.^{2}, see Supplementary Information for definition and references). While orthosilicates display a great variety of geometries, such distortion of SiO_4 units is not unusual and garnets in particular show bond angle variances in the same range (57° deg.^{2} for pyrope, for example Nakatsuka et al. 2011).

In tetracarbonate there are two non-equivalent CO_4-tetrahedra, two "outer" and two "inner" that form four-membered C_4O_{13} truncated chains (Fig. 5.2b). In both Mg-bearing (Merlini et al. 2015) and pure iron tetracarbonate the "inner" tetrahedra are significantly more distorted than the "outer": the bond angle variances are 35.7 deg.^{2} compared to 13.0 deg.^{2} for pure iron tetracarbonate at 97(2) GPa, and 146.2 compared to 19.0 deg.^{2} for the Mg-bearing phase at 135 GPa. Indeed the same tendency is observed in tetrasilicates (Wierzbicka et al. 2010). Moreover, the Si-O-Si angles in tetrasilicates are ~122° and 125-143° (for "outer" and "inner" and "inner"-"inner" tetrahedral, respectively Wierzbicka et al. 2010), while for tetracarbonates the corresponding C-O-C angles are ~113 and 122-125°. Thus, the analogous structural behavior of silicates and CO_4-based carbonates is obvious: based on experimental observations there is no reason that "high-pressure" carbonate structures should be more limited than those of silicates. Moreover, iron (III) orthocarbonate, $Fe_4C_3O_{12}$, with its unique structure is an example of the diversity of atomic arrangements that are possible in high-pressure CO_4-bearing carbonates.

5.4.2 Chemical transformations of FeCO₃ at high pressures and temperatures

Heating $FeCO_3$ above 1750(100) K at pressures to at least ~50 GPa (Fig. 5.1) resulted in partial decomposition of the material with formation of iron oxides (α-Fe_2O_3 below ~25 GPa and high-pressure orthorhombic h-Fe_3O_4 at higher pressure). These observations are in agreement with results obtained in large volume apparatus: for example according to Kang *et al.* 2015, $FeCO_3$ partially decomposes upon melting according to the following reaction:

$$6\ FeCO_3 = 2\ Fe_3O_4 + C + 5\ CO_2 \qquad (5.1),$$
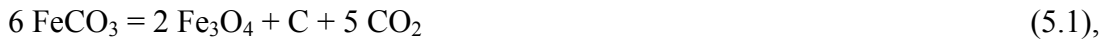
Formation of *tetrairon(III) orthocarbonate, Fe₄C₃O₁₂*, at pressures above ~74 GPa (Fig. 5.1) may be described by the simple equation:

$$4\ FeCO_3 = Fe_4C_3O_{12} + C \qquad (5.2),$$
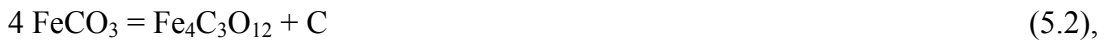
According to Eq. (5.2) and known equations of state of $FeCO_3$ (with low-spin Fe^{2+}) and diamond (Lavina et al. 2009; Dewaele et al. 2008) the gain in volume on decomposition of $FeCO_3$ is about 4%. Thus, redox reaction (5.2) may be driven by a volumetric effect.

Diiron(II) diiron(III) tetracarbonate, $Fe_4C_4O_{13}$, appears upon heating of $FeCO_3$ or *Fe₄C₃O₁₂* above ~74 GPa, but at temperatures significantly higher than needed to form *tetrairon(III) orthocarbonate* (Fig. 5.1). Moreover, the experiment at ~110(2) (Fig. 5.5) GPa demonstrates that tetracarbonate forms after further heating of already synthesized *orthocarbonate*. Thus, we can conclude that tetracarbonate is a product of the chemical evolution of orthocarbonate. Some schemes that may lead to formation of tetracarbonate are the following:

$$13\ Fe_4C_3O_{12} + 9\ C = 12\ Fe_4C_4O_{13} + 4\ Fe, \qquad (5.3),$$

or

$$7\ Fe_4C_3O_{12} + 3\ C = 6\ Fe_4C_4O_{13} + 2\ Fe_2O_3, \qquad (5.4),$$
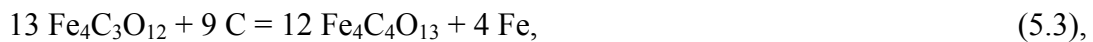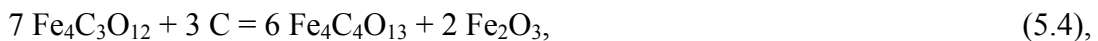
Eqs. (5.3) and (5.4) suggest that carbon (as a decomposition product of $FeCO_3$ according to Eq. (5.2) or as diamond from the anvils) reduces Fe^{3+}. However, this process is unlikely because carbon (diamond) cannot reduce iron at pressures above ~25 GPa (Rohrbach and Schmidt 2011; Bykova et al. 2016). Moreover, we did not observe evidence of pure iron or its alloys (or carbides) in reaction products, which adds to the arguments against reaction (5.3).

Another process which could lead to formation of tetrairon tetracarbonate is

$$8 \ Fe_4C_3O_{12} = 6 \ Fe_4C_4O_{13} + 4 \ Fe_2O_3 + 3O_2, \hspace{3cm} (5.5),$$
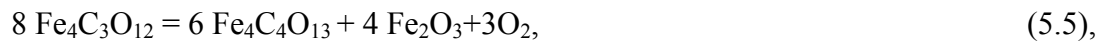
In this case iron is reduced by oxygen. The same phenomenon was observed in studies of iron(III) oxide at pressures above ~70 GPa (Bykova et al. 2016). Moreover, together with iron tetracarbonate we observed (Fig. 5.1, Table S3) $CaIrO_3$-structured η-Fe_2O_3 and possible products of its further decomposition (Merlini et al. 2015; Bykova et al. 2016): monoclinic (space group *C2/m*) Fe_5O_7, monoclinic (space group *C2/m*) $Fe_{13}O_{19}$, and orthorhombic (space group *Bbmm*) $CaTi_2O_4$-type structured h-Fe_3O_4 phases. These observations support the schematic process described by Eq. (5.5) and imply that the presence of iron oxides among products of HPHT treatment of iron carbonate(s) above 75 GPa is not a signature of their full breakdown, but rather an indication of the intrinsic process of formation of CO_4-bearing phase(s) containing iron in different oxidation states.

5.4.3 Implications for fate of carbonates in Earth interiors

Modern estimates indicate the concentration of carbon in altered oceanic crust to be in the range of 500-600 ppm (Kelemen and Manning 2015). A recent study concludes that a relatively small amount of carbon is recycled into the convecting mantle based on a careful reevaluation of carbon fluxes in subduction zones, where carbon is preferentially stored in the lithospheric mantle and the crust (Kelemen and Manning 2015). Our experiments clearly show that along an average subducting slab temperature profile (Fig. 5.1), Fe-carbonates will incongruently melt during subduction. This finding is consistent with reports[4] that show that the majority of slab geotherms intersect a deep depression along the melting curve of carbonated oceanic crust at depths of approximately 300 to 700 kilometres, creating a barrier to direct

carbonate recycling into the deep mantle. Nevertheless, a portion of the subducted carbonates can still be recycled in the convecting mantle, not taking part in hydrothermal alteration reactions, partial melting, and formation of carbonatitic magmas and "premature" carbon degassing processes. For instance, cold subducting slabs (Komabayashi et al. 2009; Syracuse et al. 2010) (Fig. 5.1) could stabilize carbonates down to mid lower mantle depths, favouring Fe-partitioning into carbonates due to Fe^{2+} high- to low-spin crossover, which starts in carbonates at much shallower depths than in other Fe^{2+}-bearing minerals (Kantor et al. 2006; Kupenko et al. 2015). In this case, the average composition of carbonates in the Earth's lower mantle could be significantly enriched towards the "$FeCO_3$" component. While self-redox reactions involving iron may potentially destabilise Fe-bearing carbonates, our experiments demonstrate that at pressures above ~70 GPa (corresponding to a depth of ~2000 km), iron carbonates drastically change their structures, forming CO_4-bearing compounds, and may persist to temperatures above 3000 K in the 100 GPa range (i.e., exist above the mantle geotherm). Thus, based on our experimental observations we conclude that CO_4-based carbonates may be carriers of carbon in the lower mantle.

5.5 Methods

5.5.1 Sample preparation

Single crystals of $^{57}FeCO_3$ were grown from $^{57}FeCO_3$ powder at 18 GPa and 1600 °C in a 1,200-t Sumitomo press at Bayerisches Geoinstitut (Bayreuth, Germany). $^{57}FeCO_3$ powder was synthesized using ^{57}Fe-oxalate ($^{57}FeC_2O_4$) as a precursor, which in turn was obtained via chemical reactions starting from ^{57}Fe-metal (see Cerantola et al. 2015b for more details).

Single crystals with an average size of $0.015 \times 0.015 \times 0.005$ mm^3 were pre-selected on a three-circle Bruker diffractometer equipped with a SMART APEX CCD detector and a high-brilliance Rigaku rotating anode (Rotor Flex FR-D, Mo-Kα radiation) with Osmic focusing X-ray optics.

Selected crystals together with small ruby chips (for pressure estimation) were loaded into BX90-type DACs (Kantor et al. 2012) and European Synchrotron Radiation Facility (ESRF) high pressure membrane cells. Neon was used as a pressure transmitting medium and was loaded at Bayerisches Geoinstitut and/or at ESRF.

5.5.2 X-ray diffraction

The single-crystal X-ray diffraction experiments were conducted on the ID09A beamline at ESRF, Grenoble, France (MAR555 detector, λ=0.4126 Å); on the ID27 beamline at ESRF (PerkinElmer flat panel detector, λ=0.3738 Å); and on the 13-IDD beamline at the Advanced Photon Source (APS), Chicago, USA (MAR165 CCD detector, λ=0.3344 Å). The X-ray spot size was dependent on beamline settings and varied from e.g. 3×2.5 μm^2 (13-IDD) to 10×10 μm^2 (ID09a), where typically a smaller beam was used for laser heating experiments. A portable double-sided laser heating system (Kupenko et al. 2012) was used for experiments on ID09A (ESRF) to collect *in situ* single-crystal X-ray diffraction data, while a state-of-the art stationary double-sided laser heating setup at IDD-13 (APS) was used to collect temperature-quenched single-crystal X-ray diffraction data. Crystals were completely immersed in laser radiation and there was no measurable temperature gradient within the samples. In the case of prolonged heating experiments the temperature variation during the heating did not exceed ±100 K. Pressures were calculated from the positions of the X-ray diffraction lines of Ne (Fei et al. 2007). X-ray diffraction images were collected during continuous rotation of DACs typically from –35° to +35° on ω; while data collection experiments were performed by narrow 0.5–1° scanning of the same ω range.

Integrated patterns (Fig. 5.5) from XRSD experiment were processed using Fit2d (Hammersley, 1997) and indexed by using the Rietveld method implemented in the GSAS and EXPUI packages (Larson and Von Dreele, 2000; Toby, 2001).

5.5.3 Data analysis

Integration of the reflection intensities and absorption corrections were performed using CrysAlisPro software (CrysAlisPro software system, 2014) The structures were solved by the direct method and refined in the isotropic approximation by full matrix least-squares refinements using SHELXS and SHELXL software (Sheldrick, 2008) respectively.

5.5.4 SMS spectroscopy

Energy-domain Mössbauer spectroscopy measurements were carried out at the nuclear resonance beamline ID18 at ESRF using the synchrotron Mössbauer source (SMS) (see Potapkin et al. 2012 for more details). The collection time for one $FeCO_3$

spectrum before heating was ~ 20 minutes, whereas after heating (depending on the sample composition) the collection time varied from 30 minutes to 6 hours (the latter for the new *HP*-carbonates). The velocity scales of all Mössbauer spectra were calibrated relative to 25 μm-thick α-Fe foil, and all spectra were fitted using the software package MossA (Prescher et al. 2012).

5.6 Supplementary material
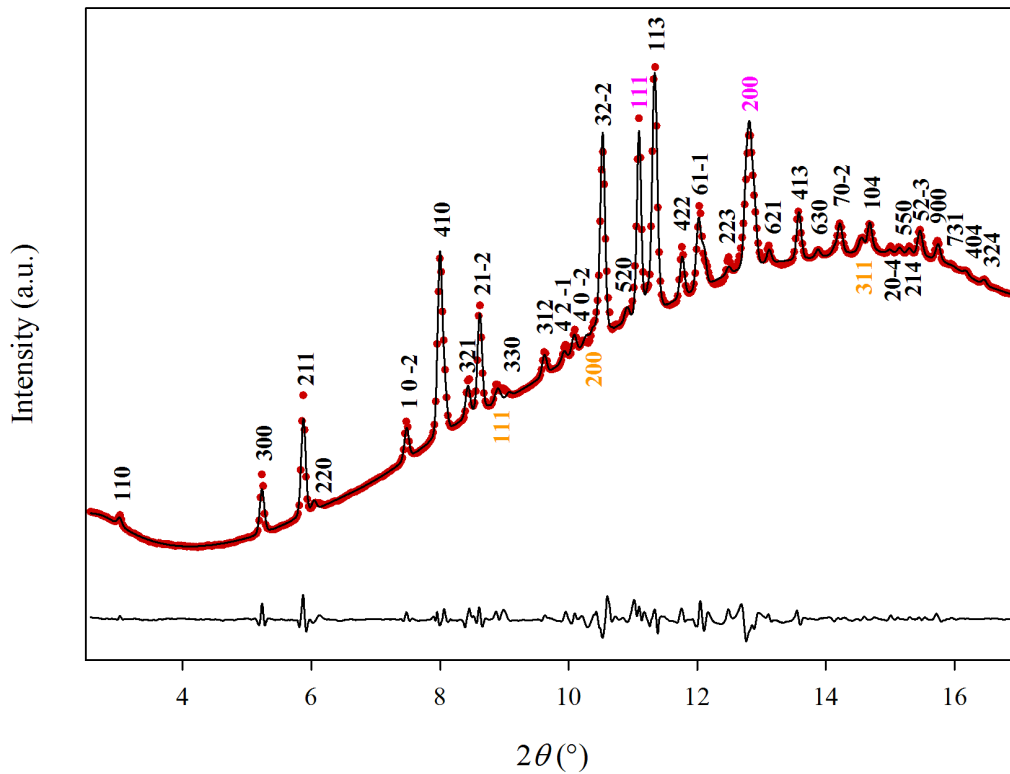
Figure S5.1 | Rietveld refinement of X-ray diffraction pattern provided by Liu *et al.* 2015. The pattern was collected after heating magnesio-siderite $(Mg_{0.35}Fe_{0.65})CO_3$ at 90 GPa and 2200 K. The high-pressure carbonate data were fitted using our model of tetrairon (III) orthocarbonate (Table S1). Red dots: measured powder diffraction pattern; black solid line: refined profile; black solid line (bottom): residual of the difference between observation and refinement. Indices of $(Mg,Fe)_4C_3O_{12}$ are in black, Ne in purple, and Au in orange. The refinement was performed using the GSAS package (Larson and Von Dreele, 2000; Toby, 2001).
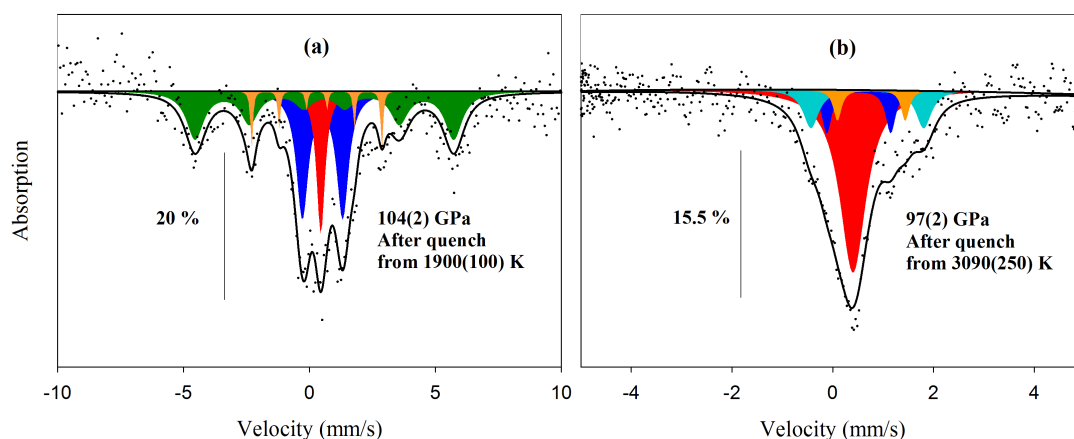
Figure S5.2 | Synchrotron Mössbauer spectra of the run products after heating FeCO₃ at high *P-T*. The spectra were collected after laser heating at (*a*) 104(2) GPa and 1900(100) K, and (*b*) at 97(2) GPa and 3090(250) K. The hyperfine parameters for each component are reported in Table S4. The subspectrum (orange) does not add up to the total spectrum due to the properties of the full transmission integral fit (see Methods). The relative absorption is indicated to the left of each spectrum.
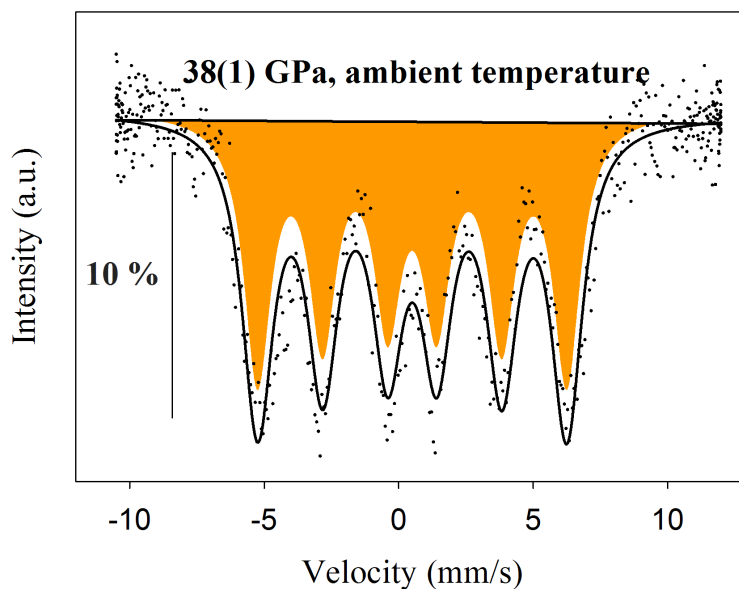
Figure S5.3 | Synchrotron Mössbauer spectrum of pure h-Fe₃O₄ at 38(1) GPa and ambient temperature. The hyperfine parameters are reported in Table S4. The subspectrum (orange) does not add up to the total spectrum due to the properties of the full transmission integral fit (see *Methods*). The relative absorption is indicated to the left of the spectrum.

Table S1. Details of crystal structure refinements of *HP*-carbonates and atomic coordinates

Crystallographic data	$Fe_4C_3O_{12}$	$Fe_4C_4O_{13}$
P, T conditions of XRD experiment	104(2) GPa	97(2) GPa
	after heating at 1900(100) K	after heating at 3090(250) K
Crystal system	Trigonal	Monoclinic
Space group	R 3 c	C 1 2/c 1
a (Å)	12.535(1)	10.261(3)
b (Å)	12.535(1)	3.985(3)
c (Å)	5.224(1)	13.455(5)
α (°)	90	90
β (°)	90	107.85(4)
γ (°)	120	90
V (Å³)	710.8(1)	523.76(28)
Z	18	4
Independent reflections / R_{int}	1733/0.0792	1503/0.0705
Refinement method	Full matrix least squares on F^2	Full matrix least squares on F^2
Data / restraints / parameters	308 / 0 / 27	346 / 0 / 53
Goodness of fit on F^2	3.42	1.214
Final *R* indices [$I > 2\sigma(I)$] R_1 / wR_2	0.0773/0.0724	0.03830.0964
ICSD reference N		

Site	x	y	z	Uiso	Site	x	y	z	Uiso
Fe1	0	0	0.0222(6)	0.0129(12)	Fe1	0.1242(1)	0.4730(2)	0.0936(1)	0.0119(5)
Fe2	0.3334(4)	0.4395(3)	-0.0036(5)	0.0135(6)	Fe2	0.1693(1)	0.4698(2)	0.8360(1)	0.0116(5)
O1	0.1794(14)	0.2885(15)	0.004(2)	0.018(3)	O1	0.1855(5)	0.0342(8)	0.3799(4)	0.0107(8)
O2	0.7234(13)	0.2600(14)	0.105(2)	0.012(3)	O2	0.0873(5)	0.3820(8)	0.4552(4)	0.0111(8)
O3	0.8736(14)	0.0783(13)	0.0106(18)	0.008(3)	O3	0.0742(4)	0.2853(8)	0.2048(4)	0.0095(8)
O4	0.6645(14)	0.0647(14)	0.017(3)	0.017(3)	O4	0	0.2020(11)	0.7500(1)	0.0096(11)
C1	0.125(2)	0.4757(19)	0.022(4)	0.012(5)	O5	0.0007(5)	0.1162(9)	0.5893(4)	0.0112(8)
					O6	0.1811(5)	0.0764(9)	0.0397(4)	0.0117(8)
					O7	0.1876(4)	0.1948(8)	0.7120(3)	0.0094(8)
					C1	0.1183(8)	0.0558(14)	0.4494(6)	0.0105(11)
					C2	0.0695(8)	0.0315(12)	0.6912(6)	0.0123(12)

Table S2. Selected geometric parameters of *HP*-carbonates (Å, °).

$Fe_4C_3O_{12}$		$Fe_4C_4O_{13}$			
104(2) GPa after heating at 1900(100) K		97(2) GPa after heating at 3090(250) K			
Fe1 − O2	1.924(14)	Fe1 − O2	1.874(5)	O2 − C1 − O1	106.7(5)
Fe1 − O2	1.924(12)	Fe1 − O3	1.879(5)	O6 − C1 − O1	114.7(6)
Fe1 − O2	1.924(17)	Fe1 − O6	1.890(5)	O6 − C1 − O2	113.3(5)
Fe1 − O2	1.928(13)	Fe1 − O1	1.904(5)	O6 − C1 − O5	106.5(6)
Fe1 − O2	1.928(13)	Fe1 − O7	2.020(4)	O2 − C1 − O5	108.0(5)
Fe1 − O2	1.928(17)	Fe1 − O5	2.060(4)	O1 − C1 − O5	107.3(6)
Fe2 − O4	1.872(22)	Fe1 − O2	2.097(5)		
Fe2 − O2	1.881(16)	Fe2 − O6	1.901(5)	O4 − C2 − O3	113.9(4)
Fe2 − O4	1.912(13)	Fe2 − O7	1.989(4)	O4 − C2 − O7	103.5(6)
Fe2 − O1	1.917(16)	Fe2 − O3	1.991(4)	O4 − C2 − O5	104.5(5)
Fe2 − O3	1.983(19)	Fe2 − O7	2.052(4)	O3 − C2 − O5	111.8(5)
Fe2 − O3	2.025(14)	Fe2 − O1	2.055(3)	O7 − C2 − O5	104.2(6)
Fe2 − O1	2.074(13)	Fe2 − O1	2.065(3)	O3 − C2 − O7	117.6(4)
Fe2 − O1	2.178(14)	Fe2 − O4	2.086(3)		
C1 − O4	1.254(24)	Fe2 − O2	2.111(6)	C1 − O5 − C2	112.6(6)
C1 − O1	1.334(32)	C1 − O6	1.299(8)	C2 − O4 − C2	121.6(5)
C1 − O2	1.371(23)	C1 − O2	1.324(11)	C1 − C2 − C2	91.4(4)
C1 − O3	1.385(31)	C1 − O1	1.346(7)		
		C1 − O5	1.357(8)		
O3 − C1 − O4	120.1(19)	C2 − O3	1.275(6)		
O2 − C1 − O3	98.3(15)	C2 − O5	1.328(8)		
O1 − C1 − O3	108.6(21)	C2 − O4	1.378(8)		
O4 − C1 − O1	108.9(18)	C2 − O7	1.394(9)		
O4 − C1 − O2	115.6(18)				
O1 − C1 − O2	104.0(1)				

Table S3. Examples of iron oxide phases found in decomposition products of $FeCO_3$ treated at different P,T conditions.
Phase identification is based on the results of single crystal X-ray diffraction data.

Crystallographic data	$Fe_{13}O_{19}$	h-Fe_3O_4	Fe_5O_7	ppv-Fe_2O_3
P, T conditions of XRD experiment	104(2) GPa	51(1) GPa	74(1) GPa	74(1) GPa
	after annealing at 1900(100) K	after annealing at 2150(100) K	after annealing at 2200(100) K	after annealing at 2200(100) K
Crystal system	Monoclinic	Orthorhombic	monoclinic	orthorhombic
Space group	C 1 2/m 1	C m c m	C 2/m	C m c m
a (Å)	19.233(2)	2.673(1)	8.638(4)	2.631(1)
b (Å)	2.582(1)	9.150(9)	2.635(1)	8.585(2)
c (Å)	9.550(11)	9.202(4)	7.977(3)	6.326(9)
α (°)	90	90	90	90
β (°)	118.39(3)	90	106.02(4)	90
γ (°)	90	90	90	90
V (Å^3)	417.2(5)	225.0(2)	174.56(15)	142.9(2)
Z	8	4	2	4
Independent reflections / R_{int}	415/0.0588	169/0.0474	231/0.0203	157/0.0096
Refinement method		Full matrix least squares on F^2		
Data / restraints / parameters	246 / 0 / 48	86 / 0 / 17	158 / 0 / 18	86 / 0 / 14
Final *R* indiced [*I* > 2σ(*I*) R_1 / wR_2	0.1273/0.0780	0.0796/0.1914	0.0672/0.1635	0.0938/0.2189
ICSD reference N	238769	430561	430563	430559

Table S4. Hyperfine parameters derived from room temperature SMS spectra of FeCO$_3$ and run products

Pressure (GPa)	Temperature (K)	Phase	Component/ Color in Figs. 3, S2 and S3	CS[a] mm/s	QS[b] mm/s	Area %	FWHM[c] mm/s	BHF[d] T
25(1)	before heating	FeCO$_3$	Fe^{2+} (HS) (blue)	1.09(2)	1.72(4)	100	0.55(9)	-
25(1)	quenche from 2000(100)	FeCO$_3$ α-Fe$_2$O$_3$	Fe^{2+} (HS) (blue) sextet (green)	1.09(2) 0.34(5)	1.77(4) -	80(4) 20(4)	0.53(5) 0.24(17)	- 49.2(4)
31(1)	before heating	FeCO$_3$	Fe^{2+} (HS) (blue)	1.02(2)	1.77(4)	100	0.42(5)	-
31(1)	quenche from 2100(100)	FeCO$_3$ h-Fe$_3$O$_4$	Fe^{2+} (HS) (blue) sextet (orange)	1.01(1) 0.61(9(	1.78(2) -	68(4) 32(4)	0.50(8) 0.97(40)	- 33.8(7)
39(1)	before heating	FeCO$_3$	Fe^{2+} (HS) (blue)	0.99(2)	1.70(4)	100	0.51(11)	-
39(1)	quenche from 2000(100)	FeCO$_3$	Fe^{2+} (HS) (blue) sextet orange	0.94(4) 0.56(7)	1.70(7) -	11(4) 89(4)	0.21(17) 1.57(17)	- 37.5(5)
44(1)	before heating	FeCO$_3$	Fe^{2+} (HS) (blue) Fe^{2+} (LS) (red)	0.94(4) 0.69(5)	1.10(8) -	43(16) 57(16)	0.25(16) 0.57(23)	- -
44(1)	570(50), *in situ* heating	FeCO$_3$	Fe^{2+} (HS) (blue) Fe^{2+} (LS) (red)	0.74(4) 0.57(8)	1.25(7) -	83(6) 17(6)	0.40(9) *0.30*	- -
38(1)	before heating	h-Fe$_3$O$_4$	sextet (orange)	0.50(3)	-	100.00	1.22(7)	35.6(2)
104(2)	1900(100)		singlet (red) doublet (blue) sextet (green) sextet (orange)	0.41(1) 0.48(1) 0.53(1) 0.26(1)	- 1.60(2) 0 0	16(1) 36(2) 41(1) 6(1)	0.63(6) 0.76(4) 0.93(4) 0.25(4)	- - 31.8(1) 15.8(1)
92(2)	3090(250)		singlet doublet doublet doublet	0.40(1) 0.52(1) 0.69(1) 0.77(1)	- 1.27(1) 2.24(2) 1.35(2)	65(2) 12(1) 16(1) 7(1)	0.64(2) 0.24(3) 0.37(3) 0.19(4)	- - - -

[a] CS: center shift relative to α-Fe
[b] QS: quadrupole splitting
[c] FWHM: full width at half maximum including the source linewidth
[d]: BHF: magnetic hyperfine field

5.6.1 Supplementary Note 1. Mössbauer spectra of high pressure carbonates

We collected SMS spectra for the run products after heating FeCO$_3$ at 104(2) GPa and 1900(100) K and at 97(2) GPa and 3090(250) K (Fig. S5.2). From XRD analyses performed on the same samples, we identified the run products at 104(2) GPa to be mixtures of Fe$_4$C$_3$O$_{12}$ + Fe$_{13}$O$_{19}$ + unreacted FeCO$_3$ (Fig. S5.2a, Table S5) and at 97(2) GPa to be Fe$_4$C$_4$O$_{13}$ + unreacted FeCO$_3$ (Fig. S5.2b, Table S5). Although it is not possible to identify unique fitting models for spectra from such multicomponent mixtures, we can unequivocally conclude that all components except one (red singlets, Figs. 5.2a and 5.2b) have hyperfine parameters (particularly CS) that are consistent with iron in the high-spin rather than the low-spin state (Table S4), which is in excellent agreement with the structural data (Fe-O bonding lengths in both *HP*-carbonate structures, Table S2). The red singlets (Fig. 5.2a and 5.2b) are highly likely due to low-spin Fe^{2+} in FeCO$_3$ based on their CS values 0.41(1) mm/s (Fig. 5.2a) and 0.40(1) mm/s (Fig. 5.2b), which are in excellent agreement with values expected for low-spin Fe^{2+} in FeCO$_3$ at those conditions (Cerantola et al. 2015b).

5.6.2 Supplementary Note 2. Bond Angle Variance

Polyhedral cation coordination in most ionic structures only approximates regular geometrical forms. Deviation from regularity can be partly characterized using distortion parameters. In order to better describe the geometry of the tetrahedral coordination complex, we measured the bond-angle distortion (or angle variance) for the CO_4 groups in the orthocarbonate. The bond angle distortion $\sigma(tet)^2$ is dimensionless and provides a convenient and meaningful measure of distortion for polyhedra that show variations in both bond angle and bond length. The distortion parameters give a quantitative measure of polyhedral distortion that is independent of the effective size of the polyhedron (Robinson et al. 1971). An undistorted polyhedron has an angle variance equal to 0. For coordination polyhedra including tetrahedral complexes, the angle variance parameter (σ^2) is given by the following equation (Robinson et al. 1971):

$$\sigma^2_{(tet)} = \sum_{i=1}^{6} (\theta_i - \theta_0)^2 / 5 \tag{5.6},$$

where θ_0 is the ideal bond angle for a regular polyhedron (e.g., 109.47° for a tetrahedron) and θ_i is the ith bond angle.

5.7 References

Bouibes, A., & Zaoui A. High-pressure polymorphs of $ZnCO_3$: Evolutionary crystal structure prediction. *Sci. Rep.* **2014**, 4, 5172.

Boulard, E. *et al.* New host for carbon in the deep Earth. *PNAS* **2011**, 108, 5184–5187.

Boulard, E. *et al.* Experimental investigation of the stability of Fe-rich carbonates in the lower mantle. *JGR* **2012**, 117, B02208.

Boulard, E., Pan, D., Galli, G., Liu, Z., and Mao, W. Tetrahedrally coordinated carbonates in Earth's lower mantle. *Nat. Commun.* **2015**, 6, 631.

Bykova, E. *et al.* Structural complexity of simple Fe_2O_3 at high pressures and temperatures. *Nat. Commun.* **2016**, 7, 10661.

Cerantola, V. *et al.* High-pressure spectroscopic study of siderite ($FeCO_3$) with focus on spin crossover. *Am. Min.* **2015**, 100, 2670-2681.

Christensen, U.R. The influence of trench migration on slab penetration into the lower mantle. *Earth Planet. Sci. Lett.* **1996**, 140, 27-39.

CrysAlisPro Software system. Version 1.171.37.35. (Agilent Technologies UK Ltd., Oxford, UK, **2014**).

Dewaele, A., Datchi, F., Loubeyre, P., & Mezouar, M. High pressure–high temperature equations of state of neon and diamond. *PRB* **2008**, 77, 094106.

Dubrovinsky, L.S. *et al.* The structure of the metallic high-pressure Fe_3O_4 polymorph: experimental and theoretical study. *JPCM*, **2003**, 15, 45.

Fei, Y. *et al*. Toward an internally consistent pressure scale. *PNAS* **2007**, 104, 9182.

Fukao, Y., Widiyantoro, S., & Obayashi, M. Stagnant slabs in the upper and lower mantle transition region. *Rev. Geophys.* **2001**, 39, 291-323.

Hammersley, A.P. FIT2D: An Introduction and Overview. *ESRF Internal Report ESRF Internal Report* **1997,** ESRF97HA02T.

Isshiki, M. *et al.* Stability of magnesite and its high-pressure form in the lowermost mantle. *Nature* **2004**, 427, 60–63.

Kaminsky, F., Mineralogy of the lower mantle: A review of 'super-deep' mineral inclusions in diamond. *Earth-Science Reviews* **2012**, 110, 127–147.

Kang, N. *et al.* Melting of siderite to 20 GPa and thermodynamic properties of $FeCO_3$-melt. *Chem. Geol.* **2015**, 400, 34-43.

Kantor, I. Yu *et al.* Spin crossover in (Mg,Fe)O: A Mössbauer effect study with an alternative interpretation of x-ray emission spectroscopy data. *Phys. Rev. B* **2006**, 73, 100101(R).

Kantor, I. *et al.* BX90: A new diamond anvil cell design for X-ray diffraction and optical measurements. *Rev. Sci. Instrum.* **2012**, 83, 125102.

Katsura, T., Yoneda, A., Yamazaki, D., Yoshino, T., & Ito, E. Adiabatic temperature profile in the mantle. *Phys. Earth Planet. Inter.* **2010**, 183, 212-218.

Kelemen, P.B., & Manning, C.E. Reevaluating carbon fluxes in subduction zones, what goes down, mostly comes up. *PNAS* **2015**, 112, E3997-E4006.

Komabayashi, T. *et al.* On the slab temperature in the deep lower mantle. *AGU Sping Meeting Abstracts* **05/2009**.

Kupenko, I. *et al.* Portable double-sided laser-heating system for Mössbauer spectroscopy and X-ray diffraction experiments at synchrotron facilities with diamond anvil cells. *Rev. Sci. Instrum.* **2012**, 83, 124501 (2012).

Kupenko, I. *et al.* Oxidation state of the lower mantle: In situ observations of the iron electronic configuration in bridgmanite at extreme conditions**.** *EPSL* **2015**, 423, 78–86.

Larson, A.C. & Von Dreele, R.B. General Structure Analysis System (GSAS). *Los Alamos National Laboratory Report* **2000**, LAUR 86-748.

Lasaga, A., & Gibbs, G.V. Applications of quantum mechanical potential surfaces to mineral physics calculations. *Phys. Chem. Minerals* **1987**, 14, 107–117.

Lavina, B. *et al.* Siderite at lower mantle conditions and the effects of the pressure-induced spin-pairing transition. *GRL*, **2009**, 36, L2330.

Lin, J-F. *et al.* Vibrational and elastic properties of ferromagnesite across the electronic spin-pairing transition of iron. *Am. Min.* **2012**, 97, 583-591.

Liu, J. *et al.* Thermal equation of state and spin transition of magnesiosiderite at high pressure and temperature. *Am. Min.* **2014**, 99, 84-93.

Liu, J., Lin, J-F., & Prakapenka, V. High-Pressure Orthorhombic Ferromagnesite as a Potential Deep-Mantle Carbon Carrier. *Scientific Reports* **2015**, 5, 7640.

Lobanov, S.S. Goncharov, A.F. & Litasov, K.D. Optical properties of siderite ($FeCO_3$) across the spin transition: Crossover to iron-rich carbonates in the lower mantle. *Am. Min.* **2015**, 100, 1059-1064.

McCammon, C. The paradox of mantle redox. *Science* **2005**, 308, 807-808.

Merlini, M., *et al.* Structures of dolomite at ultrahigh pressure and their influence on the deep carbon cycle. *PNAS* **2012**, 109, 13509-13514.

Merlini, M. *et al.* The crystal structures of $Mg_2Fe_2C_4O_{13}$, with tetrahedrally coordinated carbon, and $Fe_{13}O_{19}$, synthesized at deep mantle conditions. *Am. Min.* **2015**, 100, 2001-2004.

Merlini, M., Hanfland, M., & Gemmi, M. The $MnCO_3$-II high-pressure polymorph of rhodocrosite. *Am. Min.* **2015**, 100, 2625-2630.

Müller, U. Inorganic Structural Chemistry, *Wiley* **2007**.

Nakatsuka, A. *et al.* Static disorders of atoms and experimental determination of Debye temperature in pyrope: Low- and high-temperature single-crystal X-ray diffraction study. *Am. Min.*, **2011** 96, 1593-1605.

Oganov, A.R., Glass, C.W., & Ono, S. High-pressure phases of $CaCO_3$: Crystal structure prediction and experiment. *Earth Planet. Sci. Lett* **2006**, 241, 95-103.

Oganov, A.R., Ono, S., Ma, Y.M., Glass, C.W., & Garcia, A. Novel high-pressure structures of $MgCO_3$, $CaCO_3$ and CO_2 and their role in earth's lower mantle. *Earth Planet. Sci. Lett.* **2008**, 273, 38–47.

Oganov, A.R. *et al.* Structure, Bonding, and Mineralogy of Carbon at Extreme Conditions. *Rev. Mineral. Geochem.* **2013**, 75, 47-77.

Ono, S., Kikegawa, T., & Ohishi, Y. High-Pressure Transition of $CaCO_3$. *Am. Min.* **2007**, 92, 1246–1249.

Ovsyannikov, S. *et al.* Charge-ordering transition in iron oxide Fe_4O_5 involving competing dimer and trimer formation. *Nat. Chem* **2016,** 8, 501–508.

Potapkin, V. *et al.* The ^{57}Fe Synchrotron Mössbauer Source at the ESRF. *J. Synchrotron Radiat.* **2012**, 19, 559–569.

Prescher, C., McCammon, C., & Dubrovinsky, L. MossA: a program for analyzing energy-domain Mössbauer spectra from conventional and synchrotron sources. *Journal of Applied Crystallography* **2012**, 45, 329-331.

Rohrbach, A., & Schmidt, M.W. Redox freezing and melting in the Earth's deep mantle resulting from carbon-iron redox coupling. *Nature*, **2011**, 472, 209-212.

Sheldrick, G. M. A short history of SHELX. Acta Cryst. **2008**, 64, 112–122.

Skorodumova, N.V., Belonoshko, A.B., Huang, L., Ahuja, R., & Johansson, B. Stability of the $MgCO_3$ structures underlower mantle conditions. Am. Min. **2005**, 90, 1008-1012.

Solopova, N. A. *et al.* Melting and decomposition of $MgCO_3$ at pressures up to 84 GPa. *Phys Chem Miner* **2014**, 42, 73-81.

Stagno, V. *et al.* The stability of magnesite in the transition zone and the lower mantle as function of oxygen fugacity. *GRL* **2011**, 38, L19309.

Syracuse, E.M. *et al.* The global range of subduction zone thermal models. *PEPI* **2010**, 183, 73-90.

Tao, R. *et al.* Experimental determination of siderite stability at high pressure. *Am. Min.* **2013**, 98, 1565-1572.

Thomson, A.R. *et al.* Slab melting as a barrier to deep carbon subduction. *Nature* **2015**, 529, 76-79.

Toby, B. H. EXPGUI, a graphical user interface for *GSAS*. *J. Appl. Cryst* **2001**, 34, 210-213.

Walter, M.J. *et al.* Deep Mantle Cycling of Oceanic Crust: Evidence from Diamonds and their Mineral Inclusions. *Science* **2011**, 334, 54-57.

Wierzbicka-Wieczorek, M., Kolitsch, U., & Tillmanns E., $Ba_2Gd_2(Si_4O_{13})$: a silicate with finite Si_4O_{13} chains. *Acta Cryst. C* **2010**, 66, i29-i32.

6. Experimental investigations on FeCO$_3$ (siderite) stability in the Earth's lower mantle by XANES spectroscopy

Cerantola Valerio[1,2*], Wilke Max[3], Kantor Innokenty[4], Ismailova Leyla[2], Kupenko Ilya[5], McCammon Catherine[2] and Dubrovinsky Leonid[2]

[1] Bayerisches Geoinstitut, Universitat Bayreuth, D-95440 Bayreuth, Germany

[2] European Synchrotron Radiation Facility, 38043 Grenoble, France

[3] Universität Potsdam, 14469 Potsdam, Germany

[4] MAX IV Laboratory, 225 94 Lund, Sweden

[5] Institut für Mineralogie, Universität Münster, D-48149 Münster, Germany

* Valerio Cerantola, M.Sc. valerio.cerantola@gmail.com

6.1 Abstract

FeCO$_3$ was studied using Fe K-edge X-Ray absorption near edge spectroscopy at pressures up to 53 GPa and temperatures above 2000 K. First-principles calculations of Fe K-edges FeCO$_3$ were performed using a spin-dependent method. The amount and quality of the data collected allows the performance of a systematic study of the absorption edge features as a function of pressure and temperature in this system, which has geophysical and geochemical importance to determine the stability of Fe-carbonates in subducting plates and more in general in the whole Earth mantle. Here we shows that at conditions of mid-lower mantle, ~50 GPa and ~2200 K, FeCO$_3$ incongruently melts and partially decomposes to a mixture of FeCO$_3$ and h-Fe$_3$O$_4$. We defined the thermodynamic phase boundary between crystalline FeCO$_3$ and incongruent melting at 51(1) GPa and ~1800 K. We also identified the temperature induced spin crossover from low- to high-spin at 53(1) GPa, showing that at 1730 or 1700(100) K all Fe-atoms in FeCO$_3$ are in high spin state. The comparison between experiments and theory was necessary in order to understand in detail the effect of FeCO$_3$ decomposition observed in X-Ray absorption spectra as well as to explain the spectral changes due to pressure spin crossover in FeCO$_3$ at ambient temperature.

6.2 Introduction

Subduction zones are descending limbs of Earth's lithosphere that together with uprising mantle plumes are responsible for the active geodynamics of the Earth and its physical and chemical evolution (e.g. Takley et al. 1993; Zhao 2003; Walter et al. 2011; Chang et al. 2016). Subduction zones are also our planet's largest recycling system. They deliver crustal materials to the Earth's interior, where it re-equilibrates with the surrounding mantle mainly via complex physical mechanisms and chemical reactions (e.g. Saunders and Tarney 1984; Keppler 1996; Motti et al. 2004; Bebout 2014). What is not recycled in the upper few hundred kilometers of subduction will sink towards the core-mantle boundary (CMB), where completely different temperatures, pressures and oxygen fugacities (fO_2), govern the stability of the subducted materials (e.g. Bina and Helffrich 1994; Dubrovinsky et al. 2003; Stagno et al. 2013, Bykova et al. 2016). The subduction zones composition is well known, and it can be summarized as a layered sequence of sedimentary rocks, oceanic crust and altered peridotite. Their fate once exposed to the extreme conditions present in the interior of our planet is generally understood. However more detailed investigations should be performed with the intent to determine the stability of each subducted phase in order to achieve a complete understanding of the physics and chemistry of subducting plates at different depths inside our planet.

Carbonates are one of the major components of the sedimentary layers (Rea and Ruff, 1996). Their presence inside the Earth have been supported experimentally (Stagno et al. 2011; Liu et al. 2015; Cerantola et al. 2017) and by natural evidences, for instance being reported as inclusions in diamonds from the upper (e.g Kvasnytsya and Wirth, 2009) and lower (e.g. Brenker et al. 2007) mantle.

The three major carbonate components in the crust and upper mantle are $CaCO_3$ (calcite), $MgCO_3$ (magnesite), and $FeCO_3$ (siderite). Due to their presence in sinking subducting plates (Rea and Ruff, 1996) they can be considered the major source for carbon influx into the deep Earth. Previous high-pressure studies on the carbonate endmembers $CaCO_3$, $MgCO_3$, and $FeCO_3$ revealed high-pressure phase transitions in all phases (e.g., Isshki et al., 2004; Ono et al., 2005; Lavina et al. 2009; Boulard et al. 2012; Merlini et al., 2012; Liu et al. 2015). In particular, iron is fundamental on the fate of high-temperature carbonates (e.g. Boulard et al. 2012; Liu et al. 2015). Iron can radically change the thermodynamic stability of carbonates preserving them from breaking down at pressures and temperatures of the lower

mantle. This behavior may be a direct consequence of the pressure-induced electronic spin crossover (Lavina et al. 2009; Lobanov et al. 2015; Cerantola et al. 2015b; Lin et al. 2012), which is reported at room temperature at ~40 GPa and extends to more than 50 GPa at ~1200 K (Liu et al. 2014) for the endmember FeCO$_3$.

Despite the more energetically favorable structural configurations adopted by carbonates at high pressures and temperatures, during subduction the majority of slabs geotherms intersect a deep depression along the melting curve of carbonated oceanic crust at depths of approximately 300 to 700 km (Thomson et al. 2015). FeCO$_3$ melting in the mantle was also confirmed by other experimental studies (Tao et al. 2013, Kang et al. 2015), which investigated its the stability from ambient conditions up to 20 GPa and ~ 2150 K. At pressures below ~6.8 GPa, FeCO$_3$ does not melt but decomposes through an auto redox dissociation reaction to Fe$_3$O$_4$, a carbon polymorph and CO$_2$ (Tao et al. 2013, Kang et al. 2015). At pressures above ~6.8 GPa siderite melts incongruently, with a minor quenched Fe^{3+}-rich phase interpreted as the result of partial redox dissociation of FeCO$_3$-liquid leading to dissolved Fe^{3+} and CO$_2$ in the carbonate melt (Kang et al. 2015). Cerantola et al. 2017 recently showed that FeCO$_3$ incongruent melting extends up to ~74 GPa, where the transformation of FeCO$_3$ to its HP-carbonate structures (CO$_4^{4-}$ groups) begins (Oganov et al. 2008; Boulard et al. 2011; Boulard et al. 2012; Merlini et al. 2015, Boulard et al. 2015). In the same work, Cerantola et al. 2017 unambiguously determined that after melting FeCO$_3$, it partially recrystallizes as α-Fe$_2$O$_3$ (hematite) and h-Fe$_3$O$_4$ (Bykova et al. 2016) at pressures below and above 25 GPa, respectively. The change in redox state of the system is clearly caused by the stabilization of h-Fe$_3$O$_4$ above 25 GPa (Dubrovinsky et al. 2003, Bykova et al. 2016). The pressure dependent extent of decomposition upon melting is still under debate.

In this study, we perform an experimental and theoretical investigation on the high-pressure high-temperature behaviour of synthetic FeCO$_3$ by means of X-Ray Absorption Near Edge Structure (XANES) spectroscopy at the Fe K-edge. Our experimental conditions cover pressures and temperatures down to the shallow-mid lower mantle and represent a complementary study of the FeCO$_3$ stability fields in the Earth's mantle. In particular XANES spectroscopy in dispersive mode is an extremely powerful experimental technique capable to catch decomposition and phase transformation on the millisecond time scale due to the characteristic XANES

fingerprint of the substance. In parallel, major advances in ab-initio modeling techniques make it now possible to calculate band structures even in complex systems such as transition-metal oxides, in order to obtain theoretical simulations of the absorption spectra, which include both core-hole and spin-polarization effects. The theoretical work serves as complementary support of our experimental findings, in order to address quantitatively the observed spectral features.

The paper is organized as follows. In "Methodolody" we give experimental details on sample preparation and a description of the experimental and simulation techniques. The section "Results" carefully reports the results obtained during the experimental and theoretical work, followed by the "Discussion" that focuses on two issues: 1) the effect of extreme conditions on $FeCO_3$ absorption spectra and 2) the comparison between observed and calculated XANES spectra with focus on $FeCO_3$ spin crossover. Finally in "Implication" chapter we extend our experimental observations to the Earth's system, and their importance for the fate of carbonates within the dynamics of subduction zones.

6.3 Methodology

6.3.1 Synthesis experimental technique

Single crystals of $^{57}FeCO_3$ were grown from $^{57}FeCO_3$ powder at 18 GPa and 1600 °C in a 1,200-t Sumitomo press at Bayerisches Geoinstitut (Bayreuth, Germany). Siderite powder was synthesized using as precursor ^{57}Fe-oxalate ($^{57}FeC_2O_4$), which in turn was obtained via chemical reactions starting from ^{57}Fe-metal (Cerantola et al. 2015b for more details).

Single crystals with an average size of $0.015 \times 0.015 \times 0.010 \, mm^3$ were loaded together with small ruby chips (for pressure estimation) into BX90-type DACs (Kantor et al. 2012) and European Synchrotron Radiation Facility (ESRF) high pressure membrane cells. Diamonds with culet sizes of 250 μm and rhenium gaskets with 120 μm starting diameter hole were employed in all experiments. Neon was used as a pressure-transmitting medium and loaded at Bayerisches Geoinstitut (Kurnosov et al. 2008) and/or at ESRF. High temperatures were achieved by using the double-sided YAG laser heating system present at the ID24 beamline at ESRF. To test the degree of hydrostaticity, in some experiments we placed two or three ruby crystals in different positions inside the pressure chamber. In all cases we measured the pressure from each ruby within the same experiment to be within ± 1 GPa of each other.

6.3.2 XANES spectroscopy

Fe K-edge XANES measurements were performed at ESRF at the energy dispersive X-ray absorption spectroscopy (XAS) beamline ID24 (e.g., Pascarelli et al., 2006). The beam was focused horizontally using a curved polychromator Si 111 crystal in Bragg geometry and vertically with a bent Si mirror. The obtained cross-section is about 3x5 (HxV) μm^2. The Bragg diffraction peaks arising from the diamond anvils were removed from the energy range of interest by changing the orientation of the diamond-anvil cell and following in real time the intensity of the transmitted beam on a two-dimensional detector. The measured XANES spectra were normalized using the Athena software package (Ravel et al., 2005), and the second-order polynomial for the pixel to energy conversion parameters was calibrated using a reference α-Fe foil spectrum.

6.3.3 Details of calculations

Theoretical XANES calculations were performed using the FDMNES code (Joly, 2001; Bunau and Joly, 2009). In FDMNES, the Schrödinger equation is solved by the finite difference method (FDM) within the local density approximation. For calculation of spectra, structural models of siderite were used that were based on single-crystal diffraction data measured at the given pressure and at ambient temperature (Table 1). The cluster radius was set to 6 Å and was checked for convergence beforehand. The electron density of the potential was optimized in a self-consistent manner using the same cluster-size. Calculations included quadrupolar transitions. The natural core-hole broadening of 1.4 eV was used and the value of the Fermi energy set to include excitations to d-states in the pre-edge region. Finally, calculated spectra were shifted in energy to match the experimental ones.

6.4 Results

6.4.1 Temperature effect on FeCO₃ observed by XANES at different pressures

Here we describe the temperature effects on FeCO₃ stability at different pressures observed by XANES spectroscopy.

Figure 6.1 shows the evolution of FeCO₃ XANES spectra at 36(1) GPa with increasing temperatures. At room temperature before heating, the typical FeCO₃ XANES spectrum is observed with iron in high spin state, showing a weak pre-edge peak at ~7112 eV and two "main" peaks, identified in the figures as "1" and "2"

(Wilke et al. 2001; Cerantola et al. 2015b). Heating the sample up to 1620(100) K is marked in the spectra by the decrease in the intensity of peak 2 and by a smoothing of the EXAFS oscillations above 7160 eV. Upon further heating at 2270(150) K the spectrum radically changes with a loss of the double-peak structure at the main edge and a appearance of a new peak at ~7114 eV. Furthermore, new features at ~7155 eV, ~7173 eV and ~7210 eV appear, drastically changing the beginning of the EXAFS region. The flattening of the spectrum is a clear indication of high temperatures, and it suggests complete or at least partial melting of the sample (e.g. Aquilani et al. 2015). The spectrum after quench shows identical features to the high temperature spectrum, but more pronounced due to the absence of thermally induced disorder.
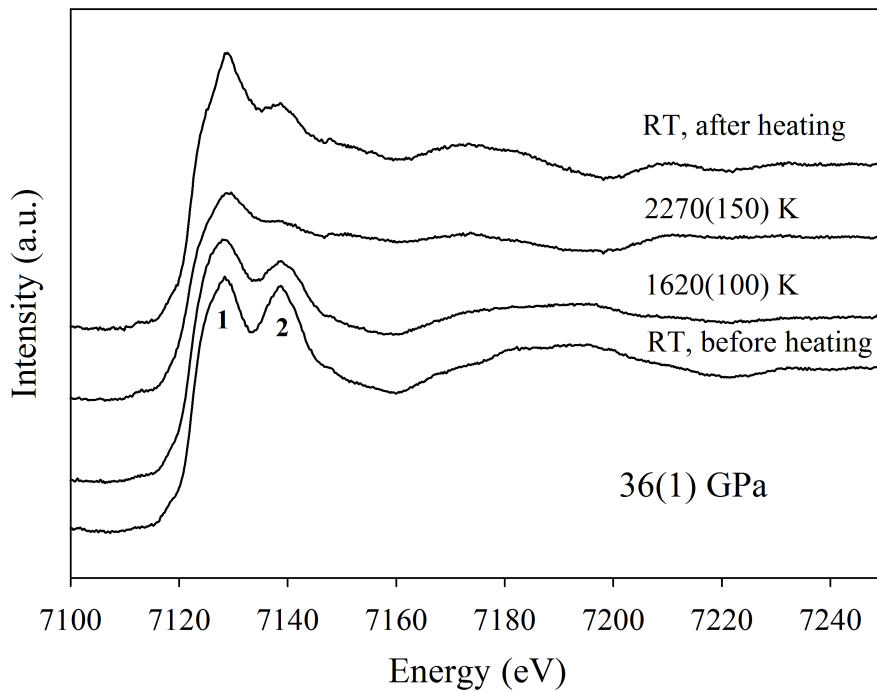
Figure 6.1. Experimental normalized XANES spectra of Fe-K edge of FeCO₃ taken at 36(1) GPa as function of temperature. After heating at 2270(150) K the spectrum radically change, indicating chemical and/or physical changes in the system.

Representative XANES spectra of FeCO₃ at 51(1) GPa and increasing temperatures are plotted in Figure 6.2. In particular, in Fig. .62a the room temperature XANES spectrum of low spin FeCO₃ shows a characteristic pre-edge at ~7112 and an additional feature at ~7117 eV. Peak 2 is more intense than peak 1 and a pronounced

hump is observed at ~7155 eV (Cerantola et al. 2015b). The temperature effect is evident at 1600(100) K and 1775(100) K, where the switch in maximum intensity between peak 1 and peak 2 and the smoothing of the first EXAFS oscillation due to the high temperatures are observed. Despite the high temperatures, the characteristic pre-edge peak position at ~7112 eV is preserved. Heating to 1890(100) K and higher completely changes the spectral shape. The maximum of the pre-edge shifts from ~7112 eV to ~7114 eV (Fig. 6.3), peak 1 shifts to slightly higher energies and "merges" with peak 2, the latter becoming rather a weak "hump" of the first peak. The ambient temperature spectrum after quench from 2025(100) K preserves the same features as at high T, which appear sharper due to the absence of heating.
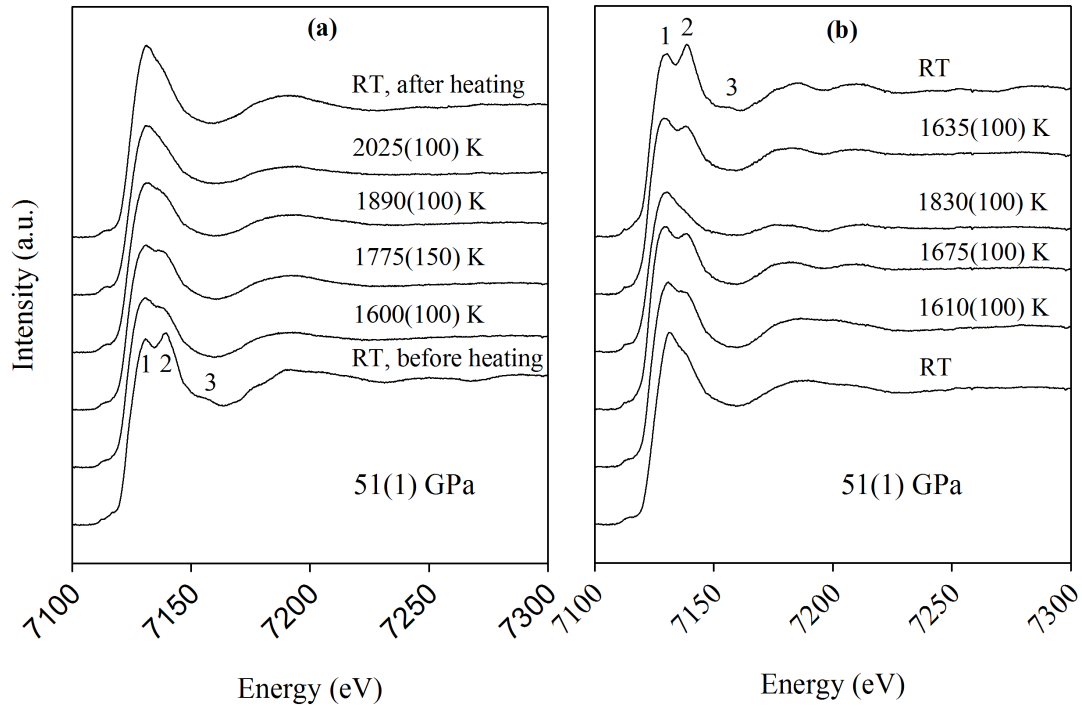
Figure 6.2. Experimental normalized FeCO₃ XANES spectra taken at 51(1) GPa and different temperatures. (a) From room temperature till ~1775 K, the FeCO₃ fingerprint is still visible in the spectra. Due to the high temperatures, all iron atoms are in high spin state (see also Fig. 6.5). Above 1775 K the spectra radically change. (b) "Moderate" temperature annealing of the run product(s) obtained after heating at higher temperature (T > 2000 K) (Fig. 6.2a).

After quenching, the same sample was re-annealed at temperatures in between ~1600-1700 K. This triggered the opposite reaction, bringing the spectra almost back to their initial configuration. The XANES region of the room temperature spectrum after annealing (Fig. 6.2b) is similar to the one before heating (Fig. 6.2a) and is characterized by the distinctive peaks marked as "1", "2" and "3" in the spectra. The EXAFS region, however, at about 7200 eV is clearly different, displaying two new humps at ~7185 and 7210 eV that are absent in the $FeCO_3$ spectrum before heating (Fig. 6.2a).
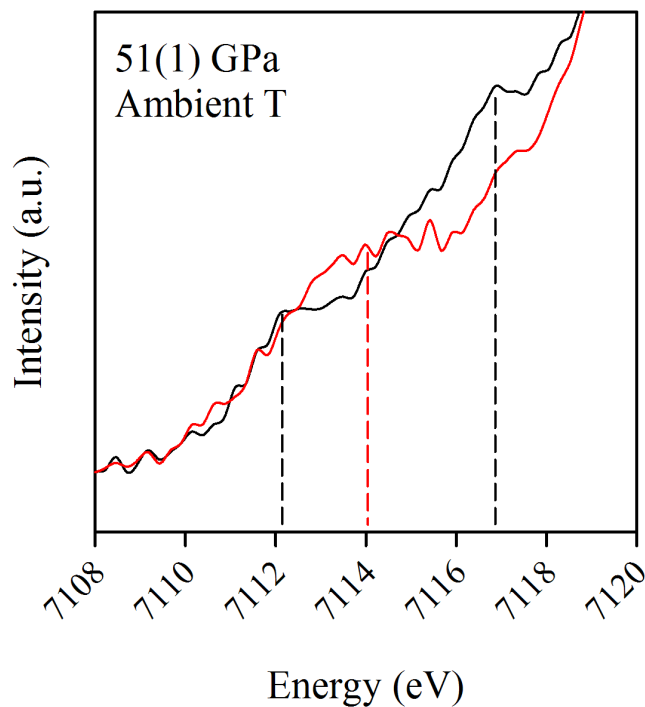
Figure 6.3. Close-up on the pre-edge region of Fig. 2(a) and 2(b) ambient temperature spectra. Black solid line: before heating; red solid line: run product(s) after quench from 2025(100) K. The black curve shows a pre-edge at ~7112 eV and a sharp feature at ~7117 eV, which perfectly match the pre-edge region in low spin $FeCO_3$ (see Cerantola et al. 2015b). The red curve has one broad hump at ~7114 eV that dominates the spectrum, and clearly indicate the presence of one or more Fe-containing phase(s).

A straightforward evidence of the temperature-based changes in the system is shown in Fig. 6.4, where the Fourier Transformed (FT) EXAFS $\chi(R)$ is displayed. Figure 6.4a shows the FT of $FeCO_3$ before heating (blue) and the run product(s) after annealing at T < 1800 K (black), whereas Fig. 6.4b presents the FT of the transformed sample (T > 2000 K) before annealing (blue) and the run product(s) after re-annealing (black). The quantitative analyses of the EXAFS pattern cannot be performed here due to the absence of a proper EXAFS region (long enough in the energy range), however qualitatively one can observe the following: 1) in Fig. 6.4a, the most intense peaks (corresponding to the distance between Fe-O) perfectly match, whereas differences emerge only at higher radial distances, where the contributions from higher neighboring shells are expected; 2) in Fig. 6.4b the most intense peaks have slightly different distance values and the patterns at higher distances are completely different, indicating no analogies between the two measured samples.
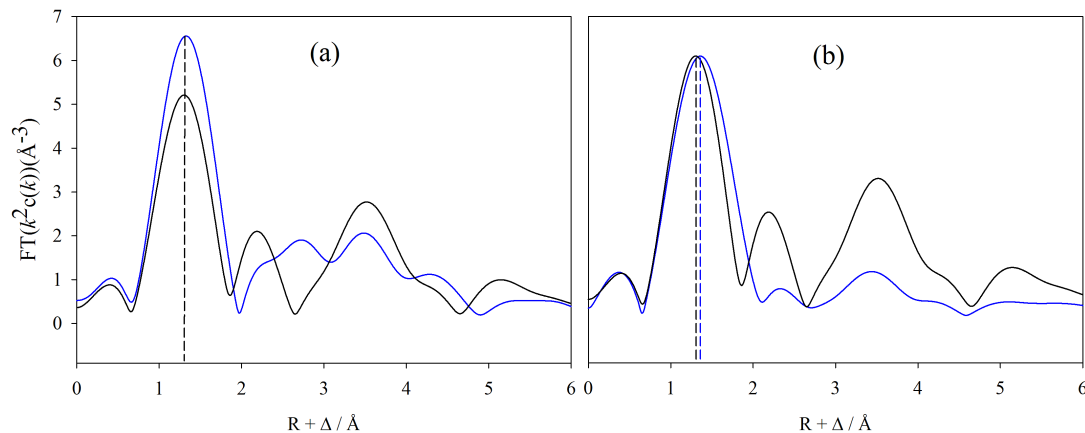
Figure 6.4. Qualitative comparison of Fourier transformed XAFS spectra (Fe K-edge) of $FeCO_3$ and run product(s) at 51(1) GPa and different temperatures. (a) $FeCO_3$ before heating (blue) and $FeCO_3$ + run product(s) after annealing at T < 1800 K (black); both spectra have same Fe-O distance, the two most intense peaks are indeed located at the same radial distance. We cannot exclude the presence of other Fe-oxides due to the mismatch in oscillations at higher distances. (b) $FeCO_3$ + run products after heating at T > 2000 K (blue) and after annealing at T < 1800 K (black); all peaks are at different distances indicating the presence of completely different phases.

The XANES spectrum evolution of low spin $FeCO_3$ at 53(1) GPa and moderate temperatures is shown in Fig. 6.5. Peak 2, which is the most intense feature in the spectrum at ambient temperature, becomes progressively less intense upon heating, peak 1 becoming the dominant peak at 1675(100) and 1735(100) K. Moreover, high temperatures are accompanied by the loss of peak "3" and the disappearance of the pre-edge peak at ~7117 eV. Similar to Fig. 6.1 and Fig. 6.2, high temperatures also tend to flatten the spectra, especially in the EXAFS regions, where the characteristic features get smoother and less pronounced. Note, that the room temperature spectrum after quenching perfectly matches the spectrum before heating.
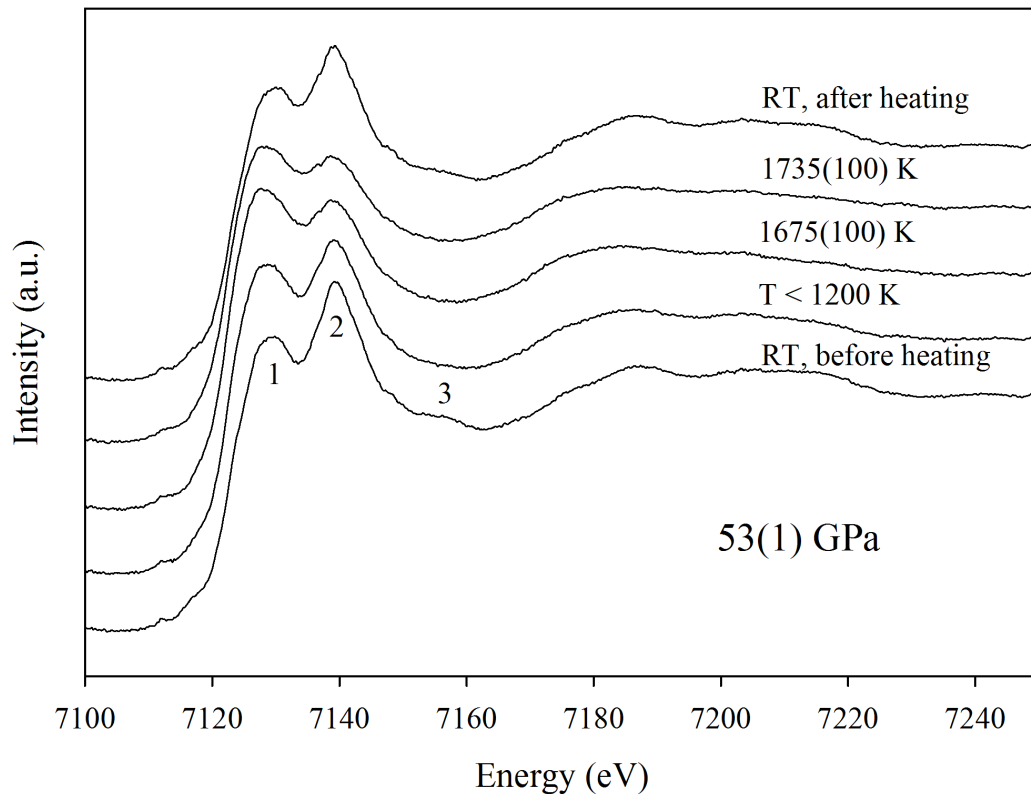
Figure 6.5. Experimental normalized $FeCO_3$ XANES spectra taken at 53(1) GPa and high temperatures. High temperatures trigger the spin crossover in the Fe-atoms from low to high spin state, observed by the change in peak 1 and peak 2 relative intensities (Cerantola et al. 2015b). There is not signature of decomposition reactions, indeed the spectrum after quench perfectly encompass the spectrum before heating.

6.4.2 FeCO₃ calculated XANES spectra: spin crossover

Siderite exhibits space-group symmetry R-3c (calcite-group rhombohedral carbonates), where, in the hexagonal setting, iron is located at the cell origin (6b), oxygen is at x, 0, 1/4 (18e), and carbon is at 0, 0, 1/4 (6a) (Bragg, W. 1913). The atomic arrangement can be envisioned as a distorted rocksalt structure with Fe as the cation and CO_3 groups as the anions. The CO_3 groups form planes perpendicular to the *c* axis with Fe occupying the interstitial octahedral voids between the planes. No bond or polyhedral edge is parallel to the *c* axis.

Here we perform a detailed analysis of FeCO₃ XANES spectra by *ab initio* simulation using the structural lattice parameters measured by XRSD diffraction at 4 GPa, 37 GPa, 55 GPa and ambient temperature (Fig. 6.6, Table 1). In general, the calculated spectra are consistent with the experimental data from Cerantola et al. 2015b. Both experimental and calculated spectra are characterized by two main peaks (identified as "1" and "2"), which shift to higher energies, ~6 eV, with increasing pressure. Their relative intensities also change with increasing pressure, so that at 55 GPa peak 2 is more intense than peak 1 (Fig. 6.6). However, some discrepancies between experiment and calculations are also observed, with the pre-edge region showing the largest variation: 1) The pre-edge peak at ~7112 eV in the experimental spectrum (black) is reproduced in the simulated ones (red) at ~7115 eV (Fig. 6.6a, 6.6b and 6.6c). Assignment of this feature in the simulation to the 1*s*-3*d* pre-edge transition is constrained by analysis of the *l*-projected density states; 2) The feature observed at ~7117.5 eV in the simulated spectra at 37 and 55 GPa almost perfectly coincide with that at 7117 eV of the experimental ones at similar pressures; 3) The calculations performed at 37 and 55 GPa are characterized by a dip at ~7125 eV visible on the left side of peak 1 that becoming sharper with pressure, but nonexistent in the experimental spectra, which instead 4) display a hump at ~7155 eV (peak 3) completely absent in the simulations.
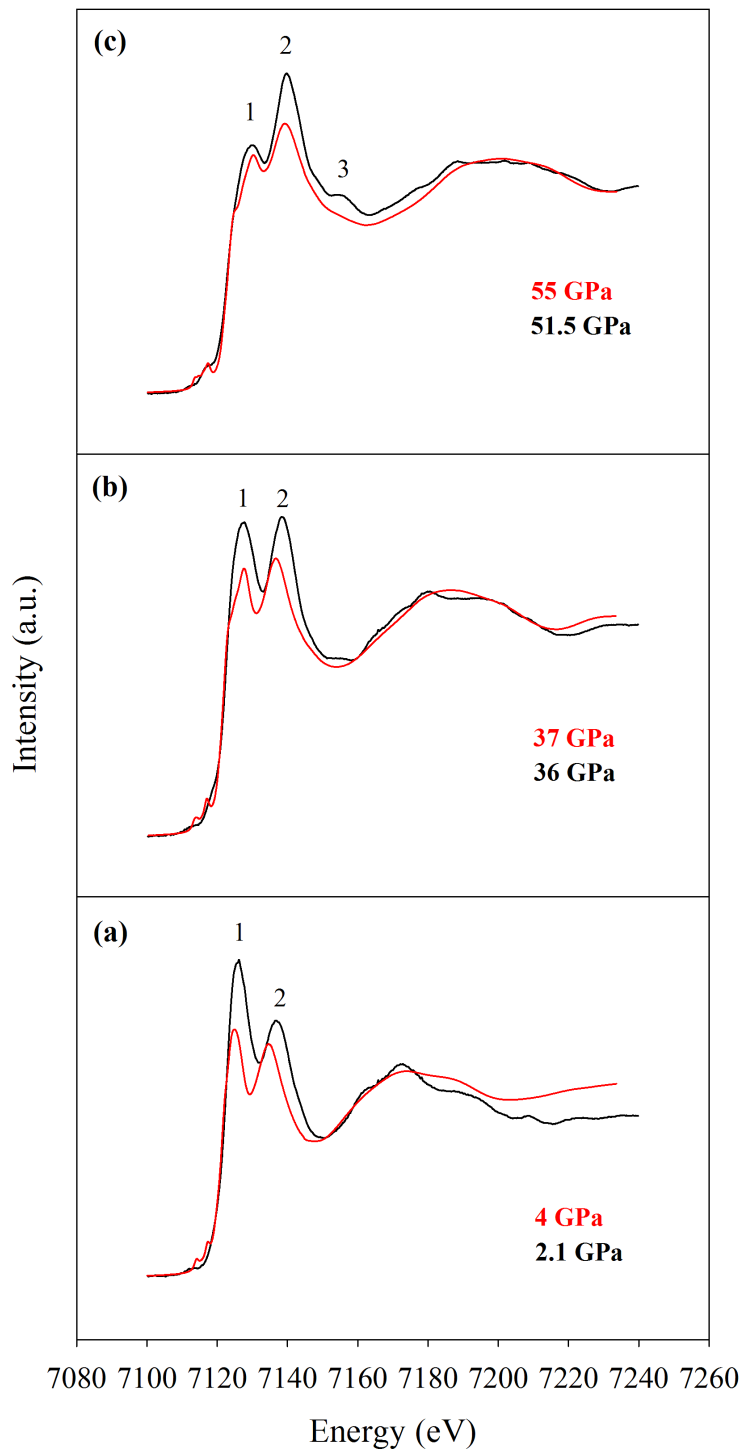
Figure 6.6. Experimental (black) and theoretical (red) XANES spectra of FeCO$_3$ at different pressures. (a) The spectra show the characteristic fingerprint of FeCO$_3$ in high spin state. Note that the pre-edge in the calculated spectrum is at 7117 eV, 5 eV higher than in the experimental spectrum. (b) The two spectra are characteristic for FeCO$_3$ in high spin state right before the spin crossover. In the experimental spectrum is evident the appearance of new feature at ~7117 eV, whereas the simulated spectrum has a pre-edge at 7117 eV and broad low intensity feature at ~7113.5 eV. (c) FeCO$_3$ XANES spectra after iron spin crossover. Analogous to the example at 37 GPa, the pre-edge peak in the calculated spectrum is at higher energy that in the experimental. The broad feature at ~7113.5 eV becomes slightly more pronounced. Note the intensity switch between peak 1 and peak 2 in both spectra and the absence of the pronounced hump at ~7155 eV in the calculated spectrum. The onset energy of each calculated spectrum was adjusted according to the variation in the Fermi energy and in the s core level energy shift.

6.5 Discussion

6.5.1 FeCO₃ incongruent melting at high pressures and tempeatures

In a recent work, Cerantola et al. 2017 investigated the phase diagram of $FeCO_3$ up to 100 GPa and T > 2500 K by means of X-Ray Single Crystal Diffraction (XRSD) and Synchrotron Mössbauer Spectroscopy (SMS). At the conditions relevant for this study, P > 36 GPa and T > 1600 K, $FeCO_3$ melts incongruently, dissociating to $h\text{-}Fe_3O_4$ and diamond. The extent of decomposition upon heating still has to be verified, but electron microprobe analyses (EMPA) (Tao et al. 2013, Kang et al. 2015), XRSD and Mössbauer spectroscopy (Cerantola et al. 2017) confirmed that even after prolonged heating the decomposition was never complete and after quench the presence of recrystallized $FeCO_3$ and $h\text{-}Fe_3O_4$ is always observed. The experimental results present in here perfectly encompass what was reported by Cerantola et al. 2017 (Fig. 6.7). At 36(1) GPa, temperatures higher than 1620(100) K (last temperature where the high spin $FeCO_3$ XANES fingerprint was clearly observed, Fig. 6.1), causes complete or partial melting of $FeCO_3$. The melting is not stoichiometric due to partial redox dissociation of liquid $FeCO_3$, leading to dissolved Fe^{3+} and CO_2 in the carbonate melt (Kang et al. 2015), so that after quench the carbonate melt recrystallizes as $FeCO_3$, $h\text{-}Fe_3O_4$ and diamond.

A similar case is observed at 51(1) GPa and temperature up to ~2000 K (Fig. 6.2). Immediately, the intensity switch between peak 1 and peak 2 at 1600(100) and 1775(150) K is evident, which is caused by the change in iron spin state from low to high spin (Liu et al. 2014; Liu et al. 2015). The characteristic pre-edge peak position at ~7112 eV and the position of peak 1 and peak 2 clearly indicate that at these conditions $FeCO_3$ is stable and no decomposition has taken place. Completely different instead are the spectra at higher temperatures, collected above 1890(100) K, which show a collapse of the $FeCO_3$ characteristic features in the XANES, the most evident change in the pre-edge, which shifts from ~7112 eV to ~7114 eV (Fig. 6.3). Again, the observed changes are caused by the non-stoichiometric recrystallization due to self-oxidation reaction during melting with the consequent formation of $h\text{-}Fe_3O_4$ (Kang et al. 2015; Cerantola et al. 2017). Interestingly, annealing the sample at moderate temperatures between 1610(100) and 1675(100) K, allowed us to bring the sample back to almost its original state, or at least to an assemblage dominated by $FeCO_3$ in low spin state (Fig. 6.2b). The recrystallization is probably incomplete and we suspect the presence of $h\text{-}Fe_3O_4$ and possibly other Fe-oxide phases, due to the

presence in the recrystallized spectra of the two humps at ~7185 eV and ~7210 eV, which are absent in the initial low spin $FeCO_3$ spectrum before heating (Fig. 6.2a). At 51(1) GPa, the changes in the spectra caused by heating below 1775(150) K and above 1830(100) K allow us to locate the thermodynamic phase boundary between $FeCO_3$ stability and incongruent melting at about 1800 K. A further support to this conclusion is given by the experiment performed at 53(1) GPa and high temperatures (Fig. 6.5). The switch in maximum intensity between peak 1 and 2 is the most evident signal of spin crossover in $FeCO_3$. At 53(1) GPa we show that heating the sample up to 1735(100) K does not melt and/or decompose the sample, but it affects only the spin state of the Fe-atoms, completely encompassing the temperature estimation we attribute to the phase boundary at 51(1) GPa. Furthermore, in order to get a more solid understanding of our experimental observations, we simulated the XANES spectrum of h-Fe_3O_4 at 51 GPa (Table 1). In Fig. 6.8a the calculated spectra of h-Fe_3O_4 at 51GPa (blue) and LS-$FeCO_3$ at 55 GPa (black) are shown. To our knowledge there are no experimental XANES spectra of pure h-Fe_3O_4 in the literature. The calculated $FeCO_3$ spectrum matches very well with the experimental one (see also Fig. 6.6). In Fig. 6.8b instead, we plot the experimental XANES spectrum obtained after laser heating $FeCO_3$ at 51(1) GPa and 2025(100) K and the sum of the calculated LS-$FeCO_3$ at 55 GPa and h-Fe_3O_4 at 51 GPa. The similarities in the main-edge region are evident: peak 1 is more intense than peak 2 and they are both at the same energy positions. Evident in the calculated spectrum is peak 3, which is not clearly present in the experimental one or shifted to lower E. Furthermore, the two spectra look quite different at higher energies, with the experimental and simulated spectra displaying the maximum of the first EXAFS oscillation at ~7180 eV and ~7195 eV respectively, which may indicate a very different average Fe-O distance in the calculated spectrum. However, it has to kept in mind that these simulations where performed for a static configuration with no thermal effects. From these spectra, it is difficult to estimate what is the relative abundance of each compound, which will clearly affect the spectral shape. For this example we have "calculated" a product containing 50 % of h-Fe_3O_4 and 50 % of $FeCO_3$, but the real relative amount of each phase is not known. The difference in the pre-edge region can be explained by the lack of ability to simulate this feature at the correct energy position as explained earlier.
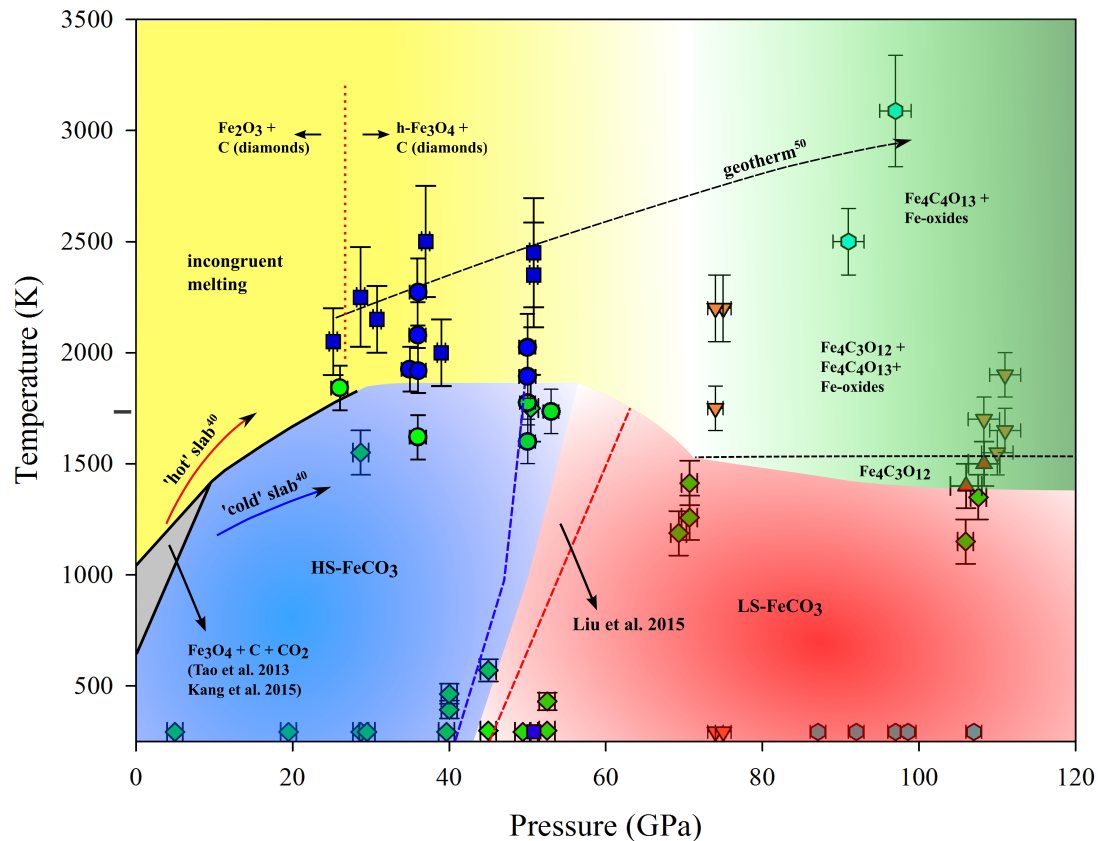
Figure 6.7. Transformational phase diagram of FeCO₃ at high *P-T* modified from Cerantola et al. 2017. Green diamonds and <u>green circle (*this study*)</u>: siderite, magnesite structured FeCO₃. Blue squares and <u>blue circles (*this study*)</u>: oxide(s) and recrystallized siderite (blue squares). Red triangles: tetrairon (III) orthocarbonate $Fe_4C_3O_{12}$. Orange inverse triangles: diiron (II) diiron (III) tetracarbonate $Fe_4C_4O_{13}$ + $Fe_4C_3O_{12}$ + oxide(s). Cyan hexagons: $Fe_4C_4O_{13}$ + oxides. FeCO₃ decomposition to Fe_3O_4 + C + CO_2 (Tao et al. 2013; Kang et al. 2015) (grey area), high spin FeCO₃ (blue area), low spin FeCO₃ (red area) (Liu et al. 2015), incongruent melting of FeCO₃ (yellow area), formation of high-pressure carbonates $Fe_4C_3O_{12}$ and $Fe_4C_4O_{13}$ (green area). Black dashed curve: expected mantle geotherm (Katsura et al. 2010). Blue and red dashed lines: region delimiting the spin transition in magnesiumsiderite at HPHT from Liu et al. 2015. Vertical dotted red line separate the regions in which the formation of α- Fe_2O_3 and h-Fe_3O_4 was observed upon incongruent melting of FeCO₃.

The modified FeCO₃ phase diagram (Fig. 6.7) from Cerantola et al. 2017 clearly shows that the interpretation of the XANES spectra given in this study is consistent

with the FeCO$_3$ stability fields that were reported at similar conditions. More in detail, the green and blue circles represent the region of stability of FeCO$_3$ and incongruent melt respectively. All other symbols come from the experimental results reported by Cerantola et al. 2017. In conclusion, this XANES study confirmed and further constrained the phase boundary of FeCO$_3$ between high and low spin state, as well as the incongruent melting with subsequent non-stoichiometric recrystallization of FeCO$_3$ + h-Fe$_3$O$_4$ and perhaps other Fe-oxide phases, which however have not been observed by XRSD.
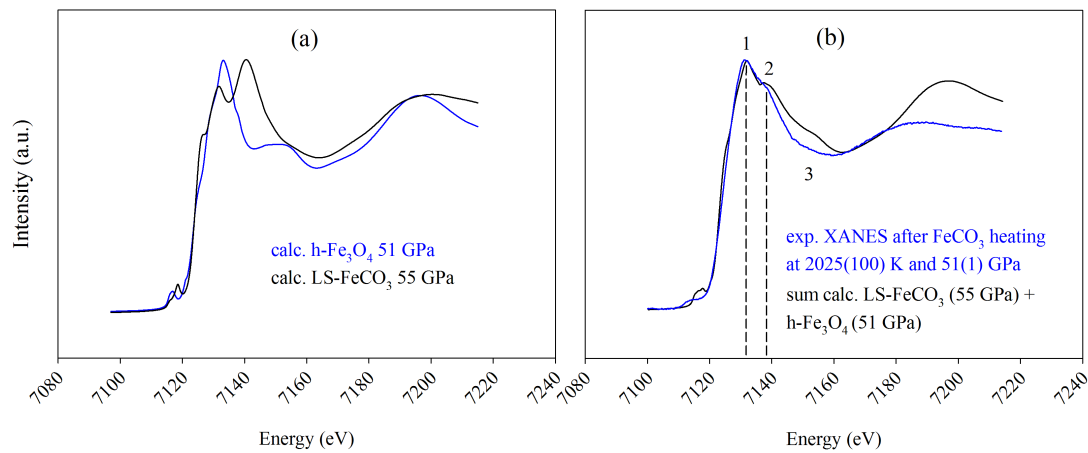
Figure 6.8. (a) Comparison between LS-FeCO$_3$ calculated XANES spectrum at 55 GPa (black) and h-Fe$_3$O$_4$ calculated XANES spectrum at 51 GPa (blue). (b) Comparison between the sum of h-Fe$_3$O$_4$ and LS-FeCO$_3$ calculated spectra (see Fig. 6.8a) (black) and the experimental spectrum of the system LS-FeCO$_3$ + run product(s) at 51(1) GPa after heating at 2025(100) K (blue). Note that the presence of recrystallized h-Fe$_3$O$_4$ after FeCO$_3$ (partial) melting at 51(1) has been observed by XRSD by Cerantola et al. 2017. The presence of other Fe-oxide phases cannot be excluded.

Table 1. Simulatios' relevant lattice cell parameters of synthetic ^{57}FeCO$_3$ and h-57Fe3O4 single crystal at ambient temperature

Sample	P (GPa)	a	b	c	vol	α	β	γ
FeCO$_3$	4(1)	4.661(1)	/	15.09(5)	283.8(4)	90	90	120
R 3 c	37(1)	4.530(4)	/	13.46(19)	239.2(3)	90	90	120
Z = 6	55(1)	4.346(1)	/	12.4(4)	202.8(2)	90	90	120
h-Fe$_3$O$_4$								
Bbmm	51(1)	9.230(13)	9.168(4)	2.6775(12)	226.6(3)	90	90	90
Z = 4								

6.5.2 Analysis of FeCO₃ spin crossover in XANES simulated spectra

Cerantola et al. 2015b reported the spin crossover in $FeCO_3$ observed by XANES for the first time. The changes in the spectra, the broadening of the peaks as well as their shift to higher energies with pressure is related to changes in the electronic structure due to shortening of Fe-O distances. The shortening is also directly reflected in the shift of the first EXAFS maximum between 7170 and 7190 eV to higher energy (of ~20 eV), which may be described by the relation ΔE x R^2 = const. (e.g., Bianconi et al., 1983, Wilke et al., 2007), where ΔE is the energy difference between the onset of the edge and the first EXAFS maximum and R is the Fe-O distance. The similarity between simulated and experimental spectra is quite remarkable and is owed to fact that the FDMNES code is not based on a multiple-scattering formalism such as FEFF (Rehr and Albers 2000). Particularly, the double peak feature at the main edge (peaks 1 and 2) has been simulated. This feature is the one that is most indicative for the change in Fe spin state in spectra shown here.

The pre-edge region at ~7112 eV in the experimental spectra and at ~7115 eV in the simulated ones is related to localized *1s* → *3d* transitions, which are quadrupolar in nature and only become dipole-allowed through hybridization of p and d orbitals for non-centro-symmetric sites. In theory, the pre-edge represents a region of the spectrum that is very sensitive to changes in Fe spin as shown by Westre et al. 1997. Simulated spectra do show slight differences in this energy region between HS and LS state, a comparison to experiment is difficult due to low resolution and low statistical quality of the data. The feature at 7117 eV, which emerges in the experimental spectra above the spin crossover is likely related to excitations of 1*s* to 4*p* electron states of the valence band (e.g., Caliebe et al., 1997). This feature becomes better resolved at higher pressures because the main edge shifts to higher energy with decreasing Fe-O distance. In the simulations this feature is at 7117.5 eV and becomes better resolved due to the shift of the main edge to higher energy, similar to the experiment. Similarly, the depression at around 7125 eV present in the simulated spectrum at 37 GPa and 55 GPa is also related to the shortening of the Fe-O upon compression and spin crossover, so that at 55 GPa is more pronounced and sharper than at 37 GPa due to the shift of the main edge. At higher energies, the presence of the hump at ~7155 eV (feature 3) in the experimental spectra above 37 GPa is not observed in the simulations, which suggests that this feature stems from

multiple scattering and cannot be adequately reproduced by the calculation performed here.

Overall, the theoretical spectra and analysis of the *l*-projected density of states show that the changes in the main-edge XANES region of the spectra are mainly related to the shift of p-states to higher energies, which is induced by the reduction of the Fe-O distance.

6.6 Implications

Carbonate-bearing subducting plates are characterized by different thermal profiles, which mainly vary based on the age of the slabs and their sinking velocity, in a way that the faster the slab subducts the colder its surface temperature is (e.g. Syracuse et al. 2010). Recently, it has been proposed that the majority of slabs geotherms intersect a deep depression along the melting curve of carbonated oceanic crust at depths of approximately 300 to 700 km during subduction (Thomson et al. 2015). At those depths, $FeCO_3$ melts incongruently, forming $\alpha\text{-}Fe_2O_3$ below ~25 GPa (Kang et al. 2015; Cerantola et al. 2017) and $h\text{-}Fe_3O_4$ above (> 750 Km) (Cerantola et al. 2017). Here, we show by XANES spectroscopy that at conditions of mid-lower mantle, ~50 GPa and ~2200 K (Katsura et al. 2010), $FeCO_3$ incongruently melts and partially decomposes to a mixture of $FeCO_3$ and $h\text{-}Fe_3O_4$. We defined the thermodynamic phase boundary between crystalline $FeCO_3$ and incongruent melting at 51(1) GPa and ~1800 K. We also identified the temperature induced spin crossover from LS to HS at 53(1) GPa, showing that at 1730 or 1700(100) K all Fe-atoms in $FeCO_3$ are in HS state, hence confirming the limit of the phase boundary identified at 51(1) GPa to be at slightly higher temperatures. In this scenario, subducting plates characterized by average surface temperature, i.e. 1400 K at 15 GPa (Syracuse et al. 2010), will undergo carbonate-melting processes, resulting in decomposition to oxides and diamond. On the other hand, subducting plates characterized by low surface temperatures, i.e. 1250 K at 15 GPa (Syracuse et al. 2010) and even colder i.e. 1500 K at 70 GPa (e.g. Kaneshima and Helffrich 2003; Komabayashi et al. 2009) could sink through the Earth's mantle without undergoing any (incongruent) melting process until pressures and temperatures are high enough to trigger the transformation of CO_3^{2-}-carbonates to their HP-structures characterized by CO_4^{4-} tetrahedra above 70 GPa (Cerantola et al. 2017).

6.7 References

Aquilani, G., Trapananti, A., Karandikar, A., Kantor, I., Marini, C., Mathon, O., Pascarelli, S., and Boehler, R. (2015) Melting of iron determined by X-ray absorption spectroscopy to 100 GPa. PNAS, 112, 12042–12045.

Bebout, G.E. (2014) Metamorphic chemical geodynamics of subduction zones. Earth Planet. Sci. Lett., 260, 373–393.

Bianconi, A., Dell'Ariccia, M., Gargano, A., and Natoli, C.R. (1983) Bond length determination using XANES. In A. Bianconi, L. Incoccia, and S. Stilpcich, Eds., EXAFS and Near Edge Structure, 27, p. 57-61. Springer Series in Chemistry and Physics, Berlin.

Bina, C.R. and Helffrich, G. (1994) Phase transition Clapeyron slopes and transition zone seismic discontinuity topography. JGR, 99, 853-860.

Boulard, E., Gloter, A., Corgne, A., Antonangeli, D., Auzende, A-L., Perrillat, J-P., Guyot, F., & Fiquet, G. (2011) New host for carbon in the deep Earth. PNAS, 108, 5184–5187.

Boulard, E., Menguy, N., Auzende, A.L., Benzerara, K., Bureau, H., Antonangeli, D., Corgne, A., Morard, G., Siebert, J., Perrillat, J.P., Guyot, F., and Fiquet, G. (2012) Experimental investigation of the stability of Fe-rich carbonates in the lower mantle. JGR, 117, B02208.

Boulard, E., Pan, D., Galli, G., Liu, Z., and Mao, W. (2015) Tetrahedrally coordinated carbonates in Earth's lower mantle. Nat. Commun., 6, 631.

Bragg, W.L. (1913) The Structure of Some Crystals as Indicated by Their Diffraction of X-rays. Proc. R. Soc. London 89, 248.

Brenker, F.E., Vollmer, C., Vincze, L., Vekemans, B., Szymanski, A., Janssens, K., Szaloki, I., Nasdala, L., Joswig, W., Kaminsky, F. (2007) Carbonates from the lower part of transition zone or even the lower mantle. EPSL, 260, 1-9.

Bunau, O., and Joly, Y. (2009) Self-consistent aspects of x-ray absorption calculations. J. Phys. Condens. Matter, 21, 34.

Bykova, E., Dubrovinsky, L., Dubrovinskaia, N., Bykov, M., McCammon, C., Ovsyannikov, S.V., Liermann, H-P., Kupenko, I., Chumakov, A.I., Rueffer, R., Hanfland, M., and Prakapenka, V. (2016) Structural complexity of simple Fe_2O_3 at high pressures and temperatures. Nat. Commun., 7, 10661.

Caliebe, W.A., Kao, C.C., Hastings, J.B., Taguchi, M., Kotani, A., Uozumi, T., and de Groot, F.M.F. (1998) 1s2p resonant inelastic x-ray scattering in γ-Fe_2O_3. Physical Review B, 58, 13452-13458.

Cerantola, V., McCammon, C., Kupenko, I., Kantor, I., Marini, C., Wilke, M., Ismailova, L., Solopova, N., Chumakov, A.I., Pascarelli, S., and Dubrovinsky, L. (2015) High-pressure spectroscopic study of siderite ($FeCO_3$) with focus on spin crossover. Am. Min., 100, 2670-2681.

Cerantola, V., Bykova, E., Kupenko, I., Merlini, M., Ismailova, L., McCammon, C., Bykov, M., Chumakov, A., Petitgirard, S., Kantor, I., Svitlyk, V., Jacobs, J., Hanfland, M. Mezouar, M., Prescher, C., Rüffer, R., Prakapenka, V. and Dubrovisnky, L. (2017) Stability of iron-bearing carbonates in the deep Earth's interior. Nat. Commun. 8, 15960 doi: 10.1038/ncomms15960.

Chang, S-J., Ferreira A.MG. and Faccenda, M. (2016) Upper- and mid-mantle interaction between the Samoan plume and the Tonga–Kermadec slabs. Nat. Commun., 7, 10799.

Dubrovinsky, L.S., Dubrovinskaia, N.A. McCammon, C. Rozenber, G.Kh., Ahuja, R. Osorio-Guillen, J.M, Dmitriev, V., Weber, H-P., Bihan, T.Le., and Johansson B. (2003) The structure of the metallic high-pressure Fe_3O_4 polymorph: experimental and theoretical study. JPCM, 15, 45.

Isshiki, M., Irifune, T., Hirose, K., Ono, S., Ohishi, Y., Watanuki, T., Nishibori, E., Takata, M., and Sakata, M. (2004) Stability of magnesite and its high-pressure form in the lowermost mantle. Nature, 427, 60-63.

Joly, Y. (2001) X-ray absorption near-edge structure calculations beyond the muffin-tin approximation. PRB, 63, 125120.

Kaneshima, S., and Helffrich, .G (2003) Subparallel dipping heterogeneities in the mid-lower mantle. JGR, 108, B5, DOI: 10.1029/2001JB001596.

Kang, N., Schmidt, M.W., Poli, S., Franzolin, E. & Connolly, J.A.D. (2015) Melting of siderite to 20 GPa and thermodynamic properties of $FeCO_3$-melt. Chem. Geol., 400, 34-43.

Kantor, I. Yu., Prakapenka, V., Kantor, A., Dera, P., Kurnosov, A., Sinogeikin, S., Dubrovinskaia, N., and Dubrovinsky, L. (2012) BX90: A new diamond anvil cell design for X-ray diffraction and optical measurements. Review of Scientific Instruments, 83, 125102.

Katsura, T., Yoneda, A., Yamazaki, D., Yoshino, T., and Ito, E. (2010) Adiabatic temperature profile in the mantle. Phys. Earth Planet. Inter, 183, 212-218.

Keppler, H.K. (1996) Constraints from partitioning experiments on the composition of subduction-zone fluids. Nature, 380, 237-240.

Komabayashi, T., Omori, S., Hirose, K., and Maruyama, S. (2009) et al. On the slab temperature in the deep lower mantle. AGU Sping Meeting Abstracts.

Kurnosov, A., Kantor, I., Boffa-Ballaran, T., Lindhardt, S., Dubrovisnky, L., Kuznetsov, A., and Zehnder, B.H. (2008) A novel gas-loading system for mechanically closing of various types of diamond anvil cells. Review of Scientific Instruments, 79, 045110.

Kvasnytsya, V.M., and Wirth, R. (2009) Nanoinclusions in microdiamonds from Neogenic sands of the Ukraine (Samotkan' Placer); a TEM study. Lithos, 113, 454-464.

Lavina B., Dera P., Downs R.T., Prakapenka V., Rivers M., Sutton S., and Nicol M. (2009) Siderite at lower mantle conditions and the effects of the pressure-induced spin-pairing transition. Geophysical Research Letters, 36, L23306.

Lin, J.F., Liu, J., Jacobs, C., and Prakapenka, V.B. (2012) Vibrational and elastic properties of ferromagnesite across the electronic spin-pairing transition of iron. American Mineralogist, 97, 583-591.

Liu, J., Lin, J.F., Mao, Z., and Prakapenka, V.B. (2014) Thermal equation of state and spin transition of magnesiosiderite at high pressure and temperature. American Mineralogist, 99, 84-93.

Liu, J., Lin, J.-F., and Prakapenka, V.B. (2015) High-pressure orthorhombic ferromagnesite as a potential deep-mantle carbon carrier. Scientific Reports, 5, 7640, doi: 10.1038/srep07640.

Lobanov, S.S., Goncharov, A.F., and Litasov, K.D. (2015) Optical properties of siderite ($FeCO_3$) across the spin transition: Crossover to iron-rich carbonates in the lower mantle. Am. Min., 100, 1059-1064.

Merlini, M., Crichton, W.A., Hanfland, M., Gemmi, M., Mueller, H., Kupenko, I., and Dubrovinsky, L. (2012) Structures of dolomite at ultrahigh pressure and their influence on the deep carbon cycle. PNAS, 109, 13509-13514.

Merlini, M., Hanfland, M., Salamat, A., Petitgirard, S. & Müller, H. (2015) The crystal structures of $Mg_2Fe_2C_4O_{13}$, with tetrahedrally coordinated carbon, and $Fe_{13}O_{19}$, synthesized at deep mantle conditions. Am. Min., 100, 2001-2004.

Motti, M.J., Wheat, C.G., Fryer, P. Gharib, J. Martin, B.J. (2004) Chemistry of springs across the Mariana forearc shows progressive devolatilization of the subducting plate. Geochim. Cosmochim. Acta, 68, 4915-4933.

Oganov, A.R., Ono, S., Ma, Y.M., Glass, C.W., & Garcia, A. (2008) Novel high-pressure structures of $MgCO_3$, $CaCO_3$ and CO_2 and their role in earth's lower mantle. Earth Planet. Sci. Lett., 273, 38–47.

Ono, S., Kikegawa, T., Ohishi, Y., and Tsuchya, J. (2005) Post-aragonite phase transformation in CaCO3 at 40 GPa. American Mineralogist, 90, 667-671.

Pascarelli, S., Mathon, O., Muñoz, M., Mairs, T., and Susini J. (2006) Energy-dispersive absorption spectroscopy for hard-X-ray micro-XAS applications. Journal of Synchrotron Radiation, 13, 351-358.

Ravel, B., and Newville, M. (2005) ATHENA, ARTEMIS, HEPHAESTUS: data analysis for X-ray absorption spectroscopy using IFEFFIT. Journal of synchrotron radiation, 12, 537–41.

Rea, D.K., and Ruff, L.J. (1996) Composition and mass flux of sediment entering the world's subduction zones: Implications for global sediment budgets, great earthquakes, and volcanism. EPSL, 140, 1-12.

Rehr, J.J., and Albers, R.C. (2000) Theoretical Approaches to X-ray Absorption Fine Structure. Rev. Mod. Phys., 72, 621.

Saunders, A.D. and Tarney, J. (1984) Geochemical characteristics of basaltic volcanism within back-arc basins. J. Geol. Soc., 16, 59-76.

Stagno, V., Tange, Y., Miyajima, N., McCammon, C.A., Irifune, T., and Frost, D.J. (2011) The stability of magnesite in the transition zone and lower mantle as function of oxygen fugacity. Geophysical Research Letters, 38, L19309.

Syracuse, E.M., van Keken, P.E., and Abers, G.A. (2010) The global range of subduction zone thermal models. Phys. Earth Planet. Inter, 183, 73-90.

Takley, P.J., Stevenson, D.J., Glatzmaier, G.A. and Schubert, G. (1993) Effects of an endothermic phase transition at 670 km depth in a spherical model of convection in the Earth's mantle. Nature, 361, 699-703.

Tao, R., Fei, Y. & Zhang, L. (2013) Experimental determination of siderite stability at high pressure. Am. Min., 98, 1565-1572.

Thomson, A.R., Walter, M.J., Kohn, S.C. & Brooker, R.A. (2015) Slab melting as a barrier to deep carbon subduction. Nature, 529, 76-79.

Walter, M.J., Kohn, S.C., Araujo, D., Bulanova, G.P., Smith, C.B., Gaillou, E., Wang, J., Steele, A., and Shirey, S.B. (2011) Deep Mantle Cycling of Oceanic Crust: Evidence from Diamonds and Their Mineral Inclusions. Science, 334, 54-57.

Westre, T. E., Kennepohl, P., DeWitt, J. G., Hedman, B., Hodgson, K. O., and Solomon, O. E. (1997) A Multiplet Analysis of Fe K-Edge 1s → 3d Pre-Edge Features of Iron Complexes. Journal of the American Chemical Society, 119, 6297-6314

Wilke, M., Farges, F., Partzsch, G.M., Schmidt, C., and Behrens, H. (2007) Speciation of iron in silicate glasses and melts by in-situ XANES spectroscopy. American Mineralogist, 92, 44-56.

Zhao, D. (2003) Global tomographic images of mantle plumes and subducting slabs: insight into deep Earth dynamics. PEPI, 146, 3-34.

7. Synchrotron Mössbauer Source technique for *in situ* measurement of iron-bearing inclusions in natural diamonds

Nestola Fabrizio[1], Cerantola Valerio[2], Milani Sula[1], Anzolini Chiara[1], McCammon Catherine[3], Novella Davide[4], Kupenko Ilya [5], Chumakov Alexandr I.[2], Rüffer Rudol[2] and Harris Jeff W.[6]

[1]Dipartimento di Geoscienze, Università degli Studi di Padova, Via G. Gradenigo 6, I-35131, Padova (Italy)

[2]European Synchrotron Radiation Facility (ESRF), F-38043 Grenoble (France)

[3]Bayerisches Geoinstitut, University of Bayreuth, 95440 Bayreuth (Germany)

[4]Lawrence Livermore National Laboratory, Livermore, California 94550 (USA)

[5]Institut für Mineralogie, Universität Münster, Corrensstraße 24, 48149 Münster, Germany

[6]School of Geographical and Earth Sciences, University of Glasgow, Glasgow G12 8QQ (UK)

7.1 Abstract

We describe a new methodology to collect energy domain Mössbauer spectra of inclusions in natural diamonds using a Synchrotron Mössbauer Source (SMS). Measurements were carried out at the Nuclear Resonance beamline ID18 at the European Synchrotron Radiation Facility (Grenoble, France). We applied this non-destructive approach to collect SMS spectra of a ferropericlase inclusion still contained within its diamond host from Juina (Brazil). The high spatial resolution of the measurement (~ 15 μm) enabled multiple regions of the 150×150 μm^2 inclusion to be sampled and showed that while Fe^{3+}/Fe_{tot} values in ferropericlase were below the detection limit (0.02) overall, there was a magnetic component whose abundance varied systematically across the inclusion. Hyperfine parameters of the magnetic component are consistent with magnesioferrite, and the absence of superparamgnetism allows the minimum particle size to be estimated as ~ 30 nm. Bulk Fe^{3+}/Fe_{tot} values are similar to those reported for other ferropericlase inclusions

from Juina, and their variation across the inclusion can provide constraints on its history.

7.2 Introduction

Natural diamonds containing silicate, oxide and sulfide inclusions are a popular focus of investigation as they uniquely provide a window into the conditions of the Earth's interior at extreme depths. Indeed, diamonds are probably the only natural sample capable of travelling from the deep mantle to the Earth's surface, bringing other "fragments" from great depths. Because of their unique physical properties, diamonds protect mineral inclusions from alteration over time and space and thus provide constraints on Earth's evolution over the past 3.2 billion years (Richardson and Harris, 1997). Studies of mineral inclusions in diamonds have yielded considerable geochemical and geophysical information. For reviews on mineralogy, geochemistry, pressure and temperature of formation, and diamond genesis ages, see e.g., Stachel and Harris (2008) and Shirey et al. (2013). Recent discoveries based on investigations of deep diamonds have considerably improved our knowledge of the Earth's deep carbon and water cycles (see e.g., Harte, 2010; Walter et al., 2011; Pearson et al., 2014; Nestola and Smyth, 2016) and the oxygen fugacity of the Earth's interior (e.g., McCammon et al., 1997; McCammon et al., 2004b; Pearson et al., 2014).

Most investigations take place after diamonds are broken open to expose the mineral inclusion. However, a non-destructive *in situ* approach to investigate inclusions entrapped in diamonds can be crucial for many reasons: (a) inclusions may be under pressure in the diamond, thus once opened they could invert to lower pressure phases on release (for example in a case of natural clinopyroxene, Alvaro et al., 2010); (b) the inclusions may retain significant residual pressure that can provide information about the depth of diamond formation (e.g., Sobolev et al., 2000; Nestola et al., 2011) that would otherwise be lost on opening the diamond; (c) crystallographic orientation relationships between the inclusion and its diamond host can provide constraints on its protogenetic *versus* syngenetic nature (Nestola et al., 2014); and (d) preservation of diamond surface growth features can provide information on late oxidation processes (Fedortchouk et al., 2011).

The so-called 'super deep' diamonds are those that are believed to have formed at depths of at least 300 km and some evidence suggests depths of at least 800 km

(Harte, 2010). A common mineral inclusion in these diamonds is ferropericlase, $(Mg,Fe^{2+})O$ (see Kaminsky, 2012 for an extensive review). Ferropericlase is the second most abundant mineral in the lower mantle, constituting up to about 20 mol% (660 to 2900 km depth). Bridgmanite, the dominant lower mantle phase and the Earth's most abundant mineral, has an affinity for ferric iron that is so profound that Fe^{3+}/Fe_{tot} is determined by bulk composition instead of oxygen fugacity. In contrast, Fe^{3+}/Fe_{tot} of ferropericlase is a strong function of oxygen fugacity (e.g., McCammon et al., 2004a) and provides a measure of the most recent redox conditions under which it equilibrated (Otsuka et al., 2013).

 Two methods have been used to determine Fe^{3+}/Fe_{tot} of ferropericlase inclusions in diamond. Mössbauer spectroscopy with a ^{57}Co point source was used to study inclusions down to 100 μm in diameter (McCammon et al., 1997; McCammon et al., 2004b), which is the limit using a radioactive point source (McCammon, 1994). Although the time required to collect Mössbauer spectra is long (at least one day per spectrum), the relative transparency of diamond to 14.4 keV gamma rays enables spectra of ferropericlase inclusions to be collected *in situ* through the diamond as demonstrated by McCammon et al. (1997). To measure Fe^{3+}/Fe_{tot} in smaller ferropericlase inclusions, Longo et al. (2011) calibrated the flank method for ferropericlase based on X-ray emission spectroscopy using the electron microprobe (Höfer and Brey, 2007 and references therein) and Kaminsky et al. (2015) applied the calibration to inclusions in diamonds from the Juina area, Brazil. Inclusions ranged in size between 20 and 50 μm, but had to be removed from the diamond prior to measurement due to the high absorption of electrons at the iron L-edge by diamond.

Results from Kaminsky et al. (2015) showed Fe^{3+}/Fe_{tot} values of 0.08-0.12 in ferropericlase inclusions, which are higher than values measured using Mössbauer spectroscopy for other ferropericlase inclusions from Juina diamonds (0.02-0.09) (McCammon et al., 1997). The difference can be attributed to the presence of exsolved Fe^{3+}-enriched clusters that were observed using a transmission electron microscope (TEM) (Kaminsky et al., 2015). The flank method measures the bulk value of Fe^{3+}/Fe_{tot} since it cannot distinguish between different phases, while Mössbauer spectroscopy records Fe^{3+}/Fe_{tot} for individual phases. The reason that these can be distinguished is because the sub-spectrum for exsolved Fe^{3+}-enriched clusters is magnetically ordered while the sub-spectrum for ferropericlase is not (see Longo et al., 2011). However, the signal to noise ratios of the Mössbauer spectra

collected by McCammon et al. (1997) were not sufficiently high to resolve the small amount of exsolved Fe^{3+}-enriched clusters due to the physical limitations of the point source; hence only Fe^{3+} in ferropericlase was detected and lower Fe^{3+}/Fe_{tot} values were obtained.

An ideal method to measure Fe^{3+}/Fe_{tot} values of ferropericlase would combine (1) the advantage of Mössbauer spectroscopy to distinguish Fe^{3+} in different phases and measure inclusions while still in the diamond, with (2) the advantage of the flank method to conduct rapid measurements with high spatial resolution. Indeed, electron energy loss spectroscopy using a TEM and X-ray Absorption Near Edge Structure spectroscopy using a synchrotron provides high spatial resolution and the latter has been applied to *in situ* measurements of ferropericlase inclusions, although for iron phase identification rather than oxidation state determination (Silversmit et al., 2011). The only method that offers the possibility to satisfy all of these requirements is the Synchrotron Mössbauer Source (SMS) (Smirnov et al., 1997; Potapkin et al., 2012). In this work we report development of a methodology to apply SMS to *in situ* determination of Fe^{3+}/Fe_{tot} in ferropericlase inclusions still contained within their diamonds.

7.3 Experimental approach

The diamond used in our study came from a suite of alluvial diamonds coming from São Luiz (Juina, Brazil). This locality is considered the main world locality of super-deep diamonds (see Pearson et al., 2014). A black tabular inclusion (referred to as "AZ2", Fig. 7.1) with dimensions of roughly 192 x 85 x 105 µm^3 was identified as ferropericlase by single-crystal X-ray diffraction (see the same experimental setup in Nestola et al., 2016). Based on the range of compositions reported for the Juina area (Fe# = Fe/(Mg+Fe) = 0.15 – 0.62) (Harte et al., 1999; Kaminsky, 2012), the dimensionless Mössbauer thickness of the inclusion lies between 4 and 13 (9 – 30 mg Fe/cm^2).

SMS spectra were collected at the Nuclear Resonance beamline ID18 (Rüffer and Chumakov, 1996) using the nuclear monochromator as described by Potapkin et al. (2012) at the European Synchrotron Radiation Facility, Grenoble. The SMS provides ^{57}Fe resonant radiation at 14.4 keV within a bandwidth of ~ 6 neV, which is tunable in energy over a range of about ± 0.6 µeV. In contrast to radioactive sources, the beam emitted by the SMS can be focused and it is fully resonant and up to 99%

polarized. SMS spectra were collected during operation in multibunch mode (7/8 + 1 filling) with the beam focused to a spot size of roughly 10×15 μm^2 using Kirkpatrick-Baez multilayer optics. The SMS linewidth was controlled before and after each sample measurement using $K_2Mg^{57}Fe(CN)_6$, whose Mössbauer spectrum consists of a single line, and the velocity scale was calibrated using 25 μm thick natural α-iron foil. Spectra at spots #1-#5 were collected for 90 min while the spectrum at spot #6 was collected for 7 h. All spectra were fitted using the program MossA with the full transmission integral and a Lorentzian-squared source line shape (Prescher et al., 2012).

Figure 7.1. Diamond containing ferropericlase inclusion AZ2 (indicated with a red circle).

To overcome the technical challenge of accurately locating the ferropericlase inclusion in the X-ray beam, we employed the same approach as that used at ID18 to locate small samples (< 50 μm diameter) in the diamond anvil cell (DAC). The set-up consists of a BX90 DAC (Kantor et al., 2012) mounted on the laser heating system platform in the experimental hutch, but no pressure or temperature is applied during sample alignment. The experimental procedure is as follows:

(1)   The diamond with the selected inclusion is attached on the tungsten carbide seat using plasticine and superglue such that the inclusion is centered over the ~ 1 mm diameter hole in the seat (Fig. 7.2).
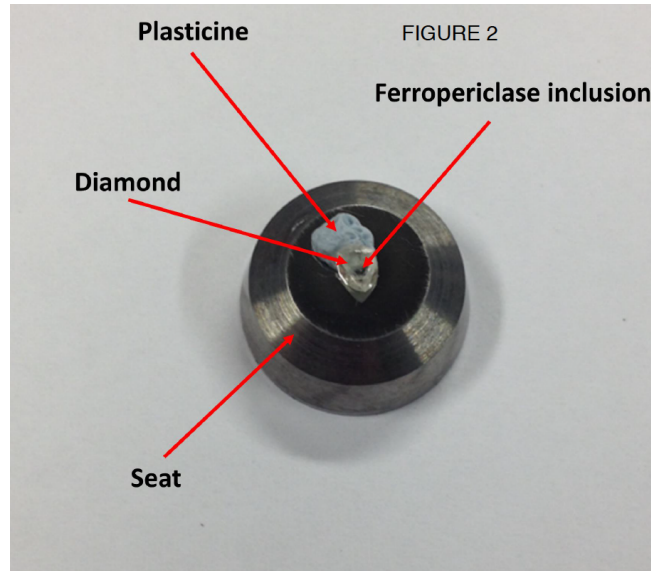
Figure 7.2. Tungsten carbide seat with the diamond centered over a ~ 1 mm diameter hole in the seat.

(2)   A Re gasket with thickness ranging from 30-100 μm and a hole of 300 μm diameter is carefully glued on the upper surface of the diamond such that the inclusion is centered in the gasket hole (Fig. 7.3).
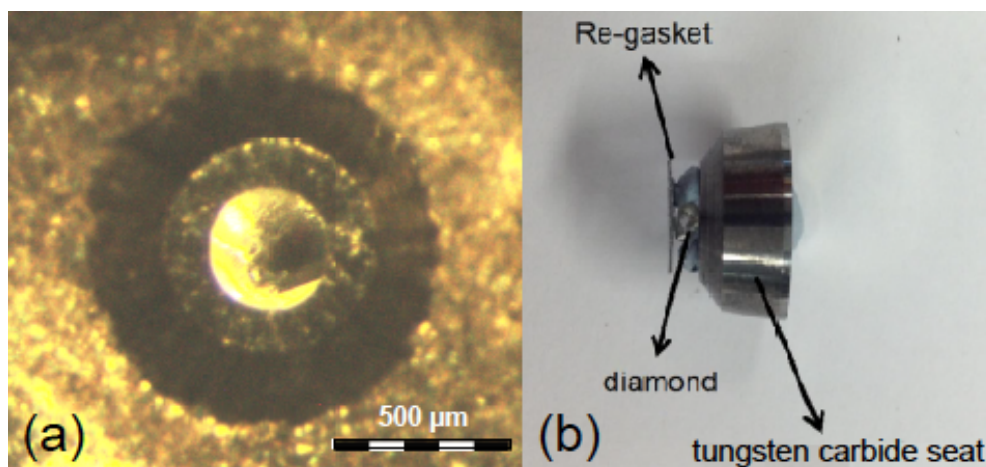
Figure 7.3. (a) Magnified image of inclusion AZ2 visible through the hole in the Re gasket; (b) Side view of the seat-diamond-gasket assembly.

(3)   The seat-diamond-gasket assembly is mounted on the lower half of the DAC (Fig. 7.4a), which is then placed in the DAC holder (Fig. 7.4b) and attached to a platform on a moveable table connected to high-precision motors (1 μm step) inside the experimental hutch (Fig. 7.5).
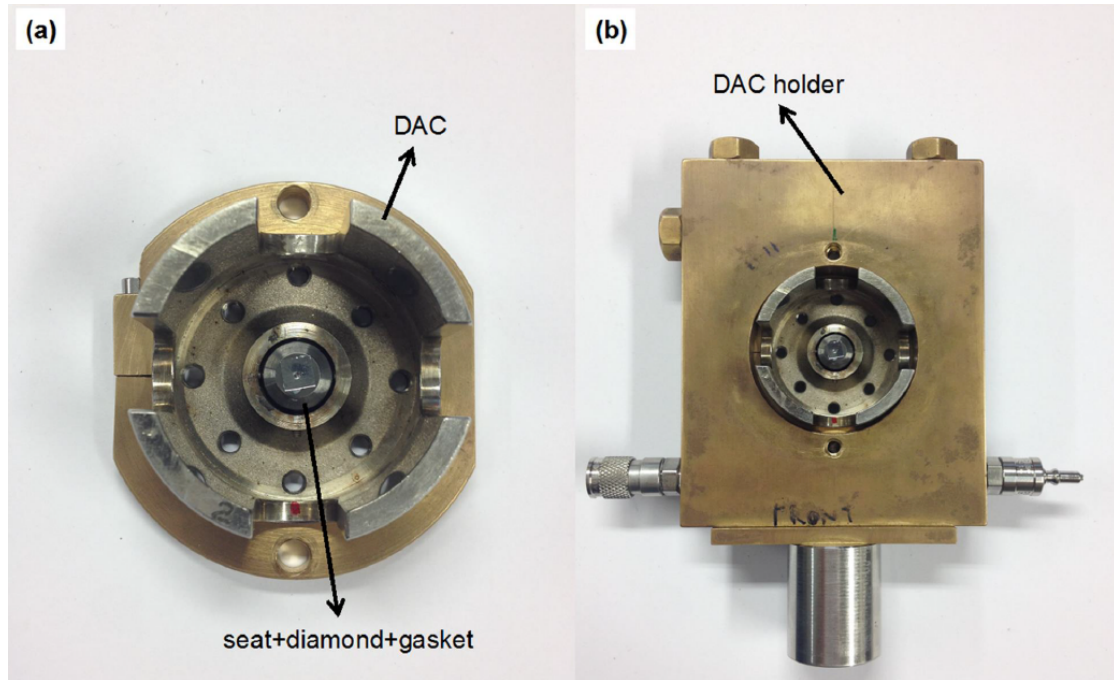
Figure 7.4. (a) Seat-diamond-gasket assembly attached to the bottom part of a BX90 DAC that is mounted inside a metallic ring; (b) DAC mounted on the DAC holder.

(4)   From the control cabin with the X-ray shutter open, the signal of the avalanche photodiode (APD) detector positioned roughly 1 m behind the sample is monitored as the table is moved in horizontal (y) and vertical directions (z). A maximum occurs when the X-rays pass through the gasket hole to reach the detector.

(5)   Once the inclusion has been located in the X-ray beam, absorption profiles are recorded and the DAC is moved to different positions so that different regions of the inclusion can be analyzed (Fig. 7.6). In this way the inclusion can be mapped without the use of an optical system.
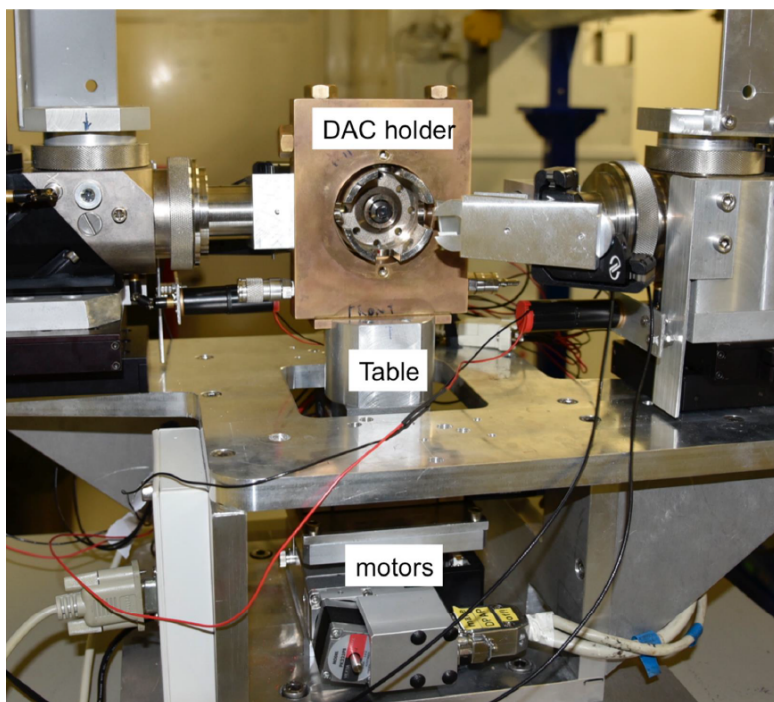
Figure 7.5. DAC holder mounted on the laser heating platform inside the experimental hutch at beamline ID18. The table is moved by piezo motors in the three directions x, y, z, with a step precision of 1 μm. The optics belonging to the double-sided laser heating system are visible on either side of the DAC. While the setup is normally used for high-pressure high-temperature DAC experiments, for this purpose only the positioning stage is needed.

Figure 7.6. Line profiles of the APD detector signal from inclusion AZ2 in the horizontal (top) and vertical (bottom) directions. The maxima correspond to the region in the gasket hole where there is no inclusion (Fig. 7.3a) and the relatively flat regions with non-zero counts adjacent to the maxima are from the inclusion. The widths indicate the approximate dimensions of the inclusion (150 × 150 μm^2) and the gasket hole (~ 300 μm diameter). The positions where the SMS spectra were collected are indicated with stars.
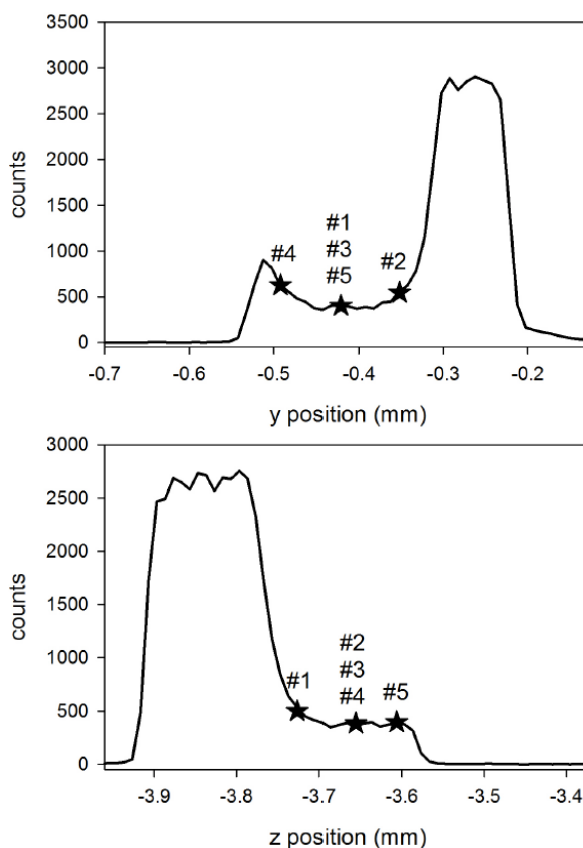
7.4. Results and discussion

Mössbauer spectra collected from spots #1-#5 are dominated by a broad quadrupole doublet (Fig. 7.7). Qualitatively they look similar to spectra collected from ferropericlase inclusions in diamond using a radioactive source (McCammon et al., 1997; McCammon et al., 2004b), but there are important differences. The SMS spectra have a significantly larger absorption (~70%) compared to radioactive source spectra (< 1%) due to the lower background of the SMS, leading to a much higher signal to noise ratio despite the much shorter collection time for SMS spectra (radioactive source spectra of ferropericlase inclusions take several days to collect). In addition, SMS spectra probe individual regions of ~ 15 μm diameter while radioactive source spectra provide only an average measurement of the entire ferropericlase inclusion (> 100 μm diameter).
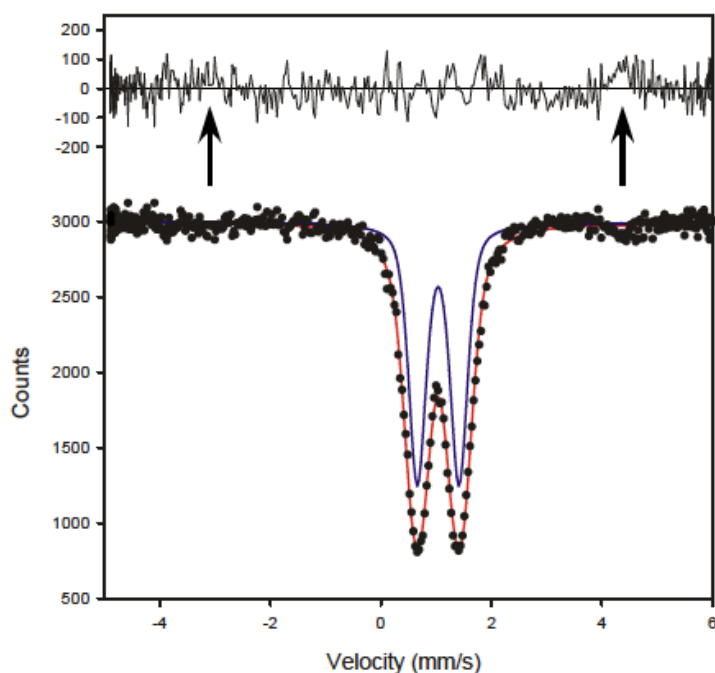
Figure 7.7. Room temperature SMS spectrum of spot #5 on ferropericlase inclusion AZ2. Solid circles: experimental data; red line: full transmission integral fit. A single quadrupole doublet was fit to the spectrum (blue line), but note that it does not add up to the total spectrum due to the properties of the full transmission integral fit. The arrows indicate regions in the residual where there are positive deviations over multiple adjacent channels, suggesting the presence of absorption due to magnetic hyperfine splitting.

SMS spectra collected from spots #1-#5 were fitted to a single Fe^{2+} quadrupole doublet with Voigt lineshape according to previous models (e.g., Longo et al., 2011) (Table 7.1). Trials were conducted to test the addition of a quadrupole doublet corresponding to Fe^{3+}, but the presence of the doublet was not statistically significant in all cases. From these trials the detection limit for Fe^{3+}/Fe_{tot} in ferropericlase was estimated to be 0.02. However, there was evidence in all SMS spectra for deviations in the residual near -3 and 4.5 mm/s to varying degrees, suggesting the presence of a magnetically ordered component. Accordingly, the velocity scale was expanded and the X-ray beam was moved back to the vicinity of spot #5 where a new spectrum was collected over a longer period of time (spot #6).

The SMS spectrum from spot #6 shows clear evidence for absorption arising from magnetic hyperfine splitting (Fig. 7.8). We therefore added a magnetic sextet with the usual constraints (equal component widths and area ratios between the outer and inner components fixed to 3) but allowed all other parameters to vary. We then refit the original spectra from spots #1-#5 with the addition of a magnetic sextet where all parameters except area were fixed to the values from the spot #6 spectrum. All spots show the presence of the magnetic component at varying levels above experimental uncertainty (Table 7.1), and correlation of amounts with their estimated positions on the inclusion based on the absorption profiles (Fig. 7.6) reveal that the magnetic component abundance is highest in the centre and left region of the inclusion (Fig. 7.9).

The hyperfine parameters provide information about the magnetic component. The centre shift and magnetic hyperfine field (Table 7.1) are indicative of Fe^{3+} and fall close to values for synthetic $MgFe_2O_4$ (averaged CS = 0.32 mm/s relative to α-Fe, averaged BHF = 48 T; De Grave et al. 1979) and Fe_3O_4 (averaged CS = 0.49 mm/s relative to α-Fe, averaged BHF = 47 T; Häggström et al., 1978) as well as solid solutions in between (O'Neill et al., 1992). The hyperfine magnetic field is close to saturated and there is no evidence for superparamagnetism within the uncertainty of the data, where a superparamagnetic component would appear as a narrow line with the same centre shift as the magnetic component.

The absence of superparamagnetism provides information about the minimum particle size of the magnetic phase. Gonser et al. (1968) precipitated magnesioferrite by annealing synthetic ferropericlase in air, and Mössbauer spectra showed clear evidence for superparamagnetism. The amount decreased as annealing time increased,

and they calculated the average size of the precipitates based on the temperature dependent behavior of the Mössbauer spectra. Room temperature spectra showed nearly complete superparamagnetism for an average particle diameter of 8 nm, while 20 nm particles were transitional between superparamagnetic and ferrimagnetic. A simple extension of their results based on magnetic relaxation time (their Eq. 3) indicates that magnesioferrite precipitates of 30 nm diameter would give a fully ordered magnetic Mössbauer spectrum at room temperature. This result is consistent with data presented by Longo et al. (2011), where TEM images showed magnesioferrite impurities in synthetic ferropericlase of at least 40 nm in size and Mössbauer spectra showed a magnetically ordered component.
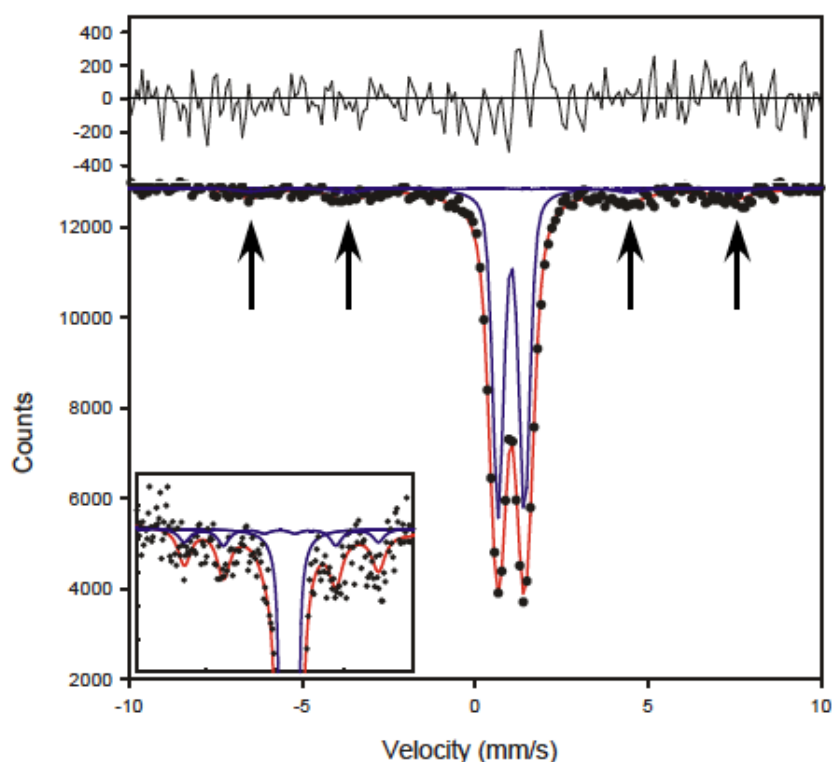
Figure 7.8. Room temperature SMS spectrum of spot #6 on ferropericlase inclusion AZ2 collected over a large velocity range. The position of spot #6 is close to spot #5. The spectrum was fitted to one quadrupole doublet and one magnetic sextet where the symbols and lines are the same as in Figure 7.7. The arrows indicate the positions of four peaks of the magnetic sextet, which can be seen more clearly in the inset that shows a magnified view near the baseline.

Previous TEM studies of ferropericlase inclusions in diamond show varying sizes of magnesioferrite precipitates. Both Harte et al. (1999) and Wirth et al. (2014) report features that exceed 100 nm in size and reach up to 3 μm long, while Kaminsky et al. (2015) report much smaller Fe^{3+}-rich regions that are less than 20 nm in size and as small as 1-2 nm. Results from the present study show a magnetic phase that is significantly larger than those observed by Kaminsky et al. (2015) in diamonds from kimberlite pipes in the same area (Juina, Brazil). Differences in size can be related to many parameters, including composition, oxygen fugacity and thermal history. While the TEM studies required removal of the inclusion from the diamond, the SMS approach provided constraints on the size of magnetic particles with the ferropericlase still in the diamond, keeping open the possibilities for further investigation using *in situ* techniques to elucidate its history.
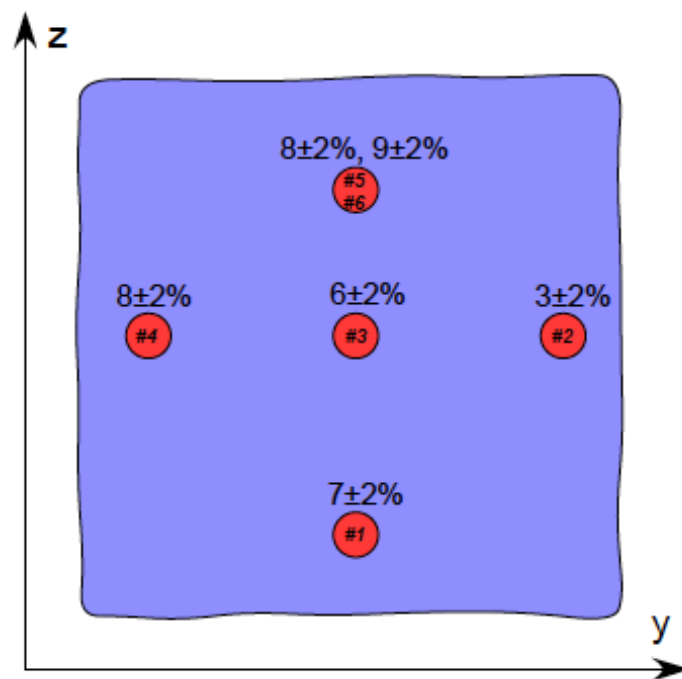
Figure 7.9. Sketch of AZ2 ferropericlase inclusion. SMS spectra were collected at the red circles, where their size (~ 15 μm diameter) is scaled relative to the dimensions of the inclusion (150 × 150 μm^2). The spots (indicated by numbers) correspond to those in Figure 7.6 and Table 7.1. Each spot is labelled with the relative area of the magnetic component measured at that position.

Bulk ferropericlase Fe^{3+}/Fe_{tot} ratios can be calculated based on the relative areas in SMS spectra assuming that the magnetic phase is endmember $MgFe_2O_4$ (Table 7.1). These ratios can be directly compared with values from bulk techniques such as the flank method that cannot distinguish between Fe^{3+} in different phases, and show a similar range to other ferropericlase inclusions from other Juina diamonds (Kaminsky et al., 2015). The different Fe^{3+}/Fe_{tot} values observed in different regions of the AZ2 inclusion are a remarkable feature that provides potential information on the history of the inclusion, for example thermal or redox gradients that influenced magnesioferrite exsolution. The amount of the magnetic phase present in the different regions of the ferropericlase inclusion can be determined from the relative areas of the Mössbauer spectra based on the estimated iron concentration in each phase. Assuming endmember magnesioferrite and an iron-poor ferropericlase composition (Fe# = 0.15), the volume fractions range between 0.5 and 2% for the different regions, while for an iron-rich composition (Fe# = 0.6) the range is 2 to 7%. The accuracy of these values can be improved by *in situ* determination of composition, for example using X-ray diffraction (Nestola et al., 2011).

Table 7.1 Hyperfine parameters derived from room temperature SMS spectra of AZ2 ferropericlase inclusion

location	component	CS[a] mm/s	QS[b] mm/s	Area %	Linewidth[c] mm/s	BHF[d] T	Fe^{3+}/Fe_{tot} bulk
spot #1	Fe^{2+}	1.04(1)	0.76(1)	93(2)	0.39(1)	-	0.07(2)
	mag	*0.43*	*0.12*	7(2)	*1*	*43*	
spot #2	Fe^{2+}	1.04(1)	0.75(1)	97(2)	0.38(1)	-	0.03(2)
	mag	*0.43*	*0.12*	3(2)	*1*	*43*	
spot #3	Fe^{2+}	1.04(1)	0.75(1)	94(2)	0.37(1)	-	0.06(2)
	mag	*0.43*	*0.12*	6(2)	*1*	*43*	
spot #4	Fe^{2+}	1.04(1)	0.76(1)	92(2)	0.38(1)	-	0.08(2)
	mag	*0.43*	*0.12*	8(2)	*1*	*43*	
spot #5	Fe^{2+}	1.04(1)	0.76(1)	92(2)	0.37(2)	-	0.08(2)
	mag	*0.43*	*0.12*	8(2)	*1*	*43*	
spot #6	Fe^{2+}	1.05(1)	0.77(1)	91(2)	0.38(2)	-	0.09(2)
	mag	0.43(12)	0.12(23)	9(2)	1.0(3)	43(5)	

Notes: values in italics were fixed during the fitting process
[a] CS: center shift relative to α-Fe
[b]: QS: quadrupole splitting
[c]: Linewidth: full widtch at half maximum (including source linewidth)
[d]: BHF: magnetic hyperfine field ("magnetic sextet")

7.5. Conclusions

We summarize our work as follows:

1)   We described a new technique to collect Mössbauer spectra of inclusions in natural diamonds that does not require breaking open the diamond. The technique uses the recently developed Synchrotron Mössbauer Source and yields high quality spectra with low background and high spatial resolution ($\sim$ 15 μm) that can be collected in a few hours or less.

2)   We collected SMS spectra at five different positions on a 150×150 μm^2 ferropericlase inclusion that showed low Fe^{3+}/Fe_{tot} overall (< 0.02) but the presence of a magnetic component whose abundance varied systematically across the inclusion.

3)   The well saturated hyperfine magnetic field rules out superparamagnetism and allowed the minimum particle size of the magnetic phase to be estimated as $\sim$ 30 nm.

4)   Bulk Fe^{3+}/Fe_{tot} values fall within the range observed for other ferropericlase inclusions in diamond reported in the literature and their variation across the inclusion provides potential constraints on the history of the inclusion.

This new experimental technique can be easily applied to investigate other iron-bearing inclusions in natural diamond. The wealth of information provided by Mössbauer spectroscopy opens a new possibility to obtain fundamental information on the Earth's interior.

7.6 Acknowledgments

7.7 References

Alvaro, M., Nestola, F., Boffa Ballaran, T., Camara, F., Domeneghetti, M.C., Tazzoli, V., 2010. High-pressure phase transition of a natural pigeonite. American Mineralogist 95, 300-311.

De Grave, E., Govaert, A., Chambaere, D., Robbrecht, G., 1979. Mössbauer effect study of $MgFe_2O_4$. Physica 96B, 103-110.

Gonser, U., Wiedersich, H., Grant, R.W., 1968. Mössbauer studies on the superparamagnetic behavior of magnesioferrite precipitates. Journal of Applied Physics 39, 1004-1005.

Fedortchouk, Y., Manghnani, M.H., Hushur, A., Shiryaev, A., Nestola, F., 2011. An atomic force microscopy study of diamond dissolution features: The effect of H2O and CO2 in the fluid on diamond morphology. American Mineralogist 96, 1768-1775.

Häggström, L., Annersten, H., Ericsson, T., Wäppling, R., Karner, W., Bjarman, S., 1978. Magnetic dipolar and electric quadrupolar effects on the Mössbauer spectra of magnetite above the Verwey transition. Hyperfine Interactions 5, 201-214.

Harte, B., Harris, J.W., Hutchison, M.T., Watt, G.R., Wilding, M.C., 1999. Lowe Mantle mineral associations in diamonds from São Luiz, Brazil. In Mantle Petrology; Field Observations and High Pressure Experimentation: A tribute to Francis R. (Joe) Boyd. Editors: Fei, Y., Bertka, C. M. and Mysen, B.O. pp. 125-153. The Geochemical Society, Special Publication No. 6.

Harte, B., 2010. Diamond formation in the deep mantle: the record of mineral inclusions and their distribution in relation to mantle dehydration zones. Mineralogical Magazine 74, 189-215.

Höfer, H.E., Brey, G., 2007. The iron oxidation state of garnet by electron microprobe: its determination with the flank method combined with major-elements analysis. American Mineralogist 92, 873-885.

Jacobsen, S.D., Reichmann, H.J., Spetzler, H.A., Mackwell, S.J., Smyth, J.R., Angel, R.J., McCammon, C.A., 2002. Structure and elasticity of single-crystal (Mg,Fe)O and a new method of generating shear waves for gigahertz ultrasonic interferometry. Journal of Geophysical Research 107, 2037.

Kaminsky, F., 2012. Mineralogy of the lower mantle: A review of 'super-deep' mineral inclusions in diamond. Earth-Science Reviews 110, 127–147.

Kaminsky, F.V., Wirth, R., Schreiber, A., 2015a. A microinclusion of lower-mantle rock and other minerals and nitrogen lower-mantle inclusions in a diamond. Canadian Mineralogist 53, 83-104.

Kaminsky, F.V., Ryabchikov, I.D., McCammon, C.A., Longo, M., Abakumov, A.M., Turner, S., Heidari, H., 2015b. Oxidation potential in the Earth's lower mantle as recorded by ferropericlase inclusions in diamond. Earth and Planetary Science Letters 417, 49-56.

Kantor, I. Yu., Prakapenka, V., Kantor, A., Dera, P., Kurnosov, A., Sinogeikin, S., Dubrovinskaia, N., Dubrovinsky, L., 2012. BX90: A new diamond anvil cell design for X-ray diffraction and optical measurements. Review of Scientific Instruments 83, 125102.

Longo, M., McCammon, C.A., Jacobsen, S.D., 2011. Microanalysis of the iron oxidation state in (Mg,Fe)O and application to the study of microscale processes. Contributions to Mineralogy and Petrology 162, 1249-1257.

McCammon, C.A., 1994. A Mössbauer milliprobe: Practical considerations. Hyperfine Interactions 92, 1235-1239.

McCammon, C.A., Hutchison, M.T., Harris, J.W., 1997. Ferric iron content of mineral inclusions in diamonds from São Luiz: a view into the lower mantle. Science 278, 434-436.

McCammon, C.A., Lauterbach, S., Seifert, F., Langenhorst, F., van Aken, P.A., 2004a. Iron oxidation state in lower mantle mineral assemblages I. Empirical relations derived from high-pressure experiments. Earth and Planetary Science Letters 222, 435-449.

McCammon, C.A., Stachel, T., Harris, J.W., 2004b. Iron oxidation state in lower mantle mineral assemblages: II. Inclusions in diamonds from Kankan, Guinea. Earth and Planetary Science Letters 222, 423-434.

Nestola, F., Smyth J.R., 2016. Diamonds and water in the deep Earth: a new scenario. International Geology Review 58, 263-276.

Nestola, F., Nimis, P., Angel, R., Milani, S., Bruno, M., Prencipe, M., Harris, J., 2014. Olivine with diamond-imposed morphology included in diamonds. Syngenesis or protogenesis? International Geology Review 56, 1658-1667.

Nestola, F., Burnham, A.D., Peruzzo, L., Tauro, L., Alvaro, M.,Walter, M.J., Gunter, M., Kohn, S.C. (2016) Tetragonal Almandine-Pyrope Phase, TAPP: finally a name for it, the new mineral jeffbenite. Mineralogical Magazine, doi: 10.1180/minmag.2016.080.059.

Nestola, F., Nimis, P., Ziberna, L., Longo, M., Marzoli, A., Harris, J.W., Manghnani, M.H., Fedortchouk, Y., 2011. First crystal-structure determination of olivine in diamond: Composition and implications for provenance in the Earth's mantle. Earth and Planetary Science Letters 305, 249-255.

O'Neill, H.S.C., Annersten, H., Virgo, D., 1992. The temperature dependence of the cation distribution in magnesioferrite ($MgFe_2O_4$) from powder XRD structural refinements and Mössbauer spectroscopy. American Mineralogist 77, 725-740.

Otsuka, K., Longo, M., McCammon, C.A., Karato, S. (2013) Ferric iron content of ferropericlase as a function of composition, oxygen fugacity, temperature and pressure: Implications for redox conditions during diamond formation in the lower mantle. Earth and Planetary Science Letters 365, 7-16.

Palot, M., Jacobsen, S.D., Townsend, J.P., Nestola, F., Marquardt, K., Harris, J.W., Stachel, T., McCammon, C.A., Pearson, D.G., 2016. Evidence for water in the lower mantle from ferropericlase included in diamond. Nature Geoscience, submitted.

Pearson, D.G., Brenker, F., Nestola, F., McNeill, J., Nasdala, L., Hutchison, M.T., Matveev, S., Mather, K., Silversmit, G., Schmitz, S., Vekemans, B., Vincze, L., 2014. A hydrous mantle transition zone indicated by ringwoodite included within diamond. Nature 507, 221–224.

Potapkin, V., Chumakov, A.I., Smirnov, G.V., Celse, J.P., Rüffer, R., McCammon, C., Dubrovinsky, L., 2012. The ^{57}Fe Synchrotron Mössbauer Source at the ESRF. Journal of Synchrotron Radiation 19, 559-569.

Prescher, C., McCammon, C., Dubrovinsky, L., 2012. MossA - a program for analyzing energy-domain Mossbauer spectra from conventional and synchrotron sources. Journal of Applied Crystallography 45, 329-331.

Richardson, S.H., Harris, J.W., 1997. Antiquity of peridotitic diamonds from the Siberian craton. Earth and Planetary Science Letters 151, 271–277.

Rüffer, R., Chumakov, A.I., 1996. Nuclear-resonance beamline at ESRF. Hyperfine Interactions 97-8, 589-604.

Shirey, S.B., Cartigny, P., Frost, D.J., Keshav, S., Nestola, F., Nimis, P., Pearson, D.G., Sobolev, N.V., Walter, M.J., 2013. Diamonds and the geology of mantle carbon. Reviews in Mineralogy and Geochemistry 75, 355-421.

Silversmit, G., Vekemans, B., Appel, K., Schmitz, S., Schoonjans, T., Brenker, F.E., Kaminsky, F., Vincze, L., 2011. Three-dimensional Fe speciation of an inclusion cloud within an ultradeep diamond by confocal µ-X-ray Absorption Near Edge Structure: evidence for late stage overprint. Analytical Chemistry 83, 6294-6299.

Smirnov, G.V., van Bürck, U., Chumakov, A.I., Baron, A.Q.R., Rüffer, R., 1997. Synchrotron Mössbauer source. Physical Review B 55, 5811-5815.

Sobolev, N.V., Fursenko, B.A., Goryainov, S.V., Shu, J., Hemley, R.J., Mao, A., Boyd, F.R., 2000. Fossilized high pressure from the Earth's deep interior: the coesite-

in-diamond barometer. Proceedings of the National Academy of Sciences of the United States of America 97, 11875-11879.

Stachel, T., Harris, J.W., 2008. The origin of cratonic diamonds—constraints from mineral inclusions. Ore Geology Review 34, 5–32.

Walter, M.J., Kohn, S.C., Araujo, D., Bulanova, G.P., Smith, C.B., Gaillou, E., Wang, J., Steele, A., Shirey, S.B., 2011. Deep mantle cycling of oceanic crust: evidence from diamonds and their mineral inclusions. Science 334, 54-57.

8. References

Abe, Y. (1997) Thermal and chemical evolution of the terrestrial magma ocean. Phys. Earth Planet. Inter., 100, 27-39.

Akahama, Y., Kawamura, H., (2006). Pressure calibration of diamond anvil Raman gauge to 310 GPa. J. Appl. Phys. 100, 043516.

Alexander, C.M.O'D. (2005) Re-examining the role of chondrules in producing the volatile element fractionations in chondrites. Meteorit. Planet Sci., 40, 943-965.

Alt et al. (2013) The role of serpentinites in cycling of carbon and sulfur: Seafloor serpentinization and subduction metamorphism. Lithos, 178, 40-54.

Alt et al. (2012) Recycling of water, carbon, and sulfur during subduction of serpentinites: A stable isotope study of Cerro del Almirex, Spain. Earth Planet Sci Lett, 327-328, 50-60.

Alvaro, M., Nestola, F., Boffa Ballaran, T., Camara, F., Domeneghetti, M.C., Tazzoli, V. (2010). High-pressure phase transition of a natural pigeonite. American Mineralogist 95, 300-311.

Anders, E., and Grevesse, N. (1989) Abundances of the elements: meteoritic and solar. Geochim. Cosmochim. Acta, 53, 197-214.

Aquilani, G., Trapananti, A., Karandikar, A., Kantor, I., Marini, C., Mathon, O., Pascarelli, S., and Boehler, R. (2015) Melting of iron determined by X-ray absorption spectroscopy to 100 GPa. PNAS, 112, 12042–12045.

Bebout, G.E. (2014) Metamorphic chemical geodynamics of subduction zones. Earth Planet. Sci. Lett., 260, 373–393.

Becker, H., and Altherr, R. (1996) Evidence from ultra-high-pressure marbles for recycling of sediments into the mantle. Nature, 358, 745-748.

Bianconi, A., Dell'Ariccia, M., Gargano, A., and Natoli, C.R. (1983) Bond length determination using XANES. In A. Bianconi, L. Incoccia, and S. Stilpcich, Eds., EXAFS and Near Edge Structure, 27, p. 57-61. Springer Series in Chemistry and Physics, Berlin.

Biellmann, C., Gillet, P., Guyot, F., Peyronneau, J., and Reynard, B. (1993) Experimental evidence for carbonate stability in the Earth's lower mantle. Earth and Planetary Science Letters, 118, 31-41.

Bina, C.R. and Helffrich, G. (1994) Phase transition Clapeyron slopes and transition zone seismic discontinuity topography. JGR, 99, 853-860.

Bouibes, A., & Zaoui A. (2014) High-pressure polymorphs of $ZnCO_3$: Evolutionary crystal structure prediction. Sci. Rep., 4, 5172.

Boulard et al. (2011) New host for carbon in the deep Earth. PNAS, 108, 5184-5187.

Boulard, E., Menguy, N., Auzende, A.L., Benzerara, K., Bureau, H., Antonangeli, D., Corgne, A., Morard, G., Siebert, J., Perrillat, J.P., Guyot, F., and Fiquet, G. (2012) Experimental investigation of the stability of Fe-rich carbonates in the lower mantle. Journal of Geophysical Research, 117, B02208.

Boulard, E., Pan, D., Galli, G., Liu, Z., and Mao, W. (2015) Tetrahedrally coordinated carbonates in Earth's lower mantle. Nat. Commun., 6, 631.

Bradley, J.P. (2003) Interplanetary dust particles. In: Treatise on Geochemistry. Meteorites, Comets and Planets. Davis AM (ed) Elsevier-Pergamon, Oxford, 689-712.

Bragg, W.L. (1913) The Structure of Some Crystals as Indicated by Their Diffraction of X-Rays. Proc. R. Soc. London 89, 248.

Brenker, F.E., Vollmer, C., Vincze, L., Vekemans, B., Szymansky, A., Janssens, K., Szaloki, I., Nasdala, L., Joswig, W., and Kaminsky, F. (2007) Carbonates from the

lower part of the transition zone or even the lower mantle. Earth and Planetary Science Letters, 260, 1-9.

Bunau, O., and Joly, Y. (2009) Self-consistent aspects of x-ray absorption calculations. J. Phys. Condens. Matter, 21, 34.

Bunker, G. (2010) Introduction to XAFS: A Practical Guide to X-Ray Absorption Fine Structure Spectroscopy. Cambridge University Press, United Kingdom.

Burbidge, E.M., Burbidge, G.M., and Fowler, G.M. (1975) Synthesis of the elements in the star. Rev. Modern. Phys, 29, 547-650.

Burns, R.G., 1993. Mineralogical applications of crystal field theory. Cambridge University Press, Cambridge, UK.

Bykova, E. *et al.* (2016) Structural complexity of simple Fe_2O_3 at high pressures and temperatures. Nat. Commun., 7, 10661.

Caliebe, W.A., Kao, C.C., Hastings, J.B., Taguchi, M., Kotani, A., Uozumi, T., and de Groot, F.M.F. (1998) 1s2p resonant inelastic x-ray scattering in γ-Fe_2O_3. Physical Review B, 58, 13452-13458.

Cerantola, V., Walte, N., and Rubie D.C. (2015a) Deformation of a crystalline olivine aggregate containing two immiscible liquids: Implications for early core–mantle differentiation. Earth Planet Sci Lett, 417, 67-77.

Cerantola et al. (2015b) High-pressure spectroscopic study of siderite ($FeCO_3$) with focus on spin crossover. Am. Min., 100, 2670-2681.

Cerantola et al. (2017) Stability of iron-bearing carbonates in the deep Earth's interior. Nat. Commun. 8**,** 15960 doi: 10.1038/ncomms15960.

Chandra Shekar, N.V., Sahu, P.C., and Govinda Rajan, K. (2003) Laser-heated diamond-anvil cell (LHDAC) in Material Science Research. J. Mater. Sci. Technol. 6, 518-525.

Chang, S-J., Ferreira A.MG. and Faccenda, M. (2016) Upper- and mid-mantle interaction between the Samoan plume and the Tonga–Kermadec slabs. Nat. Commun., 7, 10799.

Christensen, U.R. (1996) The influence of trench migration on slab penetration into the lower mantle. Earth Planet. Sci. Lett, 140, 27-39.

CrysAlisPro Software system. Version 1.171.37.35. (Agilent Technologies UK Ltd., Oxford, UK, 2014)

Dahl, T.W., and Stevenson, D.J. (2010) Turbulent mixing of metal and silicate during planet accretion – And interpretation of the Hf-W chronometer. Earth Planet Sci Lett, 295, 177-186.

Dalton, J.A., and Presnall, D.C. (1998) The Continuum of Primary Carbonatitic–Kimberlitic Melt Compositions in Equilibrium with Lherzolite: Data from the System $CaO–MgO–Al_2O_3–SiO_2–CO_2$ at 6 GPa. J. Petrology, 39, 1953-1964.

Dasgupta, R., and Hirchmann, M.M. (2006) Melting in the Earth's deep upper mantle caused by carbon dioxide. Nature, 440, 659-662.

Dasgupta, R., and Hirschmann, M.M. (2010) The deep carbon cycle and melting in Earth's interior. Earth and Planetary Science Letters, 298, 1-13.

Dasgupta, R., Chi, H., Shimizu, N., Buono, A., and Walker, D. (2013a) Carbon solution and partitioning between metallic and silicate melts in a shallow magma ocean: implications for the origin and distribution of terrestrial carbon. Geochim Cosmochim Acta, 102, 191-212.

Dasgupta, R. (2013b) Ingassing, Storage, and Outgassing of Terrestrial Carbon through Geologic Time. Rev. Mineral. Geochem., 75, 183-229.

Dasgupta, R., and Walker, D. (2008) Carbon solubility in core melts in a shallow magma ocean environment and distribution of carbon between the Earth's core and the mantle. Geochim Cosmochim Acta, 72, 4627-4641.

Dasgupta, R., Hirchmann, M.M., McDonough W.F., Spiegelman, M., and Withers, A.C. (2009) Trace element partitioning between garnet lherzolite and carbonatite at 6.6 and 8.6 GPa with applications to the geochemistry of the mantle and of mantle-derived melts. Chem Geol, 262, 57-77.

Dauphas, N. (2003) The dual origin of the terrestrial atmosphere. Icarus, 165, 326-339.

Dauphas, N., and Pourmand, A. (2011) Hf-W-Th evidence for rapid growth of Mars and its status as a planetary embryo. Nature, 473, 489-492.

De Grave, E., Govaert, A., Chambaere, D., Robbrecht, G. (1979). Mössbauer effect study of $MgFe_2O_4$. Physica 96B, 103-110.

Dewaele, A., Datchi, F., Loubeyre, P., & Mezouar, M. (2008) High pressure–high temperature equations of state of neon and diamond. PRB, 77, 094106

Dubrovinsky, L.S. *et al.* (2003) The structure of the metallic high-pressure Fe_3O_4 polymorph: experimental and theoretical study. JPCM, 15, 45.

Dubrovinsky, L., and Dubrovinskaia, N. (2004) Angle-dispersive diffraction under non-hydrostatic stress in diamond anvil cells. Journal of Alloys and Compounds, 375, 86-92.

Dubrovinsky et al. (2015) The most incompressible metal osmium at static pressures above 750 gigapascals. Nature, 525, 226-229.

Farfan, G., Wang, S., Ma, H., Caracas, R., and Mao, W.L. Bonding and structural changes in siderite at high pressure (2012). American Mineralogist, 97, 1421-1427.

Fedortchouk, Y., Manghnani, M.H., Hushur, A., Shiryaev, A., Nestola, F. (2011). An atomic force microscopy study of diamond dissolution features: The effect of H2O and CO2 in the fluid on diamond morphology. American Mineralogist 96, 1768-1775.

Fei, Y. *et al*. (2007) Toward an internally consistent pressure scale. PNAS, 104, 9182.

Fiquet, G., and Reynard, B. (1999) High-pressure equation of state of magnesite: New data and a reappraisal. American Mineralogist, 84, 856-860.

Franzolin, E., Schmidt, M.W., and Poli, S. (2011) Ternary Ca-Fe-Mg carbonates: subsolidus phase relations at 3.5 GPa and a thermodynamic solid solution model including order/disorder. Contributions to Mineralogy and Petrology, 161, 213-227.

French, B.M. (1971) Stability relations of siderite ($FeCO_3$) in the system Fe-C-O. American Journal of Science, 27, pp. 37 -78.

Frost, D.J., and McCammon, C. (2008) The redox State of Earth's Mantle. Annual Rev Earth Planet Sci, 36, 389-420.

Fukao, Y., Obayashi, M., and Nakakuki, T. (2009) Stagnant Slab: A Review. Annual Review of Earth and Planetary Science, 37, 19.

Gerbode, C., and Dasgupta, R. (2010) Carbonate-fluxed melting of MORB-like pyroxenite at 2.9 GPa and genesis of HIMU ocean island basalt. J Petrol, 51, 2067-2088.

Goldsmith, J.R., Graf, D.L., Witters, J., and Northrop, D.A. (1962) Dolomite-Magnesian calcite relations at elevated temperature and CO_2 pressures. *Geochimica* et *Cosmochimica Acta*, 7(3-4), 109-128.

Gonser, U., Wiedersich, H., Grant, R.W., 1968. Mössbauer studies on the superparamagnetic behavior of magnesioferrite precipitates. Journal of Applied Physics 39, 1004-1005.

Gorman, P.J., Kerrick, D.M., Connolly, J.A.D. (2006) Modeling open system metamorphic decarbonation of subducting slabs. Geochem Geophys Geosyst, 7, Q04007.

Gütlich, P. (1978) Mössbauer spectroscopy and transition metal chemistry. Berlin, Heidelberg: Springer-Verlag.

Greenberg, J.M. (1998) Making a comet nucleus. Astron. Astrophys, 330, 375-380.

Häggström, L., Annersten, H., Ericsson, T., Wäppling, R., Karner, W., Bjarman, S. (1978). Magnetic dipolar and electric quadrupolar effects on the Mössbauer spectra of magnetite above the Verwey transition. Hyperfine Interactions 5, 201-214.

Halliday, A.N. (2004) Mixing, volatile loss and compositional change during impact-driven accretion of the Earth. Nature, 427, 505-509.

Halliday, A.N. (2008) A young Moon-forming giant impact at 70-110 million years accompanied by late-stage mixing, core formation and degassing of the Earth. Phil Trans Royal Soc, 366, 4163-4181.

Hammersley, A.P. (1997) FIT2D: An Introduction and Overview. ESRF Internal Report ESRF Internal Report, ESRF97HA02T.

Harte, B., Harris, J.W., Hutchison, M.T., Watt, G.R., Wilding, M.C. (1999). Lowe Mantle mineral associations in diamonds from São Luiz, Brazil. In Mantle Petrology; Field Observations and High Pressure Experimentation: A tribute to Francis R. (Joe) Boyd. Editors: Fei, Y., Bertka, C. M. and Mysen, B.O. pp. 125-153. The Geochemical Society, Special Publication No. 6.

Harte, B. (2010). Diamond formation in the deep mantle: the record of mineral inclusions and their distribution in relation to mantle dehydration zones. Mineralogical Magazine 74, 189-215.

Harte, B. (2011) Diamond Window into the Lower Mantle. Science, 334, 51-52.

Herzber, C., Condie, K., and Korenaga, J. (2010) Thermal history of the Earth and its petrological expression. Earth Planet Sci Lett, 292, 79-88.

Hirschmann, M.M. (2012) Magma ocean influence on early atmosphere mass and composition. Earth Planet Sci Lett, 341-344, 48-57.

Höfer, H.E., Brey, G. (2007). The iron oxidation state of garnet by electron microprobe: its determination with the flank method combined with major-elements analysis. American Mineralogist 92, 873-885.

Hopkins, M., Harrison, T.M., and Manning, C.E. (2008) Low heat flow inferred from >4 Gyr zircons suggests Hadean plate boundary interactions. Nature, 456, 493-496.

Isshiki, M., Irifune, T., Hirose, K., Ono, S., Ohishi, Y., Watanuki, T., Nishibori, E., Takata, M., and Sakata, M. (2004) Stability of magnesite and its high-pressure form in the lowermost mantle. Nature, 427, 60-63.

Jacob, D.E. (2004) Nature and origin of eclogite xenoliths from kimberlites. Lithos 77, 295–316.

Jacobsen, S.D., Reichmann, H.J., Spetzler, H.A., Mackwell, S.J., Smyth, J.R., Angel, R.J., McCammon, C.A. (2002). Structure and elasticity of single-crystal (Mg,Fe)O and a new method of generating shear waves for gigahertz ultrasonic interferometry. Journal of Geophysical Research 107, 2037.

Jerrard, R.D. (2004) Subduction fluxes of water, carbon dioxide, chlorine, and potassium. Geochem Geophys Geosyst, 4, 8905.

Jessberger, E.K., Christoforidis, A., and Kissel, J. (1988) Aspects of the major element composition of Halley's dust. Nature, 332, 691-695.

Joly, Y. (2001) X-ray absorption near-edge structure calculations beyond the muffin-tin approximation. PRB, 63, 125120

Kaminsky, F.V., and Wirth, R. (2011) Iron carbide inclusions in lower-mantle diamond from Juina, Brazil. Can Mineral, 49, 555-572.

Kaminsky, F. (2012) Mineralogy of the lower mantle: A review of 'super-deep' mineral inclusions in diamond. Earth-Science Reviews, 110, 127–147.

Kaminsky, F.V., Wirth, R., Schreiber, A. (2015a). A microinclusion of lower-mantle rock and other minerals and nitrogen lower-mantle inclusions in a diamond. Canadian Mineralogist 53, 83-104.

Kaminsky, F.V., Ryabchikov, I.D., McCammon, C.A., Longo, M., Abakumov, A.M., Turner, S., Heidari, H. (2015b). Oxidation potential in the Earth's lower mantle as recorded by ferropericlase inclusions in diamond. Earth and Planetary Science Letters 417, 49-56.

Kaneshima, S., and Helffrich, .G (2003) Subparallel dipping heterogeneities in the mid-lower mantle. JGR, 108, B5, DOI: 10.1029/2001JB001596.

Kang, N. *et al.* (2015) Melting of siderite to 20 GPa and thermodynamic properties of $FeCO_3$-melt. Chem. Geol., 400, 34-43.

Kantor, I., Dubrovinsky, L., McCammon, C., Kantor, A., Pascarelli, S., Aquilanti, G., Crichton, W., M., R., Almeida, J., and Urusov, V. (2006a) Pressure-induced phase transition in $Mg_{0.80}Fe_{0.20}O$ ferropericlase. Physics and Chemistry of Minerals, 33, 35-44.

Kantor, I. Yu., Dubrovinsky, L. S., and McCammon, C. (2006b) Spin crossover in (Mg,Fe)O: A Mössbauer effect study with an alternative interpretation of x-ray emission spectroscopy data. Physical Review B, 73, 100101(R).

Kantor, I. (2007) High-pressure and high-temperature structural and electronic properties of (Mg,Fe)O and FeO. 150 p. Ph.D Thesis, University of Bayreuth, Bayreuth.

Kantor, I. Yu., Prakapenka, V., Kantor, A., Dera, P., Kurnosov, A., Sinogeikin, S., Dubrovinskaia, N., and Dubrovinsky, L. (2012) BX90: A new diamond anvil cell design for X-ray diffraction and optical measurements. Review of Scientific Instruments, 83, 125102.

Katsura, T., Yoneda, A., Yamazaki, D., Yoshino, T., and Ito, E. (2010) Adiabatic temperature profile in the mantle. *Phys. Earth Planet. Inter.*, 183, 212-218.

Kelemen, P.B., and Manning, C.E. (2015) Reevaluating carbon fluxes in subduction zones, what goes down, mostly comes up. PNAS, 112, E3997-E4006.

Keppler, H.K. (1996) Constraints from partitioning experiments on the composition of subduction-zone fluids. Nature, 380, 237-240.

Keppler, H., Wiedenbeck, M., and Shcheka, S.S. (2003) Carbon solubility in olivine and the mode of carbon storage in the Earth's mantle. Nature, 242, 414-416.

Kerrick, D.M., and Connolly, J.A.D. (1998) Subduction of ophicarbonates and recycling of CO_2 and H_2O. Geology, 26, 375-378.

Kiseeva, E.S. (2012) An experimental study of carbonated eclogite at 3.5-5.5 GPa- Implications for silicate and carbonate metasomatism in the cratonic mantle. J Petrol, 53, 727-759.

Kissel, J. and Krueger, F.R. (1987) The organic component in dust from comet Halley as measured by the PUMA mass spectrometer on board Vega 1. Nature, 418, 952-955.

Komabayashi, T. et al. (2009) On the slab temperature in the deep lower mantle. AGU Sping Meeting Abstracts.

Koningsberger, D.C. (1996) XAFS spectroscopy - Physical Principles, Data-Analysis and Applications. Lecture Notes, 2nd International School and Symposium on Synchrotron Radiation in Natural Science, Jaszowiec.

Kupenko, I. *et al*. (2012) Portable double-sided laser-heating system for Mössbauer spectroscopy and X-ray diffraction experiments at synchrotron facilities with diamond anvil cells. Rev. Sci. Instrum. 83, 124501.

Kupenko et al. (2015) Oxidation state of the lower mantle: In situ observations of the iron electronic configuration in bridgmanite at extreme conditions. *Earth Planet Sci Lett*, 423, 78–86.

Kuramoto, K. (1997) Accretion, core formation, H and C evolution of the Earth and Mars. Phys Earth Planet Inter, 100, 3-20.

Kurnosov, A., Kantor, I., Boffa-Ballaran, T., Lindhardt, S., Dubrovisnky, L., Kuznetsov, A., and Zehnder, B.H. (2008) A novel gas-loading system for mechanically closing of various types of diamond anvil cells. Review of Scientific Instruments, 79, 045110.

Kvasnytsya, V.M., and Wirth, R. (2009) Nanoinclusions in microdiamonds from Neogenic sands of the Ukraine (Samotkan' Placer); a TEM study. Lithos, 113, 454-464.

Larson, A.C. and Von Dreele, R.B. (2000) General Structure Analysis System (GSAS). Los Alamos National Laboratory Report, LAUR 86-748.

Lasaga, A., and Gibbs, G.V. (1987(Applications of quantum mechanical potential surfaces to mineral physics calculations. Phys Chem Minerals, 14, 107-117.

Lavina B., Dera P., Downs R.T., Prakapenka V., Rivers M., Sutton S., and Nicol M. (2009) Siderite at lower mantle conditions and the effects of the pressure-induced spin-pairing transition. Geophysical Research Letters, 36, L23306.

Lavina, B., Dera, P., Downs, R. T., Yang, W., Sinogeikin, S., Meng, Y., Shenand, G., and Schiferl, D. (2010a) Structure of siderite FeCO3 to 56 GPa and hysteresis of its spin-pairing transition. Physical Review B, 82, 064110.

Lavina, B., Dera, P., Downs, R. T., Tschauner, O., Yang, W., Shebanova, O., and Shen, G. (2010b) Effect of dilution on the spin pairing transition in rhombohedral carbonates. High Pressure Research, 30, 224-229.

Lee, C-TA., Luffi, P., Höinkn T., Li, J., Dasgupta, R., and Hernlund, J. (2010) Upside-down differentiation and generation of a 'primordial' lower mantle. Nature, 463, 930-933.

Lin, J.-F., and Wheat, A. (2011) Electronic spin transition of iron in the Earth's lower mantle. Hyperfine Interact. 207, 81-88.

Lin, J.F., Liu, J., Jacobs, C., and Prakapenka, V.B. (2012) Vibrational and elastic properties of ferromagnesite across the electronic spin-pairing transition of iron. American Mineralogist, 97, 583-591.

Liu, J., Lin, J.F., Mao, Z., and Prakapenka, V.B. (2014) Thermal equation of state and spin transition of magnesiosiderite at high pressure and temperature. American Mineralogist, 99, 84-93.

Liu, J., Lin, J.-F., and Prakapenka, V.B. (2015) High-pressure orthorhombic ferromagnesite as a potential deep-mantle carbon carrier. Scientific Reports, 5, 7640, doi: 10.1038/srep07640.

Lobanov, S.S., Goncharov, A.F., and Litasov, K.D. (2015) Optical properties of siderite ($FeCO_3$) across the spin transition: Crossover to iron-rich carbonates in the lower mantle. Am. Min., 100, 1059-1064.

Lodders, K. (2003) Solar system abundances and condensation temperatures of the elements. Astrophys. J., 591, 1220-1247.

Longo, M., McCammon, C.A., Jacobsen, S.D. (2011). Microanalysis of the iron oxidation state in (Mg,Fe)O and application to the study of microscale processes. Contributions to Mineralogy and Petrology 162, 1249-1257.

Luth, R.W. (1999) Carbon and carbonates in the mantle. In: Mantle Petrology: Field Observations and High Pressure Experimentation: A Tribute to Francis R. (Joe) Boyd. Vol 6. The Geochemical Society, 297-316.

Mao, H.K., Xu, J., and Bell, P.M. (1986) Calibration of the ruby pressure gauge to 800 kbar under quasi-hydrostatic conditions. Journal of Geophysical Research, 91, 4673.

Mao, Z., Armentrout, M., Rainey, E., Manning, C.E., and Dera, P. (2011) Dolomite III: A new candidate lower mantle carbonate. Geophysical Research Letters, 38, L22303.

Marty, B. (2012) The origin and concentrations of water, carbon, nitrogen, and noble gases on Earth. Earth Planet. Sci. Lett., 313, 56-66.

Marty, B., Alexander, C.M.O'D., and Raymond, S.N. (2013) Primordial Origins of Earth's Carbon. Rev. Mineral. Geochem. 75, 149-181.

Mattila, A., Pylkkänen, T., Rueff, J.P., Huotari, S., Vankó, G., Hanfland, M., Lehtinen, M., and Hämäläinen K. (2007) Pressure induced magnetic transition in siderite $FeCO_3$ studied by x-ray emission spectroscopy. Journal of Physics: Condensed Matter, 19, 38, 386206.

McCammon, C.A. (1994). A Mössbauer milliprobe: Practical considerations. Hyperfine Interactions 92, 1235-1239.

McCammon, C.A., Hutchison, M.T., Harris, J.W. (1997). Ferric iron content of mineral inclusions in diamonds from São Luiz: a view into the lower mantle. Science 278, 434-436.

McCammon, C., and Kopylova, M.G. (2004) A redox profile of the Slave mantle and oxygen fugacity controlin the cratonic mantle. Contrib Mineral Petrol, 148, 55-68.

McCammon, C.A., Lauterbach, S., Seifert, F., Langenhorst, F., van Aken, P.A. (2004a) Iron oxidation state in lower mantle mineral assemblages I. Empirical relations derived from high-pressure experiments. Earth and Planetary Science Letters 222, 435-449.

McCammon, C.A., Stachel, T., Harris, J.W. (2004b) Iron oxidation state in lower mantle mineral assemblages: II. Inclusions in diamonds from Kankan, Guinea. Earth and Planetary Science Letters 222, 423-434.

McCammon, C. (2005) The paradox of mantle redox. Science, 308, 807–808.

McCammon, C., Dubrovinsky, L., Narygina, O., Kantor, I., Wu, X., Glazyrin, K., Sergueev, I., and Chumakov, A.I. (2010) Low-spin Fe^{2+} in silicate perovskite and a possible layer at the base of the lower mantle. Physics of the Earth and Planetary Interiors, 180, 215-221.

McDonough, W.F. (2003) Compositional model for the Earth's core. In: The mantle and core. Vol. 2. Carlson R.W. (ed) Elsevier-Pergamon, Oxford, 547-568.

Meng, Y., Weidner, D.J., and Fei, Y. (1993) Deviatoric stress in a quasi-hydrostatic diamond anvil cell: Effect on the volume-based pressure calibration. Geophysical Research Letters, 20, 1147-1150.

Merlini, M., Crichton, W.A., Hanfland, M., Gemmi, M., Mueller, H., Kupenko, I., and Dubrovinsky, L. (2012) Structures of dolomite at ultrahigh pressure and their influence on the deep carbon cycle. Proceedings of the National Academy of Sciences, 109, 13509-13514.

Merlini, M., and Hanfland, M. (2013) Single-crystal diffraction at megabar conditions by synchrotron radiation. High Pressure Research: an International Journal, 33, 511-522.

Merlini, M., Hanfland, M., Salamat, A., Petitgirard, S. and Müller, H. (2015) The crystal structures of $Mg_2Fe_2C_4O_{13}$, with tetrahedrally coordinated carbon, and $Fe_{13}O_{19}$, synthesized at deep mantle conditions. Am. Min., 100, 2001-2004.

Merrill, L., and Basset, W.A. (1975) The crystal structure of $CaCO_3$-(II), a high-pressure metastable phase of calcium carbonate. Acta Cryst., B31, 343-349.

Morbidelli, A., Lunine, J.L., O'Brien, D.P., Raymond, S.N., Walsh, K.J. (2012) Building terrestrial planets. Ann. Rev. Earth Planet. Sci., 40, 251-275.

Mottana, A. (2004) X-ray absorption spectroscopy in mineralogy: Theory and experiment in the XANES region. EMU Notes in Mineralogy, 6, 465-552.

Motti, M.J., Wheat, C.G., Fryer, P. Gharib, J. Martin, B.J. (2004) Chemistry of springs across the Mariana forearc shows progressive devolatilization of the subducting plate. Geochim. Cosmochim. Acta, 68, 4915-4933.

Mozley, P.S. (1989) Relation between depositional environment and the elemental composition of early diagenetic siderite. Geology, 17, 704-706.

Müler, U. Inorganic Structural Chemistry, *Wiley* 2007

Nakatsuka, A. *et al.* (2011) Static disorders of atoms and experimental determination of Debye temperature in pyrope: Low- and high-temperature single-crystal X-ray diffraction study. Am. Min., 96, 1593-1605

Narygina, O., Mattesini, M., Kantor, I., Pascarelli, S., Wu, X., Aquilanti, G., McCammon, C., and Dubrovinsky, L. (2009) High-pressure experimental and computational XANES studies of $(Mg,Fe)(Si,Al)O_3$ perovskite and $(Mg,Fe)O$ ferropericlase as in the Earth's lower mantle. Physical Review B, 79, 174115.

Nestola, F., Smyth J.R. (2016). Diamonds and water in the deep Earth: a new scenario. International Geology Review 58, 263-276.

Nestola, F., Nimis, P., Angel, R., Milani, S., Bruno, M., Prencipe, M., Harris, J. (2014) Olivine with diamond-imposed morphology included in diamonds. Syngenesis or protogenesis? International Geology Review 56, 1658-1667.

Nestola, F., Burnham, A.D., Peruzzo, L., Tauro, L., Alvaro, M.,Walter, M.J., Gunter, M., Kohn, S.C. (2016) Tetragonal Almandine-Pyrope Phase, TAPP: finally a name for it, the new mineral jeffbenite. Mineralogical Magazine, doi: 10.1180/minmag.2016.080.059.

Nestola, F., Nimis, P., Ziberna, L., Longo, M., Marzoli, A., Harris, J.W., Manghnani, M.H., Fedortchouk, Y. (2011) First crystal-structure determination of olivine in diamond: Composition and implications for provenance in the Earth's mantle. Earth and Planetary Science Letters 305, 249-255.

Oganov, A.R., Glass, C.W., and Ono, S. (2006) High-pressure phases of $CaCO_3$: Crystal structure prediction and experiment. Earth Planet. Sci. Lett, 241, 95-103.

Oganov, A.R., Ono, S., Ma, Y.M., Glass, C.W., and Garcia, A. (2008) Novel high-pressure structures of $MgCO_3$, $CaCO_3$, and CO_2 and their role in earth's lower mantle. Earth Planet Sci Lett, 273, 38-47.

Oganov et al. (2013) Structure, Bonding, and Mineralogy of Carbon at Extreme Conditions. Rev. Mineral. Geochem, 75, 47-77.

O'Neill, H.S.C., Annersten, H., Virgo, D. (1992). The temperature dependence of the cation distribution in magnesioferrite ($MgFe_2O_4$) from powder XRD structural refinements and Mössbauer spectroscopy. American Mineralogist 77, 725-740.

Ono, S., Kikegawa, T., Ohishi, Y., and Tsuchya, J. (2005) Post-aragonite phase transformation in CaCO3 at 40 GPa. American Mineralogist, 90, 667-671.

Ono, S., Kikegawa, T., & Ohishi, Y. (2007) High-Pressure Transition of $CaCO_3$. Am. Min., 92, 1246–1249.

Ovsyannikov, S. *et al.* (2016) Charge-ordering transition in iron oxide Fe_4O_5 involving competing dimer and trimer formation. Nat. Chem, 8, 501–508.

Otsuka, K., Longo, M., McCammon, C.A., Karato, S. (2013) Ferric iron content of ferropericlase as a function of composition, oxygen fugacity, temperature and pressure: Implications for redox conditions during diamond formation in the lower mantle. Earth and Planetary Science Letters 365, 7-16.

Owen, T., Bar-Nun, A., and Kleinfeld, I. (1992) Possible cometary origin of heavy noble gases in the atmospheres of Venus, Earth and Mars. Nature, 358, 43-46.

Palot, M., Jacobsen, S.D., Townsend, J.P., Nestola, F., Marquardt, K., Harris, J.W., Stachel, T., McCammon, C.A., Pearson, D.G., 2016. Evidence for water in the lower mantle from ferropericlase included in diamond. Nature Geoscience, submitted.

Pascarelli, S., Mathon, O., Muñoz, M., Mairs, T., and Susini J. (2006) Energy-dispersive absorption spectroscopy for hard-X-ray micro-XAS applications. Journal of Synchrotron Radiation, 13, 351-358.

Pearson, D.G., Brenker, F., Nestola, F., McNeill, J., Nasdala, L., Hutchison, M.T., Matveev, S., Mather, K., Silversmit, G., Schmitz, S., Vekemans, B., Vincze, L. (2014). A hydrous mantle transition zone indicated by ringwoodite included within diamond. Nature 507, 221–224.

Pepin, R.O. (2006) Atmosphere on the terrestrial planets: clues to origin and evolution. Earth Planet. Sci. Lett., 252, 1-14.

Popkov, Yu. A., Eremenko, V.V., Fomin, V.I., and Mokhir, A.P. (1973) Raman scattering of light in antiferromagnetic siderite. Soviet Physics - Solid State, 14, 1985-1989.

Potapkin, V., Chumakov, A.I., Smirnov, G.V., Celse, J.P., Rüffer, R., McCammon, C., and Dubrovinsky, L. (2012) The ^{57}Fe Synchrotron Mössbauer Source at the ESRF. Journal of Synchrotron Radiation, 19, 559-569.

Prescher, C., McCammon, C., and Dubrovisnky, L. (2012a) MossA: a program for analyzing energy-domain Mössbauer spectra from conventional and synchrotron sources. Journal of Applied Crystallography, 45, 329-331.

Prescher, C., Dubrovinsky, L., McCammon, C., Glazyrin, K., Nakajima, Y., Kantor, A., Merlini, M., and Hanfland, M. (2012b) Structurally hidden magnetic transitions in Fe3C at high pressures. Physical Review B, 85, 140402.

Ravel, B., and Newville, M. (2005) ATHENA, ARTEMIS, HEPHAESTUS: data analysis for X-ray absorption spectroscopy using IFEFFIT. Journal of synchrotron radiation, 12, 537–41.

Raymond, S.N., Quinn, T., Lunine, J.I. (2006) High-resolution simulations of the final assembly of Earth-like planets I. Terrestrial accretion and dynamics. Icarus, 183, 265-282.

Ravel, B., and Newville, M. (2005) ATHENA, ARTEMIS, HEPHAESTUS: data analysis for X-ray absorption spectroscopy using IFEFFIT. Journal of synchrotron radiation, 12, 537–41.

Rea, D.K., and Ruff, L.J. (1996) Composition and mass flux of sediment entering the world's subduction zones: Implication for global sediment budgets, great earthquakes, and volcanism. Earth Planet Sci Lett, 140, 1-12.

Rehr, J.J., and Albers, R.C. (2000) Theoretical Approaches to X-ray Absorption Fine Structure. Rev. Mod. Phys., 72, 621.

Richardson, S.H., Harris, J.W. (1997). Antiquity of peridotitic diamonds from the Siberian craton. Earth and Planetary Science Letters 151, 271–277.

Robinson, K. Gibbs, G.V., and Ribbe, P.H. (1971) Quadratic elongation: A quantitative measure of distortion in coordination polyhedral. Science, 172, 567-570.

Rohrbach et al. (2007) Metal saturation in the upper mantle. Nature, 449, 456-458.

Rohrbach, A., and Schmidt, M.W. (2011) Redox freezing and melting in the Earth's deep mantle resulting from carbon-iron redox coupling. Nature, 472, 209-212.

Rosenberg, P. E. (1967) Subsolidus relations in system $CaCO_3$-$MgCO_3$-$FeCO_3$ between 350° and 500° C. American Mineralogist, 52, 787-796.

Ross, N.L., and Reeder, R.J. (1992) High –pressure structural study of dolomite and ankerite. American Mineralogist, 77, 412-421.

Rubie D.C., Nimmo F., Melosh H.J. (2007). Formation of Earth's core. Treatise Geophys. 9, 51-90.

Rubie et al. (2011) Heterogenous accretion, composition, and core-mantle differentiation of the Earth. Earth Planet Sci Lett, 301, 31-42.

Rüffer, R., and Chumakov, A.I. (1996) Nuclear Resonance Beamline at ESRF. Hyperfine Interactions, 97/98, 589-604.

Rutt, H.N., and Nicola, J.H. (1974) Raman spectra of carbonates of calcite structure. Journal of Physics C: Solid State Physics, 7, 4522.

Santillán, J., and Williams, Q. (2004) A high-pressure infrared and X-ray study of $FeCO_3$ and $MnCO_3$: comparison with $CaMg(CO_3)_2$-dolomite. Physics of the Earth and Planetary Interiors, 143-144, 291-304.

Shannon, M.C., and Agee, C.B. (1996) High pressure constraints on percolative core formation. Geophys Res Lett, 23, 2717-2720.

Shcheka, S.S., Wiedenbeck, M., Frost, D.J., Keppler, H. (2006) Carbon solubility in mantle minerals. Earth Planet Sci Lett, 245, 730-742.

Sheldrick, G. M. (2008) A short history of SHELX. Acta Cryst. 64, 112–122.

Shi, H., Luo, W. Johansson, B., and Ahuja, R. (2008) First-principles calculations of the electronic structure and pressure-induced magnetic transition in siderite $FeCO_3$. Physical Review B, 78, 155119.

Shirey, S.B., and Richardson, S.H. (2011) Start of the Wilson cycle at 3 ga shown by diamonds from subcontinental mantle. Science, 333, 434-436.

Shirey, S.B., Cartigny, P., Frost, D.J., Keshav, S., Nestola, F., Nimis, P., Pearson, D.G., Sobolev, N.V., Walter, M.J. (2013). Diamonds and the geology of mantle carbon. Reviews in Mineralogy and Geochemistry 75, 355-421.

Silversmit, G., Vekemans, B., Appel, K., Schmitz, S., Schoonjans, T., Brenker, F.E., Kaminsky, F., Vincze, L. (2011). Three-dimensional Fe speciation of an inclusion cloud within an ultradeep diamond by confocal μ-X-ray Absorption Near Edge Structure: evidence for late stage overprint. Analytical Chemistry 83, 6294-6299.

Skorodumova, N.V., Belonoshko, A.B., Huang, L., Ahuja, R., and Johansson, B. (2005) Stability of the $MgCO_3$ structures under lower mantle conditions. Am. Min., 90, 1008-1012.

Smirnov, G. V., van Bürck, U., Chumakov, A.I., Baron, A.Q.R., Rüffer, R. (1997). Synchrotron Mössbauer source. Phys. Rev. B 55, 5811–5815.

Sobolev, N.V., Fursenko, B.A., Goryainov, S.V., Shu, J., Hemley, R.J., Mao, A., Boyd, F.R. (2000). Fossilized high pressure from the Earth's deep interior: the coesite-in-diamond barometer. PNAS 97, 11875-11879.

Solopova, N. A. *et al.* (2014) Melting and decomposition of $MgCO_3$ at pressures up to 84 GPa. Phys Chem Miner, 42, 73-81

Stagno, V., and Frost, D.J. (2010) Carbon speciation in the asthenosphere: Experimental measurements of the redox conditions at which carbonate-bearing melts coexist with graphite or diamond in peridotite assemblages. Earth Planet Sci Lett, 200, 72-84.

Stachel, T., Harris, J.W. (2008). The origin of cratonic diamonds—constraints from mineral inclusions. Ore Geology Review 34, 5–32.

Stagno, V., Tange, Y., Miyajima, N., McCammon, C.A., Irifune, T., and Frost, D.J. (2011) The stability of magnesite in the transition zone and lower mantle as function of oxygen fugacity. Geophysical Research Letters, 38, L19309.

Sturhahn, W., Jackson, J. M., and Lin, J.F. (2005) The spin state of iron in minerals of Earth's lower mantle. Geophysical Research Letters, 32, 1-5.

Syracuse, E.M., van Keken, P.E., and Abers, G.A. (2010) The global range of subduction zone thermal models. Phys. Earth Planet. Inter, 183, 73-90.

Takley, P.J., Stevenson, D.J., Glatzmaier, G.A. and Schubert, G. (1993) Effects of an endothermic phase transition at 670 km depth in a spherical model of convection in the Earth's mantle. Nature, 361, 699-703.

Tao, R., Fei, Y. & Zhang, L. (2013) Experimental determination of siderite stability at high pressure. Am. Min., 98, 1565-1572

Takemura, K. (2001) Evaluation of the hydrostaticity of a helium-pressure medium with powder x-ray diffraction techniques. Journal of Applied Physics, 89, 662, DOI: 10.1063/1.1328410.

Thomas, K.L., Blanford, G.E., Keller, L.P. Kloeck, W., and McKay, D.S. (1993) Carbon abundance and silicate mineralogy of anhydrous interplanetary dust particles. Geochim Cosmoschim. Acta, 57, 1551-1566.

Thomson, A.R., Walter, M.J., Kohn, S.C. & Brooker, R.A. (2015) Slab melting as a barrier to deep carbon subduction. Nature, 529, 76-79.

Toby, B. H. (2001) EXPGUI, a graphical user interface for *GSAS*. J. Appl. Cryst, 34, 210-213.

Trots et al. (2013) The Sm:YAG primary fluorescence pressure scale. JGR: Solid Earth, 118, 5805–5813.

Trull, T., Nadeau, S., Pineau, F., Polve, M., and Javoy, M. (1993) C-He systematics in hotspots xenoliths: implications for mantle carbon contents and carbon recycling. Earth Planet. Sci. Lett., 118, 43-64.

Wagner, C., Riggs, W., Davis, L., and Moulder, J. (1979) Handbook of x-ray photoelectron spectroscopy. Edited by G.E. Muilenberg, Perkin Elmer Corporation, Eden Prairie, Minnesota.

Wallace, M.E., and Green, D.H. (1988) An experimental determination of primary carbonatite magma composition. Nature, 335, 54-57.

Walsh, K.J., Morbidelli, A., Raymond, S.N., O'Brien, D.P., and Mandell, A.M. (2005) A low mass for Mars from Jupiter's early gas-driven migration. Nature, 475, 206-209.

Walter, M.J., Kohn, S.C., Araujo, D., Bulanova, G.P., Smith, C.B., Gaillou, E., Wang, J., Steele, A., and Shirey, S.B. (2011) Deep Mantle Cycling of Oceanic Crust: Evidence from Diamonds and Their Mineral Inclusions. Science, 334, 54-57.

Weidner, D.J., Wang, Y., and Vaughan, M.T. (1994) Yield strength at high pressure and temperature. Geophysical Research Letters, 21, 753-756.

Weir, C., Lippincott, E., Van Valkenburg, A., Bunting, E., (1959). Infrared studies in the 1- to 15-micron region to 30,000 atmospheres. J. Res. NBS, Sect. A Phys. Chem. 63A.

Westre, T. E., Kennepohl, P., DeWitt, J. G., Hedman, B., Hodgson, K. O., and Solomon, O. E. (1997) A Multiplet Analysis of Fe K-Edge 1s → 3d Pre-Edge Features of Iron Complexes. Journal of the American Chemical Society, 119, 6297-6314.

Wierzbicka-Wieczorek, M., Kolitsch, U., & Tillmanns E. (2010) $Ba_2Gd_2(Si_4O_{13})$: a silicate with finite Si_4O_{13} chains. *Acta Cryst. C*, 66, i29-i32

Wilke, M., Farges, F., Petit, P. E., Brown, Jr. G. E., and Martin, F. (2001) Oxidation state and coordination of Fe in minerals: an Fe K XANES spectroscopic study. American Mineralogist, 86, 714-730.

Wilke, M., Farges, F., Partzsch, G.M., Schmidt, C., and Behrens, H. (2007) Speciation of iron in silicate glasses and melts by in-situ XANES spectroscopy. American Mineralogist, 92, 44-56.

Wöll, C., and Wühn, M. (1999) Spektroskopie von elektronischer Struktur und molekularer Orientierung mittels NEXAFS. Lehrstuhl für Physikalische Chemie I, Ruhr-Universität Bochum, Bochum.

Wood, B. J. (1993) Carbon in the Core. Earth and Planetary Science Letters, 117, 593-607.

Woodland, A.B., and Koch, M. (2003) Variation in oxygen fugacity with depth in the upper mantle beneath the Kaapvaal craton, Southern Africa. Earth Planet Sci Lett, 214, 295-310.

Yaxley, G.M., and Green, D.H. (1994) Experimental demonstration of refractory carbonate-bearing eclogite and siliceous melt in the subduction regime. Earth Planet Sci Lett, 128, 313-325.

Yi, W. et al. (2000) Cadmium, indium, tin, tellurium, and sulfur in oceanic basalts: Implications for chalcophile element fractionation in the Earth. J Geophys Res, 105, 18927-18948.

Zhao, D. (2003) Global tomographic images of mantle plumes and subducting slabs: insight into deep Earth dynamics. PEPI, 146, 3-34.

Zhao, J., Angel, R.J., and Ross N.L. (2010) Effects of deviatoric stresses in diamonds-anvil cell on single-crystal samples. Journal of Applied Crystallography, 43, 743-751.

Zhang, J., and Reeder, R.J. (1999). Comparative compressibilities of calcite-structure carbonates: deviations from empirical relations. American Mineralogist, 84, 861–870.

(Eidesstattliche) Versicherungen und Erklärungen

(§ 8 S. 2 Nr. 6 PromO)

Hiermit erkläre ich mich damit einverstanden, dass die elektronische Fassung meiner Dissertation unter Wahrung meiner Urheberrechte und des Datenschutzes einer gesonderten Überprüfung hinsichtlich der eigenständigen Anfertigung der Dissertation unterzogen werden kann.

(§ 8 S. 2 Nr. 8 PromO)

Hiermit erkläre ich eidesstattlich, dass ich die Dissertation selbständig verfasst und keine anderen als die von mir angegebenen Quellen und Hilfsmittel benutzt habe.

(§ 8 S. 2 Nr. 9 PromO)

Ich habe die Dissertation nicht bereits zur Erlangung eines akademischen Grades anderweitig eingereicht und habe auch nicht bereits diese oder eine gleichartige Doktorprüfung endgültig nicht bestanden.

(§ 8 S. 2 Nr. 10 PromO)

Hiermit erkläre ich, dass ich keine Hilfe von gewerblichen Promotionsberatern bzw. - vermittlern in Anspruch genommen habe und auch künftig nicht nehmen werde.

Grenoble, den 21. September 2017

Valerio Cerantola